

DISS. ETH NO. 26450

Distributions of molecular conformations and
interactions revealed by EPR spectroscopy -
methodology and application to hnRNPA1

A thesis submitted to attain the degree of
DOCTOR OF SCIENCES of ETH ZURICH
(Dr. Sc. ETH Zurich)

presented by
IRINA KERSTIN RITSCH
MSc ETH Interdisciplinary Science

born on 04.08.1992
citizen of Austria

accepted on the recommendation of
Prof. Dr. Gunnar Jeschke, examiner
Dr. Maxim Yulikov, co-examiner
Prof. Dr. Frédéric Allain, co-examiner
Prof. Dr. Beat Meier, co-examiner

2019

To my

Ohana



Abstract

Proteins are long chains of peptide-bond linked amino acids, which have the fascinating ability to fold into a huge variety of three-dimensional shapes. To describe peptide sequences that have particularly large conformational flexibility, the umbrella terms intrinsically disordered domains (IDDs), resp. proteins (IDPs) have emerged. Many different combinations of amino acid composition (both polar, or hydrophobic) and sequence have been identified as IDDs, with the unifying feature that the domains are enriched in only a few types of amino acids, thus also referred to as low complexity domains (LCDs). The complex conformations and interactions of IDPs have recently been shown to be important for example in cellular processes, such as stress response, which has initiated a new era in structural biology. Building on the well-established structural characterisation of folded domains, the aim of biophysical characterisation extends also to understanding the dynamics and intrinsic conformational flexibility of proteins. A multitude of biophysical and biochemical methods have been developed for the former aspect, which include X-ray crystallography, nuclear magnetic resonance (NMR), single molecule fluorescence techniques, and more recently, high resolution cryo-electron microscopy to elucidate biomolecular structures. Structural characterisation of proteins containing IDDs, however, is notoriously difficult precisely due to the large conformational space and faster inter-changing of conformations. An additional experimental complication is that disordered protein domains often have a strong tendency to interact with other biomolecules, or with themselves, making it virtually impossible to study isolated molecules.

In this thesis we present methods based on electron paramagnetic resonance (EPR) spectroscopy to characterise biomolecular structures and interactions in highly disordered systems, where a large distribution of states is encountered. As a biologically relevant application we demonstrate how well-established pulsed dipolar spectroscopy (PDS) methods can be applied for the structural characterisation of the partially disordered human protein 'heterogeneous nuclear ribonucleoprotein A1' (hnRNPA1). Approximately the last carboxy-terminal third of hnRNPA1 is an LCD, enriched in glycine and arginine residues. It is known, for example from solution state NMR, that the LCD of hnRNPA1 is an IDD, and exhibits fast dynamics at ambient temperature. Furthermore, the IDD

of hnRNPA1 is known to mediate a process known as liquid-liquid phase separation (LLPS) both *in vivo* (under conditions of stress), and *in vitro*.

We use site-directed spin labelling and a combination of continuous wave and pulsed EPR spectroscopy to address the structural characterisation of hnRNPA1 *in vitro*. We identify protein-protein interactions by pulsed double electron-electron resonance (DEER) experiments with singly spin-labelled hnRNPA1, and we determine buffer conditions in which we are able to study predominantly monomeric hnRNPA1. These stabilised conditions consequently allowed us to perform pair-wise distance measurements between spin labelling sites in the folded domains of hnRNPA1 and sites in the IDD by DEER experiments on doubly spin-labelled hnRNPA1. The probabilistic interpretation of the DEER experiments in terms of distance distributions enabled us to use a large set of distance restraints for the generation of an ensemble model of full length hnRNPA1. This ensemble model can be validated against additional, independent biophysical experiments.

Following the characterisation of the free state of the protein we present experimental results for the characterisation of samples of full length hnRNPA1 after inducing LLPS. They are of particular interest in combination with RNA-binding experiments, since it is known that RNA binding and LLPS are tightly linked processes for many protein involved in RNA processing, which is also what we found for hnRNPA1. In the experiments using RNA and hnRNPA1 we encountered situations where it is a great benefit to be able to detect multiple pair-wise distance in a spin-labelled sample. PDS with spectroscopically orthogonal spin labels has been developed as a powerful extension of conventional distance measurements between like spin labels, and offers promising opportunities towards this goal.

In the methodological part of this thesis we describe method development towards the application of spectroscopically orthogonal spin labels for the routine characterisation of biomolecules and biomolecular complexes. We discuss existing approaches with PDS and spectroscopically orthogonal spin labels, in particular the DEER experiment between Gd(III)-based spin labels and nitroxides. The RIDME technique is an emerging complementary method to the currently predominantly used DEER technique in many situations. In particular, we describe a detailed analysis of the performance of RIDME for distance measurements between nitroxide and Cu(II)-based spin labels using experiments with molecular rulers. A broadband microwave pulse version of the RIDME experiment was introduced in this context. Broadband coherent excitation of the nitroxide spin allowed both one-step orientation averaging, and EPR-correlated RIDME experiments. Building on the Cu(II)-nitroxide experiments, we performed experiments with molecular rulers for nitroxide high-spin pairs (in particular with Gd(III) and Mn(II) metal ions). Additional considerations must be made when using the RIDME experiments with high spin metal ion-based spin labels for distance analysis, due to contributions of harmonic overtones of the dipolar coupling frequency.



Zusammenfassung

In dieser Dissertation werden Methoden der gepulsten Elektronenspinresonanz (EPR) präsentiert, die zur Charakterisierung von ungeordneten biomolekularen Polymeren, im Speziellen Proteindomänen verwendet werden. Der Fokus liegt auf gepulsten EPR Methoden zur Detektion von schwachen magnetischen Dipolwechselwirkungen. Im ersten Teil der Arbeit werden gut etablierte Methoden der EPR Spektroskopie verwendet, um das partiell ungeordnete Protein hnRNPA1 zu untersuchen. An diesem, und weiteren Beispielen wird allerdings auch gezeigt, dass besonders zur Untersuchung von Systemen mit mehreren (biomolekularen) Komponenten die etablierten Methoden manchmal an ihre Grenzen kommen. Im zweiten Teil der Arbeit wird daher in mehr Tiefe auf eine neu aufkommende Methode der Dipolspektroskopie, das sogenannte 'relaxation induced dipolar modulation enhancement' (RIDME) Experiment eingegangen.

Die Erforschung der dreidimensionalen Strukturen von Biomolekülen hat zu einer Fülle an Erkenntnissen über deren Funktionen und deren Interaktionen geführt. Dazu hat massgeblich die Entwicklung hochauflösender biophysikalischer Methoden, wie zum Beispiel die Röntgenstrukturanalyse, die Kernspinresonanz oder, als relativ neue Methode, die hochaufgelöste Kryoelektronenmikroskopie, beigetragen. Zum Zeitpunkt der Verfassung dieser Dissertation sind bereits über 48000 Einträge in der 'protein data bank' (PDB), einer der grössten Datenbanken für biomolekulare Strukturen zugänglich.

Die Ausgangslage ist allerdings erschwert, wenn es sich um die strukturelle Aufklärung von Biomolekülen handelt, die die intrinsische Eigenschaften haben, mehr als eine stabile Konformation anzunehmen. Proteine, oder Proteindomänen, auf die dies zutrifft, werden intrinsisch 'ungeordnete' Domänen genannt (intrinsically disordered domain, IDD), und, zusätzlich zu der Vielfalt an Konformationen, sind sie schwierig zu charakterisieren, weil sie oft zu starken Interaktionen mit anderen Biomolekülen, oder mit sich selbst tendieren. Aufgrund der oft resultierenden hohen lokalen Proteinkonzentration, und aufgrund der hohen Flexibilität und Dynamik der Biomoleküle

ist die strukturelle Charakterisierung von IDDs mit vielen etablierten biophysikalischen Methoden schwierig. Die Elektronenspinresonanz bietet dafür spezielle Möglichkeiten, da eine Vielzahl an Experimenten entwickelt wurde, die speziell auf die Interpretation von teilweise ungeordnete Systemen angepasst sind.

Im anwendungsorientierten Teil dieser Arbeit werden Ergebnisse mit gerichteter Spinmarkierung des menschlichen Spleissingregulatorproteins hnRNPA1 (heterogeneous nuclear ribonucleoprotein A1) präsentiert. Eine Kombination aus Dauerstrich und gepulster EPR wurde verwendet, um die Konformationen der carboxyterminalen, intrinsisch ungeordneten Domäne von hnRNPA1 zu charakterisieren. Basierend auf Abstandsmessungen zwischen spinmarkierten Positionen in hnRNPA1 wurde ein atomistisches Ensemble-Modell des Proteins erstellt.

Eine Eigenschaft von ungeordneten Proteinen, oder Proteinen mit intrinsisch ungeordneten Domänen, ist die hohe Propensität Phasenseparation in der flüssigen Phase zu propagieren. Dabei entstehen mindestens zwei entmischte flüssige Phasen, was meist als Tröpfchenbildung beobachtet wird. Die so entstehenden Tröpfchen (liquid droplets, LDs) haben weiterhin die Eigenschaften einer flüssigen Phase, können zum Beispiel fusionieren. Tröpfchenbildung kann sowohl *in vivo* in Zellen unter Stressbedingungen, als auch *in vitro* unter kontrollierten Pufferbedingungen beobachtet werden. Dieser Prozess ist bei hnRNPA1 und verwandten RNA-bindenden Proteinen eng mit der Interaktion mit Oligonucleotiden verbunden. Beide Vorgänge wurden in dieser Dissertation an hnRNPA1 mithilfe von EPR Experimenten untersucht.

Besonders bei den Experimenten zur Interaktion mit RNA wird dabei deutlich, dass gleichzeitige Abstandsmessungen zwischen mehreren molekularen Positionen in einer Probe in vielen Situationen sehr hilfreiche Einblicke geben können. Eine elegante Möglichkeit dies zu erreichen kann mit spektroskopisch orthogonalen Spinmarkern realisiert werden. In den methodologischen Kapiteln dieser Dissertation wird eine neu aufkommende Methode der gepulsten EPR Dipolspektroskopie, das sogenannte RIDME Experiment (relaxation induced dipolar modulation enhancement), im Detail analysiert. Die Messungen dazu wurden an Molekülen mit wohldefinierten, und bekannten Abständen zwischen einem Nitroxide, und einem Metallionen-Komplex gemacht, welche als Modellsysteme für biologische Proben entworfen wurden. Diese molekularen Stäbchen sind gut dafür geeignet die Methode für Abstandsmessungen zu kalibrieren, und potentielle Artefaktquellen zu identifizieren. Eine Variante des RIDME Experiments mit breitbandigen, kohärenten Mikrowellenpulsen wurde entwickelt, die direkt orientierungsaufgelöste RIDME Spektroskopie erlaubt.

List of abbreviations

- ALS** amyotrophic lateral sclerosis. 1
- AWG** arbitrary waveform generator. 23
- CW** continuous wave. 9
- DEER** double electron electron resonance. 2
- DNA** deoxy-ribonucleic acid. 7
- DQC** double quantum coherence. 25
- EPR** electron paramagnetic resonance. 1
- FRAP** fluorescence recovery after photobleaching. 4
- FT** Fourier transform. 21
- FUS** fused in sacroma (protein). 7
- FWHM** full width half maximum. 23
- hnRNPA1** heterogeneous nuclear ribonucleoprotein A1. 1
- IBMPFD3** inclusion body myopathy. 5
- IDD** intrinsically disordered domain. 1
- IR** inversion recovery. 25
- LD** liquid droplet. 3

LLPS liquid-liquid phase separation. 1

MW microwave. 16

NMR nuclear magnetic resonance. 5

NOE nuclear Overhauser effect. 10

OIA offset independent adiabaticity. 21

PDS pulsed dipolar spectroscopy. 2, 25

PELDOR pulsed electron double resonance. 2

Q-band ~ 34 GHz, actually 'K_a-band'. 3, 22

RF radio frequency. 17

RIDME relaxation induced dipolar modulation enhancement. 2

RNA ribonucleic acid. 7

RRM RNA recognition motif. 2

SDSL site-directed spin labelling. 2

SIFTER single frequency technique for refocusing. 25

UP1 unwinding protein 1. 6

UWB ultra wideband. 26

W-band ~ 95 GHz. 22

X-band ~ 9.5 GHz. 9, 22

Contents

| | |
|--|------------|
| Abstract | v |
| Zusammenfassung | vii |
| List of abbreviations | xi |
| 1 General introduction | 1 |
| 1.1 Scope of this thesis | 1 |
| 1.2 Protein condensates | 3 |
| 1.3 hnRNPA1 | 5 |
| 1.4 SDSL-EPR in structural biology | 7 |
| 1.4.1 Static versus dynamic averaging of spin interactions | 8 |
| 1.4.2 Nitroxide spin label interactions in CW X-band spectra | 9 |
| 2 General EPR Theory and Methods | 13 |
| 2.1 Electron and nuclear spin | 14 |
| 2.1.1 Quantum mechanical description of spin | 14 |
| 2.2 Spin Hamiltonian and energy levels | 16 |
| 2.2.1 Zeeman interaction | 16 |
| 2.2.2 Electron spin - nuclear spin interaction | 17 |
| 2.2.3 Weak electron spin - electron spin interactions | 18 |
| 2.2.4 Strong electron spin - electron spin interactions | 19 |
| 2.2.5 Interaction with microwave irradiation | 19 |
| 2.3 Spin dynamics | 20 |
| 2.3.1 Monochromatic MW irradiation and the rotating frame | 20 |
| 2.3.2 Frequency-swept MW pulses | 21 |
| 2.4 Selected experimental EPR methods | 22 |

| | | |
|----------|---|-----------|
| 2.4.1 | Resonators | 23 |
| 2.4.2 | Continuous wave EPR | 23 |
| 2.4.3 | Pulsed EPR | 23 |
| 2.5 | Selected pulsed EPR techniques | 24 |
| 2.5.1 | Nutation experiments and resonator characterisation | 24 |
| 2.5.2 | Spin relaxation measurements | 24 |
| 2.5.3 | Pulsed dipolar spectroscopy for distance measurements | 25 |
| 3 | Identifying protein-protein interactions of hnRNPA1 by EPR | 31 |
| 3.1 | Introduction | 33 |
| 3.1.1 | Intermolecular Interactions in DEER | 33 |
| 3.1.2 | Paramagnetic Relaxation Enhancement | 38 |
| 3.2 | Results | 40 |
| 3.2.1 | Spin labelling of hnRNPA1 | 40 |
| 3.2.2 | Relating the macroscopic protein condensation state to EPR measurements | 42 |
| 3.2.3 | Residual protein-protein interactions in monomer-stabilised samples | 46 |
| 3.2.4 | Intermolecular PRE in the dispersed state | 50 |
| 3.2.5 | Intra-RRM distance measurements for beacon validation | 53 |
| 3.3 | Discussion and Conclusion | 53 |
| 3.4 | Materials and methods | 56 |
| 3.4.1 | Mutagenesis and protein over-expression | 56 |
| 3.4.2 | Protein Purification | 56 |
| 3.4.3 | Spin Labelling and DEER sample preparation | 57 |
| 3.4.4 | Circular dichroism measurements | 57 |
| 3.4.5 | DEER Measurements | 58 |
| 3.4.6 | PRE Measurements | 58 |
| 4 | Models of full length hnRNPA1 based on DEER restraints | 61 |
| 4.1 | Introduction | 63 |
| 4.1.1 | Broad distance distributions in DEER | 63 |
| 4.1.2 | The localisation and multilateration algorithms | 64 |
| 4.1.3 | <i>In silico</i> growth of flexible protein domains | 65 |
| 4.2 | Results | 67 |
| 4.2.1 | Analysis of DEER data with spin labels in the IDD | 67 |
| 4.2.2 | Distance distributions between beacon sites and residues in the IDD | 70 |
| 4.2.3 | Localisation of residues in the IDD from DEER restraints | 74 |
| 4.2.4 | Ensemble model of full length hnRNPA1 from DEER distances | 75 |
| 4.2.5 | Experimental ensemble validation | 79 |
| 4.2.6 | Towards mechanistic insights for hnRNPA1 | 84 |
| 4.3 | Materials and methods | 88 |
| 4.3.1 | Protein purification and spin labelling with MTSL | 88 |
| 4.3.2 | DEER sample preparation and measurement | 88 |

| | | |
|----------|--|------------|
| 4.3.3 | Small angle X-ray measurements | 89 |
| 4.3.4 | PRE measurements | 89 |
| 5 | RNA binding and LLPS of hnRNPA1 | 91 |
| 5.1 | Introduction | 92 |
| 5.2 | Results | 93 |
| 5.2.1 | Oligonucleotide binding | 94 |
| 5.2.2 | DEER with singly spin-labelled hnRNPA1 | 97 |
| 5.3 | Conclusions and discussion | 101 |
| 5.4 | Materials and Methods | 102 |
| 6 | Using spectroscopically orthogonal spin labels to study biomolecular interactions | 105 |
| 6.1 | Introduction | 107 |
| 6.1.1 | Selective excitation | 108 |
| 6.1.2 | Spectroscopically orthogonal spin labels in PDS | 109 |
| 6.2 | The Rpo4-Rpo7 complex as a model system | 110 |
| 6.3 | Application to hnRNPA1 | 113 |
| 6.4 | Conclusion and outlook | 114 |
| 6.5 | Materials and methods | 116 |
| 6.5.1 | Protein purification and spin labelling | 116 |
| 6.5.2 | DEER Measurements | 117 |
| 7 | Optimising nitroxide-Cu(II) RIDME for distance measurements | 119 |
| 7.1 | Introduction | 121 |
| 7.2 | Results and discussion | 123 |
| 7.2.1 | ESEEM suppression in RIDME experiments | 123 |
| 7.2.2 | RIDME Background Correction | 126 |
| 7.2.3 | Echo-crossing artifacts | 128 |
| 7.2.4 | Modulation depth build-up | 128 |
| 7.2.5 | Orientation-selective Cu(II)-Nitroxide RIDME | 131 |
| 7.2.6 | Frequency-swept Cu(II)-nitroxide RIDME | 131 |
| 7.2.7 | Comparison of RIDME with two different Cu(II) ligands | 134 |
| 7.3 | Conclusion | 136 |
| 7.4 | Materials and methods | 137 |
| 7.4.1 | Sample preparation and RIDME setup with rectangular pulses | 137 |
| 7.4.2 | DEER measurements | 137 |
| 7.4.3 | RIDME setup with coherent chirped broad-band pulses | 138 |
| 7.4.4 | Synthesis of the Cu(II)-nitroxide rulers | 138 |

| | | |
|----------|---|------------|
| 8 | Distance measurements by nitroxide-high spin metal ion RIDME | 139 |
| 8.1 | Introduction | 141 |
| 8.2 | Theory | 142 |
| 8.2.1 | Dipolar coupling with high-spin systems | 142 |
| 8.2.2 | Harmonic overtones in dipolar spectroscopy | 143 |
| 8.2.3 | Kernel-based data analysis of RIDME experiments with harmonic overtones | 145 |
| 8.3 | Materials and Methods | 147 |
| 8.4 | Results | 147 |
| 8.5 | Discussion and Outlook | 151 |
| | Conclusions and outlook | 153 |
| A | Supplementary Information for Chapter 3 | 157 |
| A.1 | Purification of the LCD construct | 157 |
| A.2 | Additional results for CW X-band lineshape fitting | 158 |
| A.3 | Spin doping experiments | 159 |
| A.4 | Additional distance simulations with the dimer model of UP1 | 162 |
| A.5 | EDEPR spectra for spin dilution experiment with mutants 231 and 271 | 162 |
| A.6 | Additional CW X-band spectra for hnRNPA1, UP1 and circular dichroism results | 163 |
| A.7 | Chemical shift differences for intermolecular PRE | 163 |
| B | Supplementary Information for Chapter 4 | 167 |
| B.1 | Spin labelling | 167 |
| B.2 | Random coil model fits for DEER | 167 |
| B.3 | Primary DEER data and analysis | 167 |
| B.4 | Input files for DEER restrained ensemble generation | 172 |
| B.5 | Ensemble characteristics | 173 |
| B.6 | SAXS data and analysis | 174 |
| B.7 | Additional PRE results | 174 |
| C | Supplementary Information for Chapter 5 | 183 |
| C.1 | Additional EMSA results | 183 |
| C.2 | Additional confocal imaging results | 183 |
| C.3 | Additional DEER results with spin dilution and single Cys hnRNPA1 | 183 |
| C.4 | Relaxation measurements with singly spin-labelled hnRNPA1 | 185 |
| C.5 | Additional DEER results with a double Cys mutant | 188 |
| D | Supplementary Information for Chapter 7 | 193 |
| D.1 | RIDME background measurements for nitroxide detected RIDME | 193 |
| D.1.1 | Orientation-Dependent Relaxation Measurements for Cu(II) | 194 |
| D.1.2 | Comparison of Cu(II)-nitroxide DEER and RIDME measurements at Q-band | 195 |
| D.2 | Echo crossing | 199 |
| D.2.1 | Sensitivity | 200 |

| | | |
|----------|--|------------|
| D.3 | Classical orientation selection | 201 |
| E | Supplementary Information for Chapter 8 | 203 |
| E.1 | Numerical simulation of coefficients build-up | 203 |
| E.2 | Extended coefficients table for Mn(II)-ruler temperatures series | 204 |
| E.3 | RIDME with an additional Mn(II)-based ruler | 205 |
| E.4 | RIDME with additional Gd(III)-based rulers | 205 |
| E.5 | DEER with the molecular rulers Gd(III)-based rulers | 205 |
| | List of publications | 247 |
| | Acknowledgements | 249 |
| | Curriculum Vitae | 253 |



Chapter 1

General introduction

1.1 Scope of this thesis

In this introductory Chapter 1 we summarise how IDD of proteins have been identified as key players in the liquid-liquid phase separation (LLPS) phenomenon both *in vivo* and *in vitro*. Extensive experimental evidence has been collected on LLPS in the last decade, in particular on the conditions required for formation of phase separated compartments both in cells and *in vitro*, but little information is available on functions and structures of the components at the molecular level. In particular we introduce the protein heterogeneous nuclear ribonucleoprotein A1 (hnRNPA1), which has come to a lot of attention, because mutations in hnRNPA1 have been linked to fibrillization and neurodegenerative diseases, such as amyotrophic lateral sclerosis (ALS). We furthermore outline why electron paramagnetic resonance (EPR) spectroscopy is well suited to contribute to the characterisation of IDDs and complex, distributed systems in biology.

The general introduction is followed by Chapter 2, where the theory foundations for the interpretation of EPR experiments are presented. The focus is set on pulsed EPR methods for measurements of distance distributions in frozen solutions of spin-labelled biomolecules, which have over the past decades become a valuable tool in the characterisation of biomolecular structure and interactions.

In Chapter 3 we show experiments for finding conditions that allow us to prepare samples of spin labelled hnRNPA1 in a predominantly monomeric state. This is important for structural characterisation, because most proteins carrying IDDs are prone to self-assemble (or unspecifically aggregate). If not accounted for, this may introduce complications for the interpretation of pulsed EPR data. Systematic characterisation of the C-terminal intrinsically disordered domain (IDD)

with a site-directed spin labelling (SDSL) approach was performed. We also report conditions under which buffered solutions of full length hnRNPA1 undergo LLPS and describe EPR strategies to study these protein condensates.

In Chapter 4 we progress to the characterisation of the IDD of hnRNPA1 in the free state by pair-wise distance measurements with doubly spin labelled proteins. The basic strategy is to exploit the fact that in addition to the IDD, hnRNPA1 contains two folded RNA recognition motif (RRM) domains (RRM1 and RRM2), which can be used as anchor points for a coarse-grained structural characterisation of residues in the IDD. Particular focus is put on explicitly including the distribution aspect of the distance information gained by SDSL-EPR. We demonstrate how several experimental results can be combined as restraints for the generation of a structural ensemble. The EPR-restrained domain structural ensemble can then be compared to experimental results obtained with additional biophysical methods, to strengthen its validity, and to promote multi-scale, hybrid structural approaches.

In Chapter 5 we progress to strategies to use SDSL and EPR for probing intermolecular interactions and conformational changes of the IDD of hnRNPA1 upon LLPS induced by the addition of RNA. High local protein concentrations are expected when the protein solution has undergone LLPS, which imposes a challenge for the interpretation of pulsed EPR distance measurements, due to at least two reasons. First, the high local concentrations are expected to enhance spin-spin relaxation, leading to shorter observable spin evolution times, which in turn limits the experimental resolution. Second, at high local protein concentrations distances arising from intramolecular spin pairs cannot be easily distinguished from distances arising from inter-molecular pairs if all molecules are spin labelled with the same type of spin label, especially when intermolecular and intramolecular distances fall into a similar distance range. The immediate remedy for the increased spin-spin relaxation rates is to dilute the spin labelled proteins in high ratios with diamagnetic unlabelled protein, and we show experimental strategies to realise this for the case of SDSL with hnRNPA1.

An alternative way to tackle this ambiguity is to use so-called spectroscopically orthogonal spin labels, which are introduced in more detail in Chapter 6. Two spin labels are considered spectroscopically orthogonal when they can be manipulated independently by microwave pulses, similar to multi-colour experiments in optical methods. The range of successfully applied spin labels ranges from paramagnetic metal ions to organic radicals, and is continuously being extended. The different spin labels can either be attached at different sites of one particular biomolecule, or to different biomolecules. Suitable setup of the pulsed EPR experiments then allows selective determination of distances between chosen types of spin labels. In order to select the desired combination of spin for distance measurements, pulsed dipolar spectroscopy (PDS)) experiments have been developed that are particularly suitable for studying spectroscopically orthogonal spin pairs. The double electron electron resonance (DEER) experiment, which is also also known as pulsed electron double resonance (PELDOR), as well as the relaxation induced dipolar modulation enhancement (RIDME) experiment, belong to this type of pulsed EPR methods. DEER on orthogonal spin pairs has

been well characterised and applied in several elegant studies, and it can be considered a robust method. The potential sources of artifacts are well understood. At the end of the chapter we present efforts to use DEER with the spectroscopically orthogonal spins nitroxide and Gd(III) to understand molecular arrangements in the liquid droplet (LD) state, and domain rearrangements upon RNA binding. Quantitative interpretation, however, could not be achieved due to limitations in sensitivity, which highlights the importance of continued PDS method development.

In Chapter 7 the RIDME experiment is presented in-depth, with a focus on detecting on the nitroxide spin in a spectroscopically orthogonal nitroxide-Cu(II) ion spin pair. RIDME is an emerging complimentary technique to DEER, which promises higher sensitivity when dealing with the broad EPR spectra of metal ions (compared to available excitation bandwidth). In contrast to DEER, nitroxide-detected RIDME is still significantly less well characterised and applications are to date limited to a few select cases. In this chapter we thus present a detailed study of the RIDME experiment with rigid molecular rulers. Molecular rulers are defined as molecules with a known, narrowly distributed inter-spin distance, which allows validation of the spectroscopic method. The chapter deals with nitroxide-Cu(II) pairs. Both spin species are low-spin (electron spin quantum number $S=1/2$) and thus present a well-behaved model system to optimise experimental conditions for nitroxide-detected RIDME. Several sources of artifacts that prevent accurate distance analysis have already been identified in the literature, and work-arounds had to be devised. Nitroxide-Cu(II) pairs are interesting in another aspect, namely that both spectra feature noticeable correlation of the resonance condition and the orientation of the molecule in the external magnetic field already at moderate EPR frequencies (~ 34 GHz, actually 'K_a-band' (Q-band), ~ 34 GHz). Limited excitation bandwidths of microwave pulses leads to spectroscopic selection of a sub-set of orientations, which must be averaged prior to analysis of dipolar time domain data in terms of distance distributions. In this section we describe how this can be achieved in one step, by using broadband excitation pulses.

The insights obtained in the low-spin case (nitroxide-Cu(II)) enabled us to advance to study the dipolar coupling information encoded in nitroxide-high-spin metal ion ($S>1/2$) RIDME. Nitroxide-high-spin metal ion RIDME is treated in Chapter 8. The fundamental difference to low-spin RIDME is that in the high-spin case the z -projection of the spin state of the metal ion can effectively change by more than one angular momentum unit. This manifests in higher orders of dipolar coupling frequencies contributing to the time-domain EPR signal, which need to be considered in the data analysis in terms of distance distributions. A potentially calibration-free procedure to deal with the higher harmonics in nitroxide detected RIDME is described. The surprising robustness of the approach with model compounds is a promising step towards routine nitroxide-high-spin metal ion RIDME for distance measurements.

1.2 Protein condensates

It is a common feature of proteins which contain IDD, like hnRNPA1, to aggregate (or 'self-assemble') into small or large protein condensates.^[189,218,271,299] Protein condensate is an umbrella

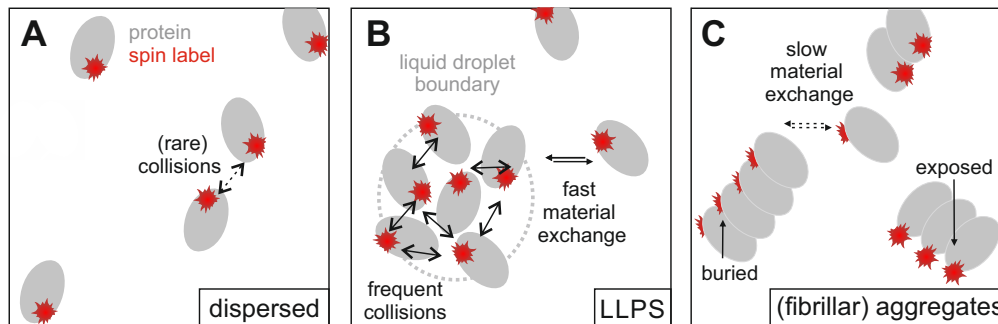


Figure 1.1: Protein samples can exist in various aggregation (or 'self-assembled') states. Spin labels are schematically indicated, to illustrate some effects we may observe in SDSL-EPR. Three limiting cases (A) dispersed, (B) liquid-liquid phase separated, (C) fibrillar, are presented.

term that includes both liquid-like assemblies, such as liquid droplets, or solid-like aggregates such as fibrils, and anything in between, like hydrogels. The various types of protein interactions differ in the local density of protein (and thus spin label), as well as the dynamics (protein backbone, side-chains and overall tumbling). Three limiting cases that are relevant for this work are schematically represented in Figure 1.1.

Case (A): If a protein solution is very dilute, or if the protein of interest has no high propensity to interact with itself (i.e. self-assembly is not observed), we expect to deal with a fully dispersed system, where the molecules are monomeric and isolated. The free state of the protein can be studied with samples prepared in this state. It may not be possible to reach such conditions even at very low concentrations of strongly self-interacting proteins like some proteins carrying IDD, unless the buffer conditions can be tuned that intermolecular interactions are suppressed. Ionic strength, solvent polarity, pH, temperature, and the content of specific small molecules are all examples of buffer properties that can be optimised to suppress protein-protein interaction.^[8,81,218,299] Dynamic properties of the protein are the overall protein tumbling and diffusion rate, which are expected to correlate with the molecular weight of the molecule, as well as the local dynamics of the (partially or fully) folded protein chain. Transient intermolecular interactions due to concentration dependent stochastic collisions are typically only expected to be observed at high concentrations.

Case (B): A buffered solution of a protein may undergo LLPS *in vitro*.^[249] LLPS is known in the field of structural biology for a long time,^[94] but recently it has come to much attention because it was also demonstrated to occur and to be functional in cells.^[34,215,228] We then observe at least two populations: some fraction of the protein remains dispersed in solution, and a second population emerges in the phase separated, second liquid phase. For example, fluorescence recovery after photobleaching (FRAP) experiments both *in vitro* and in cells have confirmed that the two phases in protein samples after LLPS indeed behave like liquids (fast recovery of the fluorescence intensity).^[264] Not much is currently known about the density and distribution of protein in the two phases, or the spatial arrangement of protein within one phase. It is known, however, that

material is exchanged rapidly between the two phases, and that the liquid droplets are enriched in protein (high local concentrations).^[46,218,299] nuclear magnetic resonance (NMR) experiments suggest that the individual proteins in both phases remain highly dynamic and disordered.^[46] Transiently forming secondary structure motifs, however, have been identified in some cases.^[63]

Case (C): The third limiting case is when the protein condensate forms a solid-like aggregate. For example, fibrillar aggregates are often encountered in pathological samples of neuro-degenerative diseases, most of which have extended β -sheet cores.^[186] Overall protein tumbling is strongly reduced due to the large change in effective molecular weight. Local dynamics may remain high, if a given residues is not at the aggregation interface. Material exchange between the proteins in the fibrils, and the proteins remaining in solution is expected to be significantly slower than in liquid-like condensates.

Of course, in real samples we may observe states that are a combination of the limiting cases presented above. Nonetheless we can summarise two important consideration for molecular level characterisation of protein condensation: firstly, local dynamics in a protein chain may vary for individual sites, and contain information on the secondary structure at a particular sites, as well as interaction interfaces between molecules. Secondly, changes in local protein concentration (and thus spin label concentration in SDSL-EPR) are expected upon protein condensation. If the proteins remain highly mobile in the high-density state we expect to observe mostly transient protein encounters with ambient temperature experiments. Depending on the spin label sites we may be able to observe a broad distribution of intermolecular distances in the frozen state. If the proteins interact rigidly, we expect to see reduced overall dynamics, well defined intermolecular distances, and very little exchange between aggregated and soluble material. Importantly, spin label spectra and interactions are affected differently by all of these effects, which should enable us to characterise intermolecular interactions in protein condensates by combining results from ambient temperature and frozen samples.

1.3 hnRNPA1

The protein hnRNPA1 is a member of a large family of human regulatory splicing factors that form extensive RNA-protein and protein-protein interaction networks responsible for pre-mRNA processing, splicing, and mRNA export.^[36,90,133] It is predominantly located in the nucleus, but can shuttle between the nucleus and the cytoplasm.^[148,190] It has been found to associate with stress-granules in cells under stress conditions, where it is believed to package translationally stalled mRNA.^[215] Unsurprisingly, hnRNPA1 is a nucleotide binding protein,^[26,191,223,230,307] which will not be further discussed here, but is the focus of Chapter 5. In recent time hnRNPA1 has attracted attention due to its implication in the neuro-degenerative diseases ALS,^[166,190] and a form of inclusion body myopathy (IBMPFD3).^[166] Furthermore there is evidence that hnRNPA1 is involved in hepatitis C virus replication,^[165] and is involved in several other viral infection processes.^[187,188,263] Three iso-forms have been reported, and the most abundant form consists of 320 amino acids (~ 37 kDa). The longest iso-form has 52 additional amino acids in the C-terminal

domain. Interestingly, the alternative splicing of the isoforms of hnRNPA1 has been demonstrated in cells to be tightly regulated by TDP-43, another splicing regulator strongly linked to ALS.^[70] A truncated version that is entirely lacking the C-terminal domain has also been identified in cells (residues 1-196 of the full length protein), which is by itself known as unwinding protein 1 (UP1). UP1 contains the two conserved RRM s, and the respective structures have been solved by X-ray crystallography,^[72] and solution NMR methods.^[19] Some examples of structures of partial hnRNPA1 constructs are shown in Figure 1.2.

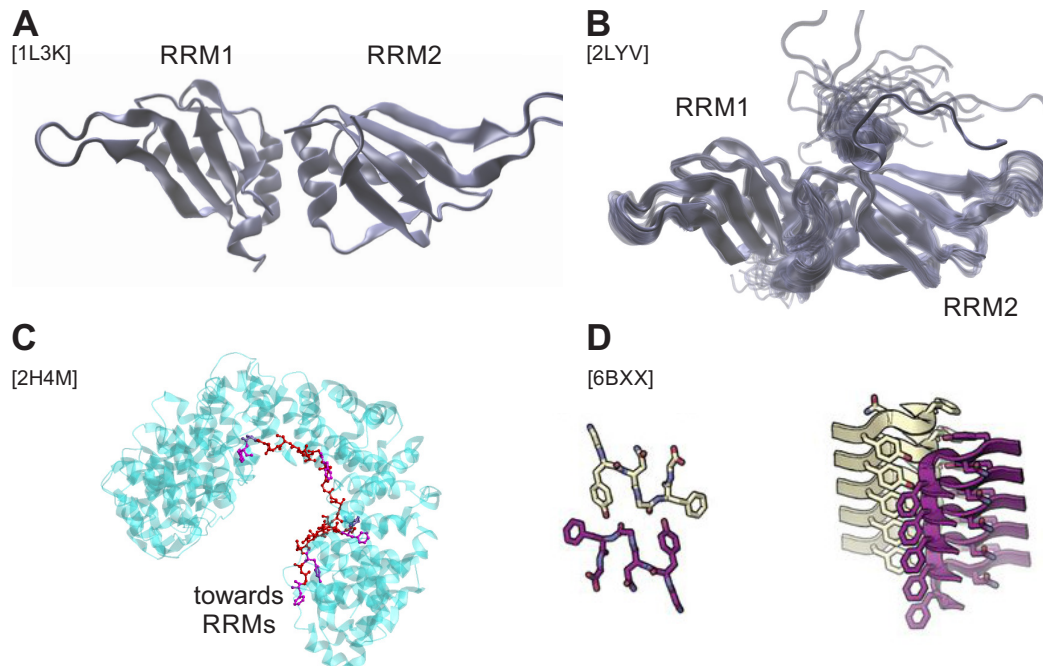


Figure 1.2: Partial structural models of free hnRNPA1; pdb codes are indicated in the panels. (A) 1.1 Å resolution crystal structure of UP1 (the RRM s of hnRNPA1);^[294] (B) NMR solution structure of UP1;^[19] (C) M9 nuclear localisation sequence (red, canonical residues 315-335 bound to transportin-1 (cyan)^[182]; (D) adapted from Hughes et al.^[127]; steric zipper conformation of hexa-peptide 'GYNGFG';

In vitro it was found that solutions of purified hnRNPA1 can self-assemble into fibrillar aggregates, which may be related to aggregates found in pathological samples, but it is still unclear what the exact role of the aggregates is in disease.^[110,166] The point mutations that were linked to the disease state are all in the (C-terminal) IDD of hnRNPA1 (Q277K, D314N, N319S, P340S).^[154,166,190] More recently it was observed that a small hexapeptide sequence (GYNGF) found in the IDD of hnRNPA1 is sufficient to form fibrillar aggregates.^[127] This type of structural transition, from very disordered to very ordered, is in contrast to LLPS, in which proteins remain highly dynamic.^[218] *In vitro* this usually is observed as the formation of small (micrometer-sized) LDs that can fuse and mature over time.^[12,218] Eventually, a hydrogel may form.^[218] It has been hypothesised that fibrillar aggregates of proteins can form from the LD or the hydrogel state.^[12,218]

The phase separation behaviour of hnRNPA1 and other similar proteins has been reported on a macroscopic level in detail. In particular arginine - tyrosine interactions were shown to be the major driving force of LLPS via IDD of the type of hnRNPA1 (referred to as the "FUS-like family" by Wang et al.^[299], based on the compositional similarity with the IDD of the protein fused in sacroma (protein) (FUS)).

1.4 SDSL-EPR in structural biology

EPR experiments are sensitive to paramagnetic centres in the sample, which may be part of an arbitrarily large biomolecule or biomolecular complex. These can be present either as native paramagnetic centres (such as biologically important metal ions, e.g. copper, iron or manganese),^[4,15,25,87,112,153,159,311] or as artificially introduced EPR-active centres. To the latter type belong paramagnetic centres which are covalently attached to the biomolecule of interest. They are, analogously to fluorescence labels, called 'spin labels'^[23,64,125] and serve as a particularly useful source of information when the spin label is attached at a chosen site in the biomolecule. Such targeting of a particular molecular site is known as site-directed spin labelling (SDSL). A large body of work has been invested towards the development of SDSL protocols for peptides and proteins of nearly arbitrary size,^[39,113,252] and (SDSL)-EPR has long found its way into the structural biologist's toolbox.^[24,40,89,252,267,287] Among many other biological applications of EPR, the structural information that can be obtained with EPR includes information on local dynamics,^[125] and inter-spin distance information in the nanometer regime.^[140] The first protein samples to be investigated were proteins with well-defined globular structures, but applications to more complex samples, such as membrane proteins, followed soon.^[40] In addition to SDSL of proteins, approaches are being developed to achieve universal, robust and size-independent SDSL methods also for oligonucleotides (deoxy-ribonucleic acid (DNA) or ribonucleic acid (RNA)).^[84,229,259,267,268,272]

The ability of EPR to deal with samples of high complexity is promising for the application to intrinsically disordered systems, and the first successful studies have been reported.^[79,181,220,222]

The most popular choice for spin labelling of proteins is based on cysteine-targeting chemistry. The commercially available spin label MTSL (Figure 1.3(A)) is one of the most prominent spin labelling reagents, among other reasons because the paramagnetic N-oxyl-pyrroline moiety, which is linked to the cysteine via disulfide formation, is small and flexibly attached to the peptide backbone, which reduces the risk of perturbing the structure of the labelled molecule. A major field of application for SDSL are distance measurements within and between biomolecules by PDS.

Along with the nitroxide-based spin labels other organic radical based (e.g. trityl^[7,71,132,177]) spin labels and different types of metal ion-based^[65,97,107,244] spin labels have been developed and successfully tested in PDS experiments. Particular benefits may arise when different spin labels can be excited and detected independently, when they are thus said to be 'spectroscopically orthogonal'. An example of the EPR spectra of the orthogonal pair nitroxide and Gd(III)-ions in a stable chelator is shown in Figure 1.3.

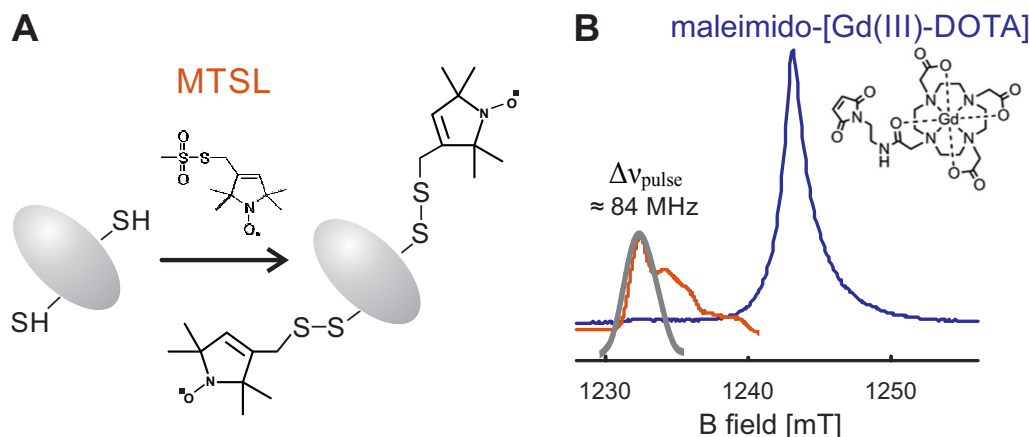


Figure 1.3: SDSL of biomolecules; (A) a biomolecule with two (engineered or natural) cysteines can be labelled with a thiol-reactive spin label (here MTSL); (B) echo-detected spectra of a nitroxide (orange), resp. a Gd(III)-based spin label (purple) at Q-band

1.4.1 Static versus dynamic averaging of spin interactions

In this section we briefly describe how ensemble averaging of immobile resp. of mobile spins affects the EPR signals in the presence of anisotropic interactions. The interpretation of anisotropic interactions is one of the reasons why EPR spectroscopy is a powerful method to characterise distributed systems, because it is possible to study (static) distributions of molecular properties by studying immobilised samples, as well as dynamic properties at molecular sites by ambient temperature experiments. An illustration with a nitroxide spin label is shown in Figure 1.4.

Anisotropic interactions in EPR (e.g. hyperfine interactions, \mathbf{g} -tensor, dipolar coupling, ...) can be described by the orientation of the external magnetic field with respect to an interaction tensor (for details see Chapter 2).

In an ordered sample, like a single crystal, all spin centres have the same, fixed orientation, and thus a fixed coupling strength that changes when rotating the sample in the external magnetic field. But samples of this type are rather an exception in biological EPR, and not relevant for this thesis. In this thesis we deal mostly with frozen solutions at cryogenic temperatures (80 K and below). We can assume that molecular motions (except for small librational motions) are frozen out in these conditions.^[80,175] No large-scale inter-conversion between conformations, and no molecular collisions are possible during an experiment. We thus (ideally) see a snapshot of all conformations at the moment of flash freezing that the ensemble of molecules has adopted. This can be treated as an immobile ensemble of spins with local order (fixed geometry around the electron spin), but no long-range order. In such samples we observe what is called a powder-averaged spectrum, which in the context of dipolar coupling is often referred to as Pake averaging.^[232] The powder averaged spectrum can be calculated as a weighted sum of single-orientation spectra. The weighting assumes that all molecular orientations are equally probable.

When considering EPR experiments in solution (at ambient temperature) we need to consider

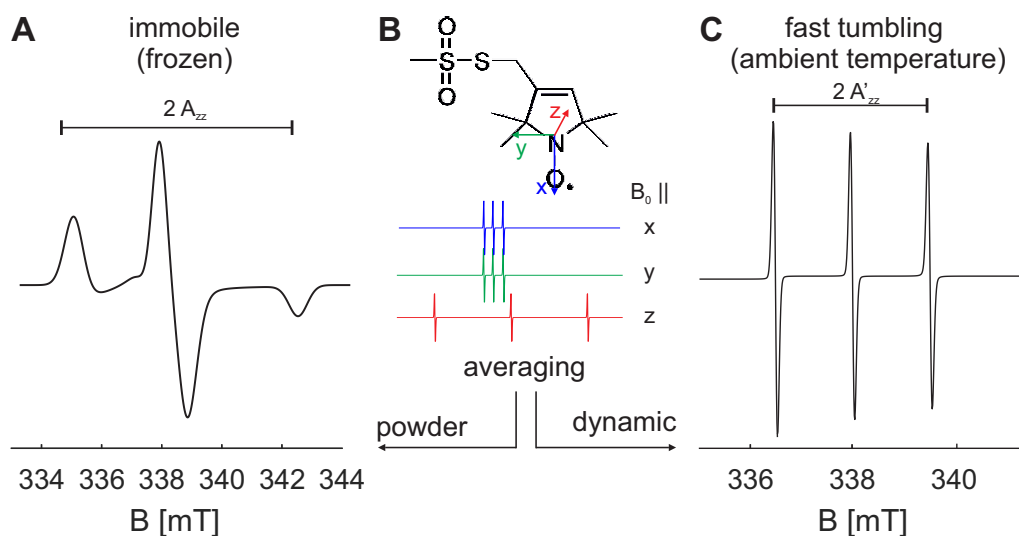


Figure 1.4: Static vs. dynamically averaged interactions in the nitroxide spectrum; simulated (EasySpin^[280]) first derivative lineshapes are shown; (A) powder averaged spectrum, the maximal splitting at X-band is given by the z -component of the hyperfine interaction A_{zz} (axis system shown in color). (B) Definition of the coordinate system, and simulations of single orientation along the principle axes; (C) ambient temperature spectrum in the isotropic fast tumbling regime, tumbling leads to a narrowed spectrum due to (partial) averaging of the anisotropy (note the different axis range compared to (A)); an apparent maximal splitting A'_{zz} can be defined.

molecular motion. If the motions are fast enough to lead to a rearrangement of the anisotropic interactions with respect to the quantisation axis during the EPR measurement we can no longer calculate the spectrum as a simple sum of orientations. The larger the anisotropy, the faster the tumbling must be to achieve complete averaging. An extensive theory framework has been developed to calculate the fast and intermediate tumbling spectra of nitroxides using time-dependent perturbations (stochastic Liouville theory),^[93,261] which was implemented and is available in the user friendly EasySpin software package.^[280] We can also consider that molecular collisions may occur frequently when the (local) concentration is high. If molecular collisions occur between two paramagnetic spins, Heisenberg exchange interactions may be observed. This is only expected to be observed at high (local) spin concentrations.^[217] In summary, nitroxide-based spin labels studied with continuous wave (CW) ~ 9.5 GHz (X-band) EPR spectroscopy can be a valuable source of information of local dynamics and spin-spin interactions at the site of the spin label.^[125,183] Note that for most spin labels the relaxation properties at ambient temperature are too fast to perform pulse EPR experiments.^[27]

1.4.2 Nitroxide spin label interactions in CW X-band spectra

Extensive effort has been put into the interpretation of CW X-band spectra of nitroxide-labelled biomolecules in terms of local spin label dynamics and spin-spin interactions, and excellent sum-

maries and monographs have been published.^[23] When dealing with ambient temperature spectra, we have the situation of partial dynamic averaging of anisotropic contributions in the Hamiltonian. In nitroxides, the relevant anisotropies are the hyperfine coupling to the ^{14}N nucleus, and the g -factor anisotropy (for general introduction to the couplings, nomenclature and definition of the parameters see Section 2.2 in Chapter 2). In some situations it is also possible to resolve hyperfine couplings to naturally abundant ^{13}C nuclei in the nitroxide spin label. The largest splitting of the spectrum is given by the axial hyperfine coupling to the nitrogen (A_{zz}). Fast spin label tumbling in solution leads to more efficient averaging of this anisotropy and thus narrower lines. Unfortunately, data analysis can become very complicated and often even ambiguous if the spin label motion itself is anisotropic.^[11] Detailed structural and dynamic interpretation of CW EPR spectra of spin labelled sites in an IDD, however, is not the focus of this chapter, and would in fact deserve its own dedicated study. We limit the discussion instead to outlining the expected hallmarks of protein-protein interaction in CW X-band nitroxide spectra. The two major effects that we may observe when two spin-labelled proteins interact is (i) a change in overall spin label mobility, and (ii) an increase of spin-spin interactions between spin labels on the same or different protein molecules. For the latter case we could have effects from both dipole-dipole coupling, and Heisenberg exchange coupling at very high local spin concentrations. In the following we outline how these interactions are expected to influence ambient temperature CW EPR spectra of nitroxide labelled sites in an IDD. The two limiting cases we look at are (a) fully dispersed protein (isolated molecules) and (b) protein in a dense liquid-droplet state (dynamically interacting molecules).

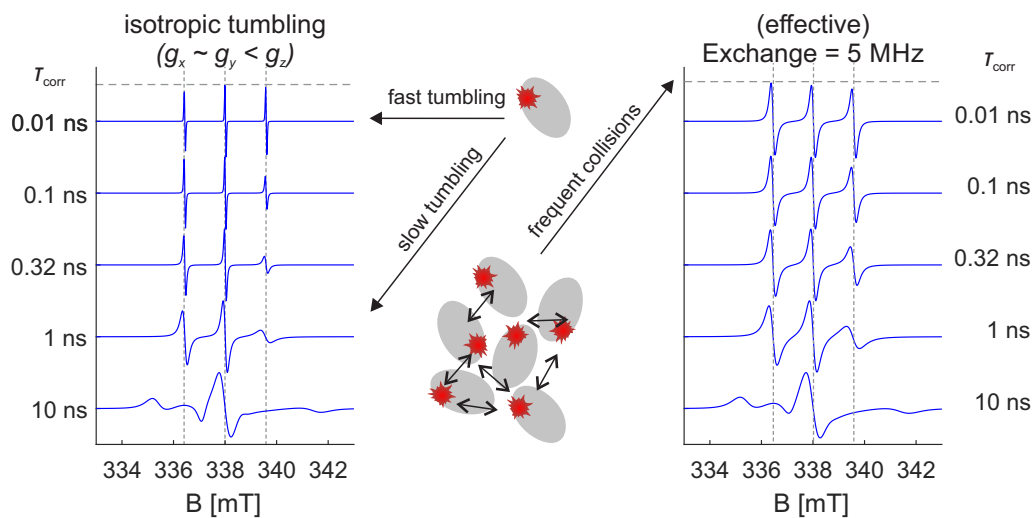


Figure 1.5: Simulated spectra of fast to intermediate isotropic tumbling nitroxides; (A) influence of isotropic molecular tumbling rate τ_{corr} , resp. (C) Heisenberg exchange interaction D . (B) possible implications for protein interaction state.

CW EPR spectra of isolated proteins Very fast dynamics has been reported from relaxation and nuclear Overhauser effect (NOE) measurements with IDD backbone and side-chain resonance in solution state NMR.^[134,172] This leads us to expect almost unrestricted tumbling of

a spin label at labelling sites in the IDD. Such fast spin label dynamics has been observed by CW EPR.^[79,181,220] The simplest model for molecular motion is isotropic tumbling of the nitroxide label in a fast to intermediate motion time-regime (picoseconds to nanoseconds). In this simple approximation, a single parameter, the isotropic rotational correlation time τ_{corr} , is required to describe the spectral shape, as has been rigorously described^[93]. The effect of spin-label mobility is shown in Figure 1.5(A). The resulting CW EPR spectra with very fast ($\tau_{\text{corr}} = 10$ ps) to intermediate ($\tau_{\text{corr}} = 10$ ns) isotropic tumbling are displayed. In the very fast isotropic tumbling case we find three narrow lines, and the intensities of the three hyperfine lines are approximately the same. Spectra in this limit are often observed for free spin label in buffer. Notice that the weak hyperfine couplings to naturally abundant ^{13}C nuclei can be detected in case of very fast tumbling. The exact ratio of the amplitudes of the hyperfine lines for fast tumbling below the fast limit carries information on the anisotropy of the tensors, on the anisotropy of the nitroxide tumbling, and on the rotational correlation time. Variations of A_{zz} may have a noticeable effect on the observed lineshape for a fixed τ_{corr} . This should be considered when determining absolute tumbling rates, because A_{zz} strongly depends on (local) solvent polarity, proticity and dielectric screening.^[41,108,169,231]

CW EPR spectra at high protein concentration When many spin-labelled proteins come together in a protein condensate, such as in the LD state, the local spin label dynamics may or may not change due to crowding effects. This depends on whether the spin label is located close to a biomolecular interaction interface. Because we expect high local spin label densities and frequent molecular collisions in the LD state, we may additionally observe spectroscopic effects due to Heisenberg exchange coupling (illustrated in Figure 1.5(C)). This can be considered as an effective coupling D , that depends both on the rate of molecular collisions and the efficiency of each collision to alter the spin states of the colliding spins.^[217] In general, Heisenberg exchange broadening up to approximately $D/A_{zz} = 0.1$ leads to broadening of all three hyperfine lines. At higher values of D/A the hyperfine splitting reduces and the lines then collapse into a single broad line. In extreme cases of exchange coupling ($D \gg A_{zz}$) the single line becomes more narrow again (not expected to be relevant in biological systems and thus not shown).

Also dipolar coupling may be significant in high local spin density states. Converting the estimated dipolar couplings into spin-spin distances from ambient temperature CW EPR spectra, however, is an almost impossible task, because like other anisotropic interactions, the dipolar interaction is affected by averaging through molecular tumbling, due to the angular dependence on the dipolar angle θ . Furthermore, already at distances at and above $R \approx 2.0$ nm, dipolar couplings are too weak to be resolved underneath the natural linewidth of nitroxide spin labels.^[18] This is the dipolar coupling regime that is much better addressed by pulsed dipolar spectroscopy methods like DEER (see below). If very short distances indeed seem to be dominating, they may be estimated from frozen (or otherwise immobilised) samples by CW EPR spectroscopy. For example, distances below $R=1.5$ nm have been successfully measured on doubly spin-labelled peptides by measuring CW EPR spectra in X-band in the frozen state.^[18]



Chapter 2

General EPR Theory and Methods

Scope of this chapter In this work we present electron paramagnetic resonance (EPR) methods to address biological questions in the context of structural biology of proteins, and of biomolecular interactions. We focus on EPR as a tool to manipulate and detect unpaired electrons in magnetic fields with the use of microwave radiation. These phenomena are well understood at the fundamental theory level, and in the following we introduce a summary of the relevant EPR interactions and experimental methodology, mainly following Schweiger and Jeschke^[266]. The section on pulsed dipolar spectroscopy was in large parts adapted from Ritsch et al.^[251] and Ritsch et al.^[250].

2.1 Electron and nuclear spin

In quantum mechanical descriptions an intrinsic angular momentum $\hbar\vec{S}$ is attributed to an electron and can be described with the spin operator \vec{S} . The spin quantum number for one electron is $S = 1/2$, and it has no classical mechanics analogue. We can nonetheless use it as an effective angular momentum (in addition to the orbital angular momentum \vec{l}) to introduce magnetic resonance spectroscopy in a semi-classical description. Classically, we expect to observe a magnetic dipole moment $\vec{\mu}_S$ (in the following shortened to 'magnetic moment') associated with a moving charged particle. In the presence of an external magnetic field the magnetic moment $\vec{\mu}_S$ aligns parallel to the \vec{B}_0 -axis, and the two spin states are not degenerate in energy. Following Boltzmann statistics, the population difference of the two states results in a non-zero total magnetisation $\vec{M} = \sum_{i=1}^n \langle \vec{\mu} \rangle_{S,i}$ in an ensemble of n isolated electron spins. Many experimental findings in magnetic resonance can be well explained in such a semi-classical description, but for the majority of this work we will use a quantum description of electron and nuclear spin.

2.1.1 Quantum mechanical description of spin

The magnetic moment of an isolated free electron ($\vec{l} = 0$) in the quantum mechanical description is given by $\vec{\mu}_S = -g_{\text{free}}\mu_B\vec{S}$, where the so-called g -factor ($g_{\text{free}} \approx 2.002319$) is a well-characterised scaling factor, $\mu_B = -\hbar e/2m_e$ the Bohr magneton, and $\vec{S} = (\hat{S}_x, \hat{S}_y, \hat{S}_z)$ is the total electron spin operator vector composed of the three orthogonal projection components. We can treat the nuclear spins I , and nuclear magnetic moments $\vec{\mu}_N$ analogously. The magnitude of μ_B is much larger than $\mu_N = +\hbar e/2m_N$, because the electron mass m_e is much smaller than the nuclear mass m_N (e is the elementary charge, and Z the proton number). In the presence of an external magnetic field (by convention chosen to point along the z -axis) we can associate the aligned components of $\vec{\mu}_S$ of an electron spin with total spin quantum number S with the spin projection states $m_S = -S, -S + 1, \dots, +S$, which denote the eigenstates of the z -spin projection operator \hat{S}_z . In EPR we use irradiation to excite transitions between different sublevels of the energy level scheme of an (interacting) system of electron and nuclear spins. The energy levels E_i of the system can be found by solving the time-independent Schrödinger equation

$$\hat{H} |\Psi_i\rangle = E_i |\Psi_i\rangle, \quad (2.1)$$

after defining a (quantum mechanical) Hamilton operator \hat{H} . A useful choice of the basis functions $|\Psi_i\rangle$ is given by the eigenfunctions of the total Hamiltonian. The operator \hat{H} can be constructed by addition of interaction terms between spins and magnetic fields, as will be treated in Section 2.2.

Spin ensembles In experimental EPR we are usually dealing with large ensembles of electron spins. Each spin in general may be coupled to multiple other electron and nuclear spins by the interactions presented above, but in the experiments described in this work it is a good assumption that a given electron spin system interacts only weakly with other electron spin systems, and they can thus be treated individually (dilute samples). Ensembles of spins can be treated, by introducing

the time-dependent density operator

$$\hat{\sigma}(t) = \sum_{l=1}^{(2S+1)} \sum_{k=1}^{(2S+1)} \overline{c_l(t)c_k^*(t)} |l\rangle \langle k|, \quad (2.2)$$

where $|l\rangle$, resp. $|k\rangle$ are the $n = (2S + 1)$ ortho-normal basis functions of the spin operator, and $\overline{c_l(t)}$ and $\overline{c_k^*(t)}$ are ensemble averaged (indicated by bar), time-dependent coefficients. $\hat{\sigma}(t)$ can be written as a Hermitian $n \times n$ -dimensional matrix, where the diagonal entries ($l = k$) are interpreted as 'populations', and the off-diagonal elements as 'coherences' (coherent superposition of states l and k).^[265] The description can be extended to more than one coupled (electron and/or nuclear) spin, with the basis functions from the corresponding $n_H = \prod_i (2S_i + 1)$ -dimensional Hilbert space.

Thermal equilibrium For spins in an external magnetic field in the so-called high temperature approximation ($\Delta E(l, k) \ll k_B T$, with the Boltzmann constant k_B and temperature T) we expect no coherences at thermal equilibrium. The coefficients of the diagonal elements of $\hat{\sigma}$ are distributed according to Boltzmann statistics. This allows us to denote the equilibrium state to first order approximation as

$$\hat{\sigma}_{eq} = \mathbb{1} - C\hat{S}_z, \quad (2.3)$$

where C is a normalisation constant that depends on the dimensions of \hat{H} . The unity operator is typically neglected because it has no time-evolution and thus does not correspond to detectable magnetisation.

Time evolution of spin ensembles Similarly to the evolution of a single state we can describe the evolution of $\hat{\sigma}(t)$ by using the 'Liouville-von-Neumann' equation

$$\frac{d}{dt}\hat{\sigma}(t) = -i[\hat{H}, \hat{\sigma}(t)] - \hat{\Gamma}[\hat{\sigma}(t), \hat{\sigma}_{eq}]. \quad (2.4)$$

Here we already give an extended version which includes a relaxation term with the relaxation super-operator $\hat{\Gamma}$, that ensures that all coefficients eventually relax back to the equilibrium state. Neglecting relaxation for now (will be treated phenomenologically later), and assuming we have prepared our spin ensemble in a well-known initial state $\hat{\sigma}_0$, we can find the solution after time-evolution under the time-independent Hamiltonian \hat{H} as

$$\hat{\sigma}(t) = \exp(-i\hat{H}t)\hat{\sigma}_0 \exp(i\hat{H}t). \quad (2.5)$$

This propagation of $\hat{\sigma}(t)$ with the total Hamiltonian can be split into iterative propagation with partial Hamiltonians, as long as they commute. It offers a powerful method to describe time-evolution of coupled spin systems, because the observable of interest can be represented as a spin operator \hat{O} , with expectation value

$$\langle \hat{O}(t) \rangle = \text{tr}(\hat{\sigma}(t)\hat{O}). \quad (2.6)$$

For example, the detection operator for an EPR experiment in a conventional pulsed experimental setup is given by $\langle \hat{S}^+(t) \rangle = \text{tr}(\hat{\sigma}(t)\hat{S}^-(t))$.

2.2 Spin Hamiltonian and energy levels

The total EPR Hamiltonian \hat{H} for a given spectroscopic problem can be constructed by selection of the appropriate interaction terms.

$$\hat{H} = \hat{H}_{\text{EZ}} + \hat{H}_{\text{NZ}} + \hat{H}_{\text{HF}} + \hat{H}_{\text{D}} + \hat{H}_{\text{J}} + \hat{H}_{\text{ZFS}} + \hat{H}_{\text{MW}} + \dots \quad (2.7)$$

The individual terms are the electron (\hat{H}_{EZ}), resp. nuclear (\hat{H}_{NZ}) Zeeman interaction, the hyperfine interaction between electron spin and nuclear spins (\hat{H}_{HF}), the electron spin dipole-dipole coupling (\hat{H}_{D}), the electron spin exchange interaction (\hat{H}_{J}), and the zero-field splitting (\hat{H}_{ZFS} , only for $S > 1/2$). Other system-inherent interactions, like the nuclear quadrupole interaction (\hat{H}_{NQ} , only for $I > 1/2$) may have to be considered, but are not relevant for this particular work, and are thus not further discussed. \hat{H}_{MW} denotes the term that arises if microwave (MW) irradiation is applied.

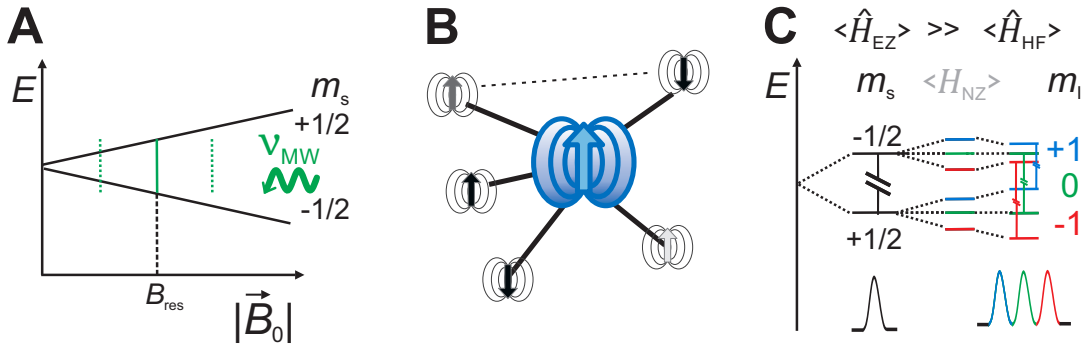


Figure 2.1: Interactions in EPR; (A) the Zeeman effect leads to an energy level splitting of the electron spin projection number m_S levels. An EPR signal is only observed if the resonance condition is met (solid green line). (B) Typical coupling scheme in EPR: a single electron is coupled to many nuclear spins (solid lines); the inter-nuclear couplings (e.g. dashed line) can be neglected. (C) Energy level scheme of one electron spin $S = 1/2$ (left) with one additional nuclear spin $I = 1$ (middle), and in the presence of hyperfine coupling (right); typically the Zeeman effect dominates, and the hyperfine induced splitting (here $a_{\text{iso}} > 0$, depends on m_S and m_I) is only a small perturbation. The EPR-allowed transitions are indicated by solid vertical lines (selection rules: $\Delta m_S = \pm 1$, $\Delta m_I = 0$).

2.2.1 Zeeman interaction

The magnetic dipole moment of an electron or a nuclear spin couples to an external magnetic field. This is known as the Zeeman effect, and it is illustrated in Figure 2.1(A). In most EPR experiments relevant for this work we can assume to good approximation that the electron Zeeman term is the

dominating interaction in the total Hamiltonian. The magnitude is given by

$$\hat{H}_{\text{EZ}} = -\tilde{\mu}\vec{B}_0 \quad (2.8)$$

$$= -\frac{\mu_B}{\hbar}\vec{B}_0^T \mathbf{g}\vec{S}. \quad (2.9)$$

The second form is written for an electron spin \vec{S} , and \vec{B}_0^T is the transpose of the magnetic field vector. The (3×3) tensor \mathbf{g} takes the place of the free electron g -factor (without the contribution from spin orbit coupling), and contains information on the asymmetry of the electron spin electronic environment. It may for example serve as a source of information for the coordination geometry of paramagnetic ions in chelators. The coordinate system in which \mathbf{g} is diagonal is known as the principal axes system (PAS), with components $g = (g_{xx}, g_{yy}, g_{zz})$. We discuss only experiments where the external magnetic field points along a single direction $\vec{B}_0 = (0, 0, B_0)$ and defines the quantisation axis for the electron spins. The orientation of \vec{B}_0 with respect to the PAS (e.g. defined by the azimuthal angle θ , and the polar angle ϕ) results in an effective g -factor

$$g_{\text{eff}}(\theta, \phi) = \sqrt{g_{xx}^2 \sin^2 \theta \cos^2 \phi + g_{yy}^2 \sin^2 \theta \sin^2 \phi + g_{zz}^2 \cos^2 \phi}. \quad (2.10)$$

The anisotropy of the Zeeman term scales with B_0 , which leads to an increase of the total width of an EPR spectrum at higher experimental fields (resp. frequencies). This can be a disadvantage, because the spectral density of broader spectra is lower, which reduces sensitivity. It may also be exploited as a source of information, in orientation-resolved EPR experiments.

An analogous definition to \hat{H}_{EZ} can be made for nuclear spins (thus \hat{H}_{NZ}), by substituting \vec{S} with the nuclear spin vector operator \vec{I} , and using the magnitude of nuclear magnetic moment μ_N . Due to the significantly lower magnitude of the magnetic moment of nuclear spins we have an almost three orders of magnitude smaller nuclear Zeeman energy level splitting. The resulting resonance frequencies ω_{res} are shifted accordingly for nuclear spins (radio frequency (RF) regime) and electron spins (MW regime). In all cases relevant for this work we do not directly excite transitions of nuclear spins by RF irradiation, and we can thus neglect the nuclear Zeeman term in the Hamiltonian.

2.2.2 Electron spin - nuclear spin interaction

If nuclear spins are in close proximity to an electron spin we observe coupling of the magnetic moments, which is known the hyperfine interaction. The hyperfine interaction is one of the major sources of information in many EPR experiments, and we typically assume that each pair-wise interaction of an electron spin with the surrounding nuclear spins can be treated independently. Nuclear spin-nuclear spin couplings can be neglected in EPR experiments, because we do not directly drive nuclear spin state transitions, and because the couplings are usually far too weak to be resolved (illustrated in Figure 5.1). The hyperfine Hamiltonian to first order between one electron spin S and n nuclear spins I is given by

$$\hat{H}_{\text{HF}} = \sum_{i=1}^n \vec{S}^T \mathbf{A}_i \vec{I}_i = \sum_{i=1}^n \vec{S}^T (a_{\text{iso},i} \mathbf{1} + \mathbf{T}_i) \vec{I}_i, \quad (2.11)$$

with the respective hyperfine coupling tensors \mathbf{A}_i . Coupling to different nuclei can be treated independently. For each \mathbf{A} we can also find a PAS (which may be tilted with respect to the PAS of the g -tensor) with the three diagonal elements $\mathbf{A} = (A_{xx}, A_{yy}, A_{zz})$. For many applications it is useful to split the interaction into an isotropic component a_{iso} , and the remaining anisotropic component \mathbf{T} . The physical origin of the two components is different, and provides information on the spin system. a_{iso} can be related to the electron spin density at the location of the nucleus (Fermi contact term), \mathbf{T} is given by the through-space dipole-dipole coupling between the electron and nuclear magnetic moment vectors. In some cases additional terms (isotropic and anisotropic) may have to be considered if the orbital magnetic moment of the electron is large. Note that in contrast to the g -factor anisotropy, the A -anisotropy is field-independent. It may thus be the major source of spectral broadening at low fields and EPR frequencies, while being unresolved at high fields. A simple energy level scheme for a coupled system of one electron spin $S = 1/2$ and one nuclear spin $I = 1$ is shown in Figure 2.1. The single line observed due to the electron Zeeman effect splits into three lines in the presence of hyperfine coupling.

2.2.3 Weak electron spin - electron spin interactions

In systems with more than one electron spin we may have to consider terms in the Hamiltonian from electron spin coupling. Electron spins which are strongly coupled are usually better described by a group spin $S > 1/2$ ('high spin' systems), which will be treated in a later section. Here we describe the combined electron spin - electron spin interaction \hat{H}_{ee} for two coupled electron spins when the interaction is weak

$$\hat{H}_{\text{ee}} = \hat{H}_{\text{DD}} + \hat{H}_{\text{J}} \quad (2.12)$$

$$= \vec{S}_1^T (\mathbf{D} + \mathbf{J}) \vec{S}_2, \quad (2.13)$$

with the dipolar contribution \hat{H}_{DD} (dipolar coupling tensor \mathbf{D}), and the exchange contribution \hat{H}_{J} (exchange coupling tensor \mathbf{J}).

Dipolar coupling Two magnetic moments (here two electron spins \vec{S}_1, \vec{S}_2) are mutually influenced by the magnetic field originating from the respective other spin. This is known as the dipolar (or dipole-dipole) coupling. The contribution to the EPR Hamiltonian is

$$\hat{H}_{\text{DD}} = \frac{\mu_0}{4\pi\hbar R^3} g_1 g_2 \mu_B^2 \left(\vec{S}_1 \vec{S}_2 - \frac{3}{R^2} (\vec{S}_1 \vec{r}) (\vec{S}_2 \vec{r}) \right), \quad (2.14)$$

where g_1 and g_2 are the g -factors of the two spins, μ_0 is the vacuum permittivity, \vec{r} is the interspin vector, and R the interspin distance. \hat{H}_{DD} has both a distance dependence and a dependence on the orientation of interspin vector with respect to the external magnetic field \vec{B}_0 . $\vec{B}_0 \parallel \vec{z}$ defines a unique axis and the orientation can be described by the dipolar angles θ and ϕ . \hat{H}_{DD} is often split into six terms (the 'dipolar alphabet') that have varying angular, and spin operator dependence, but all but one term can be neglected if the high field approximation is valid. In the high field (or 'weak coupling') approximation we assume that the electron Zeeman interaction is much stronger than the electron spin-electron spin coupling. In the following we treat the weak coupling situation

between two electron spins $S_1 = S_2 = 1/2$. This allows us to drop the non-secular terms (all spin operators that do not contain \hat{S}_z operators for both spins) from the full dipolar coupling equation and we remain only with the term

$$\hat{H}_{\text{DD}} = -\omega_{\text{DD}} \hat{S}_{1z} \hat{S}_{2z}. \quad (2.15)$$

The dipolar coupling frequency ω_{DD} is given by

$$\omega_{\text{DD}}(R, \theta) = \frac{\mu_0}{4\pi\hbar R^3} g_1 g_2 \mu_B^2 (1 - 3 \cos^2 \theta). \quad (2.16)$$

Exchange coupling Heisenberg exchange coupling is a consequence of the possibility of two electron spins to be indistinguishable, i.e. to be exchangeable in the wave function. It requires that the wave functions of the electrons overlap significantly. For through-space interactions in a rigid arrangement of well-localised electron spin density this can usually be neglected for distances larger than ~ 1.5 nm. This may not hold if the spin density is strongly delocalised, for example in electron spins connected by a conjugated π -electron system. Exchange coupling can also occur in solution if molecular collisions occur during which the overlap exists for a short time. The sign of the isotropic part of \mathbf{J} depends on the relative strength of ferromagnetic coupling (contributes with negative sign) and anti-ferromagnetic coupling (contributes with positive sign), in addition to polarisation effects, which may have either sign. The anisotropic contribution to \mathbf{J} arises from spin-orbit coupling, and is usually neglected in organic radicals.

2.2.4 Strong electron spin - electron spin interactions

In electron systems with $S > 1/2$ the electronic ground state is not degenerate for different values of the projection of the effective spin quantum number even in the absence of external magnetic fields. This is caused by dipolar coupling and spin-orbit coupling, and the effect is known as zero-field splitting. Note that an important exception are systems with cubic symmetry, which leads to cancellation of the spin-spin interactions. In analogy to low spin dipolar coupling we can define the zero-field splitting Hamiltonian (with the zero-field interaction tensor \mathbf{D})

$$\hat{H}_{\text{ZFS}} = \vec{S}^T \mathbf{D} \vec{S}, \quad (2.17)$$

$$= D \left(\hat{S}_z^2 - \frac{1}{3} S(S+1) \right) + E \left(\hat{S}_x^2 - \hat{S}_y^2 \right). \quad (2.18)$$

The second form can be obtained by using basic properties of angular momentum operators. It is convenient because it leads to a simplified expression in cases of axial symmetry, where $D \neq 0$ and $E = 0$.

2.2.5 Interaction with microwave irradiation

All former interactions are system inherent properties that depend on the spin types, environment and geometries of the spin system. By remaining with the quantum description for the spin states, and using a semi-classical description of microwave irradiation we can also define a Hamiltonian term that describes the effect of oscillatory fields $B_1(t)$ on the electron spins.

When applying a (time-dependent) magnetic field of strength B_1 to a spin system we also have to consider the coupling of the spins to this additional field. The interesting regime is when the frequency of the oscillating field is resonant with spin transitions, which for electrons spins at commonly used magnetic fields is in the microwave regime. A possible Hamiltonian for a single electron spin and monochromatic, on-resonance MW irradiation

$$\hat{H}_{\text{MW}} = \omega_1 \cos(\omega_{\text{MW}}t + \phi) \hat{S}_x \quad (2.19)$$

is time-dependent with frequency ω_{MW} and phase ϕ . In this Hamiltonian we use the \hat{S}_x operator, which implies that the irradiation happens along the x -direction. $\omega_1 = g\mu_B B_1/\hbar$ is the angular nutation frequency, which depends on the strength of the driving field. Because of the time-dependence of \hat{H}_{MW} we cannot directly obtain solutions with Equation (2.1). This can be remedied by transforming to a rotating coordinate system, and the description of spin dynamics in this framework will be the topic of the following section.

2.3 Spin dynamics

Semi-classical description of precession If the magnetic moment $\vec{\mu}_S$ of an electron spin (or classically the total magnetisation \vec{M}) is not aligned with an external magnetic field \vec{B} , it is subject to a torque

$$\frac{d\vec{S}}{dt} = -\frac{1}{\hbar} (\vec{\mu}_S \times \vec{B}_0) = -\frac{g\mu_B}{\hbar} (\vec{S} \times \vec{B}_0), \quad (2.20)$$

that leads to a rotation of $\vec{\mu}_s$ around the field axis. The rotation is known as precession. Precession around the static external field \vec{B}_0 occurs at the so-called 'Larmor' frequency $\omega_S = g\mu_B B_0/\hbar$. Precession can also be induced when a second, time-dependent magnetic field $\vec{B}_1(t)$ is applied (at an angle with respect to \vec{B}_0). The resulting precession at ω_1 in the presence of MW irradiation is often called nutation, or Rabi oscillation. For example MW irradiation with frequency ω_{MW} can be described as such an oscillating field.

2.3.1 Monochromatic MW irradiation and the rotating frame

For a static $\vec{B}_0 \parallel z$ we have a fixed Larmor frequency of a given electron spin. We can transform to a coordinate system that rotates with the 'Larmor' frequency ω_S , which helps to describe the remaining interactions (hyperfine, dipolar, etc.). If we also transform the oscillating MW field defined in Equation (2.19) into such a 'rotating frame' where $\omega_{\text{MW}} = \omega_S$ (i.e. when describing MW irradiation that is exactly resonant with the electron spin) we find a time-independent term of magnitude B_1 along one transverse direction, and transverse terms that rotate in the transverse plane at twice the microwave frequency. The latter terms can in good approximation be neglected in most situations, because they average out quickly. The static component induces a rotation of the spin state. Only the perpendicular component of \vec{B}_1 contributes to this torque. By effectively tilting the direction of \vec{B}_1 we thus have a convenient way to treat spins that are not exactly on resonance with ω_{MW} , and thus 'nutate' with

$$\omega_{\text{eff}} = \sqrt{\Omega^2 + \omega_1^2}, \quad (2.21)$$

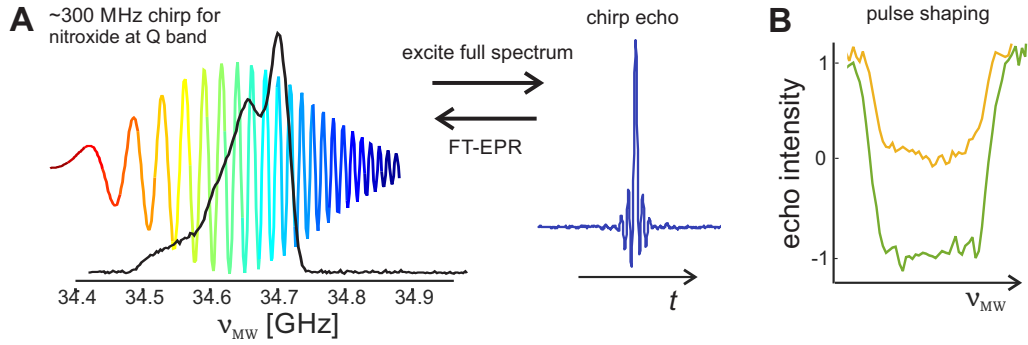


Figure 2.2: Frequency swept pulses; (A) at Q-band we excite the entire nitroxide spectrum with a frequency swept MW pulse; the resulting time-domain echo is shown on the right. Inversely, Fourier transform of the echo yields the EPR spectrum. (B) Echo intensity as a function of MW frequency for a broadband chirp inversion pulse. By pulse shaping we can obtain specific excitation profiles, here shown for a broadband $\pi/2$ pulse (yellow), resp. π pulse (green);

where $\Omega = \omega_S - \omega_{\text{MW}}$ is the resonance offset. If B_1 is only switched on during time t_p , we have applied an ideal rectangular MW pulse, which has induced a rotation of

$$\beta = \omega_{\text{eff}} t_p, \quad (2.22)$$

which is referred to as the flip angle of a pulse.

2.3.2 Frequency-swept MW pulses

Recent technological advances have led to the introduction of frequency-swept pulses with large bandwidth in EPR with the ability to perform pulse shaping.^[73,276] The principle is illustrated in Figure 2.2. With sufficient bandwidth the full nitroxide spectrum at least up to Q-band can be excited with a single MW pulse. Fourier transform (FT) of the echo transient yields the nitroxide spectrum in frequency domain. The excitation profile $p(\nu_{\text{MW}})$ of the pulses can be tuned to have uniform ('flat') excitation profiles at the desired frequencies, and steep flanks at the edges that minimise undesired excitation.

Adiabatic spin inversion pulses have been developed, where the spins at different resonance offsets Ω follow a slowly changing effective field ω_{eff} . The most important theory results for adiabatic frequency-swept pulses in EPR from Doll et al.^[76] and Doll and Jeschke^[75] will be summarised in the following. Adiabatic behaviour can be achieved when the sweep rate of the frequency is low compared to the effective MW field strength, which is characterised by the adiabaticity

$$Q = \frac{\omega_{\text{eff}}}{d\theta/dt} \gg 1. \quad (2.23)$$

Because Q implicitly depends on the resonance offset it is important for uniform excitation of an EPR spectrum to compensate for the offsets with so-called offset independent adiabaticity (OIA) schemes. This can be achieved by slow frequency sweep rates, and by performing passage sweeps, i.e. sweeps that start far below and end up far above the resonance condition. The simplest form

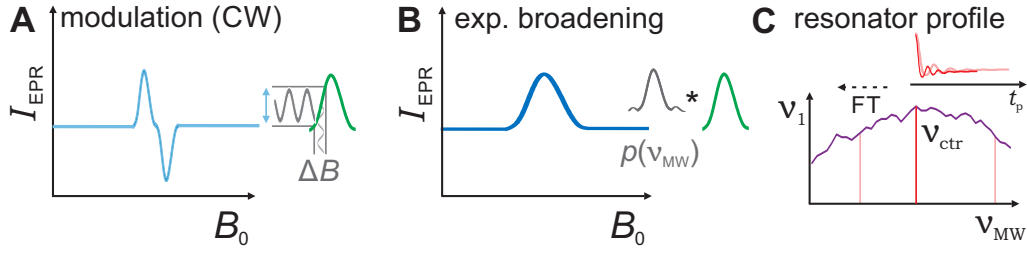


Figure 2.3: EPR measurement considerations; (A) modulation of the MW irradiation with amplitude ΔB leads to a detection of the numerical derivative of the EPR line. (B) Especially in pulse EPR the line may be distorted by broadening due to the excitation profile of a MW pulse. (C) the spectral profile of the MW cavity ('resonator profile', shown in purple) can be estimated with a series of nutation experiments (represented by red traces in inset) at different ν_{MW} . Typically the resonator is adjusted to have a maximum B_1 (and thus the highest nutation frequency ν_1) for a fixed input MW amplitude at the centre frequency ν_{ctr} .

of frequency modulation is a linear frequency ramp ('chirp' pulse') with sweep rate k , but better pulse profile control can be obtained with hyperbolic secant frequency scaling at the cost of power efficiency.^[75] The quality of a linear frequency chirp pulse with pulse length t_p , and bandwidth $\Delta\nu = \nu_{max} - \nu_{min}$ can be summarised by the critical adiabaticity^[21]

$$Q_{crit}^{(chirp)} = \frac{\nu_1^2}{k} = \frac{2\pi t_p \nu_1^2}{\Delta\nu}. \quad (2.24)$$

It quantifies how efficiently the MW pulse inverts a spin at the moment t_0 when the spin is on resonance with the current MW radiation ($\Omega = 0$). An optimal $\pi/2$ pulse requires $Q_{crit} \approx 0.4413$.^[75] Note that in practice it is also strongly recommended to apodize the flanks of a broadband pulse (by e.g. quarter-sine waves) in order to suppress ripples from the steep flanks of a sudden switching of MW irradiation.^[75] Additional consideration can be made to account for the Bloch-Siegert phase shift, which accumulates during a frequency swept pulse.^[75] If more than one frequency swept pulse is applied in an EPR experiment we need to consider the phase acquired after each pulse. To get correct refocusing of all resonance offsets we need to fulfil

$$0 = \sum_l s_i t_{p,i} \Delta o_i, \quad (2.25)$$

where i is the number of pulses, and for each pulse we have the sign of the sweep rate s_i ('+1' for $\nu_{start} < \nu_{end}$, '-1' otherwise) the pulse length $t_{p,i}$ and the change of coherence order before and after the pulse Δo_i ('1 for a $\pi/2$ pulse, '2' for a π pulse).

2.4 Selected experimental EPR methods

In this work we show EPR measurements in the low to intermediate field regime, which includes X-band, Q-band and ~ 95 GHz (W-band).

2.4.1 Resonators

Modern CW EPR spectrometers at X-band to W-band are usually equipped with a microwave resonant cavity (a 'resonator'), characterised by a quality factor (Q-factor). It is defined as the ratio of the full width half maximum (FWHM) bandwidth over the resonance frequency ν ($Q_{\text{res}} = \Delta\nu_{\text{FWHM}}/\nu$), and it is a measure of the energy storing ability of the resonator. High- Q_{res} resonators offer high sensitivity, by providing strong B_1 fields, and high detection efficiencies (for more details see e.g. Doll et al.^[77] and Tschaggelar et al.^[290]), at the cost of low resonator bandwidth. This is what is typically desired for CW operation. For pulsed experiments it may be desirable to work at lower Q_{res} , which yields better actual bandwidth, but unfortunately also reduces detection efficiency (compare Figure 2.3).

2.4.2 Continuous wave EPR

As the name suggests the EPR signal in this type of spectrometers is acquired during constant MW irradiation at a fixed MW frequency. The EPR spectrum is detected by sweeping the external magnetic field magnitude B_0 . We typically assume that a steady-state signal is observed, which is ensured by fast spin relaxation. The signal is detected in reflection mode, using high-Q MW resonators. To reduce the bandwidth of the noise, the MW irradiation is modulated at a low frequency (usually 100 kHz), which can be demodulated in phase-locked detection ('lock-in' detection). This leads to the characteristic first derivative-like appearance of the EPR spectrum (see Figure 2.3). The conventional ('absorption') spectrum can be obtained by integration, and the double integral of a CW EPR spectrum is proportional to the number of contributing spins. It can thus be used for spin counting, assuming power saturation effects are avoided. Most commercial spectrometers are only able to detect a fixed phase of the transverse magnetisation. Note that recently an alternative detection mode is emerging, in which the magnetic field is swept very rapidly (faster than spin relaxation) by auxiliary sweep coils.^[281] This 'rapid scan' technique currently has only slightly better sensitivity than the standard CW method for typical nitroxide spin labels, but is a promising alternative to increase sensitivity in samples with slow relaxation.^[221]

2.4.3 Pulsed EPR

A microwave pulse is characterised by its spectral excitation profile $p(\Omega)$ and its duration t_p . The simplest (idealised) model is a rectangular ('on'/'off'), mono-chromatic pulse at ν_{MW} , which corresponds to a sinc function $p(\Omega)$, with $\Delta\nu \approx 1/t_p$. The action of such an ideal pulse on an ensemble of spins $S = 1/2$ has been semi-classically and quantum mechanically discussed above. In commercial pulsed EPR machines equipped with high power MW amplifier upgrades and suitable pulse EPR resonators^[238] the shortest pulse length that can be obtained for a π -pulse is on the order of $\sim 4 - 6$ ns in frozen aqueous samples. One of the newest developments which is relevant for this work was the introduction of fast arbitrary waveform generator (AWG)s in EPR spectrometer hardware.^[76,277] AWG-synthesised pulses enable spin excitation over a large bandwidth (up to 2 GHz). This bandwidth can be achieved by frequency modulation of the MW pulse.^[75] In the reported practical cases this was implemented as a linear frequency ramp ('chirp' pulse), or

as hyperbolic secant frequency scaling.^[74,78] At these high bandwidths it becomes important to consider the non-ideality of common MW amplifiers, and the transfer function induced by the experimental setup (predominantly due to the MW resonator).^[73,75] With pulse amplitude modulation, and resonator-compensated pulses it is possible to obtain almost flat inversion profiles (in frequency domain) with very steep flanks. This is particularly useful when pulse excitation bandwidths overlap must be minimised.^[240,285]

2.5 Selected pulsed EPR techniques

2.5.1 Nutation experiments and resonator characterisation

To determine the interaction strength of the spins with MW irradiation we can for example apply a MW pulse with fixed amplitude for an increasing pulse length t_p . This is known as a nutation experiment, and in EPR it is usually read out with a subsequent Hahn echo pulse sequence (see below) to avoid spectrometer dead-time issues, and to minimise effects of sample inhomogeneity. The simplest refocused nutation pulse sequence is shown in Figure 2.4. The Fourier transform of a nutation trace give the nutation frequency ν_1 , which can be used to experimentally determine resonator profiles.^[73] Note that ν_1 depends on the magnetic moment and total spin S . This is a valuable tool for separation of overlapping spectra in multi-spin label studies.^[96,313] Nutation-encoded experiments can be used to simultaneously study different magnetic species in a sample, for example using the phase-inverted echo-amplitude detected nutation (PEANUT) experiment.^[279]

2.5.2 Spin relaxation measurements

If we consider an ensemble of $S = 1/2$ electron spins right after having performed an ideal $\pi/2$ MW pulse, we expect all excited spins to be perfectly aligned in some direction in the transverse plane. After the pulse each spin begins to precess, and small differences in the precession frequency arise due to slightly different micro-environments around the spins, and sample inhomogeneity (which affects B_0). This quickly leads to decoherence of the initially aligned magnetic moments, which can be reversed, for example in the Hahn echo (HE) pulse sequence. In the HE experiment the precession direction of the spins is inverted at time τ by a π pulse, which leads to a refocusing of the magnetisation at 2τ (neglecting the duration of the MW pulses). However, not all interactions can be inverted like this and additional relaxation processes attenuate the EPR signal. This has been an active field of research for many decades, and a full summary cannot be given here. Instead we refer to the excellent summaries presented in Eaton and Eaton^[82, 83], Schweiger and Jeschke^[266], and only list the major experimental methods.

Transverse relaxation Transverse relaxation (also called spin-spin relaxation) denotes processes that lead to a decay of signal intensity during times in an EPR experiment where electron spin coherence evolves in the transverse plane. Phenomenologically, it is usually studied by HE experiments with variable refocusing delays τ . In many cases the data can be fitted by a one or two (stretched) exponential decays. At the spin concentrations which are relevant for this work

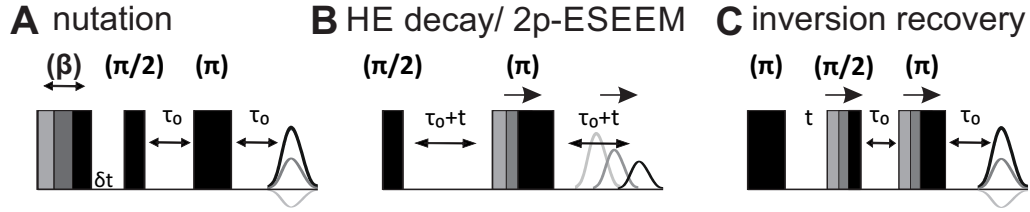


Figure 2.4: Commonly used pulse sequences;

($\lesssim 200 \mu\text{M}$) it has been demonstrated that transverse relaxation in frozen solutions of nitroxide is dominated by nuclear and spin diffusion.^[82,83] Nuclear spin diffusion can be counteracted by multiple refocusing of the spin echo.^[50,274,291] Instantaneous diffusion (which happens during MW pulses) is often negligible, unless many consecutive pulses are used.^[274]

Longitudinal relaxation Longitudinal relaxation describes events that return non-equilibrium magnetisation to the thermal equilibrium state. This type of relaxation requires energy absorption, which is why it is also known as spin-lattice relaxation. In pulse EPR it can for example be studied by the saturation recovery experiment, or the inversion recovery (IR) experiment (used in this work). The characteristic relaxation time for transverse relaxation T_m can never be longer than the longitudinal relaxation time T_1 .

2.5.3 Pulsed dipolar spectroscopy for distance measurements

PDS exploits the dipolar coupling between weakly coupled electron spins to obtain distance information in the nanometre range (see Equation (2.16)). The most commonly applied pulse experiments are Double Electron Electron Resonance (DEER, also known as PELDOR),^[136,213] Relaxation Induced Dipolar Modulation Enhancement (RIDME),^[174,210] double quantum coherence (DQC),^[37] single frequency technique for refocusing (SIFTER),^[74,141,262] and the '2+1' pulse sequence.^[176]

The PDS pulse sequences differ in the way the two spins of a dipole-dipole coupled pair are excited. In one set of techniques (e.g. SIFTER and DQC), both spins of a pair are excited by all pulses.^[34,57–59] Such techniques are mostly used for distance measurements with pairs of identical spin labels. The other set of PDS techniques (like DEER, also known as PELDOR, and RIDME)^[60,61,62,63] requires selective excitation of different spin populations. One of the spins in the pair is the observer (spin A) and the other one is flipped by pump excitation at a second frequency or, statistically, by relaxation (spin B).

The extraction of distance distributions from pulsed dipolar experiments relies on the dependence of the parameter ω_{\perp} (for perpendicular orientation of the interspin vector with respect to \vec{B}_0) on the inter-spin distance R :

$$\omega_{\perp}(R) = \frac{\mu_0 \beta_e^2 g_A g_B}{4\pi \hbar R^3} \quad (2.26)$$

$$\approx \frac{52.04 \text{ MHz}}{(R/1 \text{ nm})^3} \quad (2.27)$$

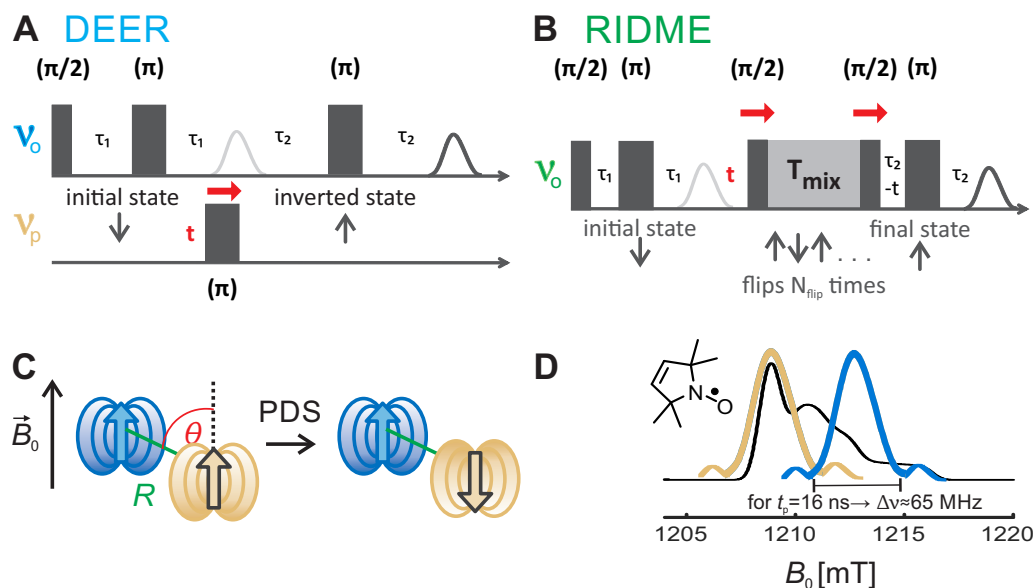


Figure 2.5: Pulsed dipolar spectroscopy; (A) 4-pulse DEER sequence; (B) 5-pulse RIDME sequence; the red arrows indicate which pulses move to generate the PDS time-axis t (C) definition of inter-spin distance R and dipolar angle θ ; in the DEER family of PDS experiments one of the two spins is selectively inverted, which inverts the local field at the site of the other spin. (D) typical observer (blue) and pump pulse (yellow) positions for nitroxide-nitroxide DEER at Q-band;

What is typically neglected for nitroxides and other organic radicals is the deviation of the g factor of the radical from that of the free electron, thus $g_A = g_B \approx g_e$, which results in the approximation given in Equation (2.27), which is made in the kernel-generating function of DeerAnalysis.^[144] For the case of metal ion complexes with known g -factor anisotropy (like Cu(II) complexes), an approximate correction has been previously reported.^[196] For the often observed approximately square planar coordination of Cu(II), the largest deviation of g_{Cu} from g_{free} is along the z -axis and, as an example, a value of $g_{\text{Cu},z} = 2.2$ leads to a deviation of $\omega_{\text{dd,eff}}$ of $100\% \cdot (g_B - g_e)/g_e = 9.9\%$. This translates to an error in the distance calculation of 3.2%. In this work, we neglect such effects and use the standard kernel implemented in DeerAnalysis^[144] to process the pulse EPR data.

DEER In DEER, we need to place pulses at two different MW frequencies (pump ν_p and detection ν_d frequencies) within the EPR spectrum. The spin labels in DEER can be but do not have to be of the same type. DEER with pairs of nitroxides, is currently the most common application of PDS. The method works best when the pump and detection bandwidths together cover a substantial fraction of the EPR spectra, which can be achieved for example by using ultra wideband (UWB) in Cu(II) spectra.^[48] However, overlap of the microwave pulse bandwidths must be avoided because it leads to signal reduction and may introduce artefacts.^[47,253,285]

RIDME The RIDME experiment exploits a different principle for achieving inversion of the B spin, which is particularly promising for the combination of organic radicals with paramagnetic

metal ion centres. The non-equilibrium magnetisation of the A spins is stored along the direction of the static magnetic field during the mixing time T_{mix} . During this period, the B spins flip stochastically with a certain probability, depending on their longitudinal relaxation time. These spin flips invert the magnetic field induced by spin B at the site of spin A and thus shift the A spin resonance frequency by the dipole-dipole interaction. This effect can be detected after transferring the magnetisation of the A spins back to the transverse plane to form a spin echo. RIDME requires pulses at only one microwave frequency, and B spin inversion is thus not limited by the bandwidth of an additional pump pulse. If we consider a Poisson stochastic flipping process in a two-level spin system, characterised by the flip rate W , it is possible to show^[122] that the probabilities for the even and the odd number of spin flips N_{flip} after a time T_{mix} are given by

$$P_{\text{even}} = \frac{1}{2} (1 + \exp(-2WT_{\text{mix}})), \quad (2.28)$$

$$P_{\text{odd}} = \frac{1}{2} (1 - \exp(-2WT_{\text{mix}})). \quad (2.29)$$

A simple example is given by pairs of Cu(II) ions and nitroxide, which both have an electron spin of $S=1/2$ with only two possible projection states. Only those B spins contribute to dipolar modulation that undergo an odd number of spin flips during the mixing block. Thus, the build-up kinetics for the RIDME modulation depth follows the law for $P_{\text{odd}}(T_{\text{mix}})$. We can assign $2W = T_{1,B}$, where $T_{1,B}$ is the longitudinal relaxation time of the B spins. The dipolar modulation amplitude in the RIDME experiment grows with a characteristic rate of $1/T_{1,B}$ and reaches a steady state value of 50% of the total spin echo amplitude after a time $T_{\text{mix}} \gg T_{1,B}$. This approximation for the RIDME modulation buildup kinetics has been used in the past.^[257] Note that longitudinal relaxation of the A spins must be sufficiently slow, so that the non-equilibrium A-spin magnetisation survives during T_{mix} .

This approximation neglects that longitudinal relaxation of paramagnetic centres in frozen glasses is typically not mono-exponential and that the B-spin flip may induce a flip of the A spin with certain probability. Such processes are of relevance in Gd(III)-Gd(III) RIDME^[162] and a reduced modulation depth at elevated temperatures has also been found in Cu(II)-nitroxide RIDME.^[250] The neglected correlated flip-flops of the A-B pairs can lead to a reduced limiting value of the modulation depth, since the average number of B spin flips for the modulated part of the spin echo signal is always larger than the average number of B spin flips for the unmodulated part of the spin echo.

Data analysis in PDS In general, the output of any PDS measurement is a time-dependent signal $V(t)$ containing oscillations from a distribution of dipolar frequencies which originates from the underlying intramolecular distribution $P(R)$ of the spin-spin distances and the orientation distribution (powder averaging). The signal is given by the averaged sum of signals of N detected spins A, each of which is coupled to the spins B with the dipolar frequency $\omega_{AB}(R, \theta)$

$$V(t, R, \theta) = \frac{1}{N} \sum_{A=1}^N \left(\prod_{A \neq B} [1 - \lambda(1 - \cos(\omega_{AB}(R, \theta)t))] \right). \quad (2.30)$$

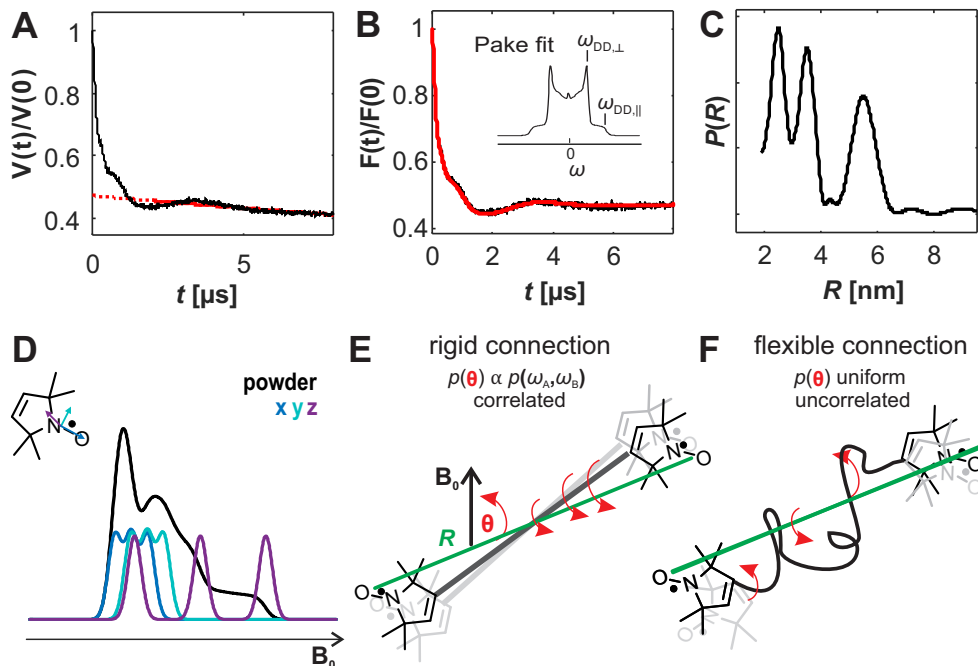


Figure 2.6: (A-C) Data analysis for PDS; (A) simulated primary data $V(t)$ (black), and background fit (red) (B) form factor $F(t)$ after background correction; inset: Fourier-transform, which give the typical Pake spectrum; (C) distance distribution $P(R)$; (D-F) orientation selection effects in PDS; (D) simulated nitroxide spectrum at Q-band and projection of the components along the principle directions; (E) rotation of a bi-radical with a rigid connection of two nitroxides leads to correlated changes in the resonance frequencies ω_A and ω_B ; for a fixed setting of pump and observed pulses in DEER we consequently observe a non-uniform distribution of the dipolar angle $p(\theta)$. (D) If the linker is sufficiently flexible, the correlation is lost, and a uniform excitation of $p(\theta)$ is expected.

The experimental parameter λ is the inversion efficiency of the B spins, and $\omega_{AB}(R, \theta)$ is given by Equation (2.26). To calculate the ensemble signal given $P(R)$, the Equation (2.30) can be integrated over the dipolar angle θ and relevant distance range $R_{min} < R < R_{max}$ to find (here written for a single A spin)

$$V(t) = 1 - \lambda \int_{R_{min}}^{R_{max}} \int_0^{\pi/2} P(R) [1 - \cos \omega_{AB}(R, \theta)t] \sin \theta d\theta dR. \quad (2.31)$$

Here we have assumed that there is no orientation correlation of the spin excited by the MW pulses and θ (illustrated Figure 2.6).

The data analysis procedure to extract distance distributions from $V(t)$ is illustrated in Figure 2.6(A-C). The high sensitivity of PDS methods allows to work with spin concentrations in the low micromolar range, which is sufficiently dilute that we can treat each individual spin pair as an isolated system. We can thus separate the signal into a contribution of remote spins (the 'background', $B(t)$), and nearby spins in the form factor $F(t)$

$$V(t) = F(t)B(t). \quad (2.32)$$

Data analysis usually begins with the fitting and removal of $B(t)$. In order to convert the obtained $F(t)$ to the distance domain, it is necessary to invert Equation (2.31), which is known to be an ill-posed problem. This can be addressed by kernel based fitting of the underlying distance distribution

$$F(t) = K(R, t)P(R). \quad (2.33)$$

The powder averaged dipolar kernel is given by

$$K(R, t) = \int_0^1 \cos[(3x^2 - 1)\omega_{DD,\perp}t]dx. \quad (2.34)$$

Solutions can either be found by a model-based approach (e.g. fitting with a trial Gaussian distribution), or in a model-free fashion (e.g. using Tikhonov regularisation).^[52,85,144] Note that new approaches, for example, based on neural networks^[305] or the simultaneous analysis of several PDS datasets^[248] are being developed.

In Tikhonov regularisation a single regularisation parameter α is used to balance fit quality ρ with the smoothness of the fitted distribution η

$$G(\alpha) = \rho + \alpha\eta = \|K(R, t)P(R) - F(t)\|^2 + \alpha\left\|\frac{d^2}{dR^2}P(R)\right\|^2. \quad (2.35)$$

The best solution for a given α is found with the minimal $G(\alpha)$. Recently, several methods have been tested to automatically find the optimal α using for example the L -curve criterion or the GCV criterion (the latter was used predominantly in this study).^[85]

Sensitivity range of PDS methods Due to transverse relaxation of the detected spins, it is often difficult to resolve coupling frequencies smaller than 50 kHz, which correspond to a maximum accessible distance of $R_{\max} \approx 10$ nm, or a period of dipolar oscillations of about 20 μ s. Because the average number of intermolecular spin pairs in a homogeneous solution increases with the square of the distance, these intermolecular dipole-dipole interactions are not fully negligible for distances up to several tens of nanometres,^[136,140,143] even though the coupling frequencies become very small. The lower limit of accessible distances R_{\min} is given by the distance at which the strength of the electron spin-spin interaction is comparable to the excitation bandwidth of the microwave pulses. For commonly used EPR setups R_{\min} is usually between 1.2 and 1.8 nm. It may also happen that at short spin-spin distances, spin exchange interaction becomes relevant or even dominant, which strongly complicates the analysis of distance distributions.

The angular dependence in Equation (2.16) implies that the orientation of a given spin pair with respect to the external magnetic field must be fixed on the time scale of the experiment, in order to avoid time-averaging of the dipolar interaction. This is typically achieved by freezing the sample, but other methods to immobilise biomolecules for PDS are emerging, which even have enabled PDS at ambient temperature.^[177,268,311]

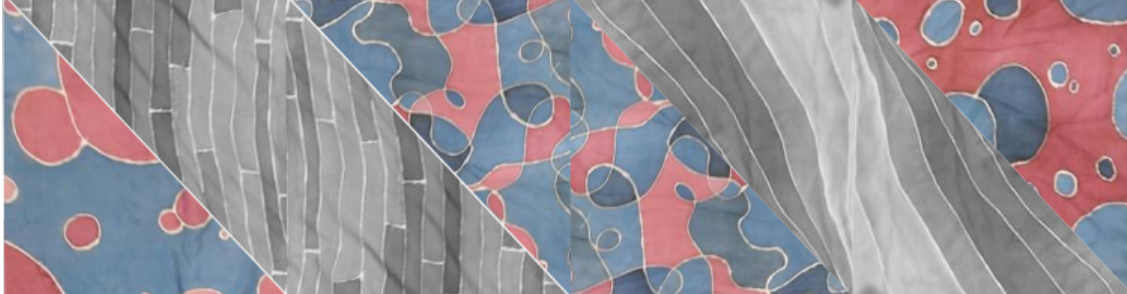
Orientation selection Orientation selection in dipolar EPR spectroscopy has been studied extensively for more than a decade.^[2,32,44,45,103,152,196,200,201,208,214,236,257,258] Here we give only a short summary of the theory as it is described in the Supporting Information of Ritsch et al.^[250]

Geometry of an arbitrary spin pair consisting of one A spin and one B spin is fully described by five angles and one distance (e.g. using Euler angles (α, β, γ) that relate the molecular frame of the B spin to the one of the A spin and the two polar angles (θ_{dd}, ϕ_{dd}) that specify the direction of the spin-spin vector in the A spin molecular frame). For the orientation averaging problem, it is convenient to consider the orientations of the static magnetic field \vec{B}_0 in the two molecular frames and the angle between the magnetic field and the spin-spin vector, which is uniquely defined for spin A by the angles θ_A and ϕ_A (and results in resonance frequency of the A spins $\omega_{A,k}(\theta_A, \phi_A)$, with the index k indicating the nuclear spin state of a hyperfine coupled nucleus). Analogously, for the B spin we can write the EPR frequency as a function of the two eigenframe angles and the corresponding nuclear spin state: $\omega_{B,j}(\theta_B, \phi_B)$. Like in the above sections θ is the dipolar angle (between the spin-spin vector and the static magnetic field).

In the case of (semi-)rigid molecules we cannot assume that the two angle pair distributions of A and B spin are uncorrelated with each other and with the distribution of θ (see Figure 2.6). This can be expressed as conditional probabilities, for example $P(\theta | \omega_A)$ is the probability of detecting a molecule with interspin orientation θ , given that the resonance frequency of the A spin is ω_A . The description with conditional probabilities can be conveniently related to the situation in PDS experiments by including the excitation profiles the MW pulses for the detected A spin $P_d(\omega_A)$, resp. the inverted B spins $P_{inv}(\omega_B)$. Including summation over the nuclear spin states, we then obtain an expanded version of Equation (2.31) for the dipolar time evolution signal in the form

$$V(R, \theta, t) = P_{inv} \sum_{k,k'} \int_0^{2\pi} \int_0^{\pi} P(\theta | \theta_A, \phi_A) P_d(\omega_{A,k}(\theta_A, \phi_A)) \times \cos[\omega_d(R, \theta)t] \sin \theta_A d\theta_A d\phi_A. \quad (2.36)$$

Here we have assumed that the inversion profile of the B spins $P_{inv}(\omega_B)$ is uniformly distributed, i.e., that the probability of B spin inversion does not depend on orientation of the B label. The aim of an experimental orientation averaging procedure to perform distance analysis in rigid molecules would be to set up one or several dipolar evolution measurements in such a way that the product of the excitation profiles ($P_d P_{inv}$) approaches a uniform distribution over ω_A and ω_B . If this is the case we arrive back at Equation (2.30), and data analysis can be performed with standard Pake powder averaging.



Chapter 3

3

Identifying protein-protein interactions of hnRNPA1 by EPR

Scope of this Chapter It is known that buffered solutions of the human splicing regulator protein heterogeneous nuclear ribonucleoprotein (hnRNPA1) can undergo (reversible) liquid-liquid phase separation (LLPS) depending on protein concentration, thermodynamic conditions (e.g. temperature and pressure), and buffer composition.^[218] This phase transition is mediated by the intrinsically disordered C-terminal domain of hnRNPA1^[218] (for a more detailed introduction to hnRNPA1 and protein condensates see Section 1.2). Detailed studies of the conditions that lead to LLPS of hnRNPA1 have been reported,^[218,299] but little is known about the (un-)structural transitions of the IDD that induce the macroscopic phase transition. *In vitro*, LLPS manifests as the formation of liquid droplets (LDs) which have been observed in the size range of a few to several tens of micrometers, and have the ability to fuse with one another. The droplets can be visualised by light microscopy, and the LD state is typically also responsible for visible changes of sample turbidity, since the droplets scatter light.^[218] In this chapter we focus on the investigation of dynamics and interactions between proteins by EPR using nitroxide-based spin labelling strategies. The aim is to find conditions in which spin labelled hnRNPA1 can be studied in the monomeric state.

In this chapter we will address how EPR can be used to characterise interactions between molecules of hnRNPA1. We focus on detecting protein-protein interactions in the predominantly dispersed state, but we include selected examples of samples prepared in the liquid droplet state. The focus is predominantly set on how we can stabilise the monomeric state of hnRNPA1 in order to be

able to characterise the corresponding conformational states of the IDD. The structure of the two RNA-recognition motifs (RRMs) of hnRNPA1 has been solved by X-ray crystallography^[307] as well as solution-state NMR.^[19] These structured protein domains provide us with reference points to study the conformational ensemble of the C-terminal IDD. The two main EPR methods that we will use in this chapter are continuous wave (CW) EPR spectroscopy in X-band (~ 9.5 GHz), and the double electron-electron resonance (DEER, also known as PELDOR) experiment in Q-band (~ 35 GHz). Their ability to report on protein-protein interactions will be first described in the Theory section. We then present the results of EPR and auxiliary experiments to characterise samples of spin-labelled hnRNPA1 in the dispersed and in the liquid-droplet state. We furthermore performed intermolecular PRE experiments to identify intermolecular interactions in solution in the dispersed state. We confirm that frozen solutions of spin-labelled hnRNPA1 prepared for EPR contain predominantly monomeric protein, by measuring distance distributions between spin labelling sites in the folded RRM for a singly spin-labelled protein. In the Conclusions section we summarise our results in the context of the current state of the field for understanding the phase separation behaviour of hnRNPA1. The methods and experimental details can be found at the end of the chapter.

Author contributions and acknowledgements The NMR experiment were performed in the group of Prof. Frédéric Allain (ETH Zurich), and Dr. Elisabeth Lehmann is gratefully acknowledged for her contribution to the experimental NMR part and the re-assignment of the backbone resonance NMR spectrum of the full length hnRNPA1 Cys-free mutant. Laura Esteban-Hofer and Dr. Leonidas Emmanouilidis are thanked for the development of the agarose stabilisation protocol. The confocal imaging was performed at the ScopEM facility, and we thank Justine Kusch in particular for the training on the confocal microscope. For the circular dichroism experiments we thank Prof. Roland Riek (ETH Zurich) for access to the spectrometer, and Dr. Jason Greenwald and Dr. Witold Kwiatkowski for support in the acquisition of the data.

3.1 Introduction

The general forms of the interactions in EPR are described in Chapter 2. Here we focus on sensitivity of these interactions to changes in local spin concentration and local spin dynamics, and how to exploit them to characterise protein-protein interactions. We also briefly introduce the paramagnetic relaxation enhancement (PRE) effect as a related method from the field of solution state NMR. All considerations in this sections are valid for nitroxide-based spin labels. A quantity that we will use frequently is the spin labelling efficiency $\eta = c_{\text{spin}}/c_{\text{site}}$, which is the ratio of the concentration of spins and the concentration of the potential spin labelling sites in protein molecules.

3.1.1 Intermolecular Interactions in DEER

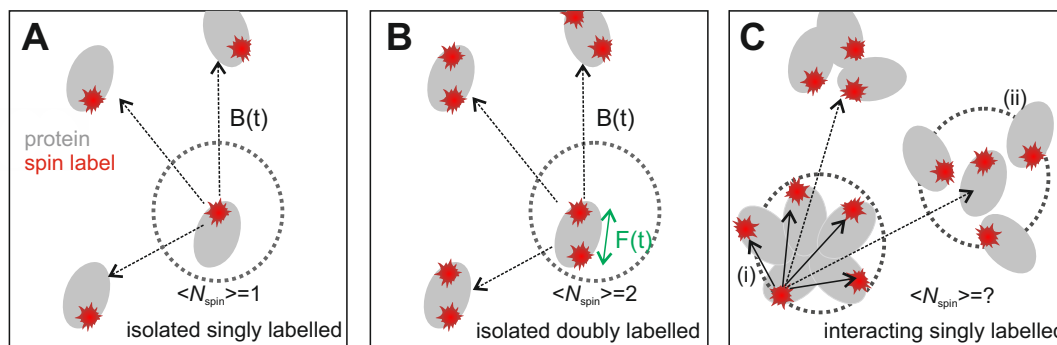


Figure 3.1: DEER with spin labelled proteins; $\langle N_{\text{spin}} \rangle$ is the number of spins in a nano-object (encircled areas). (A) If the proteins are singly labelled and fully isolated we should observe no contribution in the form factor $F(t)$, and a concentration dependent background decay $B(t)$. (B) For doubly spin-labelled proteins we observe the intramolecular contribution in $F(t)$, and the intermolecular contributions in the background decay $B(t)$. (C) For clusters of interacting proteins the number of spins in a nano-object may vary. Protein clusters may be partially ordered (i), or fully disordered (ii).

DEER was developed to measure small dipolar couplings between two sites (i.e. for doubly spin labelled molecules) in strongly diluted samples, where the isolated spin pair approximation holds (for more details see for example Figure 2.2 in Chapter 2).^[140] The lower distance limit (~ 1.5 nm) depends on the excitation bandwidth of the microwave pulses, and the upper limit (~ 10 nm, strongly sample dependent) is influenced by the phase memory time, which limits the frequency resolution that can be experimentally reached.^[18,140] The background correction by the factor $B(t)$ was introduced to remove intermolecular contributions from remote spins from the time-domain data $V(t)$ prior to distance analysis,^[143,213] such that intramolecular contributions in doubly spin labelled molecules can be interpreted independently.

Due to its large range of sensitivity in the distance domain, DEER is also well suited to study biomolecular interactions. Following well-established theory, we define a nano-object as a cluster of

spins that are close, and thus comparatively strongly coupled to one another, but only weakly to spins in other clusters. A cluster of spins can for example arise from a cluster of N spin-labelled biomolecules. N_{spin} is the number of spins in a single cluster. Assuming complete spin labelling and n spin label sites per biomolecule we have $N_{\text{spin}} = n \cdot N$. In this chapter we will illustrate how we can treat samples with a distribution of cluster size N , and how to account for incomplete spin labelling.

For the characterisation of intermolecular interactions between spin-labelled biomolecules by DEER it is best to consider first experiments with singly spin-labelled biomolecules ($n = 1$). Any modulation depth or an increase in background decay rate compared to the expected homogeneous exponential decay can then be traced back to protein-protein interactions (illustrated in Figure 3.1). We first discuss the currently used models for the background decay. We then show how the modulation depth Δ can be used for quantification of biomolecular interactions. In dense protein condensates we expect complications from the high local spin density. First, we may observe filtering effects.^[17] Filtering effects can occur if different fractions of spins have different relaxation properties, which alter their relative contribution to a spin echo in a pulsed EPR experiment. An example would be a different transverse relaxation rate of the fraction of spin labels attached to an IDD of a protein in the LD state, compared a protein in the dispersed state. If the sample consists of a mixture of proteins in the dispersed state and the LD state, the fraction with the faster relaxation rate will be suppressed at longer inter-pulse delays. We usually assume that filtering effects can be neglected, but they could in principle be accounted for as an attenuation factor, if the filtering rates are known. Another complication arises if more than two spins are in the sensitive distance range for DEER. We then expect to observe multi-spin effects, as has been studied with model systems.^[111,145]

Intermolecular background models for DEER The background factor $B(t)$ combines all coupling terms that arise from dipolar coupling of the detected spin within a given nano-object to all spins in other, remote nano-objects. The separation of the signal into the two contributions is slightly arbitrary for the purpose of studying protein condensates, where cluster sizes may not be well defined, but it can still be useful to split the data analysis problem into one for the distance range in which we can resolve dipolar couplings explicitly ($\sim 1.5 \text{ nm} < R < 10 \text{ nm}$, resp. dipole coupling from 15 MHz to 50 kHz), and one for the range that only contributes as a general decay to the time-domain signal ($\sim 10 \text{ nm} < R < 1000 \text{ nm}$, dipole coupling smaller than 50 kHz). The former is equivalent to the form factor $F(t)$ in the study of doubly spin-labelled molecules. The exact expressions for a three-dimensional homogeneous distribution of 'background' spins can, in a very good approximation, be represented by an exponential decay,^[143]

$$B(t) = \exp^{-kt}. \quad (3.1)$$

For such homogeneously distributed spins the decay constant k can be calculated from the total spin concentration c

$$k = \frac{2\pi g^2 \mu_B^2 \mu_0 N_A}{9\sqrt{3}\hbar} \lambda c. \quad (3.2)$$

The parameters are the g -values of the coupled spins (assumed to be identical), the Bohr magneton μ_B , the magnetic permittivity μ_0 , Avogadro's constant N_A , Planck's reduced quantum \hbar , and the experimental fraction of inverted spins λ (which is an experimental parameter that has to be calibrated).^[117] Based on work on a polyelectrolyte,^[211] and already in early studies on membrane proteins it was recognised that this can be extended to a more general form with the scaling exponent $n = d/3$,

$$B(t) = \exp^{-(kt)^n}, \quad (3.3)$$

where d is the effective dimensionality of the distribution of spins in the sample.^[117,144] Setting $d = 2$ is equivalent to assuming a 2-dimensional distribution of spins (like in membranes), and $d = 3$ recovers the homogeneous 3-dimensional distribution. Note that analytical expressions for even more complicated distributions of spins (spheres and spherical shells) have been derived.^[158] In summary, from the background fit we can learn about the spatial distribution and concentration of spin clusters.

Quantification of interactions from the modulation depth An important parameter in the analysis of DEER data is the total modulation depth Δ , because it is related to the average number of spins in a nano-object $\langle N_{\text{spin}} \rangle$ by^[31,117,142,143,212]

$$\langle N_{\text{spin}} \rangle = 1 + \frac{\log(1 - \Delta)}{\log(1 - \lambda)}. \quad (3.4)$$

This quantity also depends on the inversion efficiency, which can be calibrated. For the remainder of this study we assume that $\lambda = 0.4$ (based on the expected inversion profile of a 16 ns pump pulse on the maximum of the nitroxide spectrum at Q-band, which has been calibrated with biradicals). For perfectly dispersed singly spin-labelled molecules $\langle N_{\text{spin}} \rangle = 1$, for doubly-labelled $\langle N_{\text{spin}} \rangle = 2$, etc. for samples that contain proteins in different stages of condensation $\langle N_{\text{spin}} \rangle$ can take an arbitrary value, because each cluster may consist of a different number of spin-labelled biomolecules, which in addition may co-exist with a dispersed phase. The presence of higher order oligomers or protein condensates can lead to an overestimation of $\langle N_{\text{spin}} \rangle$, because multi-spin effects artificially increase Δ .^[145] To quantify oligomerisation of spin-labelled biomolecules from DEER we also need to consider the effect of the incomplete labelling ($\eta < 1$), which will reduce the number of protein clusters that contribute to the DEER experiment.^[117]

Multispin effects in DEER Multispin effects can arise if $N_{\text{spin}} > 2$, i.e. if the number of spins in a single nano-object is larger than two. Data analysis in this situation is more complex, because coupling terms arise from $N_{\text{spin}} \cdot (N_{\text{spin}} - 1) / 2$ distances in the cluster,^[145] and sum and difference frequency terms are additionally observed.^[111,145] In combination, hallmarks of multispin effects are an increased modulation depth compared to the two-spin case, and ghost peaks in the distance distribution.^[111,145] Note that the increase of Δ with $(N_{\text{spin}} - 1)$ is less than linear. The presence of ghost peaks in the distance distribution can be detected by monitoring the distance peak intensity as a function of the inversion pulse power.^[145,206] Furthermore, if the number of spins in the cluster is known, ghost peaks can be largely suppressed in data processing by power-scaling of the time-domain data.^[111]

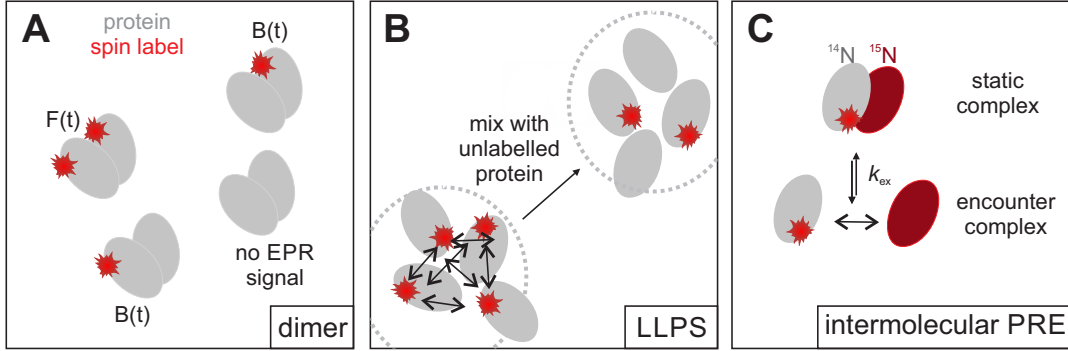


Figure 3.2: Measuring protein-protein interactions with singly spin-labelled proteins; (A) the simplest form of interaction is dimerisation, which can be quantitatively tracked with DEER. (B) In the LD state local spin concentrations can become very high, which can be remedied by spin dilution. (C) By mixing spin labelled non-isotope enriched protein with isotope-enriched non-spin labelled protein we can measure intermolecular PRE effects.

Spin dilution In cases of large clusters of biomolecules in the sample, and/or large variation of the cluster size, data analysis gets more reliable if the number of spin centres in a biomolecular cluster is artificially reduced. This can be often achieved by 'spin-dilution', which is mixing of spin-labelled protein with unlabelled protein, as is illustrated in Figure 3.2. In this work we also use the term 'spin-doping' (in analogy to the widely applied fluorescence doping), when the fraction of unlabelled protein largely exceeds that of the spin labelled variant. In spin-doping experiments we assume that multi-spins effects are negligible. Langen et al.^[179] reported that in a cluster of singly labelled proteins with fixed size N , the fraction of clusters that have i spins is given by the binomial coefficient

$$F_i(N, i, \eta) = \frac{N!}{i!(N-i)!} \eta^i (1-\eta)^{(N-i)}, \quad (3.5)$$

if the spin label has no influence on dimerisation. The labelling efficiency η has to be known independently. As a numeric example we can assume that all proteins are in a dimeric state ($N = 2$), and the labelling efficiency is 50%. We obtain 25% dimers with no labels, 50% dimers with one label, and 25% dimers with two labels. If we want to apply this for the quantification of DEER modulation depth, we can recognise that the fraction of clusters that contribute to dipolar modulations are all clusters with two spin labels, thus $F_{i>2}$. F_1 contributes to the DEER echo, but not to the dipolar modulation. F_0 is not seen by EPR at all. Unfortunately, with protein condensates it is most likely a poor assumption that only one type of cluster size N is populated, and we would need to consider a distribution of protein cluster sizes $p(N)$. The simplest example of a distribution is a mixture of monomers and dimers. This model will be analysed in detail in the next section. Quantitative analysis of clusters of higher order is not treated here.

Protein dimerisation constant We consider a sample with initial protein concentration $[P]_0$, where a fraction of the proteins is in the dimeric state (concentration $[D]$), and the rest is monomeric

(concentration $[M]$). For the dimerisation process we use the standard reaction equation



and we can define the dissociation constant K_D

$$K_D = [M]^2/[D], \quad (3.7)$$

$$= ([P]_0 - 2[D])^2/[D]. \quad (3.8)$$

To arrive at Equation (3.8) we have enforced

$$[M] + 2[D] = [P]_0, \quad (3.9)$$

which ensures that the concentrations of the monomer $[M]$, and the dimer $[D]$ add up to the constant initial total protein concentration $[P]_0$. Solving this for the concentration of the monomer, resp. dimer we get the well established relations

$$[M] = \frac{-K_D + \sqrt{(K_D^2 + 8[P]_0 K_D)}}{4}, \quad (3.10)$$

$$[D] = 1/2([P]_0 - [M]), \quad (3.11)$$

$$(3.12)$$

and we only allow positive solutions for $[M]$ in Equation (3.10). We can then define the fraction of proteins in the dimer state as

$$f_D = \frac{[D]}{[P]_0}, \quad (3.13)$$

$$f_M = \frac{[M]}{[P]_0}. \quad (3.14)$$

The maximum value that is allowed for f_D is 0.5 (fully dimerised). By inserting this definition into Equation (3.8) we find

$$K_D = ([P]_0 - 2f_D[P]_0)^2 / (f_D[P]_0). \quad (3.15)$$

$$(3.16)$$

To determine f_D experimentally we can relate it to the average number of spins in a nano-object reported by DeerAnalysis.^[144] This average number depends both on f_D and η , because the dimers and monomers have different probabilities to carry least one spin label, i.e. to be 'EPR-active'.

In a mixture of $[M]$ monomers and $[D]$ dimers we define the total concentration of clusters as

$$c_{\text{cluster}} = [D] + [M]. \quad (3.17)$$

$$(3.18)$$

The concentration of EPR-active clusters is thus

$$c_{\text{cluster}}^{(\text{EPR})} = c_{\text{cluster}} - [D](1 - \eta)^2 - [M](1 - \eta) \quad (3.19)$$

$$= [P]_0(\eta - f_D \eta^2) \quad (3.20)$$

To arrive at the last line we used the definitions of f_D and f_M , and the normalisation $1 = f_M + 2f_D$. $c_{\text{cluster}}^{(\text{EPR})}$ is the sum of c_1 , the combined concentrations of monomers plus dimers with one spin label, and c_2 , the concentration of dimer with two spin labels:

$$c_1 = [\text{M}]\eta + [\text{D}]2\eta(1 - \eta) = [\text{P}]_0(\eta - 2f_D\eta^2), \quad (3.21)$$

$$c_2 = [\text{D}]\eta^2 = [\text{P}]_0f_D\eta^2. \quad (3.22)$$

$$(3.23)$$

The average number of spins in the total number of EPR cluster can be calculated with the weighted sum

$$\langle N_{\text{spin}} \rangle = 1 \cdot \frac{c_1}{c_{\text{cluster}}^{(\text{EPR})}} + 2 \cdot \frac{c_2}{c_{\text{cluster}}^{(\text{EPR})}}, \quad (3.24)$$

$$= \frac{1}{1 - f_D\eta}. \quad (3.25)$$

Inversely, we find for the fraction of dimers

$$f_D = \frac{1}{\eta} \frac{\langle N_{\text{spin}} \rangle - 1}{\langle N_{\text{spin}} \rangle}. \quad (3.26)$$

The equation has the correct limiting behaviour, e.g. for full labelling and full dimerisation ($\eta = 1$, $f_D = 0.5$) we find $\langle N_{\text{spin}} \rangle = 2$, and for full labelling and no dimerisation ($\eta = 1$, $f_D = 0$) we get $\langle N_{\text{spin}} \rangle = 1$. A more realistic case would be intermediate labelling efficiency, and a small fraction of dimers, e.g. $\eta = 0.75$, $f_D = 0.25$ leads to $\langle N_{\text{spin}} \rangle = 1.23$. Another interesting case is low labelling efficiency, but full dimerisation, e.g. $\eta = 0.25$, $f_D = 0.5$ gives $\langle N_{\text{spin}} \rangle = 1.14$. This demonstrates that a low modulation depth can be misleading in cases of low labelling efficiency.

Together with the absolute protein concentration we can calculate the dissociation constant according to Equation (3.15).

3.1.2 Paramagnetic Relaxation Enhancement

The general theory for paramagnetic relaxation enhancement in solution state NMR is outside the scope of this work and we refer to the literature.^[58,62,129,134,216] In short, the method exploits that the natural linewidth of the resonance of a nuclear spin is strongly increased by a nearby electron spin, due to increased relaxation.^[171,275] This can be experimentally quantified by determining the ratio of the intensity of an NMR resonance in the diamagnetic state and in the presence of the electron spin $\Gamma_{\text{PRE}} = I_{\text{para}}/I_{\text{dia}}$.^[57,59] The PRE effect depends very strongly on the electron spin - nuclear spin distance (with R^{-6}). If this distance is fixed on the chemical shift exchange time-scale, the distance can in principle be calculated explicitly.^[20,88,104] In most NMR literature, such computations neglect spatial distribution of the electron spin, which is a poor approximation.^[137] In the case of IDD's the expected fast backbone dynamics lead to a rapid rearrangements of the spin label with respect to the protein residues,^[254,284,295] and intermolecular effects may appear between (transient) encounter complexes.^[130,283,296] Numerous successful applications to study

long-range interaction (on the NMR length-scale of up to ~ 2 nm) in IDD and IDPs have been reported.^[53,68,104,134,216,254,284]

In this chapter we use PRE measurements only as a qualitative source of information ('no interaction' versus 'some interaction') to study intermolecular encounters. The principle is illustrated in Figure 3.2(C). This experimental strategy has, for example, been successfully used for finding a transiently interacting segment in the low complexity domain of Tar-DNA binding protein-43 (TDP-43) in the liquid droplet state.^[63]

3.2 Results

3.2.1 Spin labelling of hnRNPA1

Protein constructs The protein constructs for this study are schematically shown in Figure 3.3(A). In addition to the full length construct we worked with a truncated version, known as UP1 (unwinding protein 1),^[116,304] that lacks the C-terminal IDD. Both hnRNPA1 and UP1 could be purified from *e.coli* in the soluble state by a two-step Ni²⁺-affinity chromatography with a TEV-digest step to remove the N-terminal His₆-tag. The final wild-type protein construct has the N-terminal Met of hnRNPA1 replaced by Gly (M1G), and an additional glycine remains at position -1, otherwise no alterations remain. Note that hnRNPA1 exists *in vivo* in more than one isoform. We here use the 20 times more abundant isoform 'A1-A', which is an alternative splicing product (252-303 missing) of the canonical isoform 'A1-B'. To complete the series we also purified the IDD without the RRM/ The IDD construct showed very low solubility in standard purification buffers, but could be purified in denaturing conditions (see further Appendix A). We however do not show spin labelling results with this domain.

Labelling sites in the RRMs For systematic distance measurements between residues in the intrinsically disordered domain (IDD, and sites in the RNA-recognition motifs (RRMs) we require suitable spin labelling sites in each domain. In any SDSL approach spin labels should be as little invasive as possible, and cysteine-targeting nitroxide spin labels are by far the best characterised and successful spin labels for this purpose.^[24] Unfortunately, it was found that incubation of wild-type hnRNPA1 with (1-oxyl-2,2,5,5-tetramethyl-2,5-dihydro-1H-pyrrol-3-yl)methyl methanesulfonothioate spin label (MTSL) led to severe precipitation of the protein, presumably due to disruption of the RRM fold upon spin label attachment to the native Cys. We attempted to purify full-length hnRNPA1 with an unnatural amino acid for bio-orthogonal spin labelling,^[173] but the yields and purity of these constructs were not sufficient for further extensive spin labelling studies. Therefore the native Cys were mutated to non-reactive amino acids (C43S, C175A). All nitroxide spin-labelled mutants shown in this study have these background mutations. Alternative Cys-based spin labelling sites were introduced as single amino acid mutations.

The new spin labelling sites for MTSL-labelling of the RRMs (later referred to as 'beacon sites' in the context the localisation method) were selected according to the following criteria: (1) be away from known interaction sites with nucleotides;^[26,300] (2) be solvent-accessible for efficient spin labelling; (3) be in intermediately flexible regions of the folded domains to minimise the risk of disturbing the local fold; (4) be within a range that all pair-wise distances connecting the beacon sites can be measured by the DEER experiment ($\approx 2 - 8$ nm); (5) at least one of the labelling sites should be in proximity (by sequence) to the C-terminal domain.

The selected mutation positions (main beacon sites) were RRM1: K52; RRM2: K144 and S182. Rotamer library-based spin label distribution simulations^[237] were performed with MMM at 298 K and the spin label MTSL at the selected sites. The resulting spatial spin label probability distributions are displayed in Figure 3.3(B) with the NMR ensemble structure of UP1.^[19] As an estimate of local backbone flexibility at these beacon sites we can compare the local root mean square de-

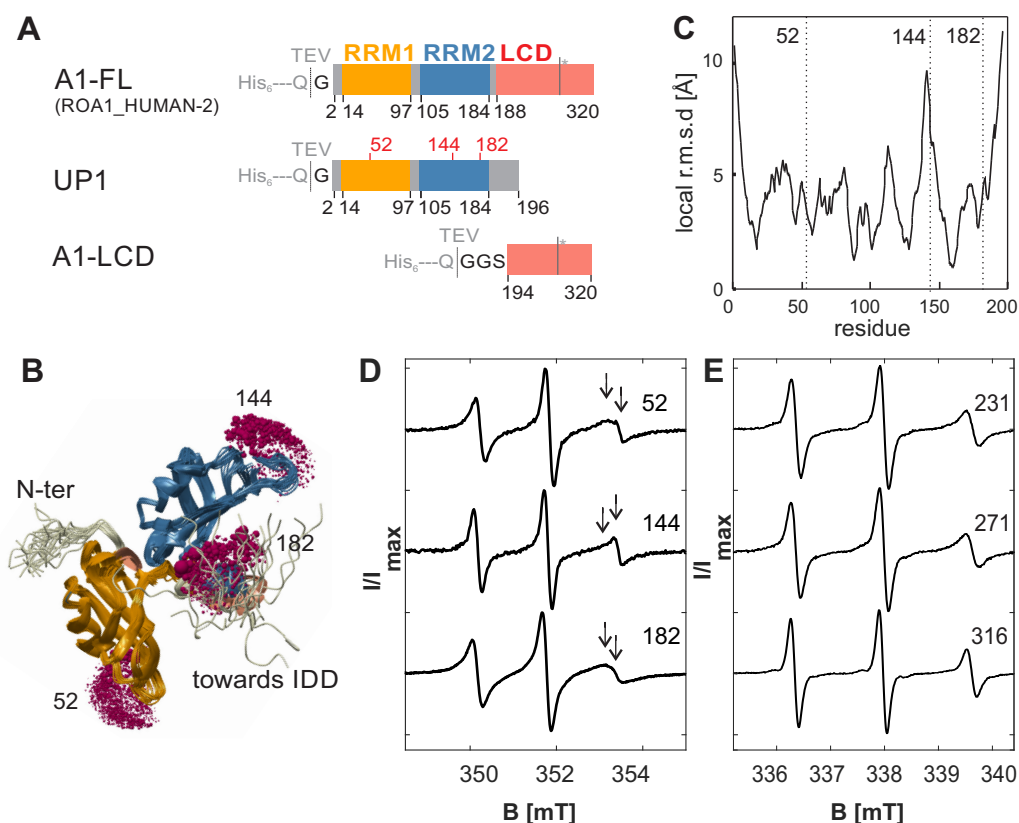


Figure 3.3: (A) Graphical overview of the constructs used in this study (B) NMR ensemble structure of UP1 (pdb: 2LYV) with rotamer simulation (red spheres) at MTSL-labelled beacon sites 52, 144 and 182; (C) local root means square deviation (RMSD) of the NMR ensemble model; (D) ambient temperature CW X-band spectra of MTSL-labelled single Cys mutants in the RRMs, resp. in the IDD; spectra were acquired at 25–50 μ M protein concentration in 50 mM sodium phosphate buffer, pH 6.5, 100 mM L-Arg, 100 mM L-Glu. (E) ambient temperature CW X-band spectra of MTSL-labelled single Cys mutants in the IDD. The magnetic field ranges differ from (D) due to acquisition with different cavities and resulting ν_{mw} .

viation (RMSD) of the backbone chain in the NMR ensemble. The local RMSD for the position of beacon sites K52 and S182 are intermediate (0.42 nm, resp. 0.45 nm), that of beacon K144 is slightly higher (0.70 nm) (Figure 3.3(C)). Note that a larger flexibility usually implies a lower probability for a mutation and subsequent spin labelling reaction leading to significant perturbation of the native fold, but also worse quality of the site as beacon for localisation measurements.^[138]

In Figure 3.3(D) we show the CW X-band spectra obtained with the MTSL-labelled beacon sites 52, 144 and 182. The EPR measurements were performed with samples in buffer conditions that inhibit phase separation, as will be discussed in more detail below. The spectra show a generally fast tumbling rate (not in the rigid limit), but are significantly broadened compared to free MTSL (not shown). The slightly reduced mobility was unexpected for these very solvent exposed labelling

sites in flexible regions of the protein, and given the large distribution of rotamers in the simulation. However, in contrast to the experiment, the simulation is performed on the structure of UP1 in the absence of the IDD, which may explain the reduced mobility at the beacon sites. The spin label in position 144 appears most mobile of the three sites. By visual inspection of the spectra at least two components can be identified in each spectrum (indicated by arrows in Figure 3.3), which complicates the interpretation. For this reason we refrain here from giving estimates of a mobility parameter.

Labelling sites in the IDD We also selected spin labelling sites in the IDD. Single amino acid mutations in the IDD are generally expected to be comparatively benign, because the sequence is not strictly conserved. Nonetheless, in the case of the short peptide amyloid-beta an influence of N-terminal labelling on the ensemble simulated by molecular dynamics has been reported.^[256] In general, not much is currently known at the molecular level about which patterns or individual residues in the IDD lead to critical changes of the conformational states. We thus mostly considered labelling sites which involve Ser to Cys mutations, due to the chemical similarity of the amino acids. Another principal consideration was to distribute the mutation positions approximately uniformly over the primary sequence. The selected cysteine mutations in the IDD were: S190C, S197C, S223C, S231C, S271C, A297C and S316C. Positions 231, 271 and 316 were selected as major reporter residues for the localisation analysis, the remaining mutants were used as auxiliary labelling sites. The ambient temperature spectra of the three MTSL-labelled single Cys mutants S231C, S271C and S316C are shown in Figure 3.3(E). The spectra appear noticeably more narrow than the spectra of the spin label at the beacon sites (compare Figure 3.3(D)), indicating faster spin label tumbling. Position 316 gives the most mobile spectrum. More detailed analysis of the lineshapes of the spin labels in the IDD will be presented in the next section.

3.2.2 Relating the macroscopic protein condensation state to EPR measurements

By tuning the composition of the buffer, we were also able to induce LLPS in samples of our purified full-length hnRNPA1 constructs at ambient temperature and pressure. This was judged by visual inspection (sample turbidity was observed), and by confocal microscope imaging, which has been established as a major method to monitor LLPS.^[8,9] The macroscopic aggregation state of the samples was thus monitored by imaging, and the microscopic state was investigated by EPR measurements in the same conditions.

In this chapter we do not present a full phase diagram study of spin-labelled hnRNPA1. Instead we define a set of reference conditions. The conditions that we compare in the following are: (i) high ionic strength dispersion buffer (50 mM sodium phosphate, pH 6.5, 100 mM L-arginine, 100 mM L-glutamate, ionic strength $I=0.181$ mM); the amino acids components will in the following be abbreviated as molar concentration of 'R/E'. The addition of R/E is known to inhibit unspecific protein-protein interactions in solution NMR experiments.^[29,30] These conditions are designed to maintain monomeric hnRNPA1. (ii) Low ionic strength dispersion buffer (10 mM sodium phos-

phate, pH 6.5, 100 mM R/E, $I = 0.114$ mM); (iii) low ionic strength LLPS buffer (same as dispersion buffer, but reduced R/E: 10 mM sodium phosphate, pH 6.5, 50 mM R/E, $I = 0.064$ mM).

Samples for DEER were either frozen with the addition of glycerol as a cryoprotectant, or with the addition of 0.2 % (w:v) low melting agarose. The samples were frozen in liquid nitrogen-cooled iso-pentane, to achieve faster freezing rates than direct flash freezing with liquid nitrogen. Note that the agarose buffer has the additional benefit to slow down droplet diffusion and gravitational sinking in the imaging experiments. This was recently demonstrated in currently unpublished work by Emmanouilidis et al., where the authors used an agarose-containing buffer for droplet stabilisation with the low-complexity domain (LCD) of Fused in Sacroma (FUS). The LCD of FUS is a fully disordered domain, and thus heat-stable during mixing with warm ($\sim 60^\circ\text{C}$) melted agarose solutions. This was a source of concern for the folded RRM of hnRNPA1, and thus following a suggestion by the authors of the FUS study we substituted the standard agarose with low-melting agarose, which is still sufficiently liquid for convenient sample handling at $35\text{-}40^\circ\text{C}$, a temperature that is expected to be sufficiently low for handling full-length hnRNPA1.

Confocal microscope imaging The confocal bright field imaging results obtained with different buffer conditions are shown in Figure 3.4(A)-(C). A homogeneous distribution of protein at the resolution and contrast of the confocal microscope was observed at low hnRNPA1 concentrations ($\sim 20\ \mu\text{M}$) in the dispersion buffer (conditions (i)). In the following we use this as the 'dispersed' reference state.

At hnRNPA1 concentrations of $100\ \mu\text{M}$ we found by confocal microscope imaging that even in seemingly 'dispersed' samples (clear by eye), we can still observe a low number of small ($\sim 1\ \mu\text{m}$) droplets in the microscope images (conditions (ii)). Note that after the addition of 50 % (v:v) glycerol to samples even at these high protein concentrations we could no longer observe droplets. This is important, because conventionally such amounts of glycerol are added to protein samples prior to flash freezing for DEER experiments. The concentration of the buffer additives R/E proved to be critical for LLPS. Diluting the concentration of both amino acids to 50 mM at a protein concentration of $100\ \mu\text{M}$ (conditions (iii)) lead to severe sample turbidity and formation of many small (diameter $\sim 1 - 5\ \mu\text{m}$) droplets. This is shown in Figure 3.4(D), and we refer to the conditions as the LD state.

Sample turbidity Sample turbidity is sometimes used as a measure for LLPS, and it can be quantified by optical density (OD) measurements (typically at a wavelength of 600 nm).^[8] In the dispersed conditions we measured $\text{OD}_{600} = 0.02(0.03)$, which is in agreement with the confocal images (i.e. no large droplets). This measurement series was however not continued with the LLPS samples because of experimental complications from droplet fusion and sinking during the measurement (which cannot easily be addressed by admixing agarose due to experimental setup restrictions). Similar complications, and other problems related to turbidity measurements as a quantification for LLPS have been pointed out in recent studies.^[9]

CW X-band spectroscopy The CW X-band EPR spectra of MTSL-labelled single Cys mutants in dispersed conditions (buffer conditions (i)) are shown in Figure 3.4(D). As we have demonstrated

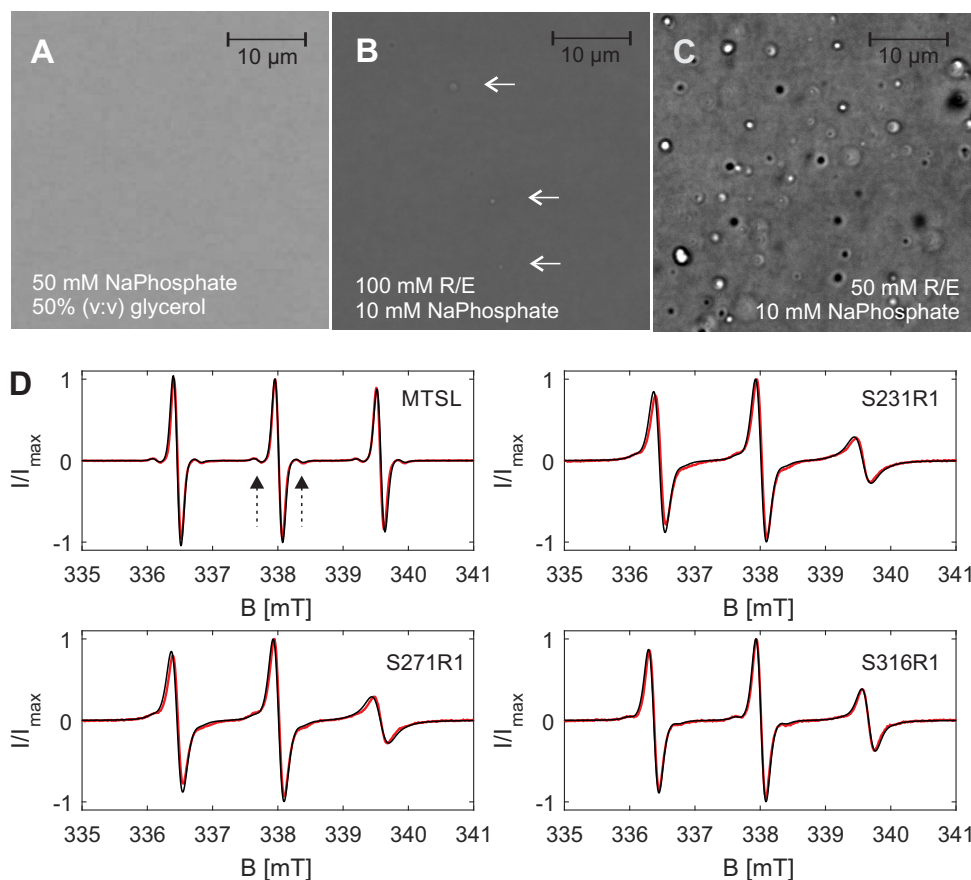


Figure 3.4: LLPS of hnRNPA1 and spin label mobility in the dispersed state; (A-C) confocal transmission images; for buffer definitions see main text (A) 20 μM hnRNPA1 at ambient temperature in high ionic strength dispersion buffer mixed with 50% (v:v) glycerol; (B) 100 μM hnRNPA1 at ambient temperature in low ionic strength dispersion buffer, stabilised with 0.2% agarose; the arrows highlight small droplets. (C) 100 μM hnRNPA1 at ambient temperature in low ionic strength LLPS buffer, stabilised with 0.2% agarose (D) ambient temperature CW X-band spectra at 9.5 GHz (red) and *chili* simulations^[280] (black) of 100 μM MTSL, resp. $\sim 25\mu\text{M}$ MTSL-labelled hnRNPA1 single cysteine mutants in high ionic strength dispersion buffer (no glycerol); the labelling site is indicated in each plot; the arrows highlight ^{13}C satellite transitions.

by confocal imaging, the majority of the protein can be stabilised in the dispersed state by using low protein concentrations (below 50 μM) in suitable buffer conditions. But from imaging and optical density measurements we cannot exclude nano-sized protein assemblies. The presence of such small clusters of spin labelled proteins may be observed in EPR measurements. Already by visual inspection of the CW EPR spectra obtained with the spin label in the IDD labelling sites we can exclude that the samples are in a very high local spin density environment like in a dense, rigid nano-cluster, because we observe ^{13}C satellite transitions (indicated by dashed arrows in the first panel of Figure 3.4(D)). These weak transitions would be hidden in a broadened peak if Heisenberg exchange effects were dominating the lineshape. For a better understanding

we performed lineshape analysis of the CW X-band EPR spectra using the EasySpin^[280] function `chili` (intermediate motion regime). Note that the g -, resp. $A(^{14}\text{N})$ -tensor parameters were fitted independently to a spectrum of a frozen solution of MTSL in dispersion buffer (see Appendix A). For the ambient temperature simulations we added four equivalent carbon nuclei (natural abundance, $A_{\text{iso}}(^{13}\text{C}) = 18\text{ MHz}$ (fitted to ambient temperature spectrum of free MTSL in dispersion buffer). Only the overall linewidth and τ_{corr} were varied for the fits of the spectra of spin-labelled hnRNPA1. The fitted isotropic rotational correlation times are given in Table 3.1. This simple model reproduces the lineshapes well (see Figure 3.4(D)), and only a minor broad component of the experimental spectra is not fitted. Adding a Heisenberg exchange contribution of up to $D = 10\text{ MHz}$ (which is approximately the limiting case of $D/A = 0.1$) to the spin system did not improve the fit quality. The broadened contribution thus most likely originates from a small population of spins that is dipolar or exchange broadened. Additional CW X-band measurements are also shown in the Appendix, and we observed that the lineshape varies slightly with the buffer conditions as well as the absolute protein concentration.

To check whether spin-spin interactions from multiple interacting proteins contribute to the EPR experiments we performed spin doping experiments, where we added a small quantity (5 %) of spin-labelled protein to solutions of wild-type hnRNPA1. Due to sensitivity limitations we had to increase the total protein concentration in these measurements to $100\ \mu\text{M}$. Spin-spin interactions should be significantly attenuated even for high density aggregates at these ratios (effective 1:20 spin dilution). To have consistent conditions with the imaging we also admixed the low-melting agarose buffer.

Unfortunately, in these spin doping experiments measured in buffer conditions (ii) and (iii) we observed an extreme change of lineshape to very narrow lines, which strongly suggests that the spin label was either cleaved off by residual reducing agent in the wild-type hnRNPA1 stock solution, or that the admixing of the agarose buffer had an adverse effect on these particular protein samples. The results are shown in the Appendix A, but unfortunately cannot be further analysed at this point. In future work, one could consider iodoacetamide or maleimide labels whose binding to the protein is less sensitive to reduction. In a preliminary test, however, we observed significantly more protein precipitation upon incubation with maleimido-proxyl spin label, and we observed more free spin label in the buffer even after extensive washing.

| | MTSL | S231R1 | S271R1 | S316R1 |
|---------------------------|-------|--------|--------|--------|
| τ_{corr} [ns] | 0.025 | 0.60 | 0.53 | 0.35 |

Table 3.1: fitted isotropic correlation times (see Figure 3.4); lw was 0.15 in all simulations; $g = [2.0098, 2.0095, 2.0047]$, $A = [15, 13, 105]\text{ MHz}$; $A_{\text{iso}}(^{13}\text{C})=18\text{ MHz}$; the spectra with the protein samples were shifted along B by 0.04 mT for best agreement.

DEER spectroscopy with single Cys mutants To assess also longer range interactions at the different conditions described above we performed DEER experiments with frozen solutions of single Cys mutants. As for the CW X-band experiments, we show the DEER results for the

buffer conditions (ii) and (iii) only in the Appendix A, because the interpretation is difficult due to potential contamination with free spin label.

In the dispersed state (buffer conditions (i)) without spin dilution at low total protein concentration (15 μM) and the addition of 50 % (v/v) d_8 -glycerol (all purple), we could observe a signal decay of the DEER time-domain data acquired with singly spin-labelled hnRNPA1. These conditions will be treated in more detail in the next section, because they are relevant for the systematic characterisation of the IDD in the dispersed state.

3.2.3 Residual protein-protein interactions in monomer-stabilised samples

Even in seemingly dispersed protein solutions at low protein concentrations we found that hnRNPA1 is not strictly monomeric. Here we present DEER experiments with four single Cys mutants (182, 231, 271, and 316) in the conditions we used to stabilise the monomer. The results are shown in Figure 3.5. DEER with singly spin labelled proteins can provide us with a valuable estimate for the degree of protein-protein interactions, and intermolecular distance information, which is important also for subsequent intramolecular distance measurements with doubly spin labelled proteins.

DEER at four different labelling sites With the three labelling sites in the IDD at 25 μM protein concentration we obtained similar modulation depths, and rather flat background decays in each case. The modulation depths for this concentration were lower than observed for the 50 μM sample measurement with labelling site 182 (see Table 3.2). The estimated fraction of dimers at 25 μM protein concentration is about 10%. When converted to the distance domain with a Gaussian fit after background correction we see the shortest mean distance $\langle R \rangle$ for labelling site 271, followed by site 231, and the longest mean distance for site 316. Like in the previous case the general picture does not change when using different data analysis procedures. Residue 271 seems to be closest to the interaction point (or points) between two IDDs of different hnRNPA1 units. In fact the distance distribution between residues 271 is truncated with a significant intensity at the sensitive edge of the DEER experiment ($R < 1.5 \text{ nm}$). This poses a challenge, because distances below approximately this limit can no longer be observed with standard DEER due to limitation in microwave pulse bandwidth.^[18] Unfortunately, CW X-band spectra of the single mutants were not acquired in this series, which would be necessary for distance analysis in this distance range. We see only very small lineshape differences in the echo-detected EPR (EDEPR) spectra at Q-band between mutant 231 and 271 (see Appendix A), and they could also arise from sample inhomogeneity and other experimental broadening contributions. The fraction of spins that are strongly coupled must thus be small.

The DEER experiment with singly spin labelled hnRNPA1 at site 182 (at the C-terminal end of RRM2) clearly showed modulation depth (50 μM protein), indicating protein-protein interactions. The results are summarised in Table 3.2. The fitted background decay rate is steeper than expected for the given sample concentration, indicating that the trace may not be long enough for the form factor contribution to have fully decayed. This may also partially explain the rise at the end of the

time-domain data (in combination with a contamination from the '2+1' artifact^[176,285]). Prior to further analysis, the data were truncated at 3 μ s, to avoid end artifact effects. We used different methods for distance analysis: 3-dimensional background fitting with subsequent single Gaussian distance domain fitting (red); no background correction and direct analysis of the time-domain data with one (blue) or two (green) Gaussian peaks; neural network processing (orange, includes own background back-calculation); with all four methods we find low probabilities at distances below ~ 3.5 nm, and a peak somewhere between 4.0 and 6.0 nm. The length of the trace does not permit to exclude that some of the intensity removed by the background fit should indeed be attributed to the form factor (as in the background-free fits). Since this labelling site is still in the RRM, and structural information is available, we have added a simulation of the expected distance from the dimer that UP1 adopts in the crystal structure in the presence of a short DNA.^[72,307] The DNA chains were removed from the model prior to simulation of the distance distribution by the rotamer library approach (additional simulations are included in Appendix A). The distance range agrees with the experiment, which is an interesting observation, but may be coincidence. No further DEER measurements with a single labelling site in one of the RRMs were performed. Note also that the formation of the mentioned UP1 dimer in the crystal was observed in the presence of short oligonucleotides,^[72,219,307] which were not present in my sample.

| site can | [P] ₀ [μ M] | η_{eff} | BG dens. | Δ | $\langle N_{\text{spin}} \rangle$ | f_D | K_D [μ M] | $\langle R \rangle$ [nm] | σ_R [nm] |
|-------------|--------------------------------|---------------------|----------|----------|-----------------------------------|-------|---------------------|-----------------------------|--------------------|
| 182 | 50 | 0.82 | 0.248 | 0.098 | 1.20 | 0.20 | 85 | 4.6 | 0.9 |
| 231 | 25 | 0.72 | 0.082 | 0.033 | 1.07 | 0.09 | 201 | 4.1 | 1.0 |
| 271 | 25 | 0.71 | 0.043 | 0.037 | 1.07 | 0.10 | 168 | 2.8 | 1.7 |
| 316 | 25 | 0.66 | 0.026 | 0.030 | 1.066 | 0.09 | 202 | 4.4 | 0.9 |

Table 3.2: Fit parameters and calculated dimer contributions from single-Cys DEER experiments; for the calculation of $\langle N_{\text{spin}} \rangle$, f_D and K_D we used Equation (3.4) (with $\lambda = 0.4$), Equation (3.26), resp. Equation (3.15);

Evaluation of the data was performed with the dimer model introduced in the Theory section, i.e. neglecting any oligomers larger than dimers (see Table 3.2). We find similar values of dimerisation for the different IDD mutants, with $f_D \approx 10\%$, whereas for labelling site 182, where we find $f_D \approx 20\%$. Converting the fractions of dimers to a dissociation constant, we arrive at $K_D \approx 200 \mu\text{M}$ for the IDD labelling sites, and $K_D = 85 \mu\text{M}$ for labelling site 182. Because the measurement with 182 was performed at a higher protein concentration, a larger fraction of interacting proteins was expected of a self-interacting system, but the difference in the K_D values found between IDD mutants and labelling site 182 is surprising. Most likely this is because the measurement with 182 is slightly biased by the background correction (due to too short trace length). Of course we would also expect deviations if the dimer model is a poor approximation. We further investigated whether the dimer model is a reasonable assumption, by performing spin dilution experiments, which are less sensitive to the uncertainty in the inversion efficiency λ .

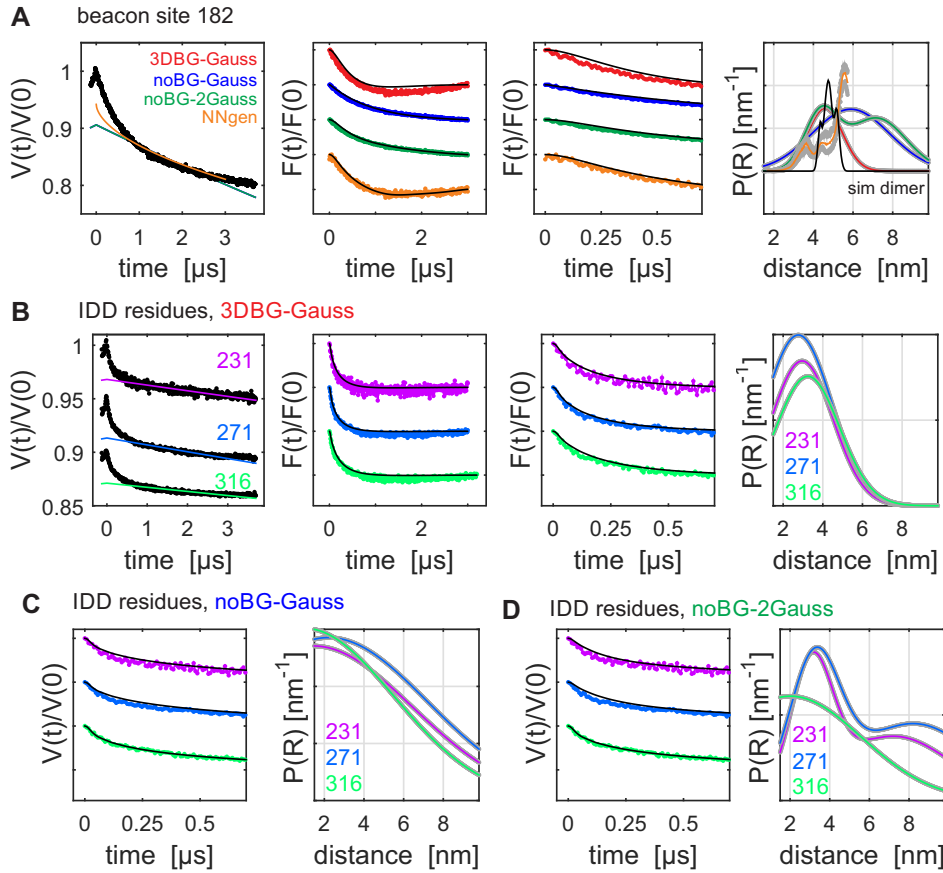


Figure 3.5: DEER with single Cys mutants in dispersed state (50 mM sodium phosphate, pH 6.5, 100 mM R/E, 50% (v:v) d_8 -glycerol). Nomenclature for fit procedures: 'noBG': no background fit, '3DBG': background fit with $n_{\text{BG}} = 3$, 'Gauss': single Gaussian fit, '2Gauss': two component Gaussian fit, 'NNgen': general neural network fit; (A) label at beacon site 182 ($c_{\text{protein}} = 50 \mu\text{M}$); left to right: primary data $V(t)$ and background fits, form factors $F(t)$, zoom of $F(t)$, and fitted distance distributions; the $P(R)$ panel includes a simulation derived from the crystallographic dimer structure (black, see main text for details) (B) analogous data acquired with spin label at sites 231, 271, resp. 316 ($c_{\text{protein}} = 25 \mu\text{M}$) fitted with '3DBG-Gauss' procedure, resp. (C) fitted with 'noBG-Gauss', resp. (D) fitted with 'noBG-2Gauss' procedure;

Spin dilution We looked at the influence of spin dilution on the observed single-Cys distance distributions and modulation depths with the two mutants 231 and 271 (see Figure 3.6 and Table 3.3). We used a 1:1 spin dilution with the Cys-free mutant of hnRNPA1, and we assume that λ is the same in all measurements (which is expected to be a good assumption for same geometry and dielectric properties of the samples, as well as measurements on the same spectrometer and with the same pulse settings). The absolute protein concentration was approximately the same in all measurements.

As expected from Equation (3.2), for site 231 the background decay rate constant is reduced

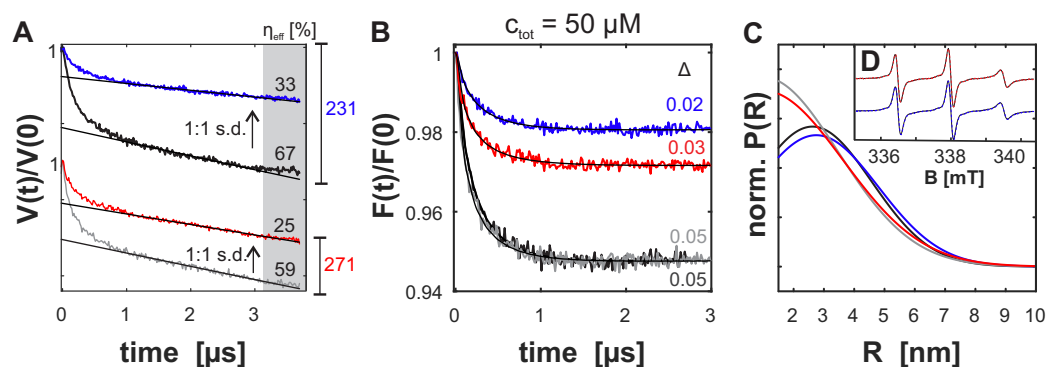


Figure 3.6: Dispersed state DEER with single Cys mutants in the IDD; DEER was measured at $\sim 50 \mu\text{M}$ total protein concentration in 50 mM sodium phosphate buffer, pH 6.5, 100 mM L-Arg, 100 mM L-Glu, 50 % (v/v) d_8 -glycerol; (A) primary DEER data for MTSL-labelled hnRNPA1* single Cys mutants S231C (black) and S271C (grey), and background fits; in colour are the primary DEER data after 1:1 (molar ratio) mixing with hnRNPA1* (Cys-free mutant); resulting effective labelling efficiencies η_{eff} (determined by CW X-band spectroscopy) are displayed; (B) form factors and fits (black); the modulation depths Δ are indicated. (C) Distance distributions $P(R)$ obtained with single Gaussian fit, normalised to unit area; (D) CW X-band spectra of the samples (without glycerol); solid lines: undiluted, dashed lines: 1:1 spin diluted

approximately by a factor of two for a spin concentration reduction of the same factor, indicating that the background decay is dominated by overall spin concentration (large inter-cluster distances in a dilute system), rather than local concentration effects. For site 271 the background decay upon spin dilution remains slightly faster than expected.

The intensity of the short distance contributions is reduced to about half of the original modulation depth for 231, but less than half for 271. The effective shape of the distance distribution is not significantly affected in both cases, but the fitted mean value is slightly longer for 231 whereas it is significantly shorter for 271. In Figure 3.6(D) we show that the lineshape of the room temperature spectra did not change upon 1:1 spin dilution. With the dimer model we find slightly higher fractions of dimers $f_D \approx 10 - 20\%$ at total protein concentration of $50 \mu\text{M}$ protein concentration than in the experiments at $25 \mu\text{M}$ presented in the previous section. When converted to a dissociation constant we find similar, but slightly lower K_D values at $50 \mu\text{M}$ protein concentration (see Table 3.3) than at $25 \mu\text{M}$ (see Table 3.2) at similar effective labelling efficiencies. The extracted K_D values are similar, but not perfectly invariant upon spin dilution for position 231, and not at all invariant for position 271. The latter may be related to a partial loss of modulation depth in the experiments with 271 due to the very short distance ($R < 1.5 \text{ nm}$) range.^[18]

In summary, we found that the protein-protein interactions that lead to the observed modulation depth are at least partially reversible on the short time-scale it takes to prepare the DEER samples. If the modulation depth came exclusively from solid-like, aggregated material (e.g. fibrils) that does not exchange with the dispersed protein, we would not expect to observe a reduction

of the modulation depth after adding unlabelled monomers. Perhaps a small contribution of such solid-like aggregates is what is causing the higher modulation depth for 271, and the enhanced contribution of very short distances.

Based on DEER data alone, we cannot exclude that a fraction of spin-spin distances may be interacting in a configuration with short inter-spin distances below the DEER detection limit of about 1.5 nm. But the CW EPR spectra at ambient temperature suggest that such a fraction cannot be large. The presence of glycerol in the DEER samples and its absence in the CW EPR samples might affect such protein interactions. Note however, that glycerol is rather expected to reduce aggregation than to facilitate it, and stronger indications of protein-protein interactions were found for the glycerol-containing samples.

| site | [P] ₀ [μM] | η _{eff} | BG dens. | Δ | ⟨N _{spin} ⟩ | f _D | K _D [μM] | ⟨R⟩ [nm] | σ _R [nm] |
|-------|--------------------------|------------------|----------|-------|----------------------|----------------|------------------------|-------------|------------------------|
| 231 | 48 | 0.67 | 0.060 | 0.054 | 1.11 | 0.15 | 164 | 2.5 | 3.0 |
| +s.d. | 42 | 0.33 | 0.030 | 0.019 | 1.04 | 0.11 | 233 | 2.7 | 2.9 |
| 271 | 48 | 0.59 | 0.067 | 0.050 | 1.10 | 0.15 | 148 | 1.9 | 2.8 |
| +s.d. | 45 | 0.25 | 0.046 | 0.028 | 1.06 | 0.21 | 72 | 1 | 3.8 |

Table 3.3: Fit parameters and calculated dimer contributions from single-Cys DEER experiments with spin dilution (for the calculation of $\langle N_{\text{spin}} \rangle$, f_D and K_D we used Equation (3.4) (with $\lambda = 0.4$), Equation (3.26), resp. Equation (3.15)). Note that $\langle R \rangle = 1$ nm in the spin diluted measurement with 271 is the limit of the fit constraints in DeerAnalysis.

3.2.4 Intermolecular PRE in the dispersed state

It was surprising that we found inter-protein interactions at low concentrations in the apparently dispersed state. Furthermore, the distance range for the interactions was found to be rather short (significant intensity below $R \approx 3$ nm). To check whether they are artifacts induced by sample freezing, we tried to detect intermolecular PRE in liquid solution at a physiologically relevant temperature. From the DEER experiments we estimate that a significant fraction of proteins are interacting even at and below 50 μM total protein concentration.

MTSL-spin labelled natural isotope abundance hnRNPA1 (¹⁴N-hnRNPA1-S231R1, $\eta = 43\%$, "NMR-silent/EPR-active") was mixed in a 1:2 molar ratio with ¹⁵N-enriched Cys-free hnRNPA1 (¹⁵N-hnRNPA1, "NMR-active/EPR-silent"). Because the spin-labelled protein stock solution was not perfectly labelled, the resulting effective labelling efficiency was only $\eta_{\text{eff}} = c_{\text{spin}}/c_{\text{total protein}} = 16\%$. Note that only a fraction of the true amount of (transient) dimers/oligomers in the sample exhibits PRE effects in a measurement with such a mixture, because the observation of the PRE effect specifically requires interaction between a spin labelled and an isotope marked protein. The PRE effect was quantified as the relative intensity of the resonance in a protein mixture and in a diamagnetic reference spectrum $\Gamma = I_{\text{para}}/I_{\text{dia}}$. We used ¹⁵N-hnRNPA1-S231R1ac as a reference sample, to account for any possible difference from the presence of the spin label. 'R1ac' refers to

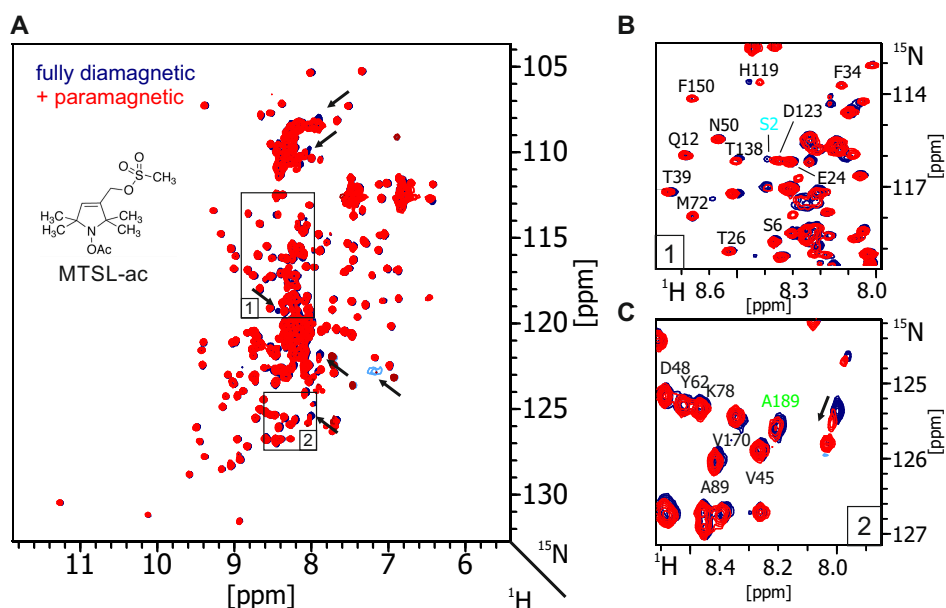


Figure 3.7: Intermolecular PRE with hnRNPA1 (spin labelling site S231C); (A) $^1\text{H}^{15}\text{N}$ -HSQC at 30°C at $\sim 50\ \mu\text{M}$ protein concentration, arrows mark strongly suppressed peaks; (B) and (C) insets as indicated in (A);

labelling with a diamagnetic analogue of MTSL, shown in Figure 3.7 and Figure 3.8

A ^1H - ^{15}N -HSQC spectrum was acquired at 30°C with each sample. For some of the residues surrounding the background mutation sites (C43S and C175A) we observed small differences of chemical shifts between the wild type hnRNPA1 (of which resonance assignment has been performed for the RRM with a UP1 protein construct^[19]), and hnRNPA1-Cys-free. The majority of peaks could be re-assigned with the aid of 3D-backbone NMR experiments with a ^{13}C - ^{15}N -isotope enriched sample of Cys-free UP1. The UP1 reference spectra for this re-assignment and the intermolecular PRE experiments were acquired in low ionic strength dispersion buffer without R/E (10 mM sodium phosphate, pH 6.5). The reference spectrum with the diamagnetic R1ac label is currently only available in high ionic strength dispersion buffer conditions (50 mM sodium phosphate, pH 6.5, 100 mM R/E). Small chemical shift differences were observed (see Appendix A), which could be caused by the slightly differing buffer. The integration position of the peaks was thus shifted accordingly to integrate the full peaks. We cannot fully exclude that the small differences in buffer concentration between the two measurements also contributes to a change of the peak amplitude of some peaks, which may affect the PRE results. This could for example be experimentally tested in future experiments by measuring relaxation and NOE profiles in combination with the PRE experiments.

The spectra of the intermolecular PRE experiment with the spin label at site 231 are shown in Figure 3.7. To account for small protein concentration differences we in the following report relative PRE effects, normalised to the spectral intensities of a selected residue. For intensity referencing we chose a buried residue in the core of the protein (I135). We observed that the

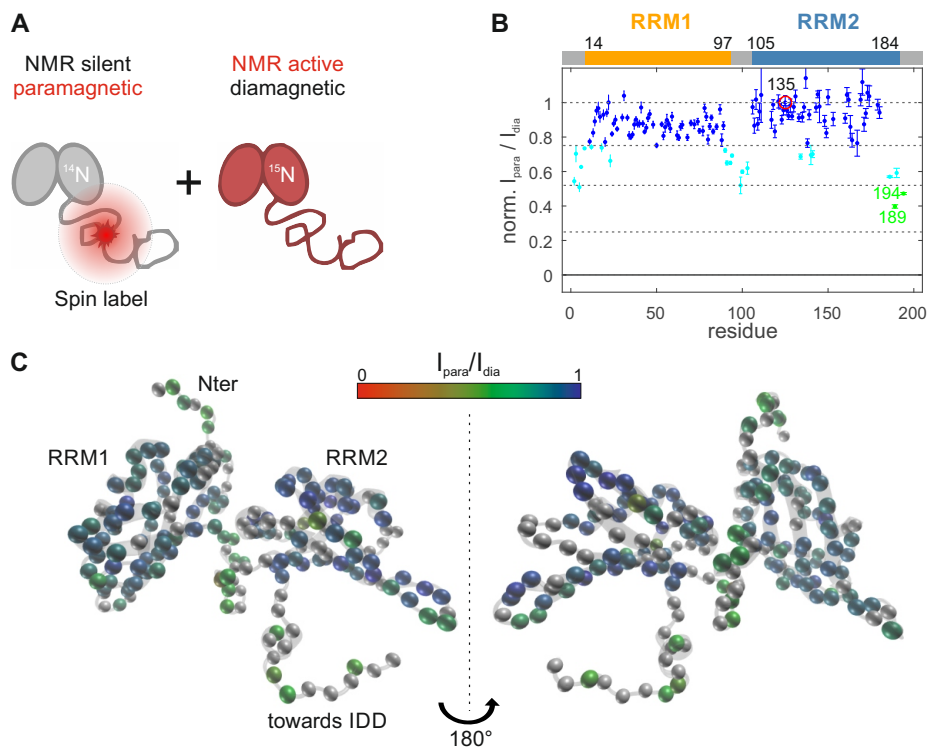


Figure 3.8: Intermolecular PRE with hnRNPA1 (spin labelling site S231C); (A) non isotope enriched (^{14}N), spin-labelled A1-FL is mixed with ^{15}N -enriched A1-FL. The spin label lead to a broadening of the NMR signals in a radial range of up to ~ 2.5 nm. (B) $I_{\text{para}}/I_{\text{dia}}$ obtained with normalised $^1\text{H}^{15}\text{N}$ -HSQC spectra (to unit intensity at residue 135, red mark); Peak suppression below 50 % is marked green, peak suppression between 50 % and 75 % is marked light blue; (C) $I_{\text{para}}/I_{\text{dia}}$ mapped to backbone nitrogens in the RRM1; no information is available for residues in white;

majority of the resonances are not, or only negligibly affected by the spin label in the IDD of a second molecule of hnRNPA1. However, some peaks, which are known to belong to residues in the IDD, are strongly affected (black arrows). Unfortunately, we have no assignment for these resonances, despite previous extensive effort (from personal communication of Elisabeth Lehmann in the Allain group). In addition, some resonances in the RRMs are weakly affected (see Figure 3.7). The linker region between RRM1 and RRM2 is most strongly affected. Quantification was not attempted, because we do not know the total fraction of interacting proteins in the sample at ambient temperature in the absence of glycerol, or the dynamics of the protein encounter. Certainly, the PRE effects are not very strong for most positions, which shows that the proteins are not interacting for the majority of the time in a fixed orientation. But the observations that PRE is observed at all, and that some residues in the IDD are strongly suppressed, suggest that even in the dispersed state the proteins interact, and that the interactions happen via the IDD of hnRNPA1.

3.2.5 Intra-RRM distance measurements for beacon validation

In the previous section we demonstrated that we can prepare frozen samples in which the concentration of dimers or higher order oligomers is low compared to the concentration of monomeric hnRNPA1. This can be supported if doubly spin-labelled mutants exhibit predominantly intramolecular contributions. In order to test this, we measured distance distributions within the folded domains of hnRNPA1, which can be *in silico* predicted from the available models. The distance distributions between these sites were simulated by MMM and compared to the experimental distance distributions (see Figure 3.9). CW X-band spectra, labelling efficiencies, circular dichroism spectra, experimental parameters and fit parameters can be found in Appendix A. The experimental distance distributions obtained with hnRNPA1 (dark blue curves) for three inter-beacon distances (52/144, 52/182, 144/182) agree well with the expected distance distributions. For two mutants, the same point mutations were also introduced in two UP1 constructs, to see whether the presence of the IDD affects the distance distributions (light blue curves). Only very minor changes in the width of the distance distribution between 144 and 188 (narrower in UP1 compared to hnRNPA1) were observed. Note that double Cys mutant 52/144 was difficult to purify and spin labelling resulted in strong precipitation, low labelling efficiency and slightly changed the circular dichroism spectrum. The remaining soluble protein, however, gives the expected main distance peak at approximately 6.5 nm, in addition to some broadly distributed intensity (below 6 nm, indicated by *), and a shoulder at longer distances (above 7 nm) which may arise from residual aggregated material in the sample. Since this problem was not observed in the other two inter-beacon experiments it seems that it is the combination of point mutations in sites 52 and 144 that is detrimental, not the sites individually.

3.3 Discussion and Conclusion

In this chapter we characterised sample conditions where we expected full-length hnRNPA1 to be monomeric and dispersed. Macroscopic characterisation of the protein condensation state was performed by microscope imaging. Using SDSL-EPR we were able to show that protein-protein interactions are present even in seemingly dispersed conditions. This observation highlights the importance of methods that can characterise proteins at the molecular level rather than bulk properties. Note that the EPR observations are not inconsistent with the microscopy results, because protein-protein interaction that we are able to identify with SDSL-EPR spectroscopy can arise from much smaller (nanoscale) protein aggregates, which cannot be identified by standard microscopy.

The conditions that we studied in more detail were protein concentrations up to 50 μM in a sodium phosphate buffer solution in the presence of high concentrations (100 mM) of the amino acids arginine and glutamate. By macroscopic observations these samples would be classified as dispersed. Using DEER experiments with singly spin-labelled hnRNPA1 we could show that the protein is indeed predominantly monomeric in these buffer conditions, but that in frozen samples a small fraction of proteins is always found in a dimerized or oligomerized state. The frozen samples show a snapshot of the dynamically exchanging proteins interactions in the sample. From the

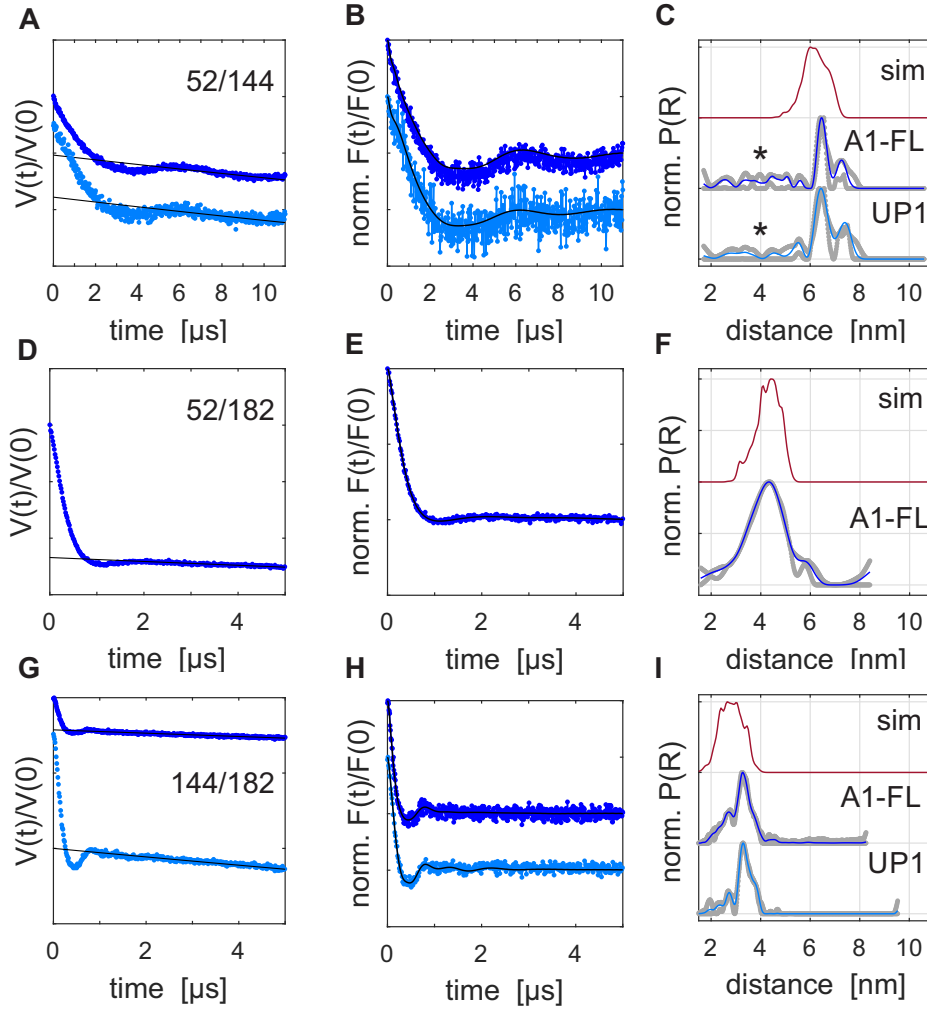


Figure 3.9: DEER for inter-beacon distances; (A)-(C) beacons 52/144; (D)-(F) beacons 52/182; (G)-(I) beacons 144/182; (A,D,G) primary data for hnRNPA1 (dark blue) and UP1 (light blue) if measured; background fits in black; (B,E,H) background corrected form factors scaled to modulation depth and fits (black); (C,F,I) normalised distance distributions; MMM simulation with NMR ensemble in red, experimental results obtained with Tikhonov regularisation (with GCV criterion) for hnRNPA1 in dark blue and UP1 in light blue (confidence estimate from validation in grey);

ambient temperature measurements we see that spin label mobility in the IDD is high ($\tau_{\text{corr}} \approx 0.5$ ns). In combination we conclude from SDSL-EPR that the interactions between molecules of hnRNPA1 are transient and that the interacting molecules exchange quickly. We found that the concentration of interacting molecules in the frozen state depends on the overall concentration. For 25-50 μM samples we can estimate that the fraction of interacting proteins is $f_D = 10 - 20\%$, by using a model that assumes that all the intensity in the DEER experiment with single Cys mutants comes from interactions of at most two proteins (i.e. protein dimers). If larger aggregates (like LDs) were dominating the signal, f_D would be an overestimate of the fraction of interacting

proteins. The interactions must be at least partially reversible, because spin dilution can reduce the experimentally observed modulation depth.

From the DEER experiments we additionally learned that the interaction happens in a conformation where the IDD of two molecules of hnRNPA1 are in close proximity, whereas the spin labels in one site of the RRM (S182) were further apart. This mode of interaction could be confirmed by solution state intermolecular PRE measurements. The largest intermolecular PRE effects were found for specific (unassigned) resonances of residues in the IDD.

Another important conclusion from the intermolecular distance measurements in the dispersed state is that, while we always observed a fraction of interacting proteins, the fraction is small enough that the DEER signal is dominated by intramolecular distance information in experiments with double labelled hnRNPA1. This could be confirmed by measuring distances with a known expected distance distribution (inter-RRM distances). The experimentally observed distance distributions and the simulations agree well.

We also prepared samples of spin labelled hnRNPA1 that had visibly undergone LLPS, as was confirmed by confocal imaging. In these samples we used a spin-doping approach to reduce the spin label concentration in the LDs. The LD state samples featured very narrow spin label spectra in CW X-band spectra, which in fact did not differ much from free spin label. This is most likely an experimental artifact due to the cleavage of the spin label from the IDD spin label site during sample preparation. Nonetheless, the local ('free') spin label density was found to be elevated in DEER experiments, which indicates that the spin label accumulates in the liquid droplets.

3.4 Materials and methods

3.4.1 Mutagenesis and protein over-expression

pET-28a plasmid (carrying a Kanamycin resistance gene) with an inset encoding N-terminally His₆-tagged wild-type hnRNPA1 (P09651, isoform A1-B) was already available in the Allain group at ETH Zurich. The construct carries an engineered TEV-protease recognition site (Glu-Asn-Leu-Tyr-Phe-Gln-|-(Gly/Ser), cleavage site indicated by -|) between the His₆-tag and the N-terminus of hnRNPA1_{2–320} for downstream cleavage of the purification tag. Note that in the final construct the N-terminal Met is replaced with a Gly. Point mutations were introduced in some cases by a two-step PCR product ligation protocol with overlapping primers, but predominantly by using a single pair of complementary PCR primers with the desired point mutation, and PCR amplification of the full plasmid. The mutated plasmids were amplified in *Escherichia coli* (TOP10 strain, Thermo Fisher Scientific) and purified using a MiniPrep kit (Quiagen). Double mutants were generated by sequential application of the Quick-Change Protocol. The plasmids for the equivalent mutant of UP1 for each mutant of hnRNPA1 were generated by elimination of the C-terminal domain from the nucleotide sequence in a two-step PCR protocol using partially overlapping primers. Protein over-expression was performed in codon-optimised *Escherichia coli* cells (BL21 Codon Optimised (DE3) RIL, Stratagene) according to established protocols.^[19] Successful transformation of the mutated plasmids was confirmed by plating on LB-kanamycin-chloramphenicol-agar plates, from which clones were selected for protein over-expression cultures. Selected colonies were picked and grown at 37 °C in LB broth growth medium (25 g/l, Chemie Brunschwig AG) to an optical density at 600 nm (OD₆₀₀) of approximately 0.8. Over-expression was induced by addition of 0.5 mM isopropyl- β -D-thiogalactopyranoside (IPTG,) and performed by incubation at 30 °C for several hours. Overnight over-expression (>5 h) did typically not give higher yields.

3.4.2 Protein Purification

Cell cultures from the over-expression were harvested by centrifugation (20 min at \approx 5000 rcf, at 4 °C). Cells harvested from cell cultures were resuspended in Lysis buffer (10 mM Tris buffer, pH 8.0, 1 M NaCl, 30 mM Imidazole, 0.5 mM DTT, 1 protease inhibitor cocktail tablet (Complete TM, Sigma Aldrich) per 1 l cell culture) to obtain a cell density between 0.1-0.3 g/ml. Cells were lysed on a microfluidizer and the lysate was clarified by centrifuging (40 min, 20'000 rcf, 4 °C). The supernatant was manually filtered (0.45 μ m pore size, Filtropur, Sarstedt) and loaded onto HisTrap FF Ni-affinity purification columns (1 ml column volume, GE Healthcare) on an Akta prime system (GE Healthcare). The presence of protein was monitored using an UV extinction cell at 280 nm. After washing with sufficient volume buffer to a flat UV extinction baseline the protein was eluted by a linear imidazole gradient up to 300 mM. The fractions were analysed using SDS-PAGE (15 % acrylamide, 37.5:1, Axon Lab AG), and the clean fractions were pooled. The pooled fractions were incubated with a 1:80 (w/w) ratio of His₆-tagged TEV protease (purified and provided by Elisabeth Lehmann), and incubated at room-temperature for several hours to cleave the purification tag. At this stage we typically observed the formation of fibrous aggregated material consisting mostly of

the cleaved tag peptide (confirmed by SDS-PAGE), which was removed by filtration (0.22 μm pore size, Filtropur, Sarstedt). Imidazole was removed from the samples by either (i) concentration of the protein and re-dilution in imidazole-free buffer, or (ii) desalting of the solution on a HighPrep26/10 desalting column (GE Healthcare) for samples up to 15 ml volume. The digested sample was passed over the HisTrap FF column again, and the flow-through was collected. Purity of the resulting mutant of hnRNPA1 was checked by SDS-Page.

HnRNPA1 Cys-free (C43S, C175A) mutant, and single Cys mutant S231C were grown in *e. coli* in one litre of ^{15}N -isotope enriched (0.5 g $^{15}\text{NH}_4\text{Cl}/\text{l}$) M9 minimal medium with 4 g/l glucose as carbon source from the same cell stocks used for the inoculation of LB medium. Protein purification and spin labelling with MTSL was otherwise performed with the same protocol as reported above. Non-isotope enriched hnRNPA1 single Cys mutant S231C was produced in LB medium, as described above, and spin labelled with MTSL in dispersion buffer.

3.4.3 Spin Labelling and DEER sample preparation

The mutants were incubated with high levels of reducing agent (5 mM DTT) for at least 2 h at room temperature. The reducing agent was removed, and the buffer was exchanged to labelling buffer (50 mM sodium phosphate buffer, pH 6.5, 100 mM L-arginine, 100 mM L-glutamate) on a PD10 desalting column (GE Healthcare) following the gravity flow protocol. MTSL (2,2,5,5-tetramethyl-3-pyrroline-3-methyl)methanethiosulfonate) was added in high molar excess (10-20x per Cys), and the protein solution was incubated over night at ambient temperature. Protein concentration during labelling was between 4 μM to 20 μM . The unreacted spin label was removed by a PD10 desalting column with the gravity flow protocol, and the labelled protein was concentrated in 10 kDa MWCO centricons (Amicon Ultra-4 Centrifugal Filter Units, Merck & Cie). Labelling efficiency was measured by comparing spin concentration from CW X-band spin-counting experiments (recorded on a Bruker Elexsys E500 spectrometer including a Bruker super high Q resonator ER4122SHQ with 100 μM solution of Tempo in HEPES buffer as reference) to the protein concentration determined by UV extinction measured on a NanoDrop Spectrophotometer ND-1000 (Witec AG), analysed with an extinction coefficient from ProtParam:^[98] $\epsilon = 23505 \text{ M}^{-1}\text{cm}^{-1}$). Samples for DEER were either mixed with d_8 -glycerol (1:1 ratio, v:v) or prepared with low-melting agarose (0.2% (w:v)), as is described in the main text. The final samples for DEER at Q-band ($\approx 35 \mu\text{l}$) were transferred to 3 mm outer diameter quartz capillaries and flash-frozen by contacting with liquid nitrogen-precooled iso-pentane.

3.4.4 Circular dichroism measurements

Circular dichroism experiments were performed in the group of Prof. Roland Riek (ETH Zurich), and Dr. Jason Greenwald and Dr. Witold Kwiatkowski are kindly thanked for an introduction to and help with the method. The protein samples were concentrated to $> 200 \mu\text{M}$ in 50 mM sodium phosphate buffer, pH 6.5, 100 mM L-arginine, 100 mM L-glutamate in Amicon centricons (MWCO 10 kDa, Vivaspin, 0.5 ml, Sartorius), and diluted with 50 mM sodium phosphate buffer (pH 6.5) without the amino acid components (which may otherwise interfere with the measurement) to a final concentration of 2 μM directly before sample acquisition. The samples (140 μl) were

transferred to a 0.1 mm path length quartz capillary (Jasco), and the circular dichroism spectra in the wavelength range of 190 to 260 nm were acquired and averaged for approximately 20 min per sample at 20 °C on a Jasco J-710 CD-spectrometer. A reference sample of the buffer was measured.

3.4.5 DEER Measurements

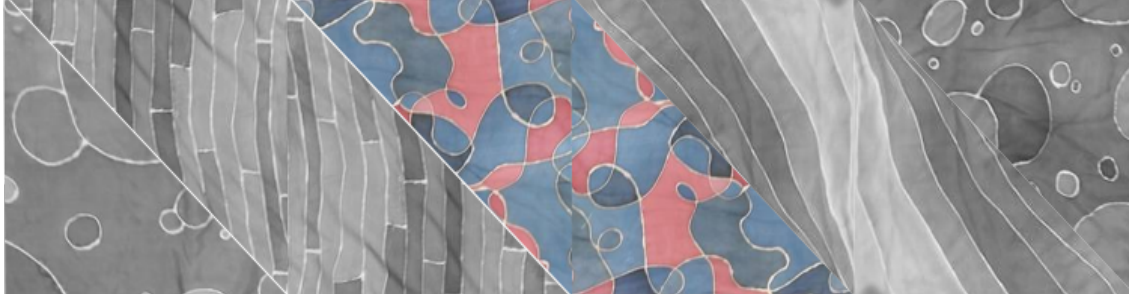
The nitroxide-nitroxide DEER measurements were performed at a home-built high power Q-band spectrometer (≈ 34 GHz) controlled by a Bruker Elexsys E580 bridge in a home-built TE001-type resonator.^[238] The experimental temperature was 50 K, and controlled in a He-flow cryostat (ER 4118CF, Oxford Instruments) and a temperature control unit (ITC 503, Oxford Instruments). The 4-pulse DEER pulse sequence was used (see Figure 2.2), and pulse lengths of $t_\pi = t_{\pi/2} = 16$ ns were used unless stated otherwise. The pump pulse ($t_p = 16$ ns) was set up on the maximum of the nitroxide spectrum, and the detection was set up 100 MHz below. At these settings the "2+1" artifact^[176,203] at the end of the trace is typically weak. The first refocusing delay was always set to $t_1 = 400$ ns, and the second refocusing delay was set as long as possible to be able to still detect a reasonably strong echo. The time-step was either 12 ns, or in cases with a steep initial decay to 8 ns.

3.4.6 PRE Measurements

For the reference spectrum we used the diamagnetic analogue acetylated MTSL (in the following 'R1ac', (1-acetoxy-2,2,5,5-tetramethyl- δ -3-pyrroline-3-methyl)methanethiosulfonate, CAS: 392718-69-3, Toronto research chemicals, Canada), and labelling with this analogue was performed under the same conditions as with MTSL. The attachment of 'R1ac' was confirmed by ESI-MS. NMR measurements were performed on a Bruker 700 MHz NMR spectrometer equipped with the AVANCE NEO console and a CryoProbe at 40 μ M 15 N-hnRNPA1-S231R1ac concentration (reference spectrum), resp. (40 μ M 15 N-hnRNPA1 + 20 μ M 14 N-hnRNPA1-S231R1) concentration in dispersion buffer. The backbone resonances of the diamagnetic analogue spectrum were weakly different from the (partial) assignment of wild-type UP1 available in the Allain group. We therefore purified 13 C- 15 N-enriched UP1 Cys-free (C43S, C175) mutant using 13 C-glucose as the carbon source in the M9-minimal medium, and with the aid of three-dimensional NMR experiments the backbone re-assignment of hnRNPA1 Cys-free was possible. The buffer concentration in the measurement with the inter-molecular PRE experiment was slightly lower (10 mM sodium phosphate), which may have small effects on the chemical shifts. 3% D₂O were added to all samples for spectrometer locking, and samples were measured in 5 mm (outer diameter, 5TA, ARMAR Chemicals) throw-away tubes. Data was recorded and processed using Topspin (Bruker). Data acquisition of the 2D- 15 N¹H-HSQC spectra was for approximately 12 h per sample. Data analysis was performed in the 'cara' software package.^[1] To integrate over the full peak in each spectrum we adjusted the peak list to the minor changes of the resonance position between the samples and by defining a peak model for NMR analysis. The peak positions and the integrated peak intensities of each spectrum were exported and analysed with a custom Matlab script. First we divided each spectrum by the intensity of the reference peak (residue 135). $I_{\text{para}}/I_{\text{dia}}$ was then calculated from the normalised spectral intensities and plotted as a function of the residue number. To generate the visualisation

on the NMR structure model we exported the $I_{\text{para}}/I_{\text{dia}}$ table to the vmd software,^[128] where a custom tcl script was used to set the colour of the residue representation according to a red to blue scale (from 0 to 1). In total 160 backbone resonances could be assigned and analysed.

Imaging Imaging was performed at the ScopEM facility with the Leica SP8 STED super-resolution confocal microscope (water-immersion objective). A volume of 15 μl sample was prepared for each condition (always with 0.2 % (w:v) low melting agarose) and loaded onto an uncoated ibidi μ -well TM (ibidi) plate slot. Imaging was performed at ambient temperature, in transmission mode or reflection mode.



Chapter 4

Models of full length hnRNPA1 based on DEER restraints

Knowledge of the biomolecular structure at atomic resolution is tremendously helpful for identifying and understanding biomolecular functions and interactions.^[216] For structured biomolecules, or biomolecule domains, an accurate description at atomic level of resolution may already be possible with a single set of coordinates for all atoms. However, also in cases where the whole biomolecule or some flexible regions in its sequence can adopt multiple conformations (flexible domains) atomistic description can be achieved by determining an ensemble of allowed conformations.

Intrinsically disordered domains (IDDs) are a new challenge for the field of structural biology, because of the very large conformational space, and because of the fast inter-conversion of conformations. A common way to arrive at structural ensemble models is to perform molecular dynamics (MD) or Monte-Carlo (MC) simulations. These methods have been extensively developed for folded proteins domains, but the currently available force fields frequently fail to produce ensemble results that can predict (the few) available experimental data for IDDs and IDPs.^[198,216,245] A dedicated force field for IDDs has been developed that is better suited for reproducing the size of the polypeptide coil.^[124] Whether such improved force fields also reproduce the different types of transient local structure is currently hard to assess owing to the lack of experimental data.

Experimental characterisation of IDDs is difficult, as the fast sampling of different conformations which in many experimental setups leads to time-averaged structural information. The DEER experiment with frozen spin-labelled biomolecules presents a promising experimental method to overcome the latter challenge, and can provide experimental restraints in highly disordered systems^[79] The major advantage is that DEER time-domain data usually can be analysed in terms

of distance distributions, rather than mean distances.^[142,143] The resulting distance distributions have been successfully used to generate models of flexible protein domains,^[10,28] and as a means to refine force fields for molecular dynamics.^[114,115,156] In this chapter we present results obtained with an approach that does not depend on a molecular force field,^[138] in which we combine multiple EPR distance measurements towards an atomistic representation of full length hnRNPA1.

Scope of this chapter In this chapter we present DEER distance measurements between spin-label sites in the RRM of hnRNPA1 and such sites in the IDD. After a brief summary of the theory aspects, we show an in-depth analysis of the experimental DEER data in terms of distance distributions. We demonstrate that, after background correction, a single Gaussian fit model is a good approximation for the distance distributions that involve spin labels attached to the IDD. We then present distance measurements for several spin label site pairs, including distance measurements within the IDD and analyse them using such a single Gaussian model. The results are combined in two modelling methods that localise the position of selected residues in the IDD with respect to the RRM in a probabilistic manner. The same distance information was consequently used in an atomistic modelling approach to generate a structural ensemble model of full length hnRNPA1. Finally, we outline how the ensemble model may be used to gain mechanistic insights into the conformational states populated by the IDD of hnRNPA1, and we analyse the DEER-derived ensemble model of full length hnRNPA1 in terms of potential conformational preferences for the IDD conformations. The experimental procedures are described at the end of the chapter.

Author contributions and acknowledgements The NMR experiments were performed in the group of Prof. Frédéric Allain (ETH Zurich), and Dr. Elisabeth Lehmann is gratefully acknowledged for her contribution to the experimental NMR part and the re-assignment of the backbone resonance NMR spectrum of the full length hnRNPA1 Cys-free mutant. Emil Dedic and Georg Dorn are thanked for the ensemble SAXS measurements, for which we were kindly allowed to use the instrumentation of the Mezzenga laboratory at ETH Zurich. Gunnar Jeschke is thanked for the development of the integrated ensemble generation and refinement software. Evelyne Parmentier is kindly acknowledged for her contribution to the purification of the UP1 mutants.

4.1 Introduction

To build an ensemble model of full length hnRNPA1 we start from the existing partial models, some of which were shown in Figure 1.2 in Chapter 1. The structures of the RNA-recognition motifs (RRMs) of hnRNPA1 have been solved by X-ray crystallography,^[294,307] and more recently by solution state NMR.^[19] Structures of the RRM in complex with some of its target nucleotides have also been reported.^[26,72,170,219,223]

The models of full length hnRNPA1 presented in this chapter are based on the NMR structure of the RRM, from which we build the IDD conformers for a model of the full length chain of hnRNPA1 (pdb: 2LYV).^[19] We do not explicitly include the structures for the small peptides that have been reported for the IDD, because they are safely known to exist only in an aggregated, fibrillised state, which we do not characterise in this study.

4.1.1 Broad distance distributions in DEER

For the general theory of the DEER experiment we refer to the general EPR Theory chapter (Chapter 2). Here we present theoretical expectations for distance measurements with broadly distributed distances.

In a typical PDS experiment (protein concentration: 20 μ M protein, sample volume: 30 μ l) we have approximately $3.6 \cdot 10^{14}$ frozen molecules (and thus potentially as many different conformations) present in a sample. All different conformations contribute to the time-domain DEER data with their respective dipolar coupling frequency, which depends on the inter-spin distance with R^{-3} , and the angle θ between the spin-spin vector and the static magnetic field (see Equation (2.16)). For distance measurements involving a spin-label site in an IDD we expect that the underlying distribution of conformations is very broad. The resulting spread in the dipolar coupling frequency may dampen any visible oscillations in the time-domain signal, and the resulting trace appears like a decay. This is illustrated for simulated single Gaussian distributions in Figure 4.1(A).

If the IDD behaves like a random coil, we may be able to model the distance distribution between two sites in the IDD with standard models from polymer physics.^[135] The maximum distance between two residues is given by the full extension of the peptide chain according to standard peptide bond lengths and angles. The maximum distance gained per amino acids is 0.38 nm/AA. Because of pleating, we assume a maximum distance gained per AA of 0.35 nm. Neglecting the contribution of the (flexible) spin label linker at the two labelling sites, $R_{\max} = 15 \text{ AA} \cdot 0.35 \text{ nm/AA} = 5.25 \text{ nm}$ for the shortest, and a staggering $R_{\max} = 135 \text{ AA} \cdot 0.35 \text{ nm/AA} = 47.25 \text{ nm}$ for the longest separation plotted here. A fully extended state, however, is statistically negligibly unlikely. The random self-avoiding walk (RSA) model is a simple model which is based on the number of residues between the sites N , and the empirical exponential scaling factor ν . The latter was calibrated specifically for peptide chains to be $\nu = 0.602 \pm 0.035$.^[91] The expected end-to-end distance distributions and simulated DEER time-domain data for three different N are shown in Figure 4.1(B). With a larger residue separation the maximum of the distribution shifts to longer distances, and the distance distribution becomes significantly more broad and asymmetric (extended tail towards long distances).

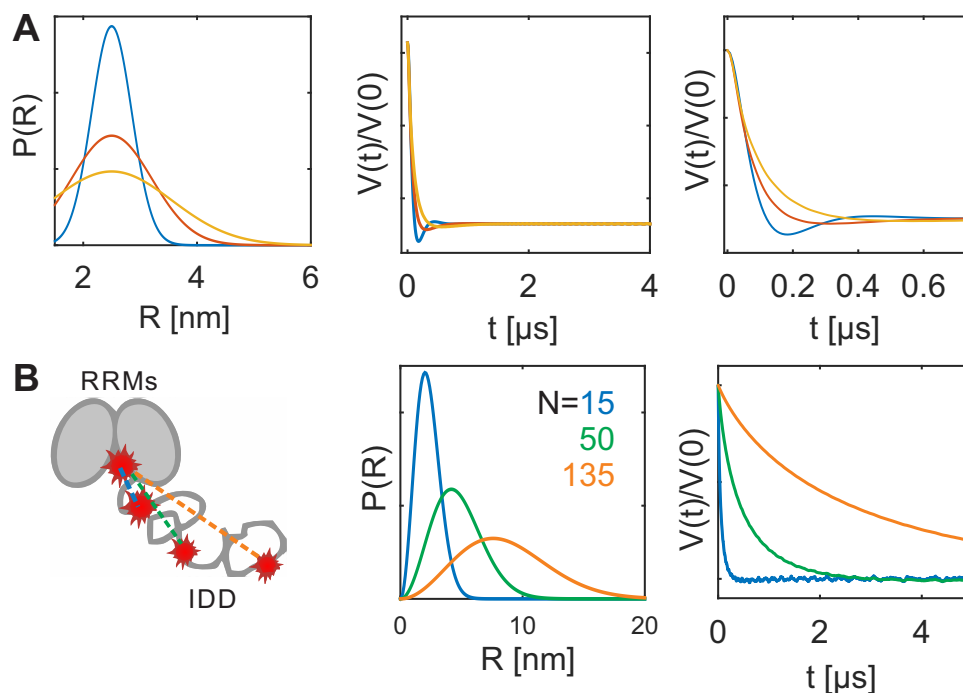


Figure 4.1: (A) Three simulated single Gaussian distance distributions with mean distance $R_m = 2.5$ nm, and varying widths; left to right: distance distributions $P(R)$, simulated primary data $V(t)/V(0)$ (no noise, no background decay) and zoom-in on early time range; (B) left: schematic representation of spin labelling scheme for a small (15 AA), intermediate (50 AA) and large (135 AA) separation of spin labels in primary sequence in the C-terminal IDD of hnRNPA1; middle: simulated distance distribution using a peptide-chain specific RSA model ($\nu = 0.602$);^[91] right: simulated time-domain DEER data (no additional background decay was used);

The simulated time-domain DEER signal in the case of large N decays significantly more slowly than for short N .

4.1.2 The localisation and multilateration algorithms

A point in three-dimensional space can be uniquely localised with respect to the locations of four other points if the pair-wise distances are known, as long as these four reference points do not lie in the same plane. With three reference points, localisation is possible only up to mirror symmetry with respect to the plane defined by the three reference points. There are many ways how this localisation approach can be implemented, and we will show in this chapter results for combining DEER distance distributions for the localisation of a spin-labelled residue with respect to so-called 'beacon' reporter sites with two methods: (i) localisation by root-mean square minimization followed by computation of an uncertainty isosurface,^[28] and (ii) localisation by a distance network-based algorithm.^[95,139] In the first method, an initial estimate of the most likely location is calculated by finding the intersections of spherical shells of radius $R_{\text{restraint}}$ around the beacon sites. The probability distribution of the query is then determined in a grid-based

calculation by a re-normalised product of the individual probabilities. The coordinates of the beacon sites must be known, and the inter-beacon distances are considered fixed (no experimentally added variation). The second algorithm (based on distance geometry) solves the problem by finding a geometric arrangement of the distances that fulfils all restraints. The algorithm then finds the best mapping to the existing structural model of the protein. The advantage of the network based algorithm is that the inter-beacon distances are not only determined by the already existing structural model, but are actively considered as experimental input. It is, however, much more experimentally demanding to extend the set of restraints by one more beacon, because at least three additional distances measurements are required per additional beacon to connect it to an existing network. Analogously to the localisation algorithm, the combined probability distributions can be determined in the network implementation.

4.1.3 *In silico* growth of flexible protein domains

Recently, an algorithm has been proposed and applied to *in silico* grow conformers of the IDD and thereby to construct an ensemble model of a flexible protein domain which enforces the fulfilment of a set of experimental restraints.^[10,28,138] A graphical summary of the algorithm can be found

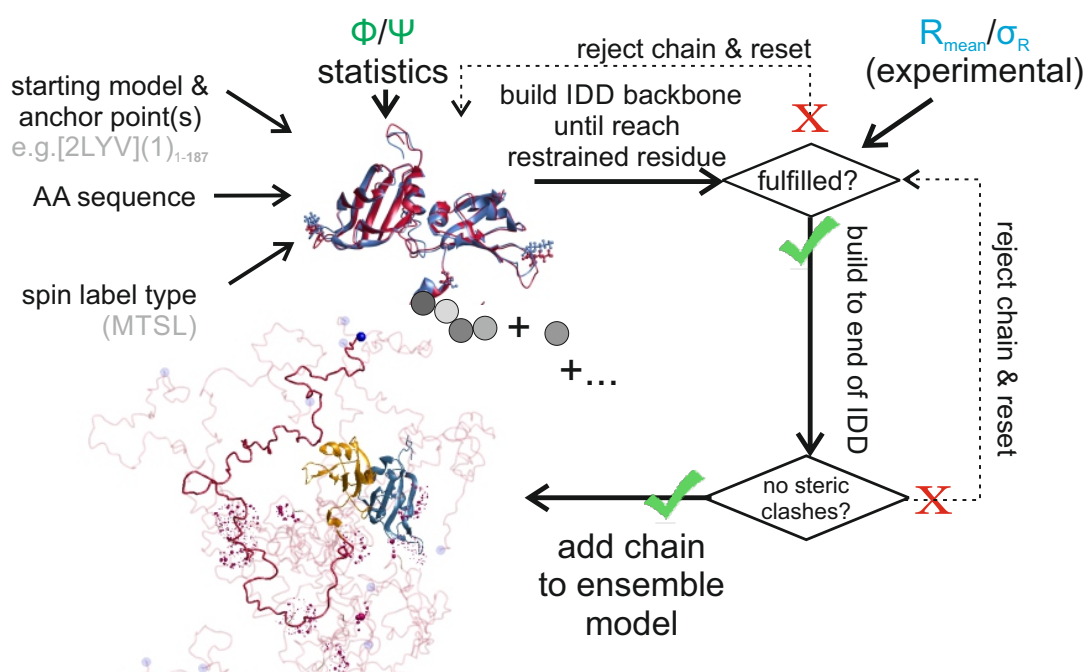


Figure 4.2: Graphical summary of the domain ensemble build module in the Matlab toolbox MMM^[138];

in Figure 4.2. The requirement is that the restraints can be defined in a probabilistic manner, like distance distribution restraints from DEER experiments. If available, the program can use an anchor structure (C-terminal, N-terminal, or both), if for example the folded part of the protein structure is known. The IDD conformers are constructed step-by-step, by adding amino acids to

the growing chain. The primary sequence must be known, and the intrinsic preferences for the dihedral angles (Φ , Ψ) of each amino acids are considered during the initial conformer generation (Ramachandran statistics, usually taken for peptide sections without secondary structure).^[121,138] When the algorithm reaches a residue for which probabilistic experimental restraints have been defined, the current conformer is only accepted if it falls within a user-chosen cutoff probability threshold (geometric mean of the probability for multiple restraints). Each individual resulting conformer is checked after completion for internal steric clashes, and finally for steric clashes with the anchor model. Several speed-up steps are implemented, which ensure that chains are not rejected too frequently.^[138] In this chapter we will use this algorithm to build conformers for the C-terminal IDD of hnRNPA1. The restraints are DEER distance distributions, obtained with MTSL-labelled hnRNPA1 double-cysteine mutants, and the effect of spin label conformation distribution is taken into account during model generation.^[138]

Note that the conformers in the final ensemble generated in this way are not sorted by similarity, or any other measure. A simple quantity that we therefore introduce to characterise the generated ensembles is the effective end-to-end distance of the disordered domain ensemble model. After defining a start and end point we can calculate the C_α - C_α distance R between these end points for each single conformer of the ensemble. In this study we will use residues 188 and 320 as the definition of the IDD of hnRNPA1, and residues 1 and 320 for the full length protein end points. We can then calculate the average effective end-to-end distance of the IDD $\langle R \rangle_{\text{IDD}}$ over all conformers in the ensemble. The width of the distribution is quantified by the standard deviation of the end-to-end distance σ_R . Another common quantity to characterise protein compactness is the radius of gyration R_{gyr} , which we also report for our protein models.^[192]

4.2 Results

4.2.1 Analysis of DEER data with spin labels in the IDD

We performed distance measurements with doubly spin-labelled (double Cys) mutants of full length hnRNPA1 to determine distances between beacon sites (32, 52, 144, and 182) in the RRM and residues in the IDD. In contrast to distance measurements between beacon sites in the RRM, there are currently no structural models available to estimate the expected mean distances for measurements between beacons and residues in the IDD. All experiments reported in the following were performed at low protein concentration in the dispersed state, where we have demonstrated in the previous chapter that hnRNPA1 is predominantly monomeric, and only up to $\sim 15\%$ of the protein exists in a dimerised or oligomerised state. In this section we demonstrate data analysis of DEER experiment where no pronounced oscillations are visible due to the broad underlying distribution of conformations. As a first example we use double mutant 182/197, for which we expect to measure a short mean distance because the labelling sites are separated in sequence by only 15 amino acids. As a second example we use double mutant 182/316, which can be used as an approximate end-to-end distance measurement of the IDD, and for which we expected the maximum of the distance distribution to be around $R_{\max} \approx 8$ nm if the IDD follows a random self-avoiding walk (see Theory section, and Figure 4.1(B)). The maxima of the probability distributions present limiting cases of short and long separation, both of them still falling into the range that is accessible by PDS distance measurement techniques, albeit at the lower and upper limit. Spin labelling was performed with MTSL in dispersion buffer (50 mM sodium phosphate, pH 6.5, 100 mM R/E), as was outlined in the previous chapter.

The primary DEER data obtained with the two double Cys mutants are shown in Figure 4.3. As expected, no distinct oscillations can be observed, which shows that the underlying distances must be broadly distributed. Even though we try to minimise the pump and observer pulse spectral overlap, we often see some intensity of the well-known '2+1' artifact at the end of the DEER trace (marked with asterisk).^[136] The trace has to be truncated before this artifact prior to data analysis to avoid artifact distance peaks.

The first step of conventional DEER data analysis is background (BG) correction, which removes signals from remote spins. Due to the low concentration at which the samples were prepared (10-50 μM) we expect only weak background intensity. Indeed, the BG fits are almost flat (BG densities, other fit parameters and fit results are reported in Section 4.2.2). For completeness, we show here also fits where the background fit dimensionality n_{BG} was allowed to vary. In most cases values close to a three-dimensional distribution ($n_{\text{BG}} = 3$) of remote spins was found. In some cases (e.g. mutant 182/316) the optimisation finds $n_{\text{BG}} < 2$. This could be because the background correction tends to suppress some of the very short-range ($R \lesssim 1.5$ nm) distance contributions, which would lead to intensity at the border of the sensitive DEER range. However this was not investigated in more detail, and since we have no physical reasons that would justify $n_{\text{BG}} < 2$ we remain with the standard $n_{\text{BG}} = 3$ background fits. After division by the background fit we obtain the form factors $F(t)$, which, in theory, contain exclusively intramolecular distance information. We know

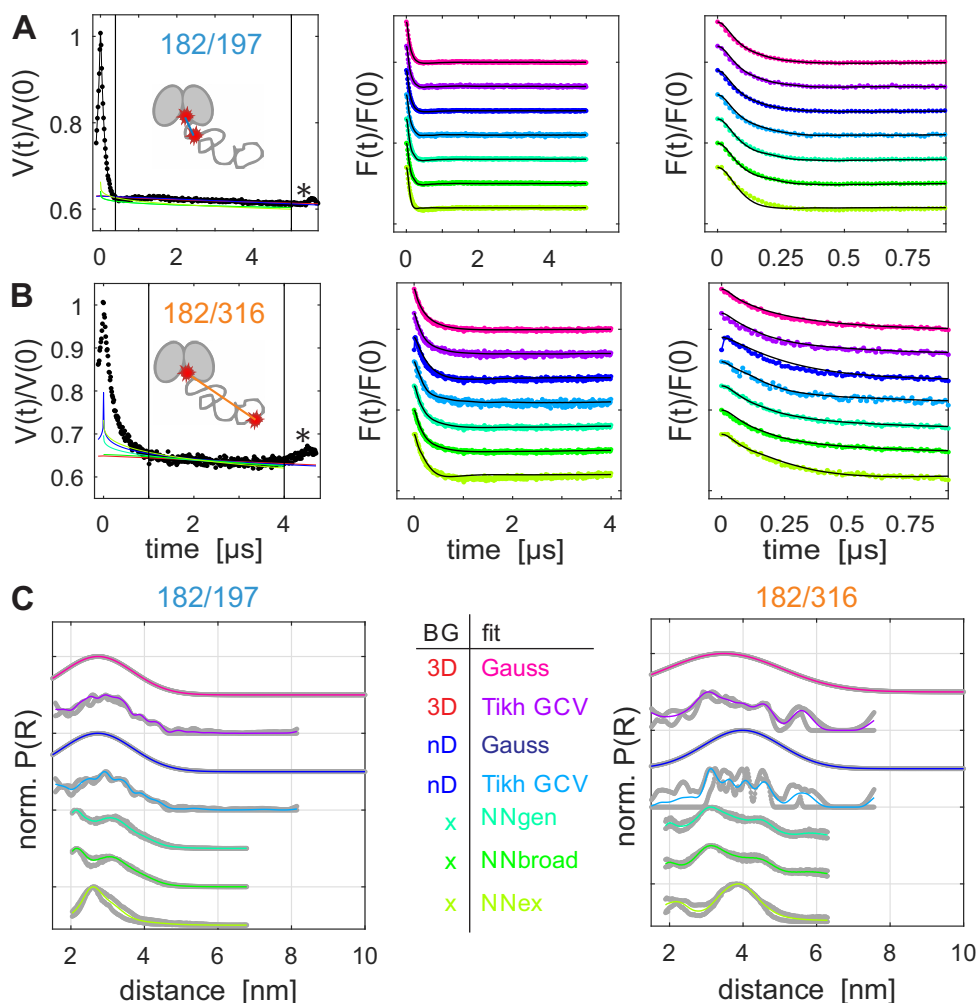


Figure 4.3: Distance Analysis for two beacon-IDD site pairs in hnRNPA1; (A,B) left to right: primary data $V(t)/V(0)$ and background (BG) fits (red: 3-dimensional, blue: n-dimensional, green: back-calculated from neural networks) background corrected, the asterisk marks a known four pulse-DEER artifact and the vertical lines show the data cutoff; form factors $F(t)/F(0)$ after background correction and model fits (black), divisions correspond to modulation depth of 0.4; zoom-in of $F(t)/F(0)$; (A) MTSL-labelled double Cys mutants 182/197; (B) MTSL-labelled double Cys mutants 182/316; (C) distance distributions obtained with different fit methods and validation results for Tikhonov fit (grey); for model abbreviations see main text;

already from singly Cys mutant experiments (Chapter 3) that this is not strictly true for DEER samples of hnRNPA1 even at 25 μM protein concentration, due to contributions of intermolecular DEER from dimers or higher oligomers at short distances. But the fraction of oligomerised protein is low, and the contributions should be less than 15 %, which is still acceptable for the intended further analyses. The final step in conventional DEER data analysis is conversion to distance domain. We show here model-free fits with Tikhonov regularisation using the GCV criterion^[85]

for the automatic choice of optimal regularisation parameters α , and fits of a single Gaussian with variable mean distance R_{mean} and width σ_R .

For additional comparison to another model-free data analysis approach, we also include distance analyses obtained with recently developed neural networks for DEER.^[305] Three different networks were tested: the general network that was based on an unspecific training set ('NNgen'), the network trained on broad distance distributions ('NNbroad'), and the network that is trained to handle exchange coupling ('NNex'), because some of the intensity of the distance distributions with other fit models falls into a range where exchange coupling may be observed. All three networks perform integrated background correction, which is then back-calculated to the background and form factor ranges for plotting. Interestingly, the shape of the back-calculated background fits resembles that of the conventional background fit with variable dimensionality.

| mutant | $n_{\text{BG}} = 3$ | | | | n_{BG} variable | | | | Neural Networks (NN) | | | | | |
|---------|---------------------|------------|-----------------|-------|--------------------------|------------|-----------------|-------|----------------------|-------|-----------------|-------|-----------------|-------|
| | Gauss | | Tikh | | Gauss | | Tikh | | NNgen | | NNbroad | | NNex | |
| | R_m | σ_R | R_{av} | s_R | R_m | σ_R | R_{av} | s_R | R_{av} | s_R | R_{av} | s_R | R_{av} | s_R |
| 182/197 | 2.74 | 0.95 | 2.95 | 0.83 | 2.73 | 0.96 | 2.98 | 0.91 | 3.03 | 0.69 | 3.02 | 0.69 | 2.92 | 0.62 |
| 182/316 | 3.48 | 1.57 | 3.73 | 1.24 | 3.98 | 1.06 | 3.94 | 1.13 | 3.78 | 1.11 | 3.78 | 1.11 | 3.64 | 0.92 |

Table 4.1: Fitted distances and widths (all data in nanometre) for mutants 182/197 and 182/316; for Gaussian fits we report model parameters: mean distance R_m and standard deviation σ_R . For other fits we report distribution-averaged distance R_{av} and deviation from 1st moment analysis s_R ;

| mutant | | | | | distance model fit r.m.s.d. | | | | | | |
|---------|--|---------------|--------------------|-----------------|-----------------------------|--------|--------|--------|--------|-------------|--------|
| | c_{spin} [μM] | dens. (BG) | r.m.s.d. BG fit | n_{BG} | Gauss | Tikh | Gauss | Tikh | gen | NN broad | ex |
| 182/197 | 26 | 0.006 | 0.003 | 3.3 | 0.0031 | 0.0056 | 0.0029 | 0.0064 | 0.0038 | 0.0037 | 0.0044 |
| 182/316 | 29 | 0.045 | 0.007 | 0.4 | 0.0071 | 0.0133 | 0.0093 | 0.0157 | 0.0080 | 0.0085 | 0.0116 |

Table 4.2: Fit parameters for DEER with mutants 182/197 and 182/316; tabulated are sample spin concentration c_{spin} (from spin counting), fitted spin density of BG fit ($n_{\text{BG}} = 3$), BG fit quality ($n_{\text{BG}} = 3$), the result of varying n_{BG} , and the fit qualities of the distance domain fit with the various models.

We now consider the results of the different distance domain fit procedures for the two measurements. In the case of 182/197 the modulation has well decayed by the end of the trace, and the majority of distances fall in a range where we should be able to also interpret the shape of the distribution with model-free fitting, such as Tikhonov regularisation. First, we point out that the general intensity distributions obtained with the various fit methods agree well. This is in line with early findings on the analysis of broad distance distributions from PDS data, which revealed that mean distance and standard deviation are fairly stable parameters irrespective of the data analysis approach.^[143] The result of the Gaussian fit approximates the envelope of the Tikhonov fit very well, so a single Gaussian fit seems to be a good choice for further modelling.

Also the result with the unspecific neural network 'NNgen' and the broad-distance specific network 'NNbroad' predict a similar shape of the distance distribution, with an additional small shoulder at short distances. The time-domain fit quality to $F(t)$, however, are similar, or even slightly worse with the network algorithms than with the Gaussian fit, so we will not interpret this difference. The exchange-resilient neural network removes the intensity at short distances and attributes it to exchange coupling, which leads to a slightly worse fit quality. This is most likely not the correct interpretation, because for such a biological spin-labelled sample we do not expect to see strong exchange coupling with a distance distribution that begins only at ~ 2 nm (only through-space, no through-bond coupling is possible).^[18,135] Interestingly, however, the resulting distribution shape resembles best the shape expected from the RSA walk prediction (compare Figure 4.1(B)).

The case of the second double mutant 182/316 is more difficult to interpret, because the underlying distances are significantly longer, which may introduce truncation artifacts at the given experimental dipolar evolution time. Nonetheless, the various methods again agree in the prediction of a generally very broadly distributed distance. Surprisingly, the distance distribution is centred at a significantly shorter distance (~ 3.5 nm) than what was predicted from the RSA walk (~ 8 nm). To a small degree this discrepancy may indeed be an artifact from data analysis, if some intensity at long distances is wrongly attributed to background contributions. But the shift is too large to be explained by fit errors alone, and we can state that the result of the DEER experiment is that the IDD of full-length hnRNPA1 does not entirely behave like a RSA polymer with the parameters found by Fitzkee et al.^[91] Explicit fits with the random coil model can be found in Appendix B, and indeed a very different scaling parameter is required to fit the two different measurements when using the respective appropriate primary sequence separation ($\nu(182/197) = 0.642$ with $\Delta N = 15$, resp. $\nu(182/316) = 0.415$ with $\Delta N = 134$).

In summary, we see that, although fitting a single Gaussian distribution for distances between beacons and residues in the IDD may not pick up fine features of the distribution, it essentially gives a reliable overall distribution and avoids over-interpretation. Note that, while some of the peaks and dips in the distance distribution obtained by Tikhonov regularization and by the neural networks may be correct, they should only be interpreted with extreme care, as they generally are not stable under fit validation. We have no good reason to claim a structured rather than unstructured distance distribution. Importantly, the general distribution is well captured by the Gaussian fit. For all remaining distance measurements this was thus the method of choice for data analysis.

4.2.2 Distance distributions between beacon sites and residues in the IDD

At least three distances from beacons in the RRM to each of the three major IDD reporter residues (231, 271 and 316) were measured. In Figure 4.4 we show the Gaussian fit analysis of this systematic trilateration distance measurement scheme. The primary data and fits can be found in

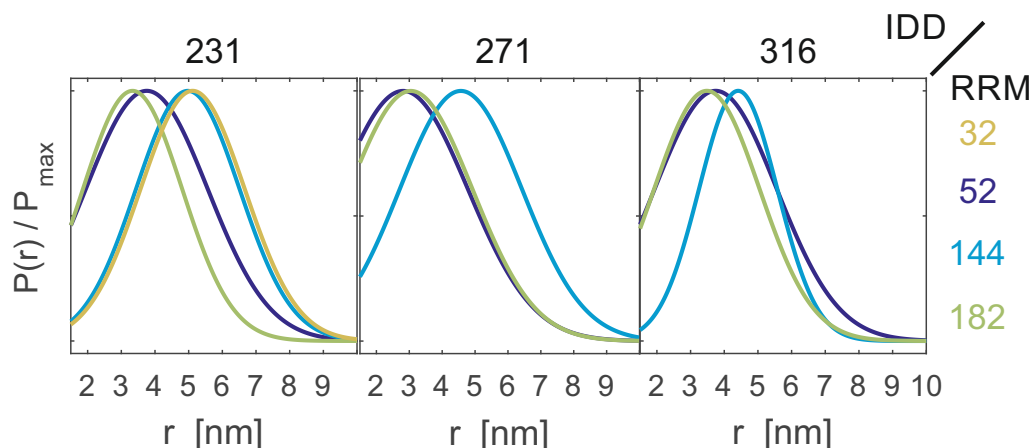


Figure 4.4: DEER data analysis for trilateration of residues 231, 271 and 316 in the IDD from beacons 32, 52, 144 and 182 in the RRM; single Gaussian fit distance distributions $P(r)/P_{\max}$ normalised to unit intensity at the maximum of the distribution; an extended version of the figure with primary data and fits can be found in Appendix B.

Appendix B. The background correction was performed with $n_{\text{BG}} = 3$ the experimental details (CW X-band spectra and labelling efficiencies) can be found in Appendix B. The overall fit quality is very good. Clearly, we observe differences between the average location of the residues in the IDD and the three main beacons in the RRM. For all three residues in the IDD, position 144 is located comparatively far away. Positions 52 and 182 are significantly closer for all three cases. Surprisingly, residue 316 is located almost as close to beacons 52 and 182 as the other two IDD residues (231 and 271), even though the separation in sequence is much larger. This may be partially an artifact of background correction, but for most cases the background fits are not significantly steeper in measurements involving labelling site 316 than in the other experiments, which would be expected if contributions of long distances were incorrectly included into the fitted BG. Only the distance measurement between residues 144 and 316 may be a case where this effect is partially observed.

In Figure 4.5 we show the Gaussian fit results of additional distance measurements which were performed with the intention of serving as auxiliary distance restraints in the ensemble model generation of the IDD. The primary data and fits can be found in Appendix B. We measured distances between the chosen spin labelling sites in the IDD, which give us an estimate of the spatial dimension of the domain ('intra-IDD' distances). All three combinations of labelling sites (231/271, 231/316 and 271/316) give comparatively narrow distributions with a short mean distance. This implies that the domain does not frequently populate very extended states. In Section 4.2.2 it can be seen that the modulation depth with the intra-IDD measurements were rather low in some cases, which may partially result from very short distance contributions that cannot be excited, and partially from the low labelling efficiencies in some cases (for CW X-band spectra see Appendix B). Spin labelling in these double IDD-Cys mutants also lead to significant protein precipitation

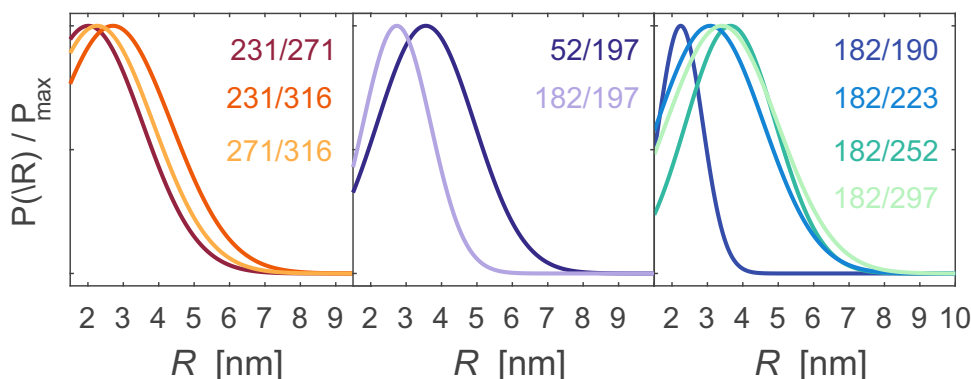


Figure 4.5: Additional DEER experiments; single Gaussian fits, normalised distance distributions $P(r)/P_{\max}$; mutation positions are indicated in the panels; an extended version of the figure with primary data and fits can be found in Appendix B.

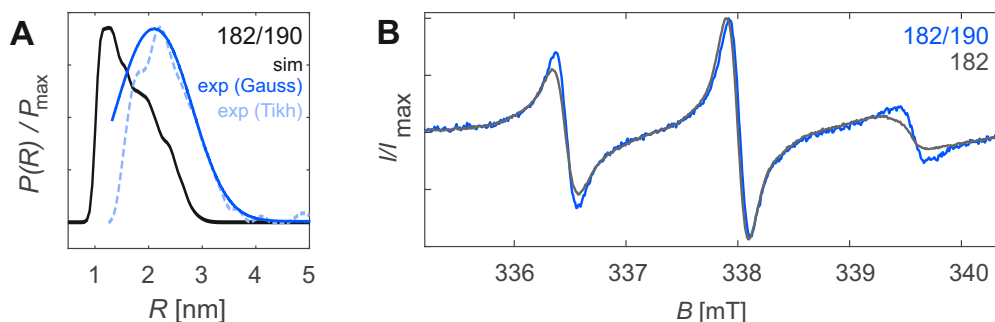


Figure 4.6: DEER between residues 182 and 190 (A) modelled distance distribution from NMR ensemble (black), and experimental DEER fits (blue; fit model indicated) for 182/190; (B) CW X-band ambient temperature spectra of MTSL-labelled 182, resp. 182/190; effective labelling efficiency per Cys was 50 % for 182/190.

upon incubation with spin label, which was not the case with the respective single Cys mutants. The precipitate could be removed prior to DEER sample preparation by centrifugation and filtering. Note that, both, low labelling efficiencies and precipitation actually support the assumption that very short distances between residues are populated in this highly flexible chain. In such a situation, the spin labelling reaction competes with fast intramolecular Cys-Cys dimerisation. Out-competing intramolecular reactions is much more difficult than out-competing intermolecular disulfide formation, which can usually be achieved by labelling at very low protein concentrations. If spin-labelling is slower than internal disulfide formation, the disulfide-linked IDD is presumably trapped in an unnaturally rigid state, which could explain the precipitation.

The second set of auxiliary distance distributions shown in Figure 4.5 localises residue 197 with respect to two beacons, 52 and 182. Results for the latter beacon were already described in the previous section as an example for distance analysis (see Figure 4.3). For the 182/197 residue pair,

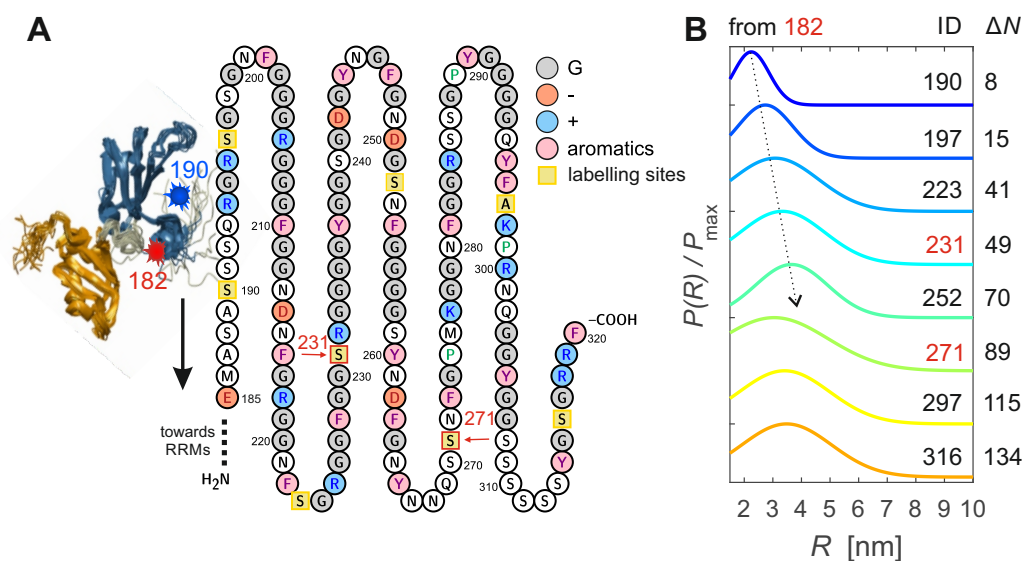


Figure 4.7: Combined distance results involving beacon 182; (A) schematic representation of the IDD primary sequence; glycines, charged amino acids, aromatics, prolines, and all used labelling positions are highlighted in colour. (B) Progression of distance distributions measured from beacon 182 with increasing primary sequence distance ΔN ; second labelling site and ΔN are indicated in plot;

the DEER data without clearly visible oscillations point to a broad distance distribution. Thus, flexibility of the protein chain in full length hnRNPA1 must be considerable already at residue 197. The distance from IDD site 197 to beacon site 52 is even more broadly distributed, which is probably also because beacon site 52 itself is in a more flexible secondary structure element in the RRM than beacon site 182.

In the last experimental series in Figure 4.5 we show data analysis of additional distance measurements between beacon 182 and residues distributed throughout the IDD with various spacing of amino acids ΔN (see Figure 4.4). The data were processed analogously to the previous results. We want to highlight the first measurement in the series, which has the smallest spacing ($\Delta N = 8$, see Figure 4.6). It is particularly interesting because it allows us to characterise how flexible the protein chain is right at the end of RRM2. In the NMR ensemble structure, beacon site S182 is localised in a C-terminal helix. The helix in the NMR model extends up to residue 188, after which the conformers in the ensemble strongly diverge. With the DEER experiment we can validate this abrupt change in flexibility that might be an artifact of NMR structure computation stemming from lack of restraints. A full continuation of the helix from 182 to 190 would result in a short, well-defined distance. The expected backbone distance evaluates to $R = 0.33$ nm (using the standard α -helix pitch of 3.6 AA/turn and 0.15 nm/turn). The lengths and orientations of the flexible spin label linkers at both labelling sites have to be added, but even then the inter-spin distance would fall into a range where exchange coupling can be expected, and standard distance analysis of

DEER data might fail. In the DEER experiment we clearly see longer distances populated, and the modulation depth (0.231) is not significantly lower than expected for the given labelling efficiency (51 %). If distances shorter than about 1.5-1.8 nm were dominating we would expect a reduced modulation depth.^[18] We can summarise that the conformational flexibility strongly increases immediately after the C-terminus of RRM2, and that the end of the helical segment predicted in the NMR structure is in agreement with the DEER data.

In Figure 4.7 we show a schematic representation of the IDD, with indications of the selected labelling sites, as well as all Gaussian fit distance distributions obtained from beacon 182 in order of ascending ΔN . Initially, we observe the expected increase in mean distance and width with increasing ΔN , up to labelling site S231. After this point the mean distance remains approximately constant, at ~ 3.5 nm. Position 271 is even slightly closer to 182 than residues 297 and 316 that are closer to the C-terminus. No systematic increase in the spin density parameter (i.e. the slope of the background fit) is observed in the DEER data analysis (see primary data panels and Section 4.2.2), which would have been an indication that long distances are wrongly removed by the background correction. We point out that the observed inflection point, where distances decrease again, falls somewhere between residues 231 and 271. Interestingly, this range, in contrast to the further C-terminal section of the IDD, is enriched in negatively charged amino acids. In particular residue D262 is of interest, because it has been linked to pathological states of hnRNPA1 in ALS (point mutation D262V).^[166] The range also contains the well-known 'steric zipper' motif^[127] of the hnRNPA1 IDD (residues). The IDD before residue S231 and after residue S271 is enriched in arginine residues. The latter part of the IDD is also the only part which contains three prolines (which have been identified as crucial for nuclear transport of hnRNPA1^[273]).

4.2.3 Localisation of residues in the IDD from DEER restraints

In Chapter 3 we pointed out that the main spin labelling sites in the RRMs (K52, K144 and S182) were, among other criteria, selected to be suitable beacons for measurements towards selected residues in the IDD. Having collected several distance restraints between the RRMs and the IDD we can now combine the information to determine the areas of most probable location of residues in the IDD with respect to the RRMs using trilateration approaches (see Introduction section of this chapter).

The data analysis for localisation of residues 231, 271 and 316 with Gaussian fits is described in detail in the previous sections. The localisation of residue 231 (query) from four DEER restraints was performed using the grid-based algorithm described in the Introduction section of this chapter, and schematically represented in Figure 4.8(A). The 50 % probability iso-surface for residue 231 is shown in Figure 4.8(B). The location of the residue is broadly distributed, but a significant volume is excluded. For residues 271 and 316 only three distance restraints are available to beacons in the RRMs, which is not sufficient for unambiguous localisation. For a rough estimate, however, we can use the intra-IDD restraints 231/271, 231/316, and 271/316 (see Figure 4.5) as additional sources of information. Fixing residue 231 at its most probable location, we can use it as an auxiliary

| mutations | η [%] | BG dens. | Δ | R_{Tikh} [nm] | σ_R [nm] | α | R_{Gauss} [nm] | σ_R [nm] |
|-----------|---------------|----------|----------|---------------------------|--------------------|----------|----------------------------|--------------------|
| 32/231 | 74 | 0.084 | 0.407 | 4.95 | 1.44 | 316 | 5.12 | 1.55 |
| 52/197 | 73 | 0.028 | 0.340 | 3.75 | 1.19 | 631 | 3.56 | 1.38 |
| 52/231 | 93 | 0.117 | 0.489 | 4.02 | 1.40 | 501 | 3.75 | 1.81 |
| 52/271 | 84 | 0.071 | 0.380 | 3.64 | 1.34 | 159 | 2.81 | 1.97 |
| 52/316 | 77 | 0.111 | 0.261 | 3.84 | 1.44 | 25 | 3.75 | 1.82 |
| 144/231 | 44 | 0.063 | 0.348 | 4.69 | 1.44 | 40 | 4.97 | 1.54 |
| 144/271 | 70 | 0.065 | 0.240 | 4.43 | 1.60 | 631 | 4.57 | 1.86 |
| 144/316 | 55 | 0.183 | 0.186 | 4.25 | 1.32 | 79 | 4.41 | 1.17 |
| 182/190 | 51 | 0.050 | 0.231 | 2.38 | 0.59 | 79 | 2.25 | 0.62 |
| 182/197 | 65 | 0.006 | 0.368 | 2.95 | 0.83 | 50 | 2.74 | 0.95 |
| 182/223 | 52 | 0.037 | 0.262 | 3.49 | 1.17 | 1000 | 3.14 | 1.42 |
| 182/231 | 82 | 0.094 | 0.459 | 3.49 | 1.14 | 398 | 3.33 | 1.48 |
| 182/252 | 67 | 0.051 | 0.145 | 3.33 | 1.12 | 398 | 3.66 | 1.27 |
| 182/271 | 73 | 0.145 | 0.353 | 3.66 | 1.25 | 1000 | 3.05 | 1.88 |
| 182/297 | 54 | 0.039 | 0.237 | 3.80 | 1.26 | 1585 | 3.41 | 1.58 |
| 182/316 | 63 | 0.045 | 0.351 | 3.73 | 1.24 | 398 | 3.48 | 1.57 |
| 231/271 | 75 | 0.095 | 0.353 | 3.08 | 0.97 | 6309 | 2.01 | 1.53 |
| 231/316 | 68 | 0.033 | 0.099 | 3.26 | 1.15 | 501 | 2.71 | 1.65 |
| 271/316 | 48 | 0.023 | 0.179 | 3.05 | 1.03 | 6310 | 2.26 | 1.58 |

Table 4.3: DEER sample characterisation and DEER results

beacon for position 271 and iteratively, position 316. The results are shown in Figure 4.8(D). This is an underestimation of the distribution of locations sampled by residue 271 and 316, since the (large) distribution of the location of the auxiliary beacon residue 231 is not taken into account. We can cautiously state that residue 271 and 316 seem to be spatially closer to RRM1 than to RRM2.

Because we have also measured distance distributions between the beacons in the RRMs (see Chapter 3), we can use a second algorithm for the localisation method, which is based on distance network analysis (also implemented in the MMM software package^[95,235]). The algorithm requires that each site of interest is connected by a distance measurement to at least three other sites. For residue 231 we have such a set, connecting positions 52, 144, 182, and 231 by six distances, and the results are shown in Figure 4.9. The general agreement with the localisation algorithm is good, but the network algorithm predicts a slight shift of the localisation distribution of residue 231 towards RRM1 and away from the central region between the RRMs.

4.2.4 Ensemble model of full length hnRNPA1 from DEER distances

Interpretation of the DEER data in terms of molecular interactions was limited in the previous analyses to a very general, coarse-grained level. A large part of the uncertainty arises because

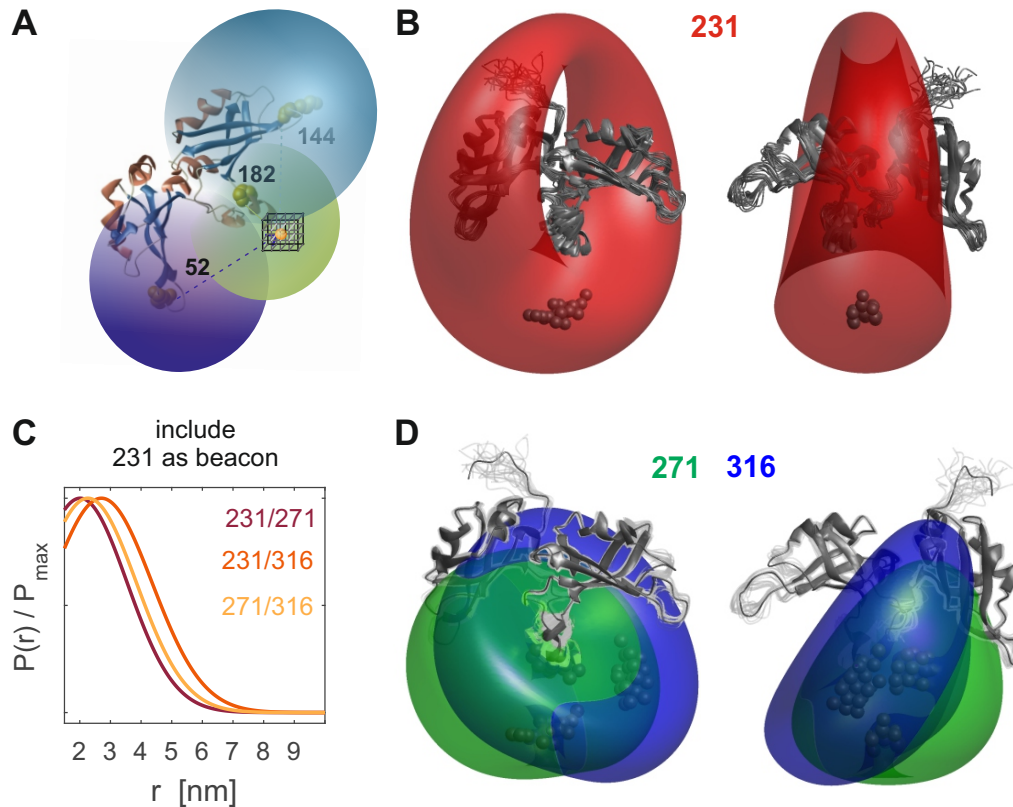


Figure 4.8: Combining distance restraints for localisation of residues; (A) schematic representation of the grid-based localisation algorithm; (B) two views of the 50 % probability iso-surface (red) of the DEER restrained localisation of residue 231 with respect to the UP1 structure; localisation was performed with four distance restraints. Small spheres indicate location of highest probability; (C) additional distance restraints from intra-IDD experiments; (D) fixing the location of residue 231 to the position of highest probability shown in panel (B) we can additionally localise residue 271 (green iso-surface), and iteratively in the same manner residue 316 (blue iso-surface); this is a rough lower bound approximation, since the location of residue 231 is not well defined.

only average localisation information could be discussed for example in the localisation approach of residues 231, 271 and 316, and no correlation between the locations of the sites was possible. In analysis up to this point we did not use the information from connectivity of the labelling sites. The bond lengths, bond angles, and torsion angle statistics are strong further restraints that can be used in modelling without using a molecular force field. Such additional analysis becomes accessible when generating atomistic ensemble models of the full length protein, as we will demonstrate in this section.

Unrestrained reference models We first generated atomistic ensemble models of full length hnRNPA1 without any experimental DEER restraints, which serve as reference for the restrained ensembles (see Figure 4.10(A) and (B)). The only conformational restrictions during the *in silico*

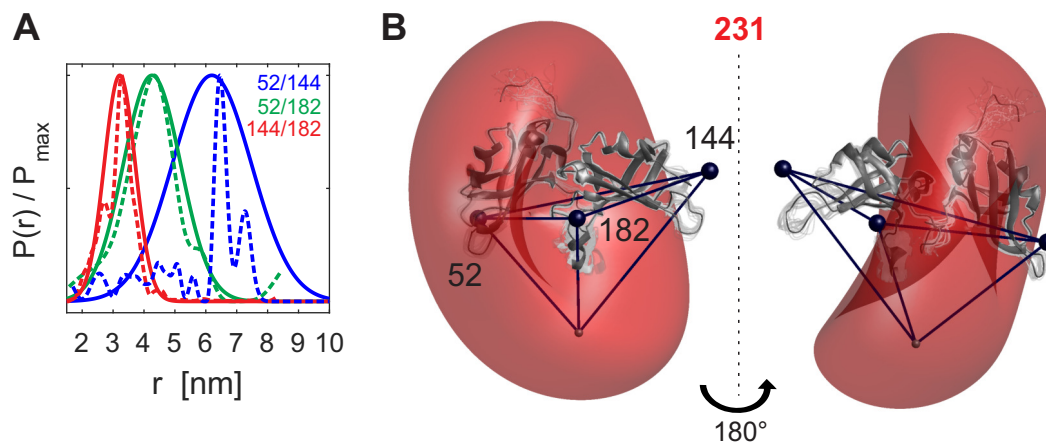


Figure 4.9: Localisation of residue 231 with the 'Network' algorithm; (A) Gaussian fits (solid lines) and Tikhonov fits (dashed lines) of intra-RRM distance measurements; (B) 50 % probability isosurface of residue 231 with network algorithm using six distance restraints; note that this solution is not unique, since the mirror image with respect to the beacon plane is also a solution (not displayed);

growth of the IDD conformers from the anchor at the N-terminal end of RRM2 are given by the Ramachandran statistics reported for the different amino acids following the primary sequence of the IDD.^[121,138] As a result the IDD conformers in the unrestrained ensembles are free to populate very extended conformations. In each panel 50 randomly selected conformers of the unrestrained ensemble are shown in the visualisation, but note that unrestrained ensemble generation of 200 conformers took only a few hours on a standard desktop PC. The colour-coding in the IDD reflects assignment of the dihedral angle of each conformation to secondary structure motif classes. All stretches of secondary structure assignment other than random coil are very short, and can be considered as the 'baseline' levels, i.e. they show the probability of forming short motifs with secondary structure by chance. To quantify the compactness of the ensemble we calculated histograms of the C_{α} - C_{α} distances between two selected pairs of residues, which can be found in Appendix B. The distribution is very broad, as expected, and the averaged distances can be found in Table 4.4.

DEER-restrained models We combined the DEER results in a simulation of the full conformer of hnRNPA1 that is constructed with the aid of the experimentally obtained distance distributions shown in Section 4.2.2. The IDD of hnRNPA1 consists of approximately 120 amino acids, and 15 restraints were measured that connect residues approximately evenly spaced throughout this sequence to the beacons 52, 144 and 182 in the RRM, and one additional auxiliary restraint (32/231) is available. Three restraints were measured within the IDD, connecting the main localisation points 231, 271 and 316. Thus, in total 19 distance restraints are available. In Figure 4.10(C) and (D) we show 50 randomly selected conformers each of the IDD of hnRNPA1 that were generated with 19 DEER distance restraints. The distance restraints were implemented as single Gaussian distributions, with mean value R_m and width σ_R (the restraint input file for the 'build

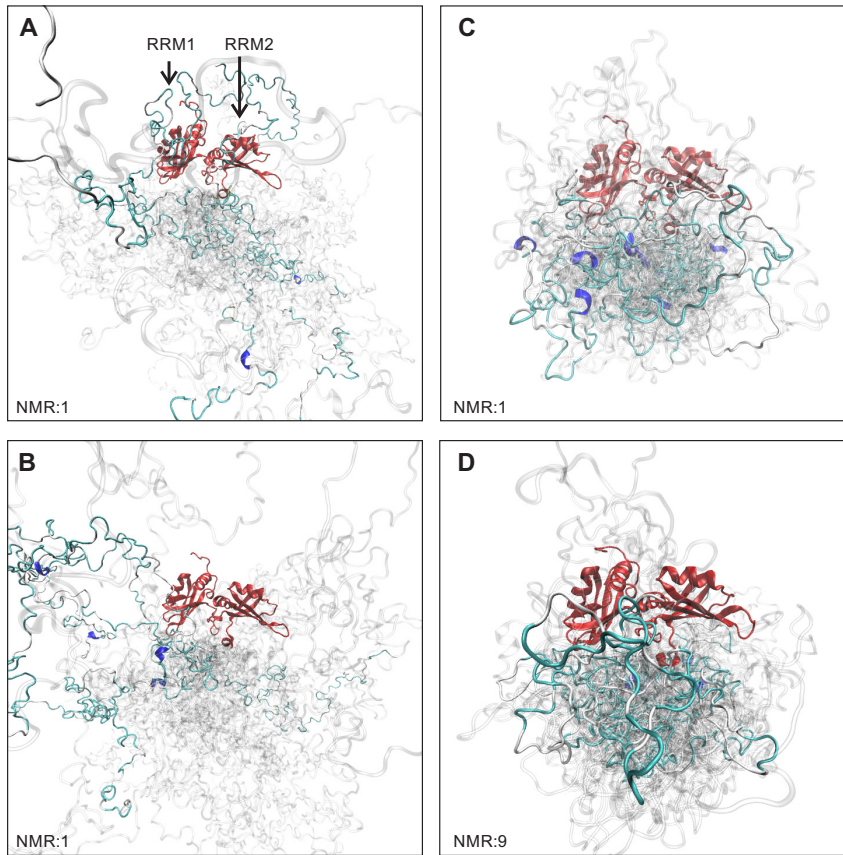


Figure 4.10: Ensemble models of full length hnRNPA1; all structures are aligned to residues 1 to 187 (the RRMs, shown in red); 50 IDD conformers (residues 188 to 320) are shown in each panel, five conformers each are displayed colour-coded by secondary structure (grey: beta-turn; cyan: coil; blue: 3_{10} -helix; the probability threshold was 0.5; (A) and (B) Two realisations of models generated without DEER restraints, using Ramachandran statistics for *loop*-type sequences; (C) and (D) models generated with 19 experimental DEER restraints (see main text) and Ramachandran statistics for *loop*-type sequences; the cutoff probability was 0.5; (C) and (D) were generated with two different RRM1/RRM2 models selected from the NMR ensemble structure (NMR:1, resp. NMR:9).

domain ensemble' module in MMM^[138,235] can be found in Appendix B). The difference between the two ensembles shown in (C) resp. (D) is the rigid-body structure of RRM1/RRM2 that serves as an anchor for the IDD (shown in red). In each case a different model from the NMR ensemble was used (conformer 1 resp. 9). These two particular conformers were chosen, because they show the largest difference (highest pairwise C_{α} -rmsd between conformers when aligning the full UP1 models) within the NMR ensemble at the sites of the two beacons 52 and 144 (both in the loop regions of the RRMs). We see that the DEER restraints lead to a more compact ensemble of IDD conformers. The predicted end-to-end distance distribution R_{A1} (between residue 1 and 320), and R_{IDD} (between residue 188 and 320) was calculated analogously to the unrestrained ensembles (see

Appendix B). For both site pairs the mean end-to-end distance of the IDD is shifted to much shorter values compared to the unrestrained reference ensembles (histograms are shown in Appendix B), and the distances are less broadly distributed in the restrained ensembles ($\sigma_R \approx 1$ nm).

| ensemble | residues | (starting) structure | N_{chains} | # | $R_{\text{gyr}}^{(\text{exp})}$ [nm] | $R_{\text{gyr}}^{(\text{sim})}$ [nm] | $\langle R_{\text{IDD}} \rangle$ [nm] | σ_{IDD} [nm] |
|----------|----------|----------------------|---------------------|----|---|---|--|-------------------------------|
| UP1 | 1-187 | 2LYV | 20 | - | 2.289±1.21 | 1.890 | - | - |
| Ref 1 | 1-320 | 2LYV:1 | 200 | 0 | 3.007±1.74 | 4.025 | 8.40 | 2.83 |
| Ref 2 | 1-320 | 2LYV:9 | 200 | 0 | 3.007±1.74 | 3.625 | 8.34 | 2.61 |
| A1 1 | 1-320 | 2LYV:1 | 186 | 19 | 3.007±1.74 | 2.324 | 2.89 | 1.02 |
| A1 2 | 1-320 | 2LYV:9 | 186 | 19 | 3.007±1.74 | 2.517 | 3.32 | 0.90 |

Table 4.4: Ensemble model properties; models 'Ref 1' and 'Ref 2' were generated without DEER restraints; 'A1 1' and 'A1 2' with 19 DEER restraints (column '#'); the IDD conformers in all full-length hnRNPA1 models were generated with a probability threshold of 0.5; the NMR ensemble model of the RRM ('UP1', only used residues 1-187 for analysis) is included for comparison. $R_{\text{gyr}}^{(\text{sim})}$, $\langle R_{\text{IDD}} \rangle$, resp. σ_{IDD} were calculated with customised scripts in vmd.^[128]

4.2.5 Experimental ensemble validation

Small angle X-ray scattering We measured small angle X-ray scattering (SAXS) curves of wild-type UP1 (protein construct lacking the IDD) and hnRNPA1 in dispersion buffer to determine the radius of gyration R_{gyr} , which we can compare to our simulated ensemble models. The data were analysed with ATSAS software,^[92] and can be found in Appendix B. The experimentally determined $R_{\text{gyr}}^{(\text{exp})}$ values are reported in Table 4.4. As expected, R_{gyr} is larger for hnRNPA1 than for UP1, but in both cases the experimental uncertainty is rather large, which unfortunately prevents detailed comparison to the different ensemble models. However, we can qualitatively compare the difference between UP1 and hnRNPA1 $\Delta R_{\text{gyr}}(\text{UP1}, \text{hnRNPA1})$. We find $\Delta R_{\text{gyr}} \approx 0.7$ nm (experiment), $\Delta R_{\text{gyr}} \approx 2.0$ nm (unrestrained ensembles), resp. $\Delta R_{\text{gyr}} \approx 0.5$ nm (restrained ensembles). It matches better for the DEER restrained ensembles, and the too small value found for the restrained ensembles may arise because the restrained ensembles were generated with a probability threshold ($p = 0.5$), and thus always are an underestimation of the true width of distributions of conformations.

A new combined fit procedure (developed by Gunnar Jeschke) was also tested, which allows post-ensemble generation model validation. The conformers of the unrestrained (Ref 1, 200 unique starting conformers used) and the DEER restrained (A1 1, 186 unique starting conformers used) ensembles were each re-weighted according to their agreement with the combined DEER restraints, and a fit of the SAXS data. This is displayed for two example distance distributions (182/197, and 182/316) in Figure 4.11. The resulting refined ensembles are visualised in Figure 4.12. We see that the initially unrestrained ensemble is able to reproduce the short sequence separation distance restraint (182/197) well, but not the long sequence separation distance restraint (182/316).

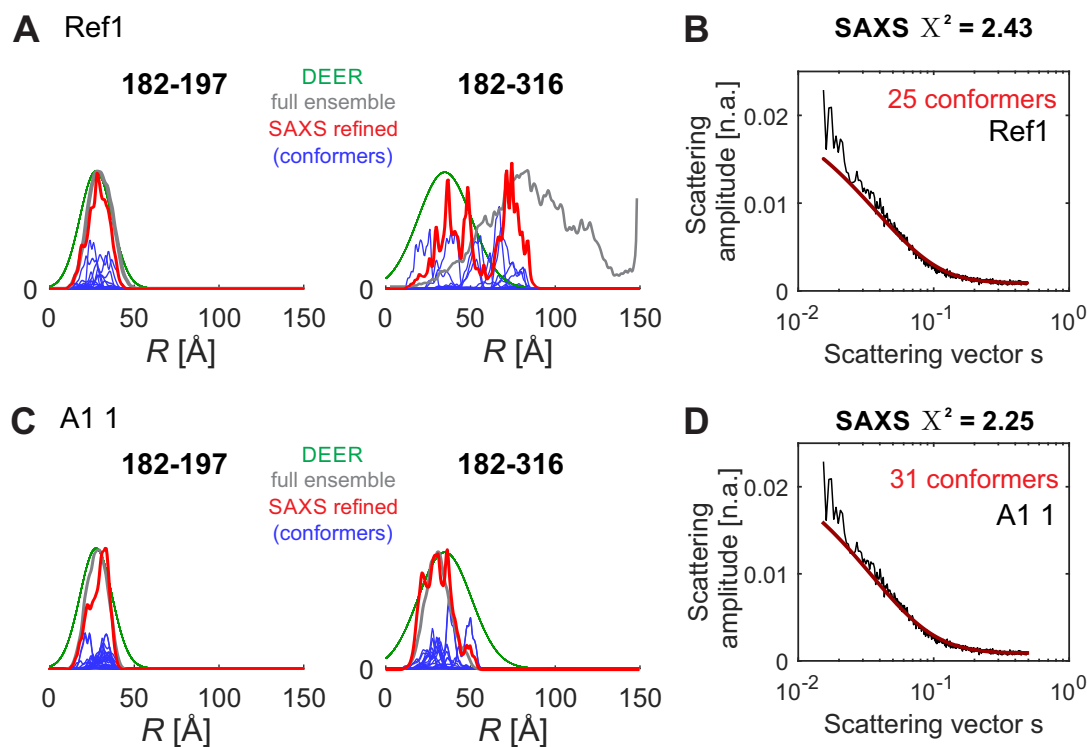


Figure 4.11: Combined DEER and SAXS ensemble refinement; (A,B) ensemble previously generated without DEER restraints ('Ref 1' 200 conformers); (C,D) ensemble previously generated with 19 DEER restraints ('A1 1' 186 conformers); (A,B) experimental DEER fits (green), full ensemble distance simulation (black), refined ensemble including SAXS fit (red), and individual conformer contributions in refined ensemble (blue); semi-logarithmic plot of the experimental ensemble SAXS curve (black) with the refined ensembles (red)

As expected, the DEER restrained ensemble fulfils both restraints well. After combined DEER and SAXS fitting, the ensembles are reduced to 25 conformers (12.5 % of former Ref 1), resp. 31 conformers (16.7 % of former A1 1). A slightly better success rate was thus found for the restrained ensemble. Also the resulting final fit RMSD of the SAXS data is better for the refined ensemble derived from the initially restrained ensemble.

Intramolecular PRE from residue 231 The DEER data surprisingly indicated that a significant fraction of conformations exists in which residue 231 is in comparatively close proximity ($R < 3$ nm) to the RRM. This is reflected in the experimentally restrained ensemble models as a preference for rather compact conformations. We wanted to have independent experimental confirmation of such compact state of the protein, especially, because DEER data are measured at cryogenic temperatures after shock-freezing the sample. We thus used the intramolecular paramagnetic relaxation enhancement (PRE) experiment, which is sensitive to electron-nuclear interactions at spin-spin distances up to ~ 2.5 nm (for theoretical considerations see Chapter 2 and Theory section of Chapter 3).

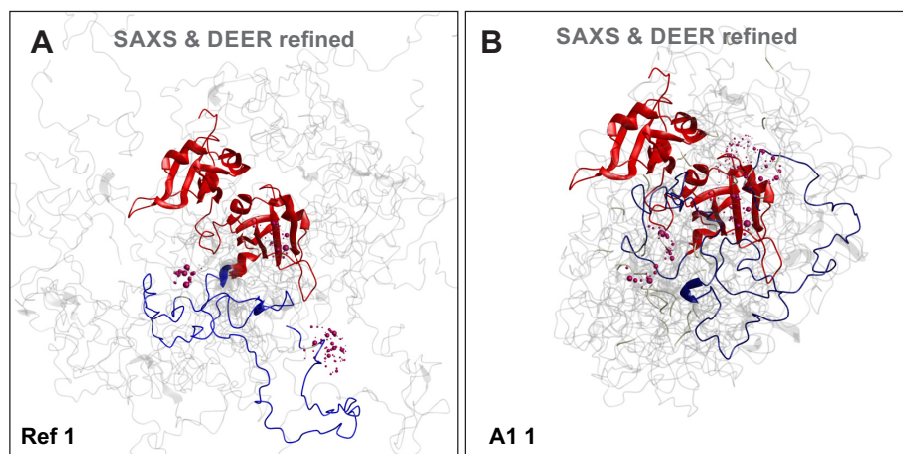


Figure 4.12: Refined ensemble models of hnRNPA1 (combined DEER and SAXS) superimposed on RRMs (red), one conformer of the IDD (blue) is shown opaque with MTSL rotamer simulation for the sites 182; 192 and 316; (A) originally unrestrained (Ref 1); (B) originally restrained with 19 DEER restraints (A1 1);

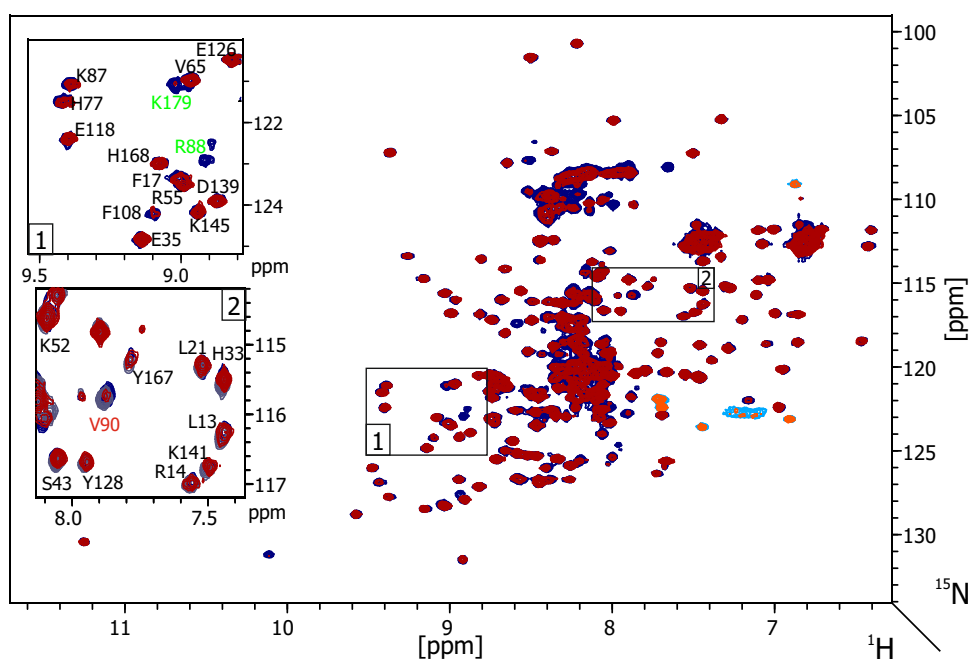


Figure 4.13: Intramolecular PRE experiment with labelling position 231; overview and two detail ranges of $^1\text{H}^{15}\text{N}$ -HSQC spectrum (30°C ; $c_{\text{protein}} \sim 50 \mu\text{M}$)

The results of PRE experiment with spin labelled and ^{15}N -isotope enriched hnRNPA1 are shown in Figure 4.13 and Figure 4.14. In contrast to the intermolecular PRE experiments shown in Chapter 3, this is an 'intramolecular PRE' experiment because the spin label is attached directly to the protein which is ^{15}N -isotope enriched, and thus 'NMR-active'. Note, however, that when

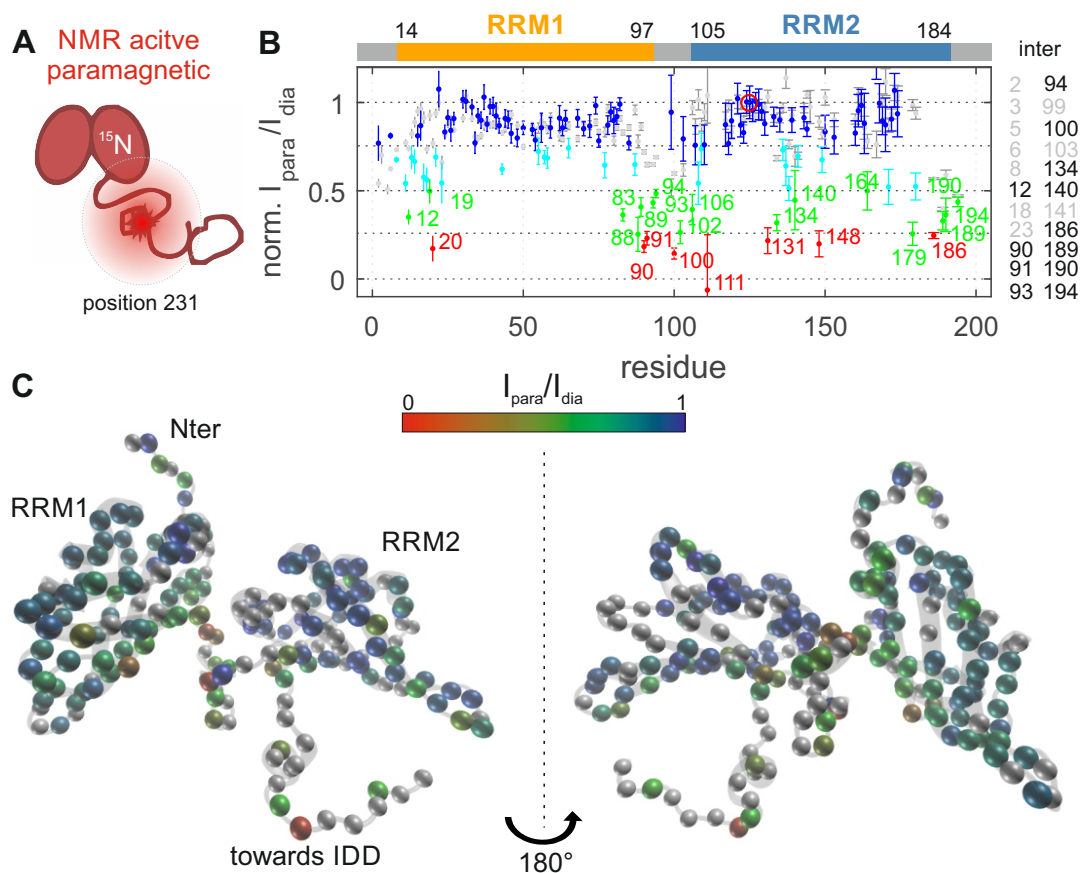


Figure 4.14: Intramolecular PRE experiment with labelling position 231; (A) schematic representation; (B) relative PRE effect normalised to intensity I_{135} (red circle); points in grey are results from intermolecular PRE measurement with same spin labelling site (compare Chapter 1 Figure 3.8); *right*: list of residues identified for intermediate intermolecular PRE (matches with intramolecular PRE printed black); (C) colour-coded mapping of PRE to backbone nitrogens in UP1 structure (no information: grey spheres);

all protein molecules in the sample are isotope enriched, intermolecular and intramolecular PRE effects cannot be directly distinguished, which may be relevant if protein-protein encounters are very frequent. We know from DEER experiments with single Cys mutants of hnRNPA1, and from the intermolecular PRE experiments that even at low protein concentrations there are some (transient) protein-protein interactions present in all samples (see Chapter 3). The intramolecular PRE patterns must thus be carefully compared to the intermolecular control PRE experiment, which are thus also plotted in Figure 4.14.

Referencing of the paramagnetic to the diamagnetic state was achieved by comparing the spectral intensities I of the backbone peaks in the 2D $^1\text{H}^{15}\text{N}$ -HSQC spectrum of MTSL-labelled single Cys mutant S231C, with intensities of the same protein labelled with a diamagnetic analogue of MTSL. Because (small) absolute differences in spectral intensities are always expected for measurements with different samples, we normalised each spectrum to unit intensity at a chosen reference residue

(buried backbone nitrogen 135) prior to further analysis. The relative PRE effect normalised to this reference residue is then given by the ratio $I_{\text{para}}/I_{\text{dia}}$ for each peak in the spectrum. In Figure 4.14 we show the relative PRE effect for each unambiguously assigned backbone resonance in the (Cys-free) RRM1 and RRM2 of hnRNPA1. Residues in which the intensity ratio is smaller than 50% are annotated explicitly, and all residues are colour-coded according to ranges ($I_{\text{para}}/I_{\text{dia}} < 25\%$, 25-50%, 50-75%, $> 75\%$). In grey we additionally plot the PRE ratios obtained in the intermolecular PRE control experiment.

The residues which are most strongly affected by the spin label at site 231 in the intramolecular PRE experiment are clustered in the linker region between RRM1 and RRM2 (residues 83-111). There is a second patch of residues that are strongly affected in RRM2 (residues 131-148). Furthermore the residues towards the C-terminal end of RRM2 are affected by the presence of the spin label in the IDD. To a lesser extent there is also a patch in RRM1 that experiences PRE (residues 12-20). Some, but not all of these ranges coincide with ranges for which intermolecular PRE was observed. In particular the N-terminal residues of hnRNPA1 (residues 2-14) were affected by intermolecular PRE, but are only weakly affected in the intramolecular experiment. In contrast, the residues in RRM1 immediately after this range are not affected in the intermolecular experiment, but significantly affected by intramolecular PRE. This is an important observation, because from this we can estimate that the intermolecular PRE effects are most likely not the dominating contribution in the intramolecular PRE experiment (assuming that the extent of protein-protein interactions was approximately the same in the two measurements).

The residues close to the linker region are the most difficult to interpret, because this was the region with comparatively strong intermolecular PRE effects. Nonetheless we observed that the C-terminal end of RRM1 (residues 83-97) experiences strong intramolecular PRE and only weak intermolecular PRE, the residues in the linker between the two RRM1s (residues 97-106), experience also strong intermolecular PRE. Also the patch in RRM2, as well as the C-terminal range of RRM2 are in ranges where intermolecular PRE was observed.

We confirmed the effect of a spin label in the IDD on peaks in the RRM1s by additional intramolecular PRE measurements with the spin label in two other locations: 271 and 316. For the additional spin labelling sites, however, we currently have no intermolecular reference experiments, and it is thus more difficult to estimate the contribution of true intramolecular PRE. The results are shown in Appendix B. Qualitatively, we can summarise that the PRE effects were similarly strong for sites 231 and 271, and weaker for 316. Interestingly, in the measurements with the spin label in 271 the residues at the RNA-binding interface (β -sheet surface) are rather strongly affected, which is not the case for site 316. For the DEER experiments with spin labels at 231 and 271, however, we can estimate that the fraction of dimers in both situations is similar.

In summary, with the combination of inter- and intramolecular PRE experiments we confirmed that compact conformations of the IDD are populated to some significant degree. Note that we cannot exclude transient population of such conformations and inter-conversion with extended conformations on a time-scale that is faster than the timescale of the PRE experiment.

4.2.6 Towards mechanistic insights for hnRNPA1

Having generated the ensemble models of full length hnRNPA1, we can use them to test hypotheses on the molecular interactions and functions of the IDD. As was stated in the introduction, this is the main reason why atomistic descriptions are valuable. If the ensemble truthfully represents the conformational preferences of full length hnRNPA1 (in the particular buffer conditions that were used), we should be able to identify interactions that are relevant under these conditions, because they are the driving forces that determine conformational preferences, and should thus be populated accordingly. Naturally, also in the unrestrained ('random') models we expect to encounter some interactions by coincidence. Any interaction in the experimentally restrained ensembles that we want to interpret as a driving force of conformational preferences must therefore be compared to the 'background' level of finding the respective interaction by chance. Like with structured domains we can screen the ensemble models for transient secondary structure motifs and charge interactions. For this we can use established modelling software tools. Additional interactions, which have been proposed to be crucial for interactions of the IDD of hnRNPA1, are arginine-tyrosine interactions,^[299] but due to lack of available software tools we only make qualitative observations, and we refrain from showing detailed analyses.

Local order The individual IDD conformers in all ensembles were found to be highly dissimilar. Alignment of all ensemble conformers (with resp. without the RRM) leads to large average backbone root mean square deviations (RMSD) between two conformers. The average pair-wise backbone RMSD between all conformers in the ensembles was calculated with a custom-written tcl script for vmd, and is reported in Table 4.5 for two unrestrained reference ensembles and the restrained ensembles (19 DEER distance restraints). While the global average RMSD (alignment

| | Ref 1 | Ref 2 | A1 1 | A1 2 |
|-------------------------|-------|-------|-------|-------|
| NMR | 1 | 9 | 1 | 9 |
| [Å] | | | | |
| RMSD ₁₋₃₂₀ | 24.57 | 24.99 | 18.90 | 18.92 |
| RMSD ₁₈₈₋₃₂₀ | 21.63 | 21.99 | 18.32 | 17.81 |
| RMSD _{M9} | 11.46 | 11.55 | 11.37 | 11.21 |
| RMSD _{zipper} | 2.20 | 2.19 | 2.25 | 2.18 |

Table 4.5: Average RMSD for backbone alignment of ensemble conformers; ensembles with 186 conformers were used in each case, 'NMR' lists the NMR model sub-ensemble conformer that was used as anchor. The average RMSD subscripts in the upper two rows gives the residue range (in our construct numbering) that was used during alignment (full range, vs. IDD only); 'M9' corresponds to alignment of nuclear localisation signal residues 257-305 (canonical residue numbering: 309-357, as used in structure bound to transportin-1^[182]); 'zipper' corresponds to alignment of residues 243-248 (steric zipper motif);^[127]

of residues 1-320) is significantly lower for the experimentally restrained ensembles than for the

reference ensembles, the difference is smaller when only aligning the IDD conformers. This suggests that in the unrestrained ensembles the orientation of the RRM with respect to the IDD is not well defined. We also included average RMSD values for aligning sequences that were previously studied by structural methods: the nuclear localisation sequence ('M9'), and the steric zipper sequence ('zipper'). The absolute RMSD values are of course smaller for the partial alignments due to the smaller number of aligned residues. Additional visualisation of the ensemble aligned to different range of the full length model can be found in Appendix B.

Secondary structure As expected, we found that the structural preferences imposed by the Ramachandran statistics are sufficient to stochastically populate small stretches of structural motifs that can be assigned to classes of secondary structure, like β -turns, or 3_{10} -helices. A graphical summary can be found in Appendix B. The motifs that were found in the unrestrained ensembles are very short (only up to 3 residues), and the majority of backbone dihedral angles fall into the structural category of unstructured. No strong differences were found between the restrained and the unrestrained ensembles, and in general the experimentally restrained conformers still adopt predominantly disordered conformations.

Charge interactions Similarly to the secondary structure classification, we scanned the ensemble models for conformations in which two charged amino acids are spatially arranged in a 'salt-bridge' conformation using the default geometric definitions in the vmd software toolbox.^[128] The results for two reference ensembles, and two restrained ensembles can be found in Appendix B. It is important to point out that no physical model was used in the generation of the ensemble models, so any identified interactions arise either by coincidence, or because the underlying true conformational ensemble of the full length protein has a significant preference for forming a given charge interaction. To estimate the contribution of the 'by chance' occurrences of interactions it is crucial to include analyses of ensembles generated with random conformations. In all ensembles (also unrestrained) we found individual conformers in which at least one salt-bridge was found within the IDD (e.g. D214-R218 occurs with comparatively high frequency, 0.5-1 % of 200 conformers in the reference ensembles, resp. 2.7-4.8 % in the restrained ensembles). We also found in all instances individual conformations classified as a salt bridge between the IDD and surface exposed amino acid side chains in the RRM.

For the unrestrained ensembles we found as expected that the list of identified interactions is not fully stable with repeated ensemble generation. This was not tested with the experimentally restrained ensembles, but it suggests that 200 conformers are not enough to draw conclusion from the interaction patterns. Nonetheless, significantly more instances that were categorised by the algorithm as a conformation with a salt-bridge interaction were found in the restrained ensembles than in the unrestrained ensembles. Note that a given residue may interact with different partners in different ensemble conformers, unlike what is typically observed for residues in folded domains. This is not surprising for highly flexible domains, and a similar observation has recently been reported in single molecule Förster resonant energy transfer (FRET) experiments, where multiple, rapidly exchanging pair-wise interactions are driving a high affinity interaction between two IDPs.^[43] In the unrestrained ensembles of full length hnRNPA1 we found that residues R194,

D214, R218, and D262 were encountered in salt-bridge like conformations with more than two different residues. In the restrained ensembles the network of interactions appears even more complex, and we additionally find that residues R194, R196, R206, R225, R232, D242, D250, and R319 were found in interaction conformations with more than one different interaction partner.

Distance measurements to the IDD We found that distance measurements between beacon sites in the RRM of hnRNPA1 to residues in the IDD result in broad distance distributions. The data were analysed with a single Gaussian fit after background correction with a three-dimensional fit. In several distance measurements we found that the dominating contributions in the distance distribution are shorter than what is expected from the random self-avoiding walk polymer model. Four distance restraints from RRM beacon sites to residue 231 in the IDD were available, which was sufficient to perform grid-based localisation of this residue. The distribution of the spatial location of the residue 231 is broad, but centred around the inter-RRMs region of hnRNPA1. An alternative algorithm (distance network), which also requires inter-beacon distance restraints, gives very similar results, with a slight shifting of the centre of the distance distribution towards RRM1. With additional auxiliary measurements we could also find lower bounds for the spatial location distributions of sites 271 and 316, which both seem to slightly favour locations closer to RRM1 and the RRM-linker region, than to RRM2. All three residues are distributed over a large spatial range, but comparatively close to the RRMs.

By combining 19 DEER distance restraints we could generate atomistic ensemble models of hnRNPA1. To the best of our knowledge this is the first reported ensemble model of the full length hnRNPA1 protein. The experimentally restrained ensemble model is much more compact than ensemble models generated without experimental restraints. From the comparison between SAXS scattering curve fits for UP1 (protein construct without IDD) and hnRNPA1 it appears that the DEER restrained ensemble better predicts the experimental change of the radius of gyration. The presence of compact conformations of the full length protein could furthermore be confirmed by intramolecular PRE experiments with the spin label at site 231. The individual IDD conformers in all generated ensembles are very diverse, with only very small local similarities (high alignment RMSD). No pronounced secondary structure patterns were observed in the IDD conformers. Analysis of the ensemble models in terms of charge interactions showed that in the experimentally restrained ensemble we more frequently encounter conformations that are classified as a salt bridge by standard definitions of molecular geometry. In all ensembles (restrained and unrestrained) residue D214 was most frequently found to be involved in these 'effective' interactions. This is an interesting finding, because D214 was recently found to be crucial for stacking interactions in reversible amyloid-like aggregates of the IDD of hnRNPA1,^[110] and a charged-to-uncharged mutation of this residues was shown to interfere with this interaction. Also for residue D262 a charge-to-uncharged mutation has been linked to ALS (D262N).^[166] Further investigation based on the ensemble models, however, requires more extensive sampling of conformations.

Our experimentally restrained ensembles predict a more compact protein conformer than what is obtained when assuming unrestrained Ramachandran statistics for all residues in the IDD. This im-

plies that there are interactions that lead to preferential population of compact conformations. As an example, we have described preliminary analysis of our ensemble models in terms of charge interactions (like transiently forming salt-bridges, which we can screen for conveniently in the atomistic ensembles with existing software tools. Other effects, like aromatic stacking, or the hydrophobic effect could in principle be considered as well. However, it is important to point out that for highly flexible, strongly interacting biomolecules we cannot easily disentangle the molecular interactions relevant for intramolecular conformations from those relevant for IDD-mediated protein-protein interaction networks. Several such driving forces and mechanisms have been proposed to mediate protein-protein interactions also in liquid-liquid phase separation (LLPS).^[120,299]

Our observation of compact states of full length chain of hnRNPA1 in conditions that stabilise the protein monomer are in fact in line with the current understanding of molecular interactions that have been proposed to mediate LLPS of hnRNPA1. For hnRNPA1-mediated LLPS, arginine - tyrosine interactions have been reported as a major driving force. Originally, this was described for LLPS with the IDD of FUS (Fused in Sacroma), another partially disordered protein with a similar amino acid composition of the IDD as hnRNPA1.^[299] The relevance of this interaction for LLPS was proved experimentally by mutation studies.^[299] It was demonstrated with FUS that interactions are not only relevant between IDDs, but that the folded RNA binding domains (RBDs) may also play a role. However, in this study the subunits were purified individually and mixed *in vitro*. In the case of FUS the arginines and tyrosines are separated between the two domains, with the majority of tyrosines being located in the IDD of FUS, and the arginines in the RRM. For hnRNPA1 the segregation is not as pronounced. We find arginines and tyrosines in both the IDD and solvent exposed sites of the RRMs. In the RRMs they are known to be crucial for nucleotide binding.^[26] For an individual interaction between a particular arginine and tyrosine it does not matter whether they are in the same or in different molecules, as long as the required geometry for interaction can be fulfilled. There is a difference, however, for the diffusion kinetics and thus interaction probabilities between intra-, and intermolecular interactions. Intermolecular interactions are sensitive to the absolute concentrations of the molecules carrying the interacting amino acids, while the intramolecular interactions are not. In a simplified picture we can now imagine the interactions between all arginines and tyrosines as a network over the entire sample, in which each arginine competes for the interaction with a given tyrosine with all the other arginines from the same or different protein units, or from the buffer. In such a competition situation we expect the intramolecular interactions to dominate at low protein concentrations. In our model this means that at low protein concentrations in the dispersed state the arginines and tyrosines encounter interaction partners within the same molecule (both in the IDD and the RRMs) significantly more frequently than interaction partners in other hnRNPA1 molecules. This leads to a preferred population of compact states.

When increasing the protein concentration we rapidly increase the number of intermolecular interaction partners, while the intramolecular number of interaction points remains constant. The probability of an intermolecular interaction to occur is thus increased. IDDs present an interesting special case in this respect, because the structural correlation between the conformations of two sites in the IDD is very low. Different sites of the IDD can therefore interact with different

molecular interaction partners, which enables the formation of large, interconnected networks with fast changing local molecular interactions. This model also explains the fast nitroxide dynamics of spin labels in the IDD, because each individual conformer remains highly flexible, even though specific sites are transiently interacting. This hypothesis is supported by the effect of the major buffer additive used in this study, which are the amino acids arginine and glutamate. The buffer was chosen over other buffers conventionally used in the study of LLPS (like HEPES or PBS) to have consistent conditions with NMR experiments. Buffers of this type have been previously and entirely empirically developed for solution-state NMR experiments, where high concentrations of protein in a monomeric state are required. We propose that the presence of arginine is sufficiently high to out-compete or at least suppress inter-, but not intramolecular arginine-tyrosine interactions, which keeps the protein in a predominantly monomeric state in compact conformations. Naturally, the ionic strength difference at high or low amino acid concentrations is also expected to influence the IDD interactions.

4.3 Materials and methods

4.3.1 Protein purification and spin labelling with MTSL

For protein purification and spin labelling with MTSL we refer to the Methods section in Chapter 3, since the same protein purification protocol was used in this study. The mutants were incubated with high levels of reducing agent (5 mM DTT) for at least 2 h at room temperature. The reducing agent was removed, and the buffer was exchanged to labelling buffer (50 mM sodium phosphate buffer, pH 6.5, 100 mM L-arginine, 100 mM L-glutamate). MTSL was added in high molar excess (up to 20x per Cys), and the protein solution was incubated over night at ambient temperature. Protein concentration during labelling was between 4 μ M to 20 μ M. The residual free spin label was washed out by a PD10 desalting column, and the labelled protein was concentrated in 10 kDa MWCO centricons. The labelling efficiency was determined by spin-counting in X-band (see Appendix B).

For the intramolecular PRE experiment, hnRNPA1 single Cys mutants S231C, S271C and S316C were grown in one litre of 15 N-isotope enriched (0.5 g 15 NH₄Cl/l) M9 minimal medium with 4 g/l glucose as carbon source from the same cell stocks used for the inoculation of LB medium. Protein purification and spin labelling with MTSL was otherwise performed with the same protocol as reported for the double Cys mutants. The labelling efficiency was determined to be 95% in the PRE sample S231R1.

4.3.2 DEER sample preparation and measurement

The protein samples in the early stages of the project were lyophilised and resuspended in 1:1 D₂O:d₈-glycerol. The lyophilisation was omitted for later sample preparation, and 50% d₈-glycerol was instead admixed directly to the samples in D₂O buffer. We checked that this did not influence the obtained distance distributions. Final samples for DEER at Q-band (\approx 35 μ l) were transferred

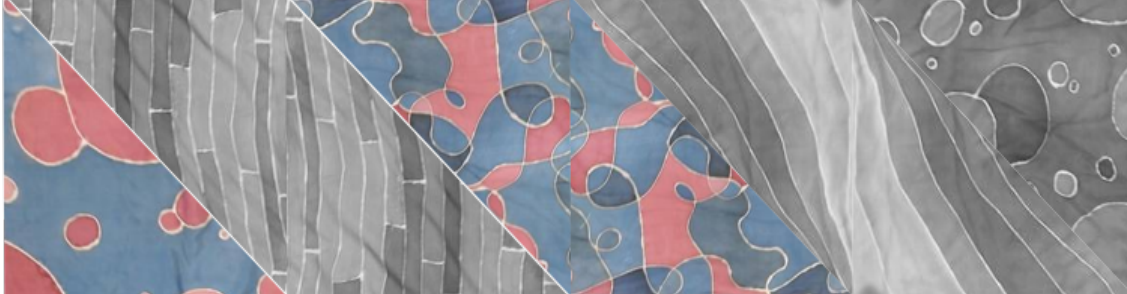
to 3 mm outer diameter quartz capillaries and flash-frozen by immersion in liquid nitrogen. The nitroxide-nitroxide DEER measurements were performed at a home-built high-power Q-band spectrometer (≈ 34 GHz) controlled by a Bruker ElexSys E580 bridge and with a home-built TE001-type resonator.^[238] The temperature was set to 50 K, and controlled in a He-flow cryostat (ER 4118CF, Oxford Instruments) and a temperature control unit (ITC 503, Oxford Instruments). The 4-pulse DEER pulse sequence was used, and pulse lengths of $t_\pi = t_{\pi/2} = 16$ ns were used unless stated otherwise. The pump pulse ($t_p = 16$ ns) was set up on the maximum of the nitroxide spectrum, and the detection was set up 100 MHz below. The first refocusing delay was always set to $t_1 = 400$ ns, and the second refocusing delay was set to approximately the 10% initial echo intensity limit. The time-step was either 12 ns, or in cases with a steep initial decay 8 ns.

4.3.3 Small angle X-ray measurements

Small angle X-ray scattering curves were measured on dilute samples of hnRNPA1 resp. UP1 (both wild-type constructs) in high ionic strength dispersion buffer (50 mM sodium phosphate, pH 6.5, 100 mM R/E, 5 mM DTT). The signal to noise is better for the sample of hnRNPA1 due to longer averaging (12 h, versus ~ 4 h for UP1). The data were analysed with the ATSAS software package^[92] to obtain a molecular distance distribution and the radius of gyration R_{gyr} .

4.3.4 PRE measurements

For the diamagnetic analogue we used acetylated MTSL (Toronto Research Chemicals, Canada), and labelling with this analogue was performed under the same conditions as with MTSL. For the measurement conditions and instrumentation we used the same conditions as reported for the intermolecular PRE measurements described in the 'Materials and methods' section in Chapter 3. NMR measurement were performed on a standard 700 MHz Bruker NMR measurement equipped with the AVANCE NEO console and a CryoProbe at 50 μ M protein concentration in dispersion buffer (50 mM sodium phosphate, pH 6.5, 100 mM R/E, 3% D₂O added for spectrometer locking) in 5 mm (outer diameter, ARMAR Chemicals) throw-away tubes. Data acquisition (using Topspin (Bruker)) of the 2D-¹⁵N¹H-HSQC spectra was for approximately 12 h per sample. Data analysis was performed by readjusting the peak list to the minor changes of the resonance position and by defining a peak model in the 'cara' software package for NMR analysis.^[1] The peak positions and the integrated peak intensities of each spectrum were exported and analysed with a custom Matlab script. First we divided each spectrum by the intensity of the reference peak (residue 135). $I_{\text{para}}/I_{\text{dia}}$ was then calculated from the normalised spectral intensities and plotted as a function of the residue number. To generate the visualisation on the NMR structure model we exported the $I_{\text{para}}/I_{\text{dia}}$ table to the vmd software,^[128] where a custom tcl script was used to set the colour of the residue representation according to a red to blue scale (from 0 to 1).



Chapter 5

RNA binding and LLPS of hnRNPA1

We have seen in Chapter 3 that solutions of full length hnRNPA1 can undergo LLPS under certain buffer conditions, and that the protein-protein interaction is mediated by the C-terminal IDD of the protein. In Chapter 4 we characterised the conformational states of the IDD (with respect to the folded RRMs) in the context of the full length protein in an ensemble model approach. In the experiments that were used for the ensemble model generation we found that the IDD in the dispersed sample state (i.e. when studying predominantly monomeric hnRNPA1) tends to adopt rather compact conformations. The compact state suggests that there are energetically favourable interactions both between sites within the IDD, as well as between the IDD and the RRMs that disfavour very extended conformations. The interaction sites of the IDD with the RRMs seem to cluster around regions where also RNA binding has been reported to occur. In this chapter we thus focus on the interplay of RNA-binding and LLPS in hnRNPA1.

Scope of this chapter In this chapter we report our experimental findings of interactions in samples of full length hnRNPA1 mixed *in vitro* with short ssRNAs. The experiments were based on the RNA sequences reported in Beusch et al.^[26]. The focus was on the effect that the presence of the short ssRNAs has on the LLPS behaviour of full length hnRNPA1. Interactions were first identified by electromobility shift assay and we made first attempts at linking the macroscopic (LLPS) properties of the samples to molecular interactions by a combination of confocal microscopy imaging and DEER spectroscopy.

Author contributions and acknowledgements The confocal imaging was performed at the ScopEM facility. Irene Beusch is thanked for helpful discussions concerning the systematic RNA binding study of the RRMs of hnRNPA1.

5.1 Introduction

The binding of hnRNPA1 to oligonucleotides is of fundamental interest because one of the core functions of hnRNPA1 is splicing regulation.^[133] We will begin by introducing the existing structural investigations that have been reported in the literature, but note that the structural results reported so far for the interactions of hnRNPA1 with DNA and RNA were obtained with protein constructs which lack the C-terminal intrinsically disordered domain (IDD) of the full length protein. In this work we will address how EPR methods can be used in combination with other biophysical techniques to study oligonucleotide binding of full length hnRNPA1. The major challenge in this study is that, both, *in vivo* and *in vitro* oligonucleotides strongly influence the liquid-liquid phase separation (LLPS) behaviour of hnRNPA1, as well as liquid-droplet (LD) maturation.^[157,189,197,239,302] Furthermore, it has been reported that RNA molecules can phase separate independently, also in the absence of proteins.^[35,288] LLPS and RNA binding are thus tightly connected processes, and thus it may be difficult, or even impossible, to perform structural investigations of RNA binding by full length hnRNPA1 in the dispersed state of the protein.

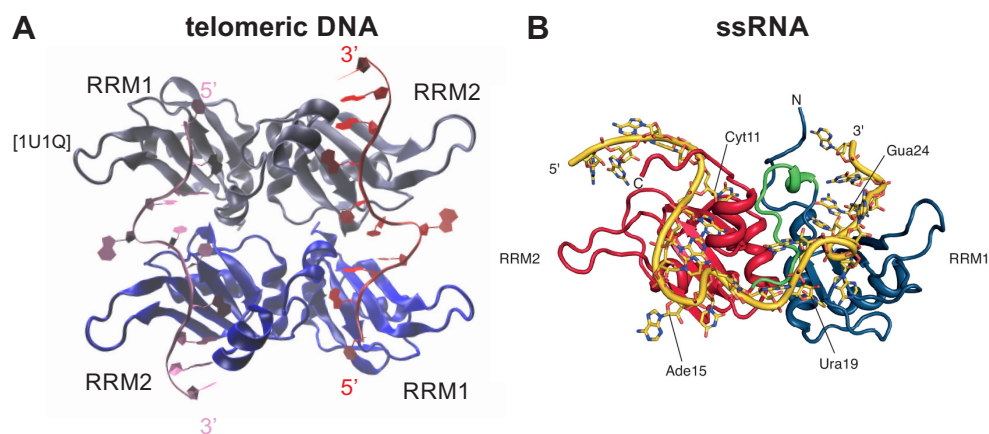


Figure 5.1: Two structure models of UP1 bound to oligonucleotides; (A) X-ray crystal structure (pdb: 1U1Q) of UP1 bound to an (inosine-containing) human telomeric repeat DNA (5'-d(TTAGGGTTA(DI)GG)-3');^[223] two protein and two DNA molecules are displayed. Each ssDNA strand is bound by both protein units. (B) Figure adapted from Beusch et al.^[26]; one possible 1:1 binding conformation of ssRNA (5'-CCAGCAUUAUGAAAGUGC-3') to UP1 derived from solution-state NMR;

Structural models of UP1 bound to oligonucleotides As we have seen in the previous chapters, hnRNPA1 contains two folded globular domains, which each adapt the well-known RNA-recognition motif (RRM) fold, and are separated by a short linker. They are typically designated as RRM1 (residues 14-97) and RRM2 (residues 105-184), and the combined RRM1-RRM2 protein construct is referred to as unwinding protein 1 (UP1). Several structures have been reported of UP1, or the two RRMs in isolation, bound to small single-stranded DNA (ssDNA) or single-stranded RNA (ssRNA) molecules,^[26,72,170,223,224] and we show two examples in Figure 5.1. The

first reported DNA complex structure was obtained by X-ray crystallography with a short telomeric repeat DNA sequence.^[72] This was followed up by a more detailed study of purine recognition by RRM, also based on crystallographic data.^[223] In the crystal lattice the protein-ssDNA complex was found to have a 2:2 stoichiometry, where each ssDNA strand is bound by two UP1 proteins. The two ssDNA molecules in the complex run in anti-parallel orientations and the orientation of the RRM is anti-parallel as well. Recently, a similar dimer structure was reported with short ssRNA, which crystallised in a very similar 2:2 dimer as the ssDNA complex.^[170] The authors argued that, due to the large contact interface and several conserved residues at the protein-protein interface, the dimerisation may be functional, as opposed to purely being a crystallographic artifact.^[72] This claim was later supported by size-exclusion chromatography experiments of UP1 bound to short telomeric repeat DNA in solution.^[224]





A solution-state structure based on NMR data of UP1 in complex with ssRNA has recently been reported by Beusch et al.^[26], and interactions of the two isolated RRM in complex with several short ssRNAs were studied in detail.^[26] The authors also performed experiments with a series of short RNAs based on a natural target of hnRNPA1 (intronic splicing silencer ISS-N1^[123]) with two, one, or no optimal binding sites for the RRM of hnRNPA1. In the same study it was demonstrated that with these short ssRNAs the binding to UP1 is also possible in solution in a 1:1 ratio, and that the two RRM have slightly different preferred binding motifs.^[26] The difference compared to the 2:2 binding in the crystal lattice was attributed to the longer linker between the two binding sites for UP1 in the ssRNA in the RNA that was used in the NMR study. These ISS-N1 derived ssRNA sequences formed the basis for our study of the interaction of full length hnRNPA1 with short oligonucleotides.

In this chapter we are dealing with RNA interaction of full length hnRNPA1, and we need to consider the contribution of the IDD to RNA binding. Interactions may, in principle, happen throughout the IDD sequence, but it is known that the arginine/glycine-rich sequences, in particular the 'RGG' motif, are enriched at the N-terminal end of the IDD. The RGG-motif is known to be able to bind oligonucleotides,^[54,100,225] and this has been found as a common feature of the RNA-binding domain superfamily of proteins.^[185,286] The mechanism of RNA binding by the RGG-motif has been described, and it is known to affect phase separation behaviour.^[54]

In summary, we expect a complex combination of interactions involving both the RRM and the IDD of hnRNPA1 to influence LLPS in hnRNPA1-RNA systems. Using this a set of ssRNAs with systematic variations of potential binding sites for the RRM of hnRNPA1 (see Figure 5.2), we want to disentangle the effect of RRM binding and IDD binding in structural investigations of interactions between hnRNPA1 and short RNAs.

5.2 Results

For the systematic interaction study of UP1 with short ssRNA we selected a set of short ssRNA molecules (18 nt), based on previously reported RNA-binding results.^[26] 'RNA_{agg}' is directly derived from the ISS-N1 RNA sequence^[26,123] and contains two optimal binding sites ('AG', highlighted in Figure 5.2). We also used the double mutated 'RNA_{aa}', in which one nucleotide is mutated per

| name | sequence | predicted binding | short |
|---------------|--------------------------------------|--|--------------------|
| ISS-N1-wt | CC <u>AG</u> CAUUAUGAA <u>AG</u> UGC | 5'-  -3' | RNA _{agg} |
| ISS-N1-g13a | CC <u>Aa</u> CAUUAUGAA <u>AG</u> UGC | 5'-  -3' | RNA _{ag} |
| ISS-N1-g24a | CC <u>AG</u> CAUUAUGAA <u>Aa</u> UGC | 5'-  -3' | RNA _{ga} |
| ISS-N1-13a24a | CC <u>Aa</u> CAUUAUGAA <u>Aa</u> UGC | 5'-  -3' | RNA _{aa} |

strong binding reduced binding

Figure 5.2: RNA sequences and schematic representations of the ssRNA constructs with varying number and position of optimal binding site for the RRM of hnRNPA1 used in Beusch et al. [26]; the proposed preferred binding configuration of the RRM of hnRNPA1 is indicated. Only experimental results with RNA_{agg} and RNA_{aa} are shown in the main text, because in the initial experimental series we were screening for the largest possible difference;

binding site (G to A mutation, effectively thus contains no optimal binding site), which results in a lower expected binding affinity. [26]. The intermediate cases were also available, with either only the 5'-binding site mutated ('RNA_{ag}'), or the 3'-binding site mutated ('RNA_{ga}'). The main design criterion for the latter single mutants was to potentially differentiate effects arising from RRM1 binding events, and RRM2 binding event in LLPS experiments. The double mutant (no optimal binding) serves as control experiment for unspecific binding.

5.2.1 Oligonucleotide binding

EMSA Mobility shifts in EMSA are affected by both the total charge and the hydrodynamic radius of a biomolecule or biomolecular complex. The EMSA assays were performed in TBE-buffered acrylamide gels at pH 7.5 under reducing conditions (1 mM DTT). We expect hnRNPA1 to have a small net positive charge at this pH, and free hnRNPA1 is thus not expected to migrate into the gel (towards the anode) with the chosen voltage settings. We thus used free ssRNA in dispersion buffer as a reference sample, which showed fast migration towards the anode. Binding of the RNA to a UP1 or hnRNPA1 protein is expected to reduce mobility due to a larger size, and lower charge of the total complex.

In the EMSA assay we clearly observed that all four RNAs (RNA_{agg}, RNA_{ga}, RNA_{ag}, and RNA_{aa}) were able to interact with both hnRNPA1 as well as UP1. The results with RNA_{agg} and RNA_{aa} can be found in Figure 5.3, and results with the RNAs with one binding site (RNA_{ag}, and RNA_{ga}) can be found in the Appendix C. We saw no strong differences in EMSA for the binding of the highest suppressed protein-binding mutant (RNA_{aa}) and the weakly suppressed mutants (RNA_{ag}, and RNA_{ga}). We therefore in the following experiments remained with the two limiting cases RNA_{agg} (expected best binding), and RNA_{aa} (expected worst binding).

In the samples where we incubated UP1 with RNA (40 μ M protein concentration incubated with 1:1 RNA:protein ratio) we observed well-defined bands that migrate into the gel matrix. The bands migrate more slowly than free RNA, which confirms interaction of the RNA with the protein. Interestingly, we found that two bands appear for RNA_{agg} when mixed with UP1, while only one

band is found with RNA_{agg} and UP1. Unfortunately, direct assignment of this band to complexes of a fixed RNA:protein stoichiometry is not possible solely based on EMSA. For hnRNPA1 (also

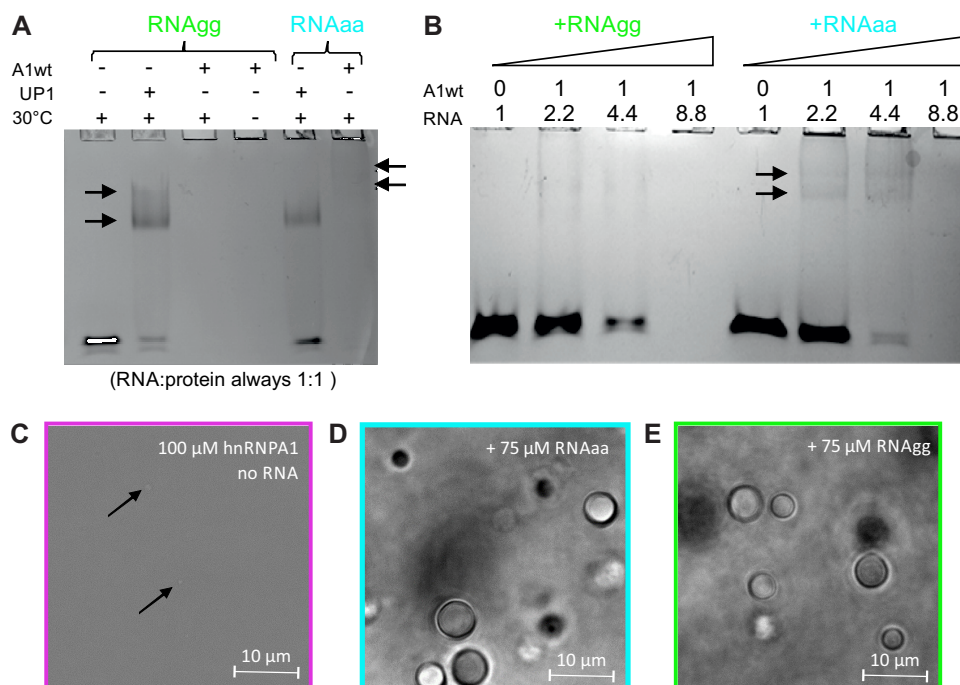


Figure 5.3: RNA binding by UP1 and hnRNPA1; (A) native PAGE of complexes of UP1, resp. hnRNPA1 with RNA_{agg} and RNA_{aaa}, stained with toluidine blue (RNA-stain); (B) native PAGE of hnRNPA1 with RNA_{agg} and RNA_{aaa} at increasing RNA ratios; (C-E) confocal images of 100 μM hnRNPA1 solutions stabilised with 0.2% agarose (C) free protein, (D) +75 μM RNA_{aaa}, (E) +75 μM RNA_{agg}

40 μM protein concentration incubated with 1:1 RNA:protein ratio) the majority of RNA material remained in the gel pocket, or even diffused out of the pocket (no material detected on gel or in pocket), independent of which of the four RNAs was used. The results with RNA_{agg} and RNA_{aaa} shown in Figure 5.3(A). Two very faint (but resolved), slowly migrating bands were observed in the presence of RNA_{aaa}, which were not detected with RNA_{agg}. The material that remains in the gel pocket most likely consist of RNA-protein aggregates that are too large to penetrate the pores of the gel matrix. Note that the band of free RNA is absent in the samples incubated with full length hnRNPA1, so it must be that the presence of the protein leads to a sequestering of the RNA, and prevents it from migrating into the gel matrix. We also did not observe a visible smear of RNA material in the samples with hnRNPA1. The absence of a smear suggests that RNA is bound rather tightly in the aggregates, otherwise we would have expected to observe more RNA molecules escaping from the aggregates over time.

We found that the manner of incubation of the RNA with the protein prior to loading on the gel made a difference (see Figure 5.3(A)). With 2 min incubation at 30 °C we observed that more material accumulated in the gel pocket in the samples with hnRNPA1. Without this short incubation

at elevated temperature we observed faint bands in the gel, where previously we saw no bands with incubation at 30 °C. Also at lower hnRNPA1 concentration (20 μM) some resolved RNA-protein complex bands were observed on the gels (see Appendix C). This demonstrated that not only the stoichiometric ratio between RNA and protein, but also the absolute concentration of hnRNPA1 is critical. Given the increased aggregation upon incubation at elevated temperature, there may be a kinetic barrier on the pathway from small aggregates that are still able to penetrate the gel matrix, to immobile, large (perhaps even on the size scale of liquid droplets) aggregates.

We performed concentration ramp experiments with the RNAs and hnRNPA1, to determine whether an excess of RNA is able to dissolve the aggregated state, for example by saturating the binding sites on hnRNPA1. The results at 40 μM hnRNPA1 concentration without sample incubation at 30 °C are shown in Figure 5.3(B). We found instead of the expected decrease in sample aggregation, that at a fixed protein concentration less RNA material is able to migrate into the gel at higher RNA concentrations (both RN_{Agg} and RN_{Aaa}), when the protein concentration was 40 μM. At lower hnRNPA1 concentrations this was not observed (see Appendix C). The RNA seems to be sequestered in a protein-bound state more efficiently at higher RNA concentrations, and at the highest RNA concentration virtually no free RNA was observed in the gel. This indicates that a cooperative process occurs in RNA interaction with full length hnRNPA1. When incubating hnRNPA1 with intermediate excesses of RN_{Aaa} we observed at least two weak, resolved bands that migrate slowly into the gel. The bands appeared also with RN_{Agg}, but are even fainter, more smeared and seem to migrate slightly faster. We found that changing the concentration of the amino acids R/E in the buffer also affected the apparent efficiency of hnRNPA1 to sequester the short RNAs in a state that does not migrate on the gel. At higher R/E concentration and (see Appendix C).

Confocal microscope imaging We complemented the EMSA assays with confocal imaging, as is shown in Figure 5.3. As was demonstrated in Chapter 3, full length hnRNPA1 is able to induce LLPS and form LDs also in the absence of RNA, if the concentration of the buffer additives arginine and glutamate (R/E) is reduced. But in the dispersion buffer (50 mM sodium phosphate, pH 6.5, 100 mM R/E, 0.2 % low melting agarose) we observed only very few, very small droplets. Note that we expect the mixing of the samples with the heated low melting agarose buffer to have a similar effect as the incubation at slightly elevated temperatures which we described in the EMSA experiments. When mixing solution of hnRNPA1 in dispersion buffer with either one of the four different RNAs at a slight molar excess of hnRNPA1 the samples immediately became very turbid upon mixing. In the confocal images we see many, large (tens of micrometers) droplets. Note that in the agarose stabilised conditions we could observe the droplets stably for at least three hours (no longer time was tested), and occasionally we were able to observe slow migration of the large droplets in the matrix as well as droplet fusion. This confirms that the observed droplets remain liquid. At these high protein concentration we could observe no differences between the limiting cases of the systematic RNA series (RN_{Aaa} versus RN_{Agg}). We are currently performing systematic experiments with the different RNAs at lower protein concentration, to see if there are small differences in the RNA-induced LLPS behaviour at the early stages of LLPS (small droplets).

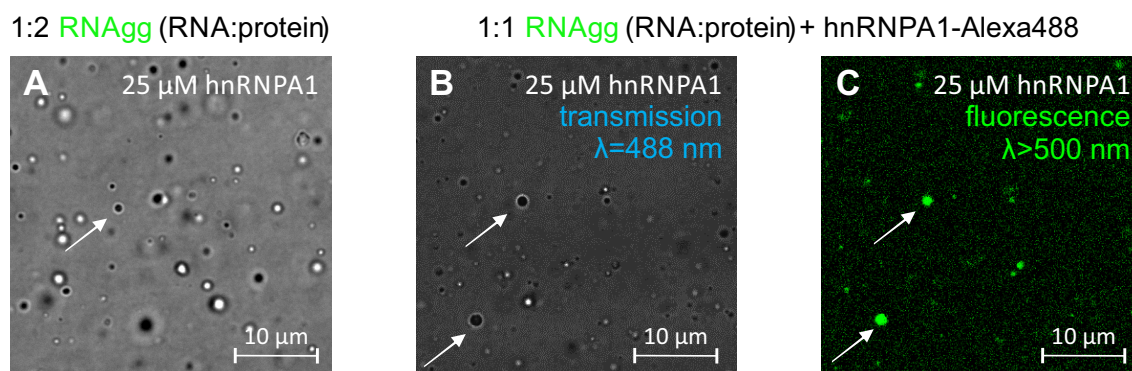


Figure 5.4: Confocal images of 25 μM hnRNPA1 solutions (with 5 mM DTT) stabilised with 0.2% agarose (A)+12.5 μM RNAgg (B,C) +25 μM RNAgg, and wild-type hnRNPA1 doped with ~ 0.5 μM maleimido-Alexa-488 labelled (unspecific) hnRNPA1 (B) imaged in transmission mode with a low-pass filter cutoff of 490 nm; (C) same imaging site in reflection mode imaged with high-pass filter cutoff of 500 nm; the arrows indicate droplets that are in the focal plane.

Fluorescence doping To estimate the distribution of RNA and protein between the LD phase and the surrounding buffer phase, we performed fluorescence doping experiments (see Figure 5.4). For this we admixed $\sim 0.2\%$ hnRNPA1 that was unspecifically labelled at surface exposed amino groups with maleimido-Alexa-488. The experiments were performed at 25 μM protein concentration at 1:2, or 1:1 RNAgg to protein molar ratios. In both situation we observed the formation of many, small (some even smaller than 1 μm) LDs. In transmission mode at the excitation laser wavelength we observed the droplets as dark spots when they are exactly in focus. The dark spots are typically enclosed by a bright zone. Droplets that are slightly out of focus are typically observed as bright spots surrounded by a dark circle. Note that this was also observed for the small droplets formed by hnRNPA1 in the absence of RNA. In fluorescent mode we observed that LDs that are in focus are uniformly fluorescent in the interior of the LD at the available resolution. Assuming that fluorescence quenching effects are not dominating, we can conclude that fluorescently labelled hnRNPA1 is enriched in the interior of the LDs, as was expected.^[218]

5.2.2 DEER with singly spin-labelled hnRNPA1

To complement the macroscopic sample characterisation by EMSA and imaging, we performed DEER experiments with MTSL-labelled single Cys mutants of hnRNPA1, which we already characterised in the dispersed state in Chapter 3. For the first series of DEER experiments we directly used spin-labelled solutions of hnRNPA1-S231R1 (MTSL labelled) without spin dilution. The results are shown in Figure 5.5, and summarised in Table 5.1.

As a reference state for dispersed, predominantly monomeric protein we used the conditions established for free hnRNPA1 in Chapter 3, which is ~ 25 μM protein concentration in dispersion buffer with 50% (v:v) d_8 -glycerol. In these conditions the background decay is slow. We observe a weak intensity of short distance contributions after background correction (centred around 2-3 nm)

when performing a single Gaussian fit, but the fit quality is not very good due to the low SNR in this particular measurement. Note that the low SNR is due to sensitivity issues in that particular measurement session, and fully equivalent measurements at the same experimental conditions with better SNR can be for example found in Figure 3.5 in Chapter 3. Addition of RNAgg in a 1:1 molar ratio after thawing and refreezing of this exact sample resulted in a similarly slow background decay, but a significantly higher modulation depth. The increased modulation depth suggests that the formation of small aggregates (dimer, or small oligomers) is increased in the presence of RNAgg. However, the observation that the background decay remains slow suggests that there is no formation of extended domains with strong protein-protein interactions (like in LDs) upon interaction with RNAgg, because this would lead to higher local densities (and thus a steep background decay). In this case, the SNR and modulation depth are good enough that distance analysis can in principle be performed (see Figure 5.5(A)), but note that the fit quality of the form factor fit in the sample with RNAgg with a single Gaussian fit is not very good, so it is most likely an over-simplified model.

We also performed DEER experiments with agarose stabilisation (0.2 % low melting agarose) instead of glycerol (Figure 5.5(B-D)), which matches the conditions for the confocal images shown in Figure 5.4. Even in the measurement with 2:1 hnRNPA1 excess over RNAgg we observe a very steep background decay. The short distance range contribution is also observed. It is weaker at higher RNAgg ratios. Note that the very poor signal-to-noise ratio (SNR) for the long trace in Figure 5.5(C) is due to very fast transverse spin relaxation in this sample, but unfortunately we also had a lower DEER echo intensity due to a small loss of sample volume during transfer to the quartz capillary. In Table 5.1 we also list results for a DEER measurement with an excess of RNAgg over hnRNPA1 (1:2, protein to RNA), but no detailed analysis of these data is shown, because the DEER echo intensity was very low in this sample, and the longest possible trace we could measure was only 1.5 μs (which still lead to a very low SNR). In this sample we can exclude loss of sample as an explanation for the very low DEER echo intensity, and it thus further confirms that the fast transverse relaxation is related to the presence of RNA, as we already saw in the sample with the 1:1 molar ratio.

When incubating with a 1:1 molar ratio of RNAaa, the effect on the transverse relaxation time is weaker, which allows measurement with a better SNR than in the sample with 1:1 molar ratio of RNAgg. The background decay is slightly slower than with RNAgg.

In the first series of experiments with undiluted spin-labelled hnRNPA1-S231R1 we found that even at low protein concentrations the transverse relaxation of the detected spins was very fast for the samples with RNA, and only very short dipolar traces could be measured. One possible explanation for the fast transverse relaxation is the effect of the high local spin concentration in the LLPS state. We should be able to remedy this partially by using only very small amounts of spin labelled protein in a large bath of wild-type protein (spin doping). First attempts with a single Cys mutant (S231C), and a double Cys mutant of hnRNPA1 (S182C/S223C) were done with a 1:20 spin labelled to unlabelled ratio. The results are shown in the Appendix C, but will not be interpreted in detail, because of concerns about partial spin label detachment during the sample preparation, as was discussed already in Chapter 3.

| hnRNPA1-S231R1 [μM] | RNA [μM] | conditions | t_2 [μs] | BG dens. | Δ | $\langle N_{\text{spin}} \rangle$ | $\langle R \rangle$ [nm] | σ_R [nm] |
|-------------------------------------|--------------------------|--|----------------------------|----------|----------|-----------------------------------|-----------------------------|--------------------|
| 25 | 0 | d ₈ -glycerol | 3.5 | 0.022 | 0.007 | 1.02 | 2.833 | 0.9775 |
| 25 | 25 | RNA _{agg} + d ₈ -glycerol | 3.5 | 0.025 | 0.019 | 1.03 | 3.07 | 1.273 |
| 25 | 13 | RNA _{agg} | 3.5 | 0.548 | 0.025 | 1.73 | 2.608 | 1.724 |
| 25 | 25 | RNA _{agg} | 2 | 0.373 | 0.010 | 1.59 | 2.334 | 0.02 |
| 25 | 25 | RNA _{agg} | 3.5 | 0.369 | 0.037 | 1.16 | - | - |
| 25 | 50 | RNA _{agg} | 1.5 | 0.278 | 0.002 | 1.05 | - | - |
| 25 | 25 | RNA _{aa} | 3.5 | 0.493 | 0.016 | 1.04 | 1 | 1.885 |

Table 5.1: Measurement conditions and fit parameters from single-Cys DEER (S231R1) experiments with no spin dilution shown in Figure 5.5; Δ is the modulation depth, $\langle N_{\text{spin}} \rangle$ is the average number of spins per EPR active cluster reported by DeerAnalysis, $\langle R \rangle$ and σ_R are the mean value, resp. width of the fitted single Gaussian distance distribution, t_2 is the second refocusing delay in 4p-DEER;

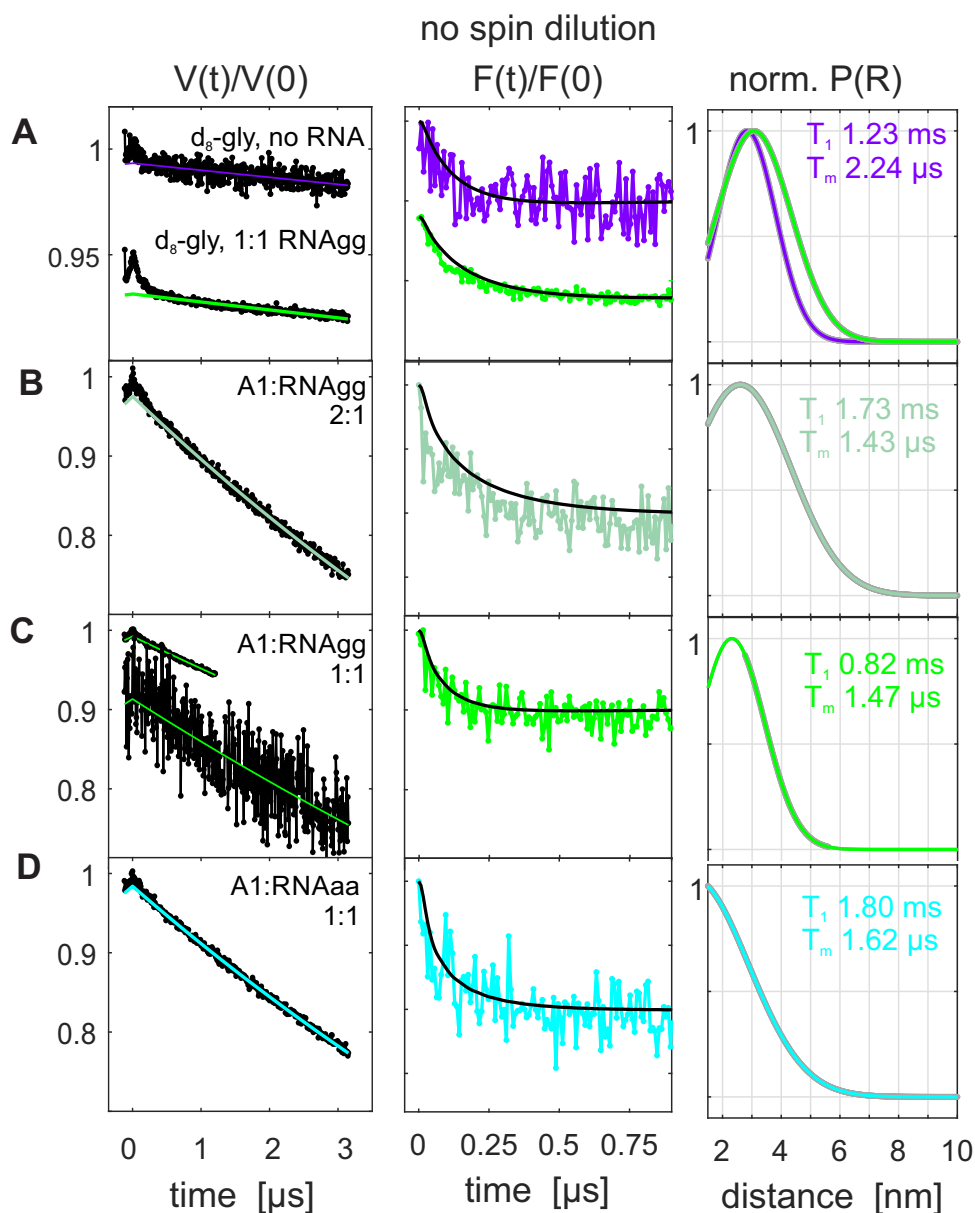


Figure 5.5: Singly spin labelled hnRNPA1 (S231R1) in RNA-induced LLPS; left to right: primary DEER data $V(t)/V(0)$, form factors after 3-dimensional background correction $F(t)/F(0)$, and normalised Gaussian distance distributions $P(R)/P_{\max}$ fitted to the form factor contribution; in the distance panel we also give the independently determined relaxation properties. (A) Samples with 50% (v:v) d_8 -glycerol in buffer; sample measured directly at 15 μ M hnRNPA1-S231R1 (purple), and same sample tube after addition of 1:1 (molar) RNAg (green); (B-D) samples without glycerol, but stabilised by 0.1% (w:v) agarose; (B) 15 μ M hnRNPA1-S231R1 with 2:1 (molar) RNAg (C) 15 μ M hnRNPA1-S231R1 with 1:1 (molar) RNAg; two DEER trace lengths were acquired (reduced SNR both from shorter T_m , and from small sample loss during transfer to capillary). (D) 15 μ M hnRNPA1-S231R1 with 1:1 (molar) RNAaa;

5.3 Conclusions and discussion

In this chapter we presented results obtained with a combination of EMSA, confocal imaging and singly spin labelled hnRNPA1 to unravel molecular interactions in oligonucleotide induced LLPS of hnRNPA1 in the presence of short ssRNAs. The addition of even sub-stoichiometric amounts of any one of the four short RNAs used in this work lead to increased LLPS at a large range of hnRNPA1 concentrations (20-100 μM). This was observed in buffer conditions where free hnRNPA1 was shown to be predominantly monomeric (dispersion buffer). At higher RNA we observed larger droplets and no more migration in the gels in EMSA experiments. This was found to be temperature dependent, and short incubation at elevated temperature lead to reduced migration in EMSA experiments.

We saw that with characterisation at the macroscopic level by confocal microscopy imaging we could clearly identify the sample state (LLPS vs. dispersed). Fast formation of very large LDs was observed upon addition of RNA to 100 μM hnRNPA1, and we saw no differences in the morphology of the LDs between the RNA with and without optimal binding sites (RNA_{agg} vs RNA_{aaa}). At low hnRNPA1 concentrations (25 μM), we observed LLPS upon addition of RNA_{agg} and RNA_{aaa} as well, but the observed droplets were significantly smaller. Most likely this is because the LD size distribution that we observed in the images is governed by droplet diffusion kinetics in the agarose stabilised conditions. Since the imaging experiments were performed in the presence of 0.2% agarose, macroscopic diffusion is strongly inhibited after the agarose gel has set. This was confirmed by imaging the same droplets for several hours, without observing noticeable diffusion. We currently have no accurate values of the cooling and setting rates, but due to the small sample volumes we observed set gels on the scale of a few tens of seconds. Most likely the the formation of large LDs (>10 μm) is dominated by droplet fusion rather than growth from the buffer reservoir of protein. Thus after the initiation of LLPS (e.g. by the mixing with RNA), the growth of large LDs is truncated as soon as the agarose buffer has set. It seems that at higher protein concentrations the initial fusion rate is faster, which is plausible because the average distance between molecules and small droplets that need to diffuse in order to fuse is also expected to be shorter.

Fluorescently labelled hnRNPA1 was enriched inside the LDs compared to the surrounding buffer. DEER experiments with singly spin-labelled hnRNPA1 (MTSL labelled in the IDD at site 231) in dispersion buffer with glycerol as cryo-protectant confirmed that the presence of RNA_{agg} increased the amount of protein-protein contacts. However, the presence of glycerol seemed to prevent LD formation, because we observed a slow DEER background decay also in the sample with added RNA_{agg}, which implies that the local spin concentration was low. A corresponding confocal microscopy imaging series with the addition of RNA in the presence of glycerol is planned to confirm this hypothesis. High local spin concentrations were observed upon RNA_{agg} and RNA_{aaa}-induced LLPS without glycerol. This is in agreement with the formation of the many, but small LDs observed in imaging. Minor differences were observed in the DEER traces between addition of RNA_{agg} versus RNA_{aaa}. The latter seemed to have a weaker effect on hnRNPA1 (less steep background decay) at equivalent molar ratios.

The major challenges that need to be addressed in future DEER experiments are sample homogeneity (e.g. quantification of the effect of freezing conditions and cryo-protectant), and methods

to deal with the fast transverse relaxation in the LLPS samples, which prevents acquisition of long dipolar evolution times. In the latter direction we performed a first series of tests where we added a small amount of spin labelled (single-Cys) hnRNPA1 into wild-type hnRNPA1. In this series we can currently only interpret local spin label distributions, because potential partial spin label cleavage from the labelling site may have occurred. The differences between the sample conditions are mostly found in the fitted longitudinal relaxation rate of the spins, which was fast in all samples except for the samples with RNAgg. In the future it may be necessary to explicitly account for relaxation filtering effects due to different relaxation rates of proteins in the LD state and residual dispersed protein. Some differences in the background decay of the DEER experiments were observed with different RNAgg concentrations, and with RNAaa.

In summary, our results show that the combination of confocal imaging and dipolar spectroscopy with spin labelled samples is a powerful approach to quantify and structurally characterise biomolecular interaction in RNA-induced LLPS.

5.4 Materials and Methods

Protein purification and spin labelling For protein purification and spin labelling with MTSL we refer to the Methods section in Chapter 3, since the same protein preparations were used in this study.

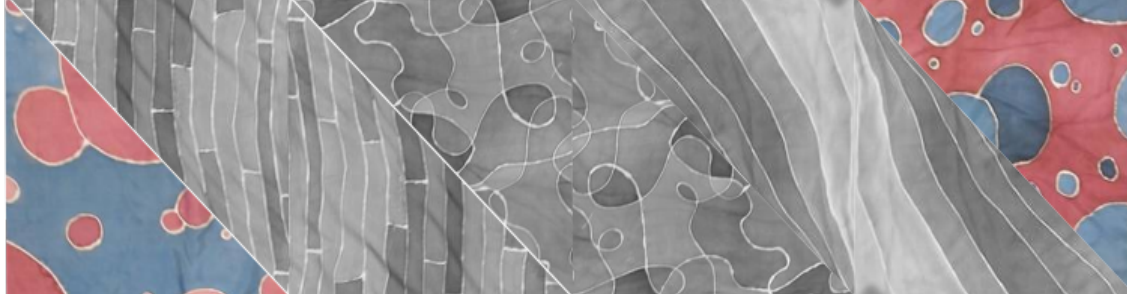
Oligonucleotides The ssRNA sequences that were studied by Beusch et al.^[26] are shown in Figure 5.2. The oligonucleotides were purchased from Dharmacon, USA, and were supplied as lyophilised aliquots with 2'-protection. The 2'-deprotection was performed according to the producers manual. After the final lyophilisation step the oligonucleotides were dissolved (1 mM) in double distilled H₂O, and stored at -20 °C until usage.

LLPS sample preparation An appropriate amount of wild-type hnRNPA1 in dispersion buffer was present in a Eppendorf reaction tube (dispersion buffer: 50 mM sodium phosphate, pH 6.5, 100 mM L-arginine, 100 mM L-glutamate; in the following amino acids in the buffer are shortened to 'R/E'). The protein stocks were thawed from -80 °C, and pelleted for 10 min at 20'000 rcf (20 °C) to remove any potential aggregates. For the spin dilution experiments the spin labelled hnRNPA1 mutant in dispersion buffer was mixed with the wild-type protein. The mixture of wild-type and spin labelled protein was incubated at ambient temperature for 2 min to allow for mixing. RNA free-samples were made by directly mixing with deuterated buffer (dispersion buffer, or other, depending on desired phase separation state, supplemented with 0.2 % low melting agarose, heated to 40 °C). Due to the small sample volumes we expect the final solution after mixing with the ambient temperature buffer to cool quickly, and indeed we observed a stable gel within a few seconds after mixing. RNA-protein mixtures were made by diluting the RNA first in deuterated buffer (supplemented with 0.2 % low melting agarose (w:v), heated to 40 °C) to the desired concentration, and the mixing with the present hnRNPA1 by gentle pipeting. In some DEER samples (see main text) we did not use agarose stabilisation. In these samples we added 50 % (v:v) d₈-glycerol directly to the protein solution after dilution with the buffer.

Imaging Unless stated otherwise, imaging was performed at the ScopEM facility with a Leica SP8 STED super-resolution inverted confocal microscope (water-immersion objective). 15 μ sample were prepared for each condition (always with 0.2 % (w:v) low melting agarose) and loaded onto an uncoated ibidi μ -well (ibidi) plate slot. Imaging was performed at ambient temperature, in transmission mode or reflection mode. For the fluorescence doping experiments we incubated hnRNPA1 with ~ 5 x molar excess of maleimido-Alexa-488 (Thermo Fisher) in 50 mM Tris, pH 8.0, 1 M NaCl. After incubation at ambient temperature in the dark for two hours the remaining unbound dye was washed out with a gravity flow desalting column (Thermo Scientific TM Zeba Spin 7KDa MWCO). The labelled protein was flash frozen in aliquots and stored at -80°C . The thawed aliquots were pelleted at 20'000 rcf (20°C) prior to each use, to remove aggregated material that was sometimes encountered after thawing.

DEER measurements Samples for DEER were loaded into 3 mm (outer diameter) quartz capillaries (New Era), and flash frozen by contacting with liquid-nitrogen pre-cooled iso-pentane. Samples were stored in liquid nitrogen until measurement. DEER measurements were performed at a home-built high-power Q-band spectrometer (≈ 34 GHz) controlled by a Bruker Eleksys E580 bridge in a home-built TE001-type resonator for over-sized (3 mm) sample tubes.^[238] All pulse lengths were set to 16 ns. A frequency separation of 100 MHz was used in the DEER experiments. The first refocusing delay was $\tau_1 = 400$ ns in all measurements, the second refocusing delay was set to a value where the echo intensity was approximately 10 % of the initial intensity. The choice of shot repetition time (*srt*) was based on monitoring echo attenuation of a standing DEER echo. For faster averaging, we accepted *srts* that slightly suppressed the echo at full recovery (by less than 10 %). The *srt* values of either 2 ms or 4 ms were used. Relaxation measurements were performed (see Appendix C) with 16 ns $\pi/2$, and 32 ns π pulse lengths. Transverse relaxation was quantified with the Hahn echo decay experiment, and longitudinal relaxation with the inversion recovery experiment (see Chapter 2). Unless stated otherwise, data were acquired at the maximum of the nitroxide Q-band spectrum. The data were phase-corrected to minimise the absolute value of the imaginary part, and the constant offset was subtracted for plotting. Data fitting was performed with a single exponential, a bi-exponential, and a stretched exponential model, and the results are reported in Appendix C.

EMSA shifts Oligonucleotide binding was studied with wild-type hnRNPA1 and UP1 using electromobility shift assays (EMSA). No agarose was used in the buffer. We used 10 % acrylamide (29:1, mono:bis-acrylamide) separation gels with 0.5x TBE buffer at pH 7.5, and 120 V input voltage for 20 min in each case. 5 μ l sample were loaded per well (BioRad electrophoresis system). Staining was performed with a toluidine solution in water (oligonucleotide stain) and washing with deionised water.



Chapter 6

Using spectroscopically orthogonal spin labels to study biomolecular interactions

As we have discussed in the previous chapters, EPR, and in particular pulsed dipolar spectroscopy can contribute to the characterisation of the distribution of molecular conformations, which is particularly valuable in (partially) disordered biomolecules. But we have also showed situations where the interpretation of PDS experiments becomes increasingly complex, because intermolecular interactions are frequent, and contribute with distances that are in the same range as the intramolecular spin label distances. This situation may for example be encountered in high-density protein condensates (compare Figure 1.1 in Chapter 1). In this chapter we describe how EPR with spectroscopically orthogonal spin labels can be exploited for monitoring biomolecular interaction in complex, and (strongly) interacting systems. Spin labels are considered spectroscopically ‘orthogonal’ if the intrinsic spectral differences between the paramagnetic centres can be exploited for selective excitation.^[96,313]

Scope of this chapter The content of this chapter is based on the publication Ritsch et al.^[251], which is here shortened and edited for consistency. We introduce additional considerations for performing PDS with spectroscopically orthogonal spin labels and illustrate the spectroscopic difference between selected common EPR spin label types. As an example we show results obtained in a rigid and stable protein complex with a nitroxide and a Gd(III)-based spin label. The materials and methods can be found at the end of the chapter. The section in the publication^[251] on the RIDME optimisation with Cu(II)-nitroxide molecular rulers is omitted here, as it will be treated in a separate, detailed chapter (Chapter 7).

Author contributions and acknowledgements We thank Anahit Torosyan (ETH Zurich) for help in the preparation of the Rpo4 mutant, Mian Qi (Bielefeld University) for the preparation of the [metal ion-PyMTA] complexes, and Dina Grohmann (University of Regensburg, Germany) for the Rpo4 and Rpo7 plasmids. Daniel Klose is thanked for the protocol for the purification of Rpo4/7. Elisabeth Lehmann is thanked for providing the short RNA.

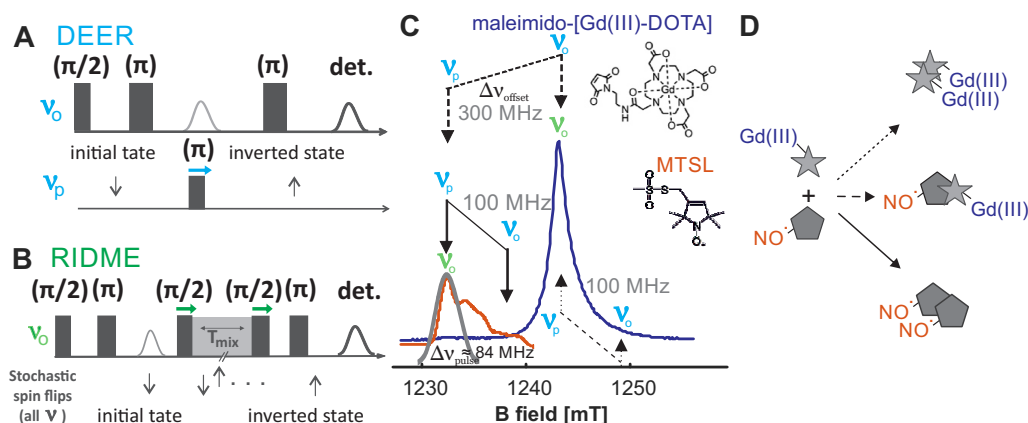


Figure 6.1: (A) Pulse sequence for 4-pulse DEER, and (B) for RIDME; DEER is a two-frequency experiment (blue ν_o and ν_p), the RIDME experiment uses pulses at only one frequency (green ν_o) (C) Echo-detected EPR (EDEPR) spectra of MTSL (orange) and maleimido-[Gd(III)-DOTA] (dark blue) at Q-band, and approximate excitation band of a rectangular pulse (grey). Typical pump (blue ν_p) and observation (blue ν_o resp. blue ν_o) positions for DEER and RIDME are indicated. The three shown DEER setups are optimised to detect nitroxide-nitroxide (solid arrows), nitroxide-Gd(III) (dashed arrows), resp. Gd(III)-Gd(III) (dotted arrows) dipolar couplings. (D) In a sample where two potentially interacting components are labelled with spectroscopically orthogonal spin labels we can distinguish different interaction combinations by performing selective PDS experiments (compare solid/dashed/dotted arrows in Panel (C)).

6.1 Introduction

One of the strengths of pulsed dipolar spectroscopy (PDS) is that distances can be determined in biomolecules that are labelled with the same type of spin label at two sites. However, identical labels can also be of disadvantage, if the biomolecules are aggregation prone or self-interact. Whenever many spin-labelled molecules are in close proximity (within the sensitive range of dipolar spectroscopy of ~ 1.5 -10 nm), short-range intermolecular distance distribution peaks appear, which cannot be distinguished directly from intramolecular distance peaks. This means that control experiments using singly-labelled proteins, and/or spin dilution experiments are required to disentangle the underlying intra-molecular distance distributions. The required degree of spin dilution has to be determined case by case. For strongly interacting or aggregating biomolecules it may be necessary to use very low ratios of labelled to unlabelled biomolecules, which reduces sensitivity. An elegant alternative possibility to monitor the aggregation state is to use spectroscopically orthogonal spin labels. These are either attached at different sites of one single biomolecule, or, if the study involves more than one type of biomolecule in a complex, each type of biomolecule is labelled with a specific spin label spectroscopically distinguishable from the other spin labels. In either case we can determine the aggregation state of the sample by performing a PDS experiment which will reveal a distance distribution if the biomolecules interact with each other, as is illustrated in Figure 6.1.^[195,313] In such experiments we not only see if there are intermolecular interactions

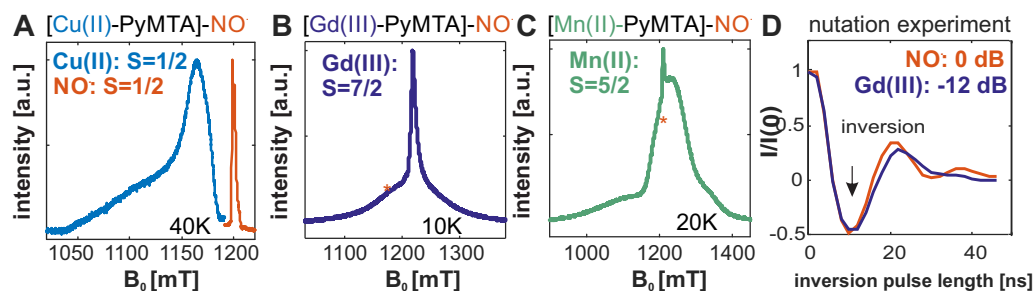


Figure 6.2: EDEPR spectra of frozen samples of paramagnetic centres; (A) the spectra of [Cu(II)-PyMTA] (dark blue) and nitroxide (orange) are spectrally separated. (B) The spectra of [Gd(III)-PyMTA] (blue) and nitroxide (expected at the position of the orange star) would overlap, but the nitroxide is suppressed with the chosen pulse settings (shot repetition rate: 100 μ s, pulse power optimised for Gd(III)). (C) Suppression of the nitroxide can also be achieved with respect to [Mn(II)-PyMTA] (green), but a weak residual intensity in the Mn(II) spectrum is still observed (indicated by orange star). (D) Nutation profiles measured on the maxima of Gd(III) (dark blue, measured with a pulse attenuation of 12 dB), and nitroxide (orange, 0 dB). A very similar nutation profile for Gd(III) (high spin) and nitroxide (low-spin) is observed because the pulse power for the Gd(III) measurement was reduced by a factor of four w.r.t. the nitroxide measurement.

present at all, but we also get distance information associated with the interaction. SDSL with orthogonal spin labels is very powerful, when two components (e.g components X and Y) of a complex interact with each other, but also interact with themselves. PDS with only one type of spin label could not distinguish the two situations, but if the components are labelled with spectroscopically orthogonal spin labels we can differentiate all three possible combinations, X-X, X-Y, Y-Y, in a sample. Clearly, selective excitation of the two species must be sufficiently good to have this benefit. The appropriate choice of spin label combination, however, mostly depends on the biological question at hand. Some metal ion complexes, for example Gd(III) complexes or trityls, are more stable than common nitroxide-based spin labels in reducing environments, which are encountered for example in the cellular cytoplasm in cell experiments.^[16,51,119,202,243,308] Active research is going on to develop more stable nitroxides for such applications.^[113,131,155,167,233,301] Other considerations are hydrophobicity, charge state or bulkiness of the spin label, all of which can disrupt protein folds, or inhibit interactions if chosen unsuitably.

6.1.1 Selective excitation

To illustrate selective excitation, which is the prerequisite for spins to be considered spectroscopically orthogonal, we show the EPR spectra of four different EPR-active species (a nitroxide, resp. Cu(II)-, Gd(III)-, or Mn(II)-based metal ion complexes) in Figure 6.2. As can be seen, the spectral shape and width of the EPR spectra are very diverse. In a biomolecule or biomolecular complex with a set of different spin labels attached at different sites, we can selectively excite the two types of electron spins by choosing the appropriate resonance frequency and microwave pulse power, or by their relaxation properties.^[96,306,313] Not surprisingly, very good spectroscopic selection can be

achieved if the EPR spectra of the two spin labels do not overlap. However, even if there is partial overlap we observe in general that the longitudinal relaxation of metal ion complexes is much faster than that of organic radicals at any given temperature. This can be exploited to achieve suppression of the signal from a simultaneously present organic radical (such as a nitroxide) by choosing very fast experiment repetition rates. The slowly relaxing spins are then saturated and thus only weakly observed (compare Figure 6.2). Such intentional saturation of spin transitions, as well as other spectroscopic filtering methods based on differences in longitudinal relaxation can be used in combination with many pulsed EPR experiments.^[195,199,313] Transverse relaxation properties between paramagnetic species differ as well, but the differences are typically much smaller than for longitudinal relaxation. Paramagnetic species can also be separated by the total spin quantum number S . Spin transitions of high-spin paramagnetic centres ($S > 1/2$) are characterised by a larger transition moment and thus require less microwave power to be excited, as compared to the case of low-spin paramagnetic centres. The optimal power for inversion can be, for example, determined by a nutation experiment, in which the duration of an inversion pulse is incremented at fixed microwave pulse power. Such pulse optimisations are useful when selectively exciting high-spin metal ion-based spin labels (often Gd(III) or Mn(II)) in the presence of nitroxides.^[306]

6.1.2 Spectroscopically orthogonal spin labels in PDS

Over the last decade there were many important advances in the development of PDS experiments with pairs of spectroscopically orthogonal spin labels. In the following we discuss additional consideration when using the DEER or the RIDME PDS method with spectroscopically orthogonal labels. For a general introduction to dipolar coupling and PDS methods please see Chapter 2.

In DEER, we need to place pulses at two different frequencies (pump ν_p and detection ν_d frequencies) within the combined EPR spectra of the two spin labels. The method works best when the pump and detection bandwidths together cover a substantial fraction of the EPR spectra. However, overlap of the microwave pulse bandwidths must be avoided because it leads to signal reduction and may introduce artefacts.^[47,253,282,285] This excitation band separation may be more easily achieved, if the two EPR spectra of the pumped and the detected spin do not overlap. Experimental complications for the DEER experiment appear, however, when the frequency gap between the EPR spectra of the spins becomes too large. The limiting factors are excitation and detection bandwidths. As a guideline, with the newest broadband spectrometers, equipped with arbitrary waveform generators (AWGs)^[75,277], a pulse bandwidth of about 1.5 GHz can be achieved,^[73] which is more than ten times larger than the bandwidth of rectangular microwave pulses in the previous generation of spectrometers (~ 100 MHz). The latter is easily sufficient for nitroxide-nitroxide distance measurements, but it is too narrow-banded for efficient excitation of spin labels based on metal ion centres, which have significantly broader EPR spectra.

Metal ion – nitroxide spin pairs were among the first investigated combinations.^[226] For DEER experiments on such systems it is suggested to pump the nitroxide spin and to detect the metal ion spin. This is favourable in most situations in terms of longitudinal relaxation properties and maximises the fraction of inverted spins. Broad-band excitation schemes can strongly increase the sensitivity.^[77,78] Gd(III)-nitroxide DEER was early recognised as a suitable technique for spectro-

scopic selection (compare Figure 6.1).^[151,193,314] The pulse setup optimisation takes into account that unwanted excitation of the detected metal ion spins by the pump pulse on the nitroxide can lead to partial suppression of the detected echo.^[96,97,314] Also Cu(II)-Cu(II)^[292] and Cu(II)-nitroxide^[226] DEER were developed. For the former a systematic comparison between the sensitivity of ultra-wideband (UWB) DEER and RIDME was recently reported.^[48] It was found that ‘orientation selection’ can interfere with data interpretation when using stiff molecular rulers. This arises because the kernel-based data analysis usually assumes a random distribution of spin-pair orientations contributing to the data (Pake powder averaging over the dipolar angle θ), and we observe artefacts if this is not fulfilled due to experimental reasons.^[22,32,33,226,292,309] Several studies were dedicated to compensating for this effect.^[44,103,208] Considerable effort was also invested in the enhancement of detection sensitivity for metal ion-based spin labels. This includes a spin pre-polarization technique for PDS experiments with detection on high-spin metal ions.^[77]

The RIDME experiment exploits a different principle for achieving inversion of the B spin, which is particularly promising for the combination of organic radicals with paramagnetic metal ion centres. The non-equilibrium magnetization of the A spins is stored along the direction of the static magnetic field for a fixed part of the pulse sequence. During this period, the B spins flip stochastically with a certain probability, depending on their longitudinal relaxation time. RIDME requires pulses at only one microwave frequency, and B spin inversion is thus not limited by the bandwidth of an additional pump pulse. The possibility to use the RIDME technique for detecting distance distributions between high-spin metal centres was demonstrated on molecular rulers.^[161–163] In RIDME with high-spin centres, higher orders of spin inversion (with an effective total change of magnetic quantum number $\Delta m_S > 1$) can occur. Such dipolar evolution data can still be analysed in terms of distance distribution by applying a slight modification to the kernel function, as was demonstrated with a calibration for Gd(III) and Mn(II)-based spin labels.^[161,162] RIDME measurements on metal ion-nitroxide spin pairs were reported, where, in contrast to DEER spectroscopy, the optimal detection position is on the nitroxide spin.^[3,15,32,33,208,250] This is dictated by the relaxation properties of metal ion and nitroxide spins, but typically also favourable in terms of transverse relaxation and reduced orientation selection.

6.2 The Rpo4-Rpo7 complex as a model system

In this section, we demonstrate the application of PDS with spectroscopically orthogonal nitroxide and Gd(III)-based spin labels, to identify intra-subunit and inter-subunit distance distributions in a protein complex. We use the complex between subunits Rpo4 and Rpo7 (formerly known as subunits F and E) of the archaeal RNA polymerase of *E. jannaschii* as a model system, which is well characterised by other structural and biochemical methods.^[13,109,118,204] The complex was found to be stable and fairly rigid.^[168] Previous studies on this model system include an early contribution to the *in silico* modelling of DEER and fluorescence data,^[168] and the first experimental demonstration of a PDS correlation experiment between three nitroxide spins in terms of a distance correlation map using the Triple Electron Resonance (TRIER) experiment.^[240,241] Our labelling strategy for this study is shown in Figure 6.3. Both cysteine mutated subunits were spin labelled individually

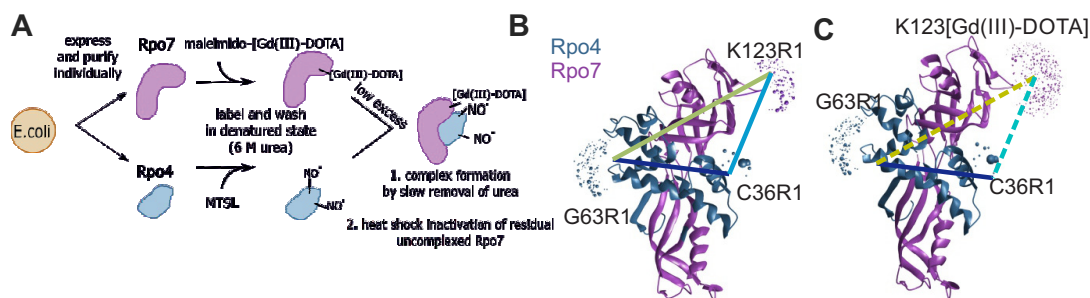


Figure 6.3: (A) Scheme for SDSL sample preparation of the Rpo4/7 complex. The subunits can be conveniently labelled individually with spectroscopically orthogonal spin labels prior to complex formation. (B) Visualisation of rotamers probability distribution ‘clouds’ generated with MMM^[237] of MTSL simulated at 298 K attached to residues 36 and 63 in Rpo4 (purple), resp. residue 123 in Rpo7 (blue) in the Rpo4/7 complex (pdb: 1G03^[118]).

in the fully denatured state (in buffer with 6 M urea), which alleviated any accessibility issues, and typically resulted in very high labelling efficiencies. Complex formation was achieved by a refolding step. In Figure 6.3 we show the X-ray crystallographic structure^[204] of the Rpo4/7 complex that was *in silico* modified to carry spin labels (e.g. MTSL-labelled (=R1) at positions Rpo7: K123R1, and Rpo4: C36R1, G63R1). The probability distribution of the location of the electron spin relative to the protein backbone is calculated using a rotamer library approach and visualised as coloured clouds.^[237] The corresponding three possible simulated spin-spin distance distributions (Rpo7: K123R1 || Rpo4: C36R1, Rpo7: K123R1 || Rpo4: G63R1, and Rpo4: C36R1 || Rpo4: G63R1) are well-separated (see Figure 6.4), and spread over a large range of distances (2 nm – 6 nm). The nitroxide-nitroxide DEER experiment on the protein complex labelled with MTSL at all three sites, was performed on a frozen sample measured at a temperature of 50 K at Q-band frequencies (34 GHz) (see Figure 6.4). The distance analysis reveals three resolved distance peaks. From this experiment alone, however, it is impossible to tell which of the three peaks corresponds to the Rpo4-internal distance (Rpo4: C36R1-G63R1) and which peaks correspond to the inter-subunit distances (Rpo4:C36R1, resp. G63R1 || Rpo7:K123R1). Because we are dealing with a three-spin system, and because the intramolecular dipolar evolution signal in DEER is a product of contributions from all possible pair-wise spin combinations, additional sum and difference frequency terms of the dipolar coupling frequencies appear.^[111,145] These terms lead to so-called ‘ghost peaks’ in the distance distribution. Computational data analysis approaches to reduce the intensities of such ghost peaks have been introduced.^[111] Experimentally, we can suppress the sum and difference terms because they depend quadratically on the pump pulse inversion efficiency.^[111,145] Accordingly, by using an attenuated pump pulse we suppress multi-spin effects and the shortest and the longest distance peaks observed in the triple MTSL-labelled sample are shifted to longer mean distances. The relative intensities of the two components in the central distance peak are also affected. Unfortunately, this also leads to a substantial reduction of the modulation depth and hence of the signal-to-noise ratio. One could also reduce multi-spin effects by ‘spin dilution’, which could simultaneously help to resolve the peak assignment issue, again at the cost of signal-to-noise

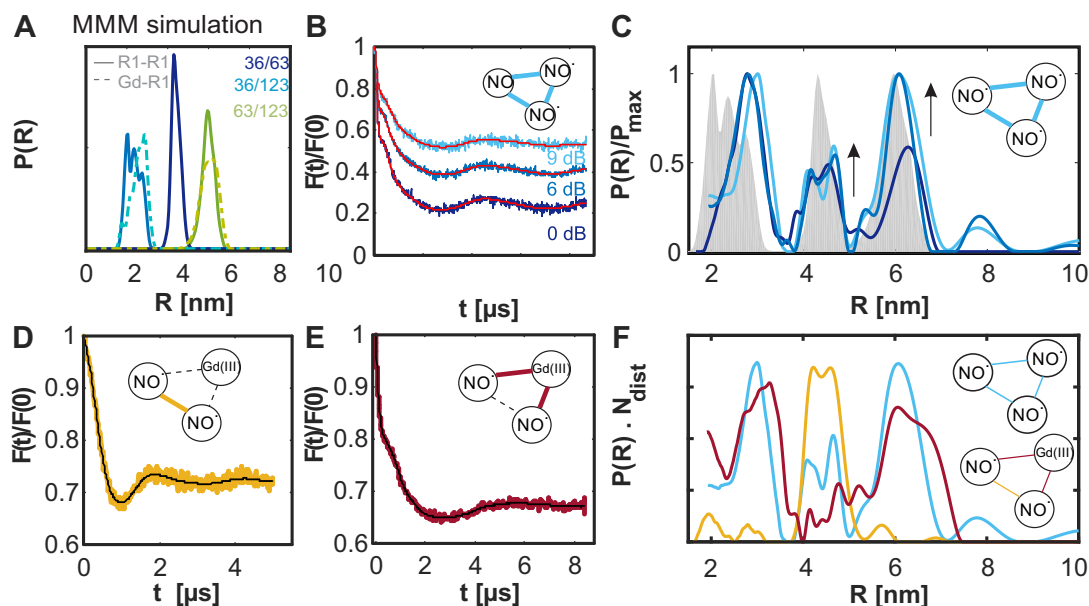


Figure 6.4: (A) Simulated distance distributions between the chosen labelling sites (R1=labelled with MTSL, Gd=labelled with maleimido-[Gd(III)-DOTA]). (B) Experimental form factors $F(t)/F(0)$ and fits (red) obtained with nitroxide-nitroxide DEER with full inversion pulse power (dark blue) and attenuated inversion pulse powers (middle and light blue, relative attenuation of inversion pulses in dB) measured on the triple MTSL-labelled complex of Rpo4 (36R1, 63R1) /Rpo7 (K123R1); (C) Fitted distance distributions and expectation from simulation (grey area) obtained from the nitroxide-nitroxide DEER in panel (B). (D) $F(t)/F(0)$ (yellow) and fit (black) from nitroxide-nitroxide DEER in the triple labelled protein complex with spectroscopically orthogonal spin labels (Rpo4 (36R1, 63R1) /Rpo7 (K123[Gd(III)-DOTA])). (E) $F(t)/F(0)$ (red) and fit (black) from nitroxide-Gd(III) DEER obtained with the same sample; (F) distance distributions obtained with the spectroscopically orthogonal spin-label protein complex (yellow: nitroxide-nitroxide, red: nitroxide-Gd(III)); the distance distribution from the sample labelled only with MTSL is overlaid (blue).

ratio.^[5] Exchanging one of the nitroxides for a Gd(III)-based spin label, which is spectroscopically orthogonal as discussed above, can solve this problem in an elegant and reliable way, as has already been demonstrated in earlier works.^[105,106,149,193] Here, the subunit Rpo4 with two labelling sites (C36, G63C) was labelled with MTSL and the subunit Rpo7 with one labelling site (K123C) was labelled with maleimido-[Gd(III)-DOTA]. The PDS data and distance distributions of this sample with mixed spin labels are shown in Figure 6.4. With the nitroxide-nitroxide DEER experiment we find only one peak, centred at $R_{\text{NO-NO}}=4.5$ nm which corresponds to the central peak in the distance distribution obtained with the triple MTSL-labelled sample. We have thus identified this peak as the intra-subunit distance within Rpo4. In an application study this distance could be used as a reporter distance that monitors whether the subunit undergoes some structural rearrangement upon complex formation or substrate binding (distance before complex formation not shown here).

The complementary DEER experiment to measure inter-subunit distances between nitroxide and Gd(III) was performed at 10 K (instead of 50 K for nitroxide-nitroxide DEER), with different pump and detection positions,^[49,131] illustrated in Figure 6.4. As expected, we find two peaks in the distance distribution, at $R_{\text{Gd(III)-NO,1}}=3.5$ nm and $R_{\text{Gd(III)-NO,2}}=6-7$ nm. The overlay of the distance distributions obtained with the two samples is shown as well. We clearly see that all three peaks found for the triple MTSL-labelled sample were also detected in the combined results from the samples with the combination of nitroxide and Gd(III)-based spin labels. We furthermore observe that the best agreement is found with the trace that was measured with the suppression of ghost peaks. For the nitroxide-nitroxide DEER, ghost peaks are absent because we only have two nitroxide moieties per protein complex. Contaminations due to Gd(III) excitation by detection and pump pulses are in principle possible, but they are very weak in nitroxide-nitroxide DEER due to (i) the fast relaxation of Gd(III) at 50 K, and (ii) the strong difference in the microwave power required for the excitation of nitroxides and Gd(III) centres. For the case of Gd(III)-nitroxide DEER there are still ghost peaks present because two different Gd(III)-nitroxide pairs contribute per protein complex. However, the number of combination frequencies is reduced, from six for the triple MTSL-labelled sample to two for Gd(III)-double MTSL-labelled sample. Furthermore, in the given experiment the two detected real distance peaks have very different mean distances, and thus a very strong difference in the corresponding dipolar frequencies. As a result, the two ghost peaks nearly coincide with the short distance peak (around 3 nm), which corresponds to about eight times larger dipolar frequency than the longer-distance peak (around 6 nm). Any type of selective Gd(III)-Gd(III) PDS experiment (e.g. Gd(III)-Gd(III) RIDME or DEER) would complete the set of available PDS measurements in the orthogonally spin labelled sample, and provide information on possible aggregation of Rpo4/7 complexes. In our example, we did not expect such aggregation and skipped this step. In the present case, we would expect to observe a smooth intermolecular decay in the Gd(III)-Gd(III) PDS experiment, where the decay rate depends on the volume concentration of protein dimers and on the particular settings of the PDS experiment.

6.3 Application to hnRNPA1

In Chapter 5 we showed experimental results obtained with the human splicing factor hnRNPA1 in combination with short single-stranded RNA molecules. Interaction with the RNA was found to induce enhanced protein-protein interactions, and in many conditions LLPS was observed. In the liquid droplets we found high local concentrations of spin label, and therefore with just one spin label type we are limited to collecting information from just one single spin labelling site per sample. Disentangling structural or interaction information from more than one spin label site would not be possible. We can, however, label two different batches of hnRNPA1 cysteine mutants independently, and use spectroscopically orthogonal spin labels. This was done with the spin label pair MTSL (at position 182), and maleimido-Gd(III)-DOTA (at position 231). The experimental design and the results are shown in Figure 6.5. After spin labelling we mixed the proteins with the two different spin labels at the two different sites (proteins were mixed to a final

concentration of 40 μM each, thus 80 μM total protein concentration). On these samples we can simultaneously monitor three different intermolecular distances: (i) the inter-RRM distances by the nitroxide-nitroxide DEER experiment between the MTSL-labelled sites 182, (ii) the IDD-IDD distance with Gd(III)-Gd(III) DEER between sites 231, and (iii) the IDD-RRM distances with the nitroxide-Gd(III) DEER experiment. We measured these three DEER experiments in conditions where the samples are dispersed at ambient temperature, to allow mixing of the components. We then induced LLPS by incubation at $+4^\circ\text{C}$, where the samples became turbid (LDs confirmed by imaging, but due to fast sample warming upon loading to the microscope only few droplets were imaged, see Figure 6.5), and froze the samples by contacting with liquid-nitrogen pre-cooled iso-pentane directly from the cold state ($+4^\circ\text{C}$). The orange DEER traces in Figure 6.5(C) were obtained in samples without RNA, for the purple traces we added a short ssRNA (1:1 molar ratio, for sequence see figure caption). Due to the much smaller ratio of the inversion pulse bandwidth and the spectral bandwidth of the pumped spin in the nitroxide-pumped experiments (NO-NO, and NO-Gd(III) DEER), compared to the Gd(III)-pumped experiment (Gd(III)-Gd(III) DEER), we expect a smaller inversion efficiency for the latter. Taking this into account we observed a comparatively steep DEER signal decay for the inter-RRM experiment (NO-NO), as well as the inter-IDD experiment (Gd(III)-Gd(III)), and a weaker decay for the RRM-IDD experiment (Gd(III)-NO). In particular, the difference between the NO-NO DEER and the NO-Gd(III) DEER is significant, because the pump pulse is the same in both experiments, and only the detection position is changed. The changes upon addition of RNA are weak in all three experiments. We see slightly faster DEER signal decays (i.e. higher local concentrations) for the measurement between the RRM and between the IDDs, and a slightly reduced decay for the RRM-IDD distances. The trace lengths that could be obtained are unfortunately not long enough to perform useful distance analysis.

At this point we would like to point out that very recently a novel spin labelling approach based on co-ligand enhanced binding of Cu(II) ions to surface exposed histidine motifs was introduced.^[101] Like many other proteins, the RRM1 of hnRNPA1 in fact naturally carries this labelling motif (RRM1:H119-H120, see Figure 6.6), but this was not investigated further in this work. It may be possible in the future to investigate dimerisation properties of wild-type hnRNPA1 with this new spin labelling strategy using both EPR and PRE, in particular, since the Cu(II) ion is more narrowly localised than a nitroxide label. Such an approach potentially presents an interesting starting point for future SDSL experiments with hnRNPA1 and spectroscopically orthogonal spin labels.

6.4 Conclusion and outlook

We summarised here pulse EPR approaches to study interactions in biomolecular complexes and aggregates, which depend on spectroscopic selection of different paramagnetic centres. The application of such approaches to biological systems of virtually arbitrary size is a powerful method for the study of complex multi-component systems, especially if the individual components of such a system can be orthogonally spin-labelled. The use of model systems, such as molecular rulers

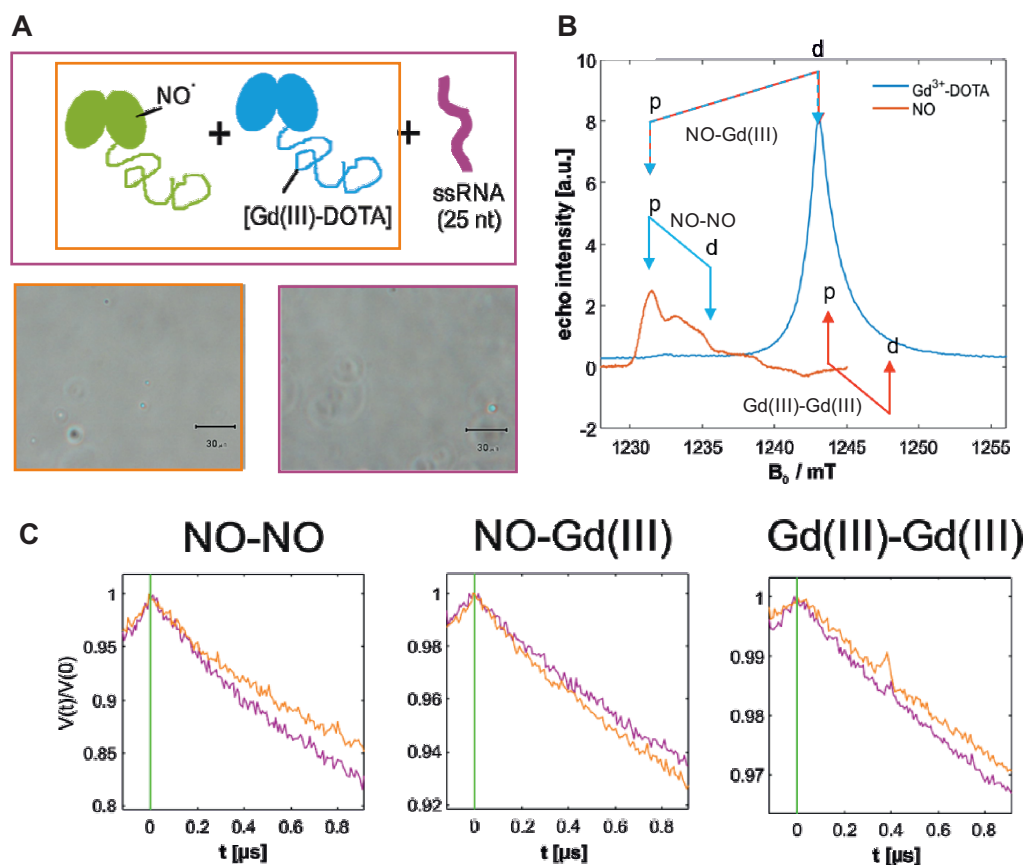


Figure 6.5: Orthogonal spin labelling with nitroxide and Gd(III)-DOTA to understand LLPS of hnRNPA1; (A) sample composition scheme; full length hnRNPA1 was independently labelled with MTSL at position 182, resp. with maleimido-Gd(III)-DOTA at position 231 (40 μ M per component) and LLPS was induced by incubation at +4 $^{\circ}$ C (orange traces); The experiment was repeated with the addition of a short RNA (same protein concentration, 80 μ M RNA, 5'-GGCUAGGGUUAUCAAGUGACUUCU-3', purified and generously provided by Elisabeth Lehmann, contains optimal binding sites for UP1); (purple traces); (B) pump and detection pulse setups for DEER with spectroscopically orthogonal spin labels; (C) primary DEER data obtained with LLPS sample without RNA (orange) and with 1:1 molar RNA (purple) between different sets of spin labels;

or protein complexes with known structure, has enabled to study the performance of nitroxides, other organic radicals, and metal ion-based spin labels for PDS experiments. The use of spectroscopically orthogonal spin labels can give better confidence and additional information about the extracted distance distributions and, often, improve sensitivity. The application of PDS methods and orthogonal spin labelling to investigate the role of protein domains that do not adopt a fixed secondary structure in solution (so-called intrinsically disordered domains) was demonstrated on the example of complex, phase separated sample of the protein hnRNPA1 in the free state, as well as in an RNA-bound state. Proteins carrying such domains usually cannot be crystallised and the

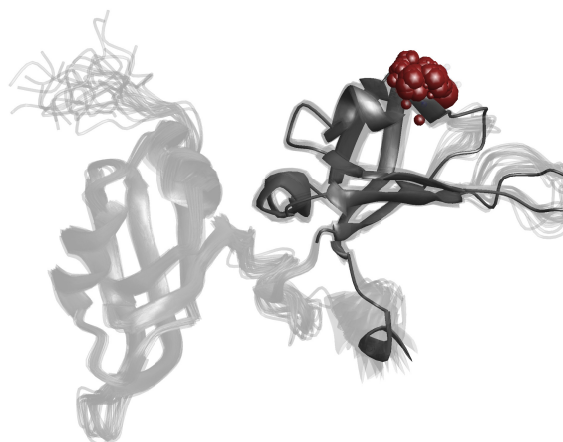


Figure 6.6: MMM rotamer simulation of the naturally occurring surface exposed 'double His motif'^[101,139] (H119, H120) in the RRM2 of hnRNPA1 for spin labelling with Cu(II)-NTA; one chain for RRM2 is shown in dark grey, with the modelled Cu(II) positions as red spheres;

broadly distributed distances inherent to the conformational ensembles are difficult to resolve by other structural methods.

6.5 Materials and methods

6.5.1 Protein purification and spin labelling

The heat-stable complex of subunits Rpo4 and Rpo7 (also known as F and E, respectively) of the archeal RNA polymerase of *M. jannaschii* were purified according to established protocols.^[168,303] For more details see also the supporting information of Pribitzer et al.^[241] The labelling sites for the Rpo4/7 complex (Rpo4: C36, G63C; Rpo7: V49C) were selected from a larger set of sites reported in^[168], where all pairwise distances from DEER experiments have been measured. The two subunits, Rpo4 and Rpo7, of the Rpo4/7 complex were individually over-expressed in *Escherichia coli* following the established protocols. Protein concentrations were determined with a NanoDrop Spectrophotometer ND-1000 (Witec AG) using the calculated extinction coefficients^[98] of $\epsilon = 29.34 \text{ L mmol}^{-1} \text{ cm}^{-1}$ for Rpo4/7. The individual subunits or the complex of Rpo4/7 were spin labelled with tenfold molar excess of MTSL ((1-oxyl-2,2,5,5-tetramethylpyrroline-3-methyl)methanethiosulfonate, Toronto Research Chemicals), resp. maleimido-[Gd(III)-DOTA] over cysteine concentration at a protein concentration of $10 \mu\text{M}$. Unreacted spin label was washed out by repeated concentration and re-dilution in a 10 kDa MWCO centrifugal concentrator (Vivaspin-500, 10 kDa MWCO, Sigma-Aldrich). Removal of the free nitroxide label and spin label attachment was checked by CW EPR spectroscopy. The final protein samples were lyophilised and resuspended in a $\text{D}_2\text{O}/\text{d}_8\text{-glycerol}$ mixture (1:1 by volume) and transferred into the 3 mm (outer diameter) sample tube.

6.5.2 DEER Measurements

Four-pulse DEER experiments were measured with the standard pulse sequence shown in Figure 6.1 on a home-built Q-band spectrometer. The detection ν_d were and 34.5-34.8 GHz. The pump/detection frequency offsets were: $\Delta\nu = \nu_p - \nu_d=0.1$ GHz for nitroxide-nitroxide DEER, resp. Gd(III)-Gd(III) DEER, and $\Delta\nu =0.3$ GHz for nitroxide-Gd(III) DEER. Pumping was always performed at the respective maxima of the pumped spectrum. The nitroxide-detected DEER measurement (nitroxide-nitroxide DEER) was performed at 50 K with a short repetition time (*srt*) of 4 ms. The Gd(III)-detected DEER experiments (Gd(III)-Gd(III)-DEER and Gd(III)-nitroxide DEER) were detected at 10 K with *srt*=2 ms. Pulse powers were optimised for the detected species using nutation experiments. All pulses had a length of 12 ns. The value of the first refocusing delay was 400 ns. A phase cycle [+ (+x)-(-x)] was applied to the $\pi/2$ observer pulse to cancel receiver offset. The data were background corrected and further analysed in DeerAnalysis2016.^[144]



Chapter 7

Optimising nitroxide-Cu(II) RIDME for distance measurements

In the previous chapter we have discussed how pulsed dipolar spectroscopy (PDS) can be a valuable tool for the characterisation of biomolecular interactions. In this chapter we treat in detail how the relaxation-induced dipolar modulation enhancement (RIDME) technique can be used for distance measurement between nitroxide spins and Cu(II) centres, as an example for a PDS method applied to spectroscopically orthogonal spin pairs.

Scope of this chapter The content of this chapter is adapted from the publication Ritsch et al.^[250]. It has been edited for consistency, and the focus has been set on distance analysis with the RIDME experiment in Cu(II)-nitroxide spin pairs, for applications to the field of structural biology. In particular we discuss approaches to experimentally suppress unwanted electron spin echo envelope modulation (ESEEM) modulations, and guidelines to perform stable background correction. The effect of orientation selection is demonstrated in the semi-rigid molecular rulers, and we present a broadband microwave pulse-adapted version of the RIDME experiment that allows full orientation averaging, resp. EPR-correlated analysis of orientation effects in RIDME. Compared to the publication^[250] we include additional results from RIDME measurements at X-band, and from UV/VIS spectroscopy. The latter are adapted from a manuscript in preparation: Katharina Keller, Irina Ritsch, Henrik Hintz, Miriam Hülsman, Mian Qi, Frauke Breitgoff, Daniel Klose Yevhen Polyhach, Maxim Yulikov, Adelheid Godt, and Gunnar Jeschke, "Accessing Distributions of Exchange and Dipolar Couplings in Stiff Molecular Rulers with Cu(II) centres".

Acknowledgements Henrik Hintz synthesised the molecular rulers, Irina Ritsch performed the EPR measurements and data analysis. We thank Mian Qi (Bielefeld University) for the preparation of the [metal ion-PyMTA] complexes. Maxim Yulikov is kindly acknowledged for the formulation of the orientation selection theory aspects.

7.1 Introduction

EPR spectroscopy is a powerful tool to study magnetic interactions in spin pairs.^[38,40,126,136,236,242] In particular, there are several research and application areas where interactions between nitroxide radicals and Cu(II)-based paramagnetic centres are of significant interest. We focus here on applications in structural biology, where accurate distance determination is desired.^[147,208,312] Complexes of Cu(II)-ions are attracting attention in bio-EPR spectroscopy both as native metal centres in proteins,^[14,22,147,159,180,205,269,270,292,298,310] and as spin labels for orthogonal pulse dipolar spectroscopy.^[66,184] The potential of the latter approach has been recognised previously and is reflected in a growing interest in Cu(II)-based spin labelling strategies.^[66,102,147,227,313] Their strength lies in the possibility of spectroscopic selection in systems of several interacting molecules, and they thus may well become a method of choice in the studies of intermolecular biomolecule interactions.^[66,96,103,105,106,150,173,246,251,306,313]

Challenges for PDS with Cu(II)-nitroxide PDS experiments on Cu(II)-nitroxide pairs pose additional challenges compared to the commonly used nitroxide-nitroxide experiments. Sensitivity of PDS experiments on Cu(II) centres suffers from the small fraction of spins within the excitation band of a typical rectangular microwave pulse. This limits the dipolar modulation depth, when pumping Cu(II) spins, or the echo signal-to-noise ratio (SNR), when detecting them. The fraction of excited Cu(II) centres generally decreases with increasing spectrometer frequency, because the spectral width of Cu(II) depends on the g -tensor anisotropy, which is the dominating factor for spectral width already at X-band frequencies around 9 GHz. The appearance of the Cu(II) EPR spectrum varies strongly with the type of ligand. Usually the EPR spectra of a nitroxide and a Cu(II) complex do not overlap at relevant frequencies for PDS spectroscopy (X-band and above), in rare cases, however, they may overlap at all frequencies. Here we address the first case, where the spectra are fully separated.

Another complication in Cu(II)-nitroxide PDS measurements arises from the strong correlation between the resonance field and the orientation of the molecular coordinate frame with respect to the external magnetic field for both spin types.^[44] On the one hand, such orientation selection can provide additional information of the geometry of the spin pair. Such approaches have been developed for the case of nitroxides and other organic radicals,^[69,201,236] which have led to several application studies.^[2,69,86,200,260] On the other hand, orientation selection significantly complicates experiments and data analysis if only the distance distribution is of interest. In order to obtain the full information, PDS data need to be measured over a broad range of detection and pump positions, which is tedious for the broad Cu(II) EPR spectra. The full information may even be inaccessible if spectral width strongly exceeds resonator bandwidth.

RIMDE for Cu(II)-nitroxide distance measurements Instead of using a pump pulse for flipping the spins B coupled to observer spins A, as is done in DEER spectroscopy, a longitudinal-relaxation mixing block ($\pi/2$) - T - ($\pi/2$) can be used that has no bandwidth limitation. This is the basis of the relaxation-induced dipolar modulation enhancement (RIDME) experiment.^[174,210] The performance of this experiment correlates with the ratio of the longitudinal relaxation time

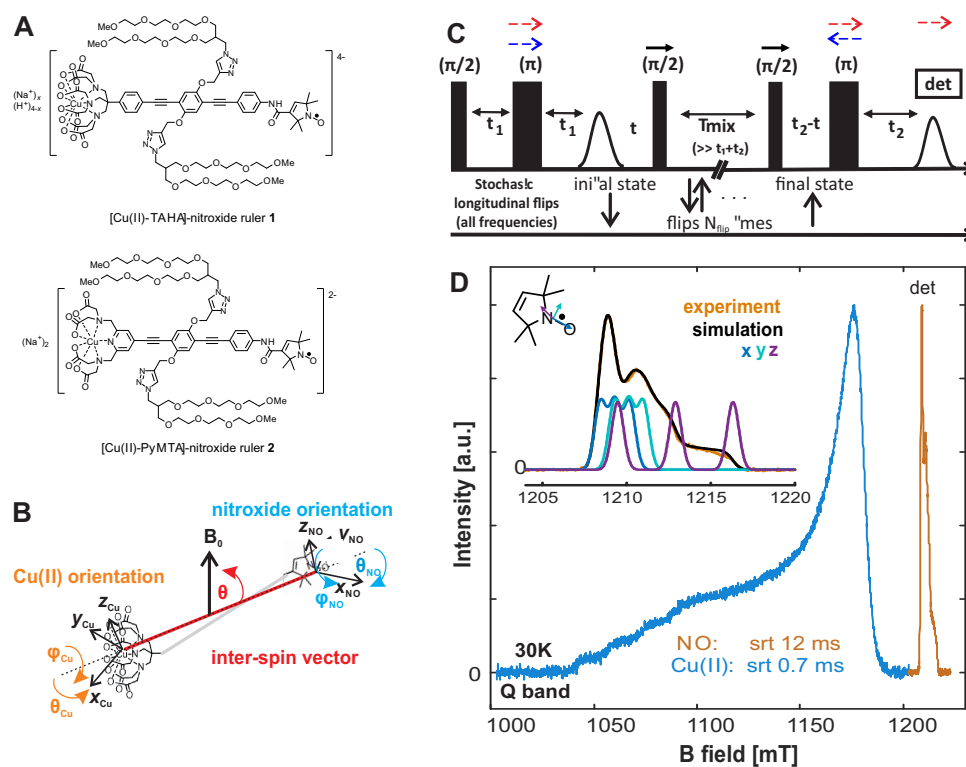


Figure 7.1: (A) Structural formulae of the Cu(II)-nitroxide rulers **1** and **2** used in this EPR spectroscopic study; (B) graphical representation of the relevant angles for orientation selection; (C) the 5-pulse RIDME sequence with first (t_1), and second (t_2) refocusing periods. The pulses that form the mixing block are stepped together (black arrows) to give the RIDME time axis t . The blue and red dashed arrows above the refocusing pulses indicate which pulses are moved in the ESEEM averaging schemes (D) Q-band spectra of the Cu(II) (blue) and the nitroxide (orange) regions for ruler **1** at 30 K. The maxima of the spectra are separated by approximately 33 mT. (*inset*) Zoom on the nitroxide spectrum and EasySpin^[280] powder spectrum fit. RIDME on the maximum of the nitroxide spectrum may result in moderate orientation selection, as is illustrated by three simulated sub-spectra of the nitroxide powder spectrum which correspond to orientations of the magnetic field along the principal axes of the nitroxide g -tensor.

of the B spins to the transverse relaxation time of the A spins. Relaxation behaviour dictates that in the Cu(II)-nitroxide RIDME experiment, the nitroxide spin takes the role of the observer spins A (slow longitudinal relaxation) and the Cu(II) centres the role of the flipped spins B (fast longitudinal relaxation). In this configuration high-quality Cu(II)-nitroxide RIDME data can be obtained.^[102,208] It also results in an essentially infinite excitation bandwidth for the B spins, while the detection sequence for the nitroxide radicals can be broadbanded or selective, depending on the chosen microwave pulse parameters. Importantly, since RIDME is a single-frequency experiment, there are no limitations in placing the detection frequency within the nitroxide spectrum, or even exciting the entire spectrum. These considerations suggest that it should be feasible to perform practically complete orientation averaging in RIDME experiments, a feat that is very difficult to ac-

comply with Cu(II)-nitroxide DEER. For a nitroxide-[Cu(II)(terpy)₂]-nitroxide model compound a five point averaging of the RIDME traces over the nitroxide spectrum led to dipolar frequency patterns reasonably close to the expected Pake pattern with somewhat suppressed parallel components.^[208] In contrast to high-spin metal centres, where dipolar frequency overtones in RIDME data complicate distance analysis,^[162] the analysis of Cu(II)-nitroxide RIDME time-domain data is practically the same as that for DEER experiments on nitroxide pairs.

For the spectroscopic experiments geometrically well-defined model compounds were needed. Furthermore, to be able to perform the experiments under conditions used to study biomolecules, solubility in water is requested. The RIDME experiments on such water-soluble rulers is demonstrated in this chapter with the molecular Cu(II)-nitroxide rulers **1** and **2**, [Cu(II)-TAHA]-nitroxide and [Cu(II)-PyMTA]-nitroxide, (Figure 7.1).

7.2 Results and discussion

7.2.1 ESEEM suppression in RIDME experiments

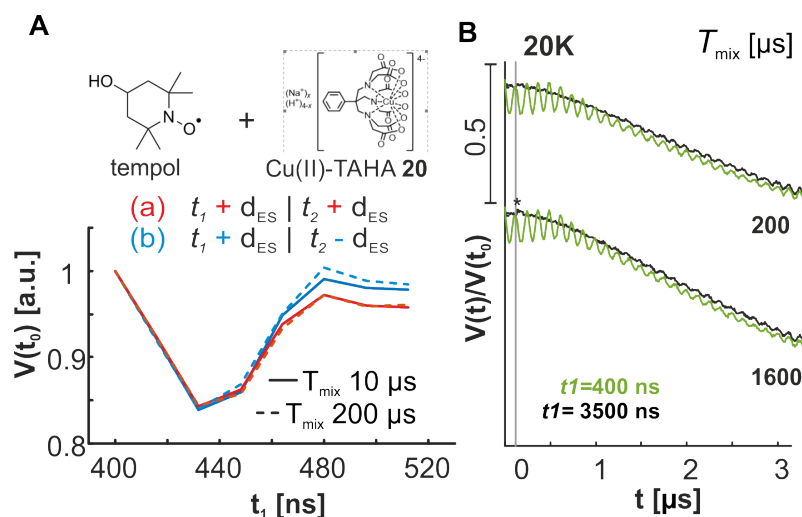


Figure 7.2: ²H-ESEEM averaging approaches tested on a 1:1 molar mixture of tempol and [Cu(II)-TAHA] **20** (100 μ M each, chemical structures given in the inset). For pulse stepping see red resp. blue arrows in Figure 7.1(C). (A) The ²H-ESEEM averaging scheme in Keller et al.^[160] (red) at two mixing times (solid vs. dashed lines). (B) Primary RIDME data with $t_1 = 400$ ns (green) and $t_1 = 3500$ ns (black), no additional ESEEM averaging for two T_{mix} , at 20 K; $t_2 = 3500$ ns in both cases.

The RIDME experiments presented in this study were performed on the Cu(II)-nitroxide rulers **1** and **2** in a glassy matrix of D₂O and d₈-glycerol. This resulted in moderately strong electron spin echo envelope modulations (ESEEM) in the RIDME traces at the deuterium nuclear Zeeman frequency (≈ 7.8 MHz), which can interfere with the analysis of the true Cu(II)-nitroxide dipolar modulations, especially for short spin-spin distances. The performance of two methods for the sup-

pression of ESEEM was tested on a 1:1 molar mixture of the nitroxide tempol (4-hydroxy-2,2,6,6-tetramethylpiperidinyloxy) and the complex Cu(II)-TAHA **20** in D₂O/d₈-glycerol (see Figure 7.2). This mixture (in the following referred to as 'reference sample') mimics the relaxation and ESEEM properties of the ruler solutions, yet the RIDME trace of this sample does not exhibit visibly resolved dipolar oscillations, and thus offers the opportunity to conveniently monitor the efficiency of an ESEEM-suppression method.

Recently, an averaging approach was presented^[160] in which the phase of the ESEEM modulations is shifted relative to that of the electron dipole-dipole contribution by step-wise incrementing the transverse evolution delays t_1 and t_2 (see Figure 7.2, averaging scheme (a) and red traces). The averaging is performed by summation of traces where the increments are chosen to cover a full period of the dominating ESEEM frequency (here ²H). For our reference sample this averaging scheme led to an almost complete cancellation of ²H-ESEEM modulations in the RIDME traces using eight steps with an averaging increment of $d_{ES} = 16$ ns. We present here in addition a modified version of ESEEM averaging (scheme (b), and blue traces in Figure 7.2) which conserves the total transverse evolution period $t_{tot} = t_1 + t_2$, by decrementing t_2 with the same step as the first delay t_1 is incremented. The resulting phase shift of the ESEEM modulations is the same as in scheme (a), but the constant time experiment may be useful for efficient ESEEM averaging in samples with fast transverse relaxation.

In the course of this study we tested yet another method to suppress ESEEM, which is based on increasing the first transverse evolution delay t_1 while keeping the second delay t_2 constant (see Figure 7.2). Again the measurements were performed with the reference sample, and all traces in Figure 7.2(B) were averaged for the same amount of time, such that the SNR can be directly compared. In this particular case the reduction in SNR for the RIDME trace with longer transverse evolution time was low. The resulting suppression of ESEEM when using a long t_1 , however, is striking. Note that this is most obvious for the easily recognisable ²H-ESEEM modulations, but in principle this suppression applies to ESEEM arising from all relevant types of nuclei, because ESEEM modulations from all nuclei decay in accordance with the homogeneous linewidths and inhomogeneous broadening of the corresponding parts of the ESEEM spectrum (see section below on ESEEM removal at X-band). For RIDME detection on nitroxide radicals in water/glycerol mixtures, the ESEEM from ¹H, ²D, and ¹⁴N nuclei are of highest importance, which all have comparable characteristic ESEEM decay times. This is an advantage over the summation-based method, where the frequency of the unwanted ESEEM has to be known beforehand, in order to set up appropriate averaging delays. Furthermore there may be cases where the frequency of the dominating ESEEM contribution is very low, such as for example ¹⁴N. In such cases even the constant-time averaging scheme reported in this work may not be sufficiently robust to enable averaging over one full period of the contaminating signal.

Of course, the two ESEEM suppression methods reported here do not mutually exclude each other, and a long t_1 can be combined with step-wise ESEEM averaging. We suggest the following empirical procedure for optimised ²H-ESEEM averaging: in our experience it is possible to find a t_1 that balances the loss of echo intensity against the amplitude of residual ESEEM contamination by measuring a 2-pulse (Hahn-echo) decay and setting t_1 to the value after which the deuterium ESEEM modulations in this Hahn-echo decay have visibly decayed. For additional experimental

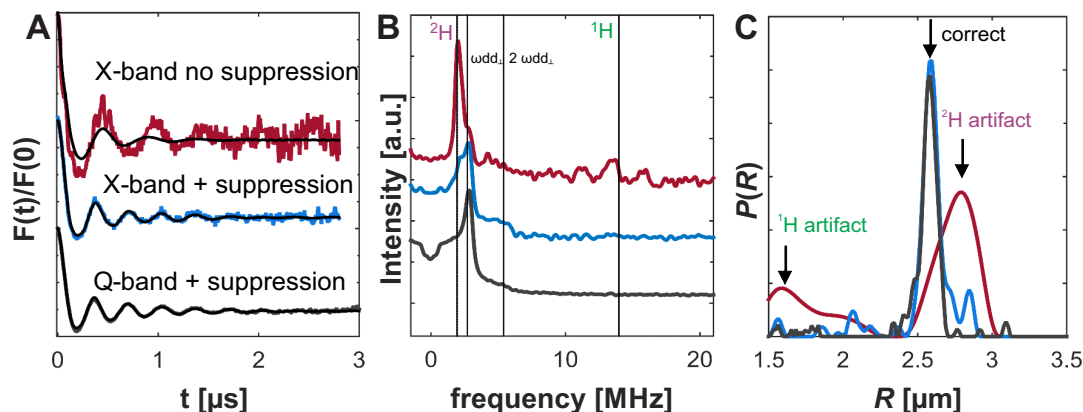


Figure 7.3: Combined protocol for ESEEM suppression at X-band; (A) form factors; X-band chirp RIDME, $t_1 = 400$ ns, no averaging (red), X-band chirp RIDME $t_1 = 6100$ ns, ^2H -ESEEM averaging (constant time) with 14 $\times 32$ ns steps (blue), and Q-band chirp RIDME $t_1 = 4100$ ns, ^2H -ESEEM with (constant time) 8 $\times 16$ ns steps; (B) FT of form factors, two vertical lines denote the expected dipolar contributions $\omega_{dd,\perp}$, resp. $2\omega_{dd,\perp}$, the nuclear Larmor frequencies for ^1H and ^2H at X-band are also indicated. (C) distance distributions obtained with standard DeerAnalysis kernel in the three cases. The expected correct distance is marked, as well as the artifact contributions from ^1H and ^2H at X-band.

results (which may serve as a guide for efficient set-up of ESEEM suppression in solvents of varying degree of deuteration) we refer to Appendix D.

We want to point out that other methods for ESEEM averaging apart from the two presented in depth here have been devised and tested.^[3,14,210] These approaches are based either on dividing a given RIDME trace by reference data, or by reducing the excitation bandwidths of the MW pulses. Both of these approaches are costly in terms of SNR, but may still be preferable in terms of SNR in cases of fast transverse relaxation (see additional results in Appendix D).

Suppression of ESEEM at X-band To put the combined ESEEM suppression protocol to the test we measured RIDME at X-band frequencies (~ 9.5 GHz), where the nuclear frequency of both ^2H as well as ^1H fall into the range that can be excited by typical MW pulse bandwidths, and can thus contribute as contamination to the RIDME signal. We measured RIDME with broadband pulses (chirp experiments are described below) on a $200\ \mu\text{M}$ sample of [Cu(II)-TAHA]-nitroxide ruler **1** in deuterated solvent ($\text{D}_2\text{O}/\text{d}_8\text{-glycerol}$). Strong ^2H -ESEEM of comparable amplitude as the dipolar modulation was observed in the RIDME signal, and considerable ^1H ESEEM modulations were observed (see Figure 7.3). Note that with this particular ruler the ^2H -ESEEM frequency by coincidence almost matches $\omega_{dd,\perp}$. When converted directly to the distance domain we obtain artifact contributions at $R \approx 1.5$ nm resp. $R \approx 3$ nm. Averaging over both ESEEM frequencies simultaneously is in principle possible, but requires a long averaging cycle. We found that using a long first refocusing delay of $t_1 = 4100$ ns is sufficient to suppress the ^1H -ESEEM modulation,

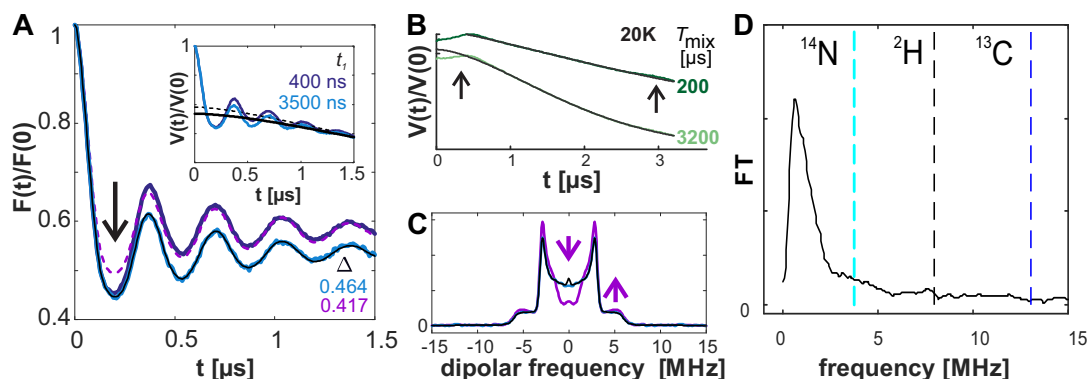


Figure 7.4: (A) RIDME primary data (inset, background fits with stretched exponential in black) and form factor with $t_1 = 400$ ns (purple), resp. $t_1 = 3500$ ns (blue) at $T=20$ K with $T_{\text{mix}} = 400$ μs on [Cu(II)-TAHA]-nitroxide ruler **1**; distance fit in black; (B) RIDME background measurements (green) with a 1:1 molar mixture of TAHA-nitroxide **18** and [Cu(II)-TAHA] **20** (100 μM each) at two mixing times, and background fits (black); (C) distortions of the dipolar spectrum are observed, which are similar in appearance to orientation selection. (D) FT of the time-domain signal in (B) after background correction with a stretched exponential and indications for the expected ESEEM frequencies of common nuclei

and can be used in combination with at 14 step cycle á 32 ns to remove the residual ^1H -ESEEM modulation. The combined ESEEM suppression is sufficient to reproduce the Q-band distance distribution.

7.2.2 RIDME Background Correction

Correct evaluation of the intermolecular background contribution is an important step in any analysis of dipolar evolution data. The background decay in a RIDME experiment is typically steeper than the background decay in a DEER experiment, which can be mainly attributed to two reasons. First, for long mixing times the number of flipped B spins is rather large for the vicinity of each A spin, and, thus, the effective excitation probability for the RIDME mixing block is larger than for the typical DEER pump pulse. Accordingly, this results in a stronger intermolecular decay contribution in RIDME as compared to DEER. Second, there are nuclear spectral diffusion events during the RIDME mixing block, which are absent in the DEER experiment, where the mixing block is substituted by a pump pulse. The additional nuclear spectral diffusion makes RIDME background decay also steeper. Importantly, both electron spin flips and nuclear spectral diffusion depend on a number of factors (e.g. temperature, electron or nuclear spin concentration, spectral width), and thus the understanding of the RIDME background properties requires a dedicated study. Such a detailed study was recently reported^[164], but here we only discuss a few practical aspects important for Cu(II)-nitroxide RIDME.

The commonly applied empirical RIDME background shape is the stretched exponential decay function,^[3,102,162,247] but also second-order polynomial functions have been used for short dipolar evolution traces.^[103,208] We have found that for measurement temperatures of 30 K or lower, the

use of the stretched exponential fitting function can lead to significant distortions in the dipolar spectra, as well as errors in the estimation of the modulation depth in the order of 10%. In the case of the Cu(II)-nitroxide rulers **1** and **2**, the problem could be identified by looking at the mismatch between the RIDME form factor and the corresponding DeerAnalysis^[144] fit, at the time range of the first dipolar oscillation (see Figure 7.4(A)). This effect can also be observed as a distortion of the dipolar spectrum (Figure 7.4(B)). In the case of the Cu(II)-nitroxide ruler **1** we do not observe a significant difference in the fitted distance distributions (Figure 7.4(C)). For a short t_1 value ($t_1=400$ ns case in the Figure 7.4(A)), a too deep first minimum in the dipolar oscillation is observed, which cannot be fitted by the standard DeerAnalysis kernel. We found that by increasing the first delay time to $t_1=3500$ ns, the shape of the primary RIDME trace had changed and a much better fit of the new form factor trace could be achieved.

This led us to investigate the shape of the Cu(II)-nitroxide RIDME background function for a reference sample, and the results can be found in Appendix D. The extent to which the background shape deviates from a single stretched exponential depends on the duration of the first transverse evolution period. Increasing the first refocusing delay t_1 suppresses the low-frequency contamination in the background traces (see Figure 7.2(B)). If t_1 is chosen sufficiently long, a stretched exponential background shape is recovered. With this choice of experimental parameters the background fitting procedure is also considerably more stable with respect to the choice of fit range. In retrospect, it is apparent that this background feature is present as well in previously published metal ion-nitroxide RIDME data.^[102,103] In some other cases reported in the literature a different background fitting methods were applied, which makes direct comparison without access to the primary data difficult. For previously reported metal-metal RIDME data this problem is either absent or too weak to be clearly detected.^[162]

Given the presented set of RIDME background measurements we cannot draw a firm conclusion on the mechanism that causes the deviation from a stretched exponential decay. It may arise due to some dephasing process, which is relevant only at short t_1 times, but disappears at long t_1 . We remark that at low concentrations (of 100 to 200 μM) it is likely that nuclear-driven mechanisms are the dominating ones for the RIDME background decay. Instantaneous diffusion processes are unlikely causes, because we have observed the background artifact both in traces measured with soft (50/100 ns) and hard (12/24 ns) pulses. We have furthermore checked that the background artefact is not related to any echo crossing. This is in line with the width of the artefact, which is much larger than for any echo crossing feature we observed in these RIDME data. Further understanding of this mechanism will be of interest in future studies. However, for practical reasons, the increase of t_1 appears to be a sufficiently good work-around for this problem in cases where some loss of RIDME signal intensity can be tolerated. In the present case an increase of t_1 sufficient to suppress this background artefact resulted in approximately 20% sensitivity loss. This work-around is essential in studies of samples with broad spin-spin distance distributions, which feature dipolar evolution traces without easily recognisable oscillations. For such samples the RIDME background decay artefact would not easily be distinguishable from the true dipolar signal. Note that the division approach,^[3] which is often used for the ESEEM artefact reduction, is also capable to suppress this background problem to an acceptable level. In the situations when transverse relaxation of nitroxide radicals through the sample is approximately the same, the use

of the elongation of t_1 appears more advantageous, due to the better overall sensitivity. However, if detected spins have a broad distribution of relaxation times, use of long t_1 might result in some relaxation filtering effects, and thus the division approach to remove the background artefact might appear more advantageous despite its higher sensitivity loss.

7.2.3 Echo-crossing artifacts

The originally reported eight-step phase cycling protocol^[210] includes two-step $[(+x) - (-x)]$ phase cycling on the first $\pi/2$ pulse and four-step $[(+x) + (+y) + (-x) + (-y)]$ phase cycling on the two $\pi/2$ pulses from the RIDME mixing block, with the same phase of the two pulses in each phase cycling step. In particular, this phase cycling protocol is designed to remove the echo crossing artefact due to the refocused stimulated echo (all five pulses act) and the two-pulse Hahn echo from the last two pulses of the RIDME pulse sequence. Together with longitudinal relaxation of the A spins, imperfections in the channel balance of the pulse EPR spectrometer lead to incomplete removal of the latter echo crossing artefact, so that a peak is observed at approximately zero time in the RIDME trace, as discussed previously.^[162] From plotting the echo transients of a RIDME experiment we also see that at very long mixing times the primary echo from the last two pulses becomes much stronger than the RIDME refocused virtual echo (which is detected), and, by offsetting part of the unmodulated echo, results in an artificially high modulation depth. This has been observed as well for Gd(III)-Gd(III) RIDME.^[162] For a more general approach to monitor echo crossings, we computed a list of coherence order pathways and resulting echos following the well-established concepts reported in Gemperle et al.^[99], where we considered only terms of coherence orders -1, 0, and 1. This identification of echos is potentially helpful to assign echo-crossing artifacts for any arbitrary choice of experimental parameters (t_1, t_2, \dots).

An important finding with this analysis was that for the setting $t_1 = t_2$, there is a stimulated echo from the first, second and fifth pulse (RIDME block does not act), which does not shift when stepping the mixing block, and which is not removed by the standard eight-step phase cycling. This echo is not modulated with dipolar frequencies as a function of the mixing block position t , but its presence leads to an apparent reduction of the dipolar modulation depth. This echo should be removed for example by the phase cycle: $[(+x) - (-x)]$ on the first $\pi/2$ pulse, $[(+x) + (+y) + (-x) + (-y)]$ on the two $\pi/2$ mixing block pulses and $[(+x) - (+y) + (-x) - (-y)]$ on the two refocusing π pulses. Measuring at $t_1 = t_2$ was not extensively tested, but may present interesting conditions, as this represents a case of a dynamically decoupled pulse sequence.

7.2.4 Modulation depth build-up

Suitable conditions for the orthogonal RIDME experiment in the Cu(II)-nitroxide spin pair were identified by screening temperature and mixing time for [Cu(II)-TAHA]-nitroxide **1**. The primary data of RIDME measurements at 30 K and the corresponding distance distributions obtained with DeerAnalysis2016^[144] using Tikhonov regularisation are displayed in Figure 7.5. Deviations of the background decay functions from the stretched exponential function characteristic for short t_1 delay times resulted in uncertainties of the determined modulation depths. Accordingly, analysis of

the modulation depth was performed using RIDME measurements with long t_1 times. The results for the modulation depth values are shown in Figure 7.5(D). No nitroxide orientation averaging scheme was used in this series.

For all tested temperatures we found that the modulation depth reaches a plateau when applying long mixing times $T_{\text{mix}} \approx 5 \cdot T_{1,\text{Cu}}$. The value of the modulation depth at this plateau $\lambda_{\text{max}}(T)$ is higher at lower temperatures. Nonetheless, even at the lowest tested temperature the value is about 10% lower than the theoretical limit of 0.5. There are at least two possible contributions to this loss of modulation depth. First, as indicated also by the measurements at higher temperatures, a non-negligible contribution from the A-spin relaxation induced by the B-spin flips might be present. Second, we cannot exclude incomplete loading of the ligand with Cu(II) as an alternative explanation of the lower modulation depth. These two effects can also amplify, because A-spins which are not in close proximity to a B-spin (i.e. ruler molecules with a nitroxide moiety, but no Cu(II) ion) do not experience this flip enhancement, and would thus be over-represented in the detected echo. Note that the same effect was discussed for high-spin Gd(III)-Gd(III) and Mn(II)-Mn(II) RIDME, where, besides the modulation depth reduction, it also affects the buildup kinetics for different dipolar frequency overtones.^[160] Longitudinal relaxation of the nitroxide spins is extremely slow at 10 K, enforcing a low shot repetition rate. This severely reduces sensitivity and we did not study RIDME modulation buildup in detail at this temperature. At 40 K we found that the extracted value of the modulation depth increases again after the plateau (data points marked as crosses). This apparent additional modulation is a consequence of the incomplete cycling of a crossing echo from the last two pulses ($\pi/2 - \tau - \pi$ sub-sequence) with opposite phase and must not be interpreted as additional dipolar modulation. This can also be seen in the form factor, where a steep initial decay of the trace is observed, which leads to artifact distance peaks at very short distances.

The best results were obtained at 20 K and 30 K, with mixing times ranging from several hundreds of microseconds to several milliseconds $T_{\text{mix,opt}} \approx 400 \mu\text{s} - 1.6 \text{ ms}$. This is much longer than the phase memory time of the detected nitroxide spins $T_{\text{mix,opt}} \approx 50 - 100 \cdot T_{\text{m,NO}}$. For the choice of mixing times within the range of the modulation depth plateau we observe that ESEEM contributions, which can still be comparatively strong at short mixing times, are suppressed by going to very long T_{mix} . This advantageous trend is counteracted by a clear loss of SNR, when T_{mix} approaches $T_{1,\text{NO}}$ for the given temperature. This is also the range, where the echo-crossing artifact contamination at zero-time becomes increasingly strong.

More detailed analysis for experimental sensitivity, as well as an empirical model to estimate sensitivity are given in Appendix D. We arrived at the following recommendation: depending on the expected spin-spin distances, the best measurement temperature slightly varies. For distances below 4 nm we recommend an experimental temperature between 30 K and 40 K. The modulation depth may still be increased (due to higher λ_{max} at low temperatures), but no benefit for sensitivity is expected from going to lower temperatures due to the slow longitudinal relaxation of the nitroxide spins. To measure distances above 4 nm it may be better to measure at the lower limit (30 K), but again, even lower temperatures (tested: 20 K) are not expected to increase sensitivity.

We tested on [Cu(II)-TAHA]-nitroxide **1** that detection of RIDME time traces with stronger partial nitroxide saturation (due to too fast repetition rates) does not change the shape of the

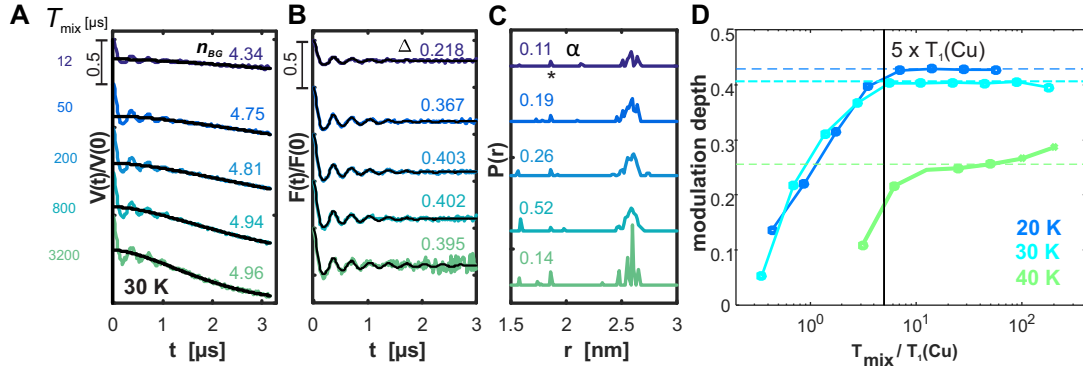


Figure 7.5: T_{mix} screening on [Cu(II)-TAHA]-nitroxide **1** measured at 30 K (no ^2H -ESEEM averaging, $t_1 = 3500$ ns). Data were analysed using DeerAnalysis^[144] with automatic choice of regularisation parameter α . (A) Primary data, shifted for clarity; and background fits (black) with dimensionality n_{BG} (B) form factors and distance fits (black) (C) distance distributions; (D) modulation depth Δ for the series shown in (A)-(C), and analogous results at different temperatures as a function of the ratio of T_{mix} and the characteristic time of longitudinal relaxation of Cu(II), $T_1(\text{Cu})$; the modulation depth plateaus are indicated (dashed lines). Data points marked with an 'x' are derived from experiments that are contaminated by an echo crossing-artifact, which artificially increases the observed Δ . The solid vertical line indicates the corner of the plateau, which for all temperatures occurs approximately at $5 \cdot T_1(\text{Cu})$.

dipolar oscillations. Adding a T_1 -relaxation enhancer^[315] might help to improve the longitudinal relaxation properties of nitroxide spins in these experiments, however, this strategy may not generally be viable for biological samples. For short spin-spin distances, the length of the RIDME time traces is not very critical, and one can optimise the modulation depth and mixing time, which is achieved at somewhat higher temperature. Note that our estimate agrees very well with the RIDME measurement temperatures used for [Cu(II)-terpyridine]-nitroxide.^[102,208]

Our treatment neglects longitudinal relaxation of Cu(II) spins during the time where A spin magnetisation is in the transverse plane, which may lead to a loss of the dipolar modulation depth. Such a case was recently reported for room-temperature RIDME measurements in trityl-nitroxide pairs.^[178] Note that for unequal A and B spins it might be even possible to reach conditions under which longitudinal relaxation of B spins is much faster than the transverse relaxation of the A spins, and the dipole-dipole interaction is thus averaged. We also neglect that the dimensionality of the background decay changes with the mixing time due to a prolonged period of spectral diffusion. This decay can eventually become so steep that part of the dipolar oscillations are suppressed, which leads to an artificial broadening of the distance distribution (see Figure 7.5). In cases of very fast background decay it may be necessary to use shorter than optimal T_{mix} . This may be partially compensated by raising the experimental temperature, where higher modulation depths can be achieved for the same absolute T_{mix} .

7.2.5 Orientation-selective Cu(II)-Nitroxide RIDME

Both Cu(II) and nitroxide are electron spin 1/2 species and for the Cu(II)-nitroxide rulers **1** and **2**, the two types of paramagnetic species have rather large resonance frequency offsets. Thus, only the secular part of the electron-electron dipole interaction needs to be considered. The analysis of dipolar evolution time-traces $V(t)$ for pairs of such spins in a homogeneous frozen glassy sample can be interpreted with the conventional point-dipole approximation for dipole-dipole coupling. This model relates the distance between the two spins R to a dipolar frequency $\omega_{DD}(R, \theta)$ which depends on the angle of the inter-spin vector to the external magnetic field (see Chapter 2). Orientation-resolved Cu(II)-nitroxide RIDME data were obtained by measuring a series of dipolar evolution time traces at different positions in the nitroxide spectrum.

The experimental results with this classical type of orientation selective PDS can be found in Appendix D. The orientation-averaged Cu(II)-nitroxide RIDME traces were obtained from the orientation-resolved RIDME data measured with the rectangular pulses setup using a procedure which is similar to the one in the recently reported work of Giannoulis et al.^[103] (see Figure 7.6). First, all primary RIDME traces were normalised to the same signal intensity at the zero time. Second, each trace was multiplied by the nitroxide EPR intensity at the corresponding spectral position. At the third step all such scaled RIDME traces were summed to obtain an orientation-averaged RIDME trace. We also tested an option of performing the background correction prior to the orientation averaging, which was then done with the form factor traces. Due to the lower SNR in the individual traces, this version of data analysis appeared somewhat less robust. Note that detection positions within the nitroxide EPR spectrum were selected such that one could neglect the overlap of the MW pulse bandwidths from the neighbouring detection positions. This, however, left relatively broad gaps between the detection positions, and accurate orientation averaging was possible only because the Cu(II)-nitroxide dipolar spectrum changes smoothly with respect to the detection position. Covering the whole nitroxide spectrum by the bandwidth of the detection subsequence would be possible if more detection positions and/or broader excitation bandwidths of the MW pulses were used, however then some orientations of the nitroxide radicals would be counted more than others due to excitation band overlap. The orientation averaged result is compared to frequency swept RIDME in Figure 7.6.

7.2.6 Frequency-swept Cu(II)-nitroxide RIDME

Using frequency-swept (chirped) pulses allowed us to detect the entire set of nitroxide orientations in a single experiment. As in the case of rectangular pulses, the chirp RIDME measurements were performed with long t_1 , in order to ensure a single stretched exponential background decay, and long mixing time for isotropic excitation probability distribution for the Cu(II) spins. Fourier transformation gives the nitroxide EPR spectrum in frequency domain. The agreement between the field-swept echo-detected EPR spectrum converted to the frequency domain, and the FT-EPR spectrum is rather good up to a slight shift of intensity close to the central frequencies of the spectrum. This might be due to imperfect offset compensation, and thus partial suppression of signal from destructive interference or due to the inhomogeneous detection efficiency imposed by the resonator.

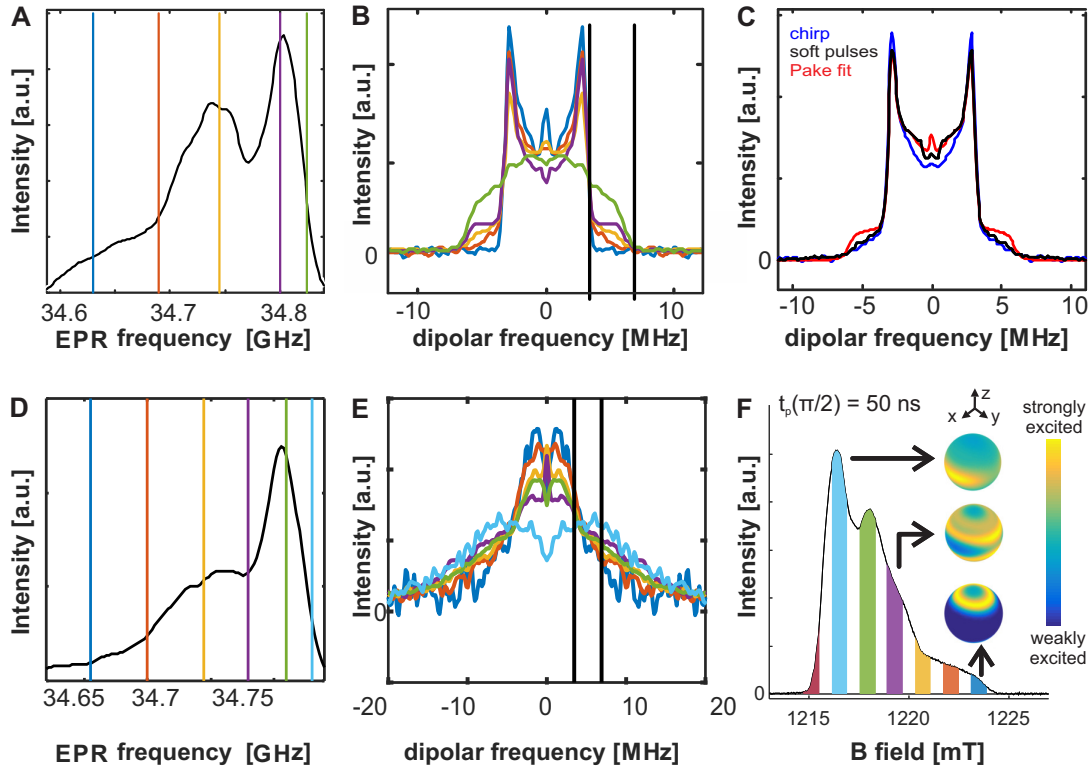


Figure 7.6: Orientation selection in nitroxide-detected RIDME (A-C) [Cu(II)-TAHA]-nitroxide ruler **1**; (D,E) [Cu(II)-PyMTA]-nitroxide ruler **2** (A,D) FT-EPR spectrum from RIDME echo measured at 20 K with $T_{\text{mix}} = 1.6$ ms, (B,E) dipolar spectra plotted for several frequency slices (vertical lines in FT-EPR spectrum) in the nitroxide spectrum; the black vertical lines are at $\nu_{\text{dd},\perp}$ ($r = 2.5$ nm), resp. $2\nu_{\text{dd},\perp}$. (C) Orientation-averaged spectra from field-stepped averaging (black) and chirp excitation (blue) are compared to a Pake fit (red). (F) EDEPR of the nitroxide of [Cu(II)-TAHA]-nitroxide ruler **1**; orientation selection averaging scheme by field-stepping indicated as shaded areas, for three positions we show EasySpin^[280] simulations (orise1) of the expected spatial orientation of the excited spins.

After background correction along the RIDME time dimension, and the corresponding Fourier transform, the EPR-correlated dipolar coupling pattern is obtained (see Figure 7.6). For selected positions in the nitroxide spectrum we show the projections of the dipolar spectra. They closely resemble the spectra obtained with field-stepped RIDME. Note that the orientation averaged spectra for the two averaging methods were compared to a Pake fit in Figure 7.6. Interestingly, the two schemes produce very similar results, but the shape of the dipolar pattern does not exactly match the shape of the predicted Pake fit (red). In both cases the best fit to the 'classical' Pake pattern is observed at the maximum of the nitroxide spectrum. Both averaging schemes are designed to excite all possible nitroxide orientations, and in the case of the chirped experiment this uniform excitation is demonstrated by noting that the FT-EPR spectrum up to minor differences gives the expected lineshape. Furthermore, the modulation depth is approximately constant over the whole

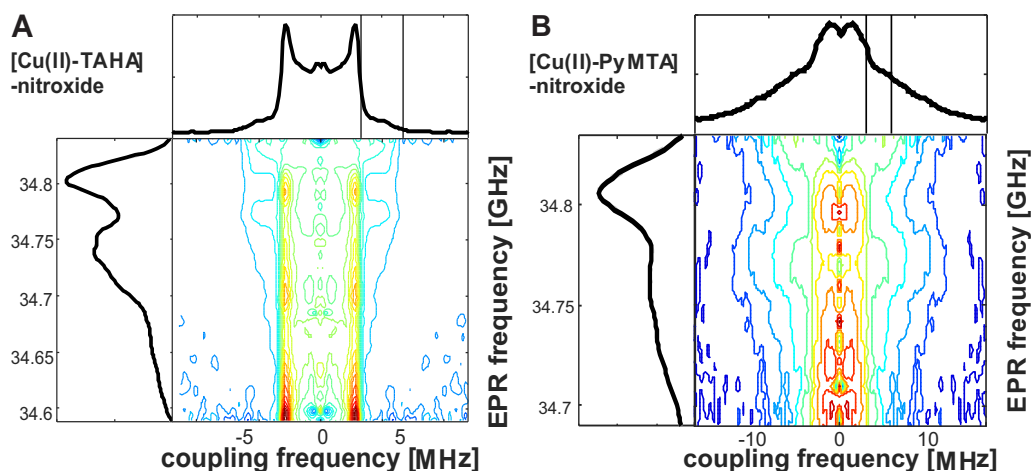


Figure 7.7: 2D-Fourier transform results of chirped RIDME data (A) measured on [Cu(II)-TAHA]-nitroxide ruler **1** and (B) [Cu(II)-PyMTA]-nitroxide ruler **2** at 20 K, $T_{\text{mix}} 1.6$ ms with 400 MHz bandwidth chirped pulses, centred on nitroxide;

nitroxide spectral range for chirp experiment), which is consistent with our hypothesis that at the chosen mixing time all Cu(II) orientations contribute with equal probability to dipolar modulation. Note that the broadband RIDME experiment at X-band (see Figure 7.3) was better at recovering the full dipolar Pake pattern than the corresponding Q-band experiment. This suggests that there is indeed still a slightly non-uniform excitation of the nitroxide spectrum at Q-band. Both broadband RIDME and RIDME with rectangular pulses are approximately equally affected, which could be because the z -orientations of the nitroxide (high field edge of the spectrum) are more strongly partially saturated at the chosen experimental temperature and comparatively fast shot repetition rate than the remaining spectrum. This is supported by the experimental observation that longitudinal relaxation of the z -orientation of the nitroxide is slower than for the x/y -orientations.

While in the presented case the orientation averaging worked equally well for the rectangular and chirp pulses setups, it is expected that for cases with very strong orientation selection (high-field detection, fully rigid well-defined structures of paramagnetic moieties) the approach with chirp pulses will provide better data than the one with rectangular pulses. We expect that due to the need of only a single measurement the chirp-pulse approach will become the standard for orientation-resolved dipolar spectroscopy experiments, once AWG setups with sufficient excitation and detection bandwidth are broadly available. Several methods for the simulation and interpretation of EPR correlated dipolar coupling patterns for nitroxides have been reported previously.^[69,201,214,236,260] In the scope of this work we do not perform a full fitting of the coupling patterns, but remain with a qualitative interpretation. Two motions of the nitroxide relative to the long axis of the ruler are possible: θ_{NO} characterises the tilting of the N-O bond relative to the long axis of the ruler, and ϕ_{NO} describes the rotation around this axis (see Figure 7.1).

To analyse the nitroxide-detected RIDME coupling patterns in terms of orientation correlation it is only relevant how B_0 is oriented with respect to the selected nitroxide spin, thus to identify the

probability of exciting A spins $P_d(\omega(\theta_A, \phi_A))$. Given an assignment of a dipolar sub-spectrum to such a selection of orientations we can then attribute the relative intensities in the Pake-like pattern to preferential orientation of the inter-spin vector with respect to B_0 (which corresponds to finding $P(\theta|\theta_A, \phi_A)$). With [Cu(II)-TAHA]-nitroxide **1** we observe that excitation of the x -orientation range in the nitroxide spectrum favours a dipolar spectrum with a high representation of parallel orientation of the inter-spin vector ($\theta = 0^\circ$), whereas excitation of z -orientations is linked to perpendicular orientations ($\theta = 90^\circ$). We see no strong differences in the dipolar coupling pattern between y -, and z -orientations of the nitroxide. This indicates cylindrical symmetry of the averaging of the second nitroxide angle ϕ_{NO} around the long axis of the ruler (i.e. a cone-like distribution). This is expected since the rotation around C-C bonds in the spacer leads to a uniform distribution of the polar angle ϕ_{NO} as described in Polyhach et al.^[236].

7.2.7 Comparison of RIDME with two different Cu(II) ligands

The projections of a chirp RIDME measurement on [Cu(II)-PyMTA]-nitroxide **2** are shown in Figure 7.7 and orientation-averaged RIDME data for the Cu(II)-nitroxide rulers **1** and **2** are compared in Figure 7.8. For the same mixing time, we obtained nearly the same dipolar modulation depths for the two rulers, which is consistent with the observation that the relaxation properties of Cu(II) in the rulers **1** and **2** are very similar. The dipolar evolution traces, however, reveal a striking difference between the two rulers (Figure 7.8). For ruler **1** several dipolar oscillations are detected, the corresponding distance distribution is narrow, and is in agreement with the expected spin-spin distance according to the molecular structure. For ruler **2**, however, we observed fast dipolar signal decay without any pronounced oscillations, encoding a broad dipolar spectrum and a too broad apparent spin-spin distance distribution, far beyond the expected flexibility of the ruler.

This suggests that the two different ligands lead to a different transfer of spin density into the π -system of the spacer that connects the two spin labels and thus to different exchange coupling between Cu(II) and nitroxide. Note that the two rulers differ in length by only about one C-C bond. However, in the case of TAHA as the ligand (ruler **1**) all N atoms are separated from the π -conjugated spacer by three saturated bonds, whereas in case of PyMTA as the ligand (ruler **2**) two N atoms are separated by only two saturated bonds and, most importantly, one N atom is an integral part of the π -system of the spacer. The spacer is in conjugation with the two olefinic C atoms of the nitroxide moiety where some of the spin density of the nitroxide is located. Therefore, exchange coupling in ruler **2** is the most plausible reason of the observed unexpectedly broad distribution of the dipolar frequencies.

This was further investigated by UV/Vis measurements of the two rulers and the corresponding ruler precursors prior to loading with metal ions (see Figure 7.8). While the addition of Cu(II) to ruler **1** makes no difference for the UV/Vis spectrum, we see a shift of the lowest energy extinction band for ruler **2** upon loading with Cu(II). Besides the complication by the exchange coupling, the overall performance of the chirp RIDME measurements with compound **2** is good and comparable to the chirp RIDME on compound **1**.

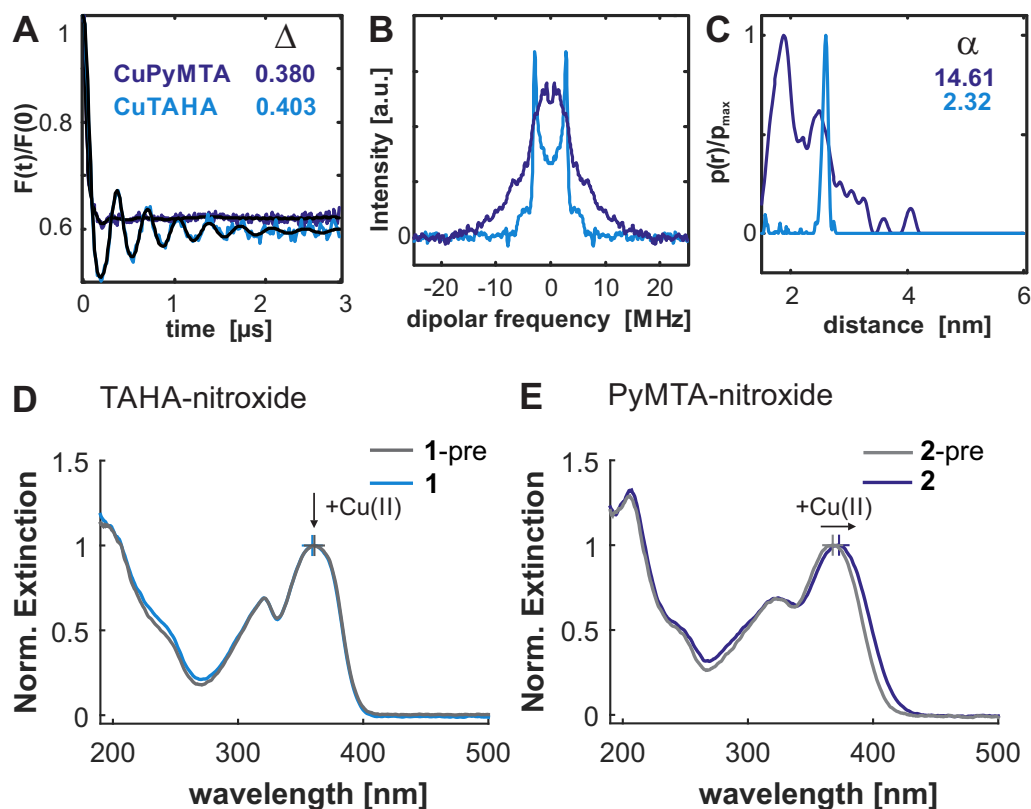


Figure 7.8: Comparison of RIDME with [Cu(II)-TAHA]-nitroxide ruler **1** (light blue, $t_1 = 4100$ ns) and [Cu(II)-PyMTA]-nitroxide ruler **2** (purple, $t_1 = 6100$ ns) at 30 K; (A) form factors after stretched exponential background correction, and modulation depths Δ ; (B) coupling spectra; (C) distance distributions after fitting with standard DeerAnalysis kernel; the regularisation parameter α is listed. (D) UV/Vis measurements of aqueous solutions of ruler **1** and precursor (**1-pre**) (E) UV/Vis of ruler **2** and precursor (**2-pre**); the maxima of the lowest energy peaks are indicated by a cross.

7.3 Conclusion

In this work, we focused on the accuracy of different steps in the measurement and data processing of nitroxide-detected Cu(II)-nitroxide RIDME. While some phenomena in Cu(II)-nitroxide RIDME, in particular regarding the background decay shape, are not yet fully understood, the measurements and their analysis can be done in a reproducible and robust way. At the expense of some sensitivity loss, the background problem can be circumvented by using a sufficiently long first interpulse delay in the observer sequence. Importantly, this modification of the RIDME method will allow for more accurate distance measurements in the cases of broad distance distributions, where the presence of the background artefact is a serious problem.

We also further elaborated on the issue of the ESEEM artefact suppression, and proposed an improved approach, based on the elongation of the first inter-pulse delay, complemented with the previously reported ESEEM artefact averaging over delay time variations that now also maintains the constant-time property of the basic RIDME experiment.

In this study we used the water soluble rulers [Cu(II)-TAHA]-nitroxide **1** and [Cu(II)-PyMTA]-nitroxide **2**, synthesised in the group of Adelheid Godt at Bielefeld University. The two rulers **1** and **2** differ essentially only in the type of Cu(II) coordinating ligand. The similarity of the relaxation properties of the three complexes Cu(II)-TAHA, Cu(II)-PyMTA, and Cu(II)-terpyridine^[207] and their comparable performance in RIDME suggests that Cu(II) complexes are a rather robust family of spin labels with no need for additional elaborate optimisation of RIDME experimental protocols for a particular complex. We recommend a measurement temperature between 20 K and 30 K, with lower temperatures being favourable for long distances, and higher temperatures for short distances. Direct coordination of Cu(II) by an atom being part of the π -system in the spacer leads to exchange interaction of the same order of magnitude as the dipole-dipole interaction at distances around 2.5 nm. This problem should not be encountered in spin labelling studies with proteins, where extended π -conjugation is usually not expected. It should, however, be taken into consideration when planning the attachment of such a spin label to a compound with a π -system, e.g. nucleic acids or light harvesting complexes. Because in Cu(II)-TAHA all donor atoms of the ligand are essentially electronically decoupled from the atom through which the label is attached to the molecule of interest, this complex appears as a valuable Cu(II)-based spin label.

RIDME experiments simplify orientation averaging for strongly anisotropic spin Hamiltonians considerably, since in the mixing time limit of maximum modulation depth orientation selection is negligible for the inverted spins. Hence, the optimal averaging scheme becomes independent of system geometry and requires only uniform detection of the observer spin. For [Cu(II)-TAHA]-nitroxide we could achieve this by a series of RIDME measurements with soft microwave pulses as well as by complete excitation of the nitroxide spectrum with a chirp observer sequence. The latter approach should be applicable even for stronger orientation correlation.

We found that with typically available microwave resonators, RIDME outperforms DEER for Cu(II)-nitroxide systems in terms of sensitivity by a large margin (a corresponding test with ultra-wideband DEER is shown in Appendix D). The relatively poor DEER performance results from the large frequency difference between the maxima of both spectra and is thus also expected for several other combinations of metal ion complexes with organic radicals, in particular at Q-band

and higher frequencies.

To summarize, we believe that the RIDME technique is well-suited for detecting dipolar interactions in Cu(II)-nitroxide spin pairs and that it has been developed to a point where practical applications in materials science and structural biology are reliable.

7.4 Materials and methods

7.4.1 Sample preparation and RIDME setup with rectangular pulses

All RIDME experiments were performed at Q-band (34-36 GHz). The EPR samples were prepared as 100 μM or 200 μM solutions in a mixture of D_2O and d_8 -glycerol in a 1:1 volume ratio. The measurement temperature was varied between 10 K and 50 K, using an Oxford Instruments He-flow cryostat system. For each sample, the Cu(II)-nitroxide ruler solution was filled into a 3 mm outer diameter thin-wall quartz tube and shock frozen by quick immersion into liquid nitrogen.

For the RIDME setup with rectangular microwave (MW) pulses, we used a home-built resonator, accommodating large-diameter samples,^[289] and a commercial Bruker E580 X/Q spectrometer upgraded to a high MW power.^[238] The conventional rectangular-pulse setup is shown in Figure 7.1(C). Unless stated otherwise the first inter-pulse delay t_1 was set to 4100 ns (see below for the reason), and the length of the second delay t_2 was set to 3500 ns. The mixing time values were varied between different RIDME measurements. This is indicated in the text and in the figure captions. The lengths of the $\pi/2$ pulses were set to either 12 ns ('non-selective rectangular pulses' setup), or to 50 ns ('selective rectangular pulses' setup). Accordingly, the lengths of the π pulses were set either to 24 ns (non-selective), or to 100 ns (selective).

The stationary refocused virtual echo^[210] that forms after the last π pulse (refocused virtual echo) was detected with a detection window of twice the pulse length of the π -pulse. The eight-step phase cycle to remove crossing echos^[210] was used. An eight-step averaging cycle with a time-increment of 16 ns and simultaneous t_1 and t_2 averaging was used to suppress unwanted electron-nuclear contributions to the RIDME time-evolution signal due to the matrix ^2H nuclei.^[160] More details on the electron-nuclear modulation averaging is given in the Results section.

7.4.2 DEER measurements

The comparative DEER measurement on [Cu(II)-TAHA]-nitroxide **1** was performed on the commercial Bruker spectrometer described above with an arbitrary waveform generator (AWG) (Agilent M8190A) setup plugged into the pump pulse channel. The experiment required a careful adjustment of the resonator mode (same resonator for 3 mm outer diameter samples as for the other experiments^[289]) to yield a very broad, strongly over-coupled resonator mode. This reduced sensitivity at the detection frequency, but was necessary in our attempt to obtain significant spin inversion at the pump frequency, given the large frequency offset of almost 1 GHz. Such an adjustment of the resonator mode also distributed the total microwave power over a larger frequency range, resulting in smaller power spectral density/smaller B_1 field at any frequency within the resonator profile. As a consequence, only relatively low critical adiabaticity could be achieved for the

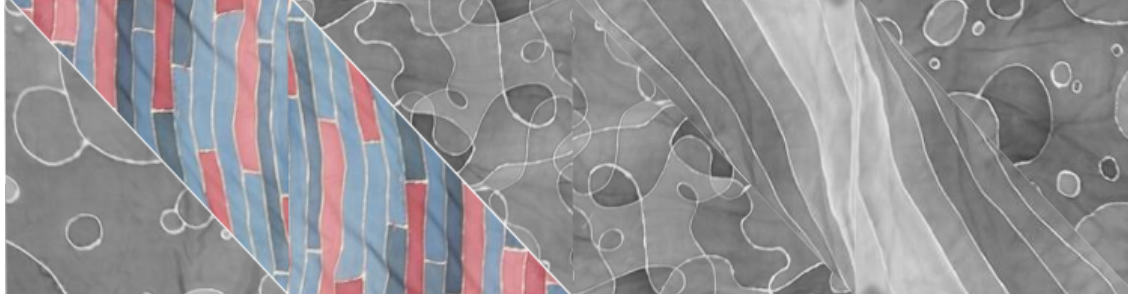
given durations of the chirp pulses, which was not sufficient to obtain full inversion of the nitroxide spectrum by the pump pulse. The DEER detection was performed at 30 K on the maximum of the Cu(II) spectrum with pulse lengths of 48 ns, resp. 96 ns pulses (for $\pi/2$, resp. π nominal flip angle). The broad resonator mode used in this setup did not allow for harder pulses due to insufficient microwave power. The delays were set to $t_1 = 400$ ns, and $t_2 = 3500$ ns. In order to maximise modulation depth we aimed at performing an inversion pulse over the full range of the nitroxide spectrum. To this end we used a linear up-chirp pump pulse with a bandwidth of 450 MHz, and an offset from the detection frequency of +900 MHz, with a pulse duration of 150 ns.

7.4.3 RIDME setup with coherent chirped broad-band pulses

All chirp-RIDME experiments were conducted at 20 K with a mixing time of $T_{\text{mix}}=1.6$ ms and at the condition $t_1 = 3.5$ μ s. The same stationary refocused virtual echo as in the experiments with rectangular pulses was detected (RIDME RVE echo). For orientation averaging the echo was integrated and the resulting dipolar evolution data were treated like a conventional RIDME trace. In addition, EPR-correlated dipolar spectra were computed by 2D Fourier transformation (FT) as follows. First, the transient time trace of the RIDME RVE echo for each position of the RIDME mixing block was apodized by a symmetric Chebychev window. FT of the RIDME RVE echo yielded the nitroxide EPR spectrum dimension. Then, the RIDME time trace at each discrete point in the nitroxide spectrum was fitted with a stretched exponential background function, the form factor was obtained by division of the primary data by the fit, and the constant offset was subtracted. After a second FT along the RIDME time dimension, i.e. the time that defines the starting position of the mixing block in the RIDME sequence, we obtained the EPR-correlated dipolar spectrum.

7.4.4 Synthesis of the Cu(II)-nitroxide rulers

The synthesis design was performed in the group of Adelheid Godt at Bielefeld University. The design was led by the goal of establishing a generally applicable procedure for the preparation of metal ion-nitroxide rulers which are soluble in water and water containing organic solvents. Such a solubility profile allows to test the spectroscopic tool under conditions used for its application to biomolecules. A further design criterion was that the ligand, which is needed for anchoring the metal ion, forms stable complexes with several metal ions of importance for metal ion-nitroxide EPR spectroscopy.^[3,32,33,103,146,151,193,194,209,226,246,255,306] To reach these goals the rod-like spacer was furnished with highly hydrophilic, branched oligo(ethyleneglycol) (PEG) chains and the ligands PyMTA^[55,161,290] and TAHA^[56,161,293] were selected (Figure 7.1). These ligands form readily 1:1 complexes with Cu(II) ions as well as with other paramagnetic ions, such as Mn(II)^[161] and Gd(III)^[56] and are of small size which becomes relevant when being used as spin labels. Cu(II)-nitroxide rulers and, more generally, compounds labeled with Cu(II) and nitroxide, reported in the literature, contain terpyridine (terpy),^[102,208,226] porphyrine,^[32] peptide-based binding loops,^[297] as the Cu(II) binding unit. For more details on the synthesis we refer to the corresponding sections in Ritsch et al.^[250].



Chapter 8

Distance measurements by nitroxide-high spin metal ion RIDME

As we have seen in Chapter 7, the RIDME experiment is very well suited for distance analysis between nitroxide and the low-spin metal ion centre Cu(II) due to the intrinsic longitudinal relaxation differences. Apart from special experimental considerations (to remove or suppress artifact contributions that may appear more strongly in RIDME compared to DEER) we can use the standard point-dipole model for data analysis, with a fixed (orientation and distance dependent) dipole-dipole coupling frequency ω_{DD} . It would be very convenient if this methodology could also be applied for interpretation of RIDME experiments measured with nitroxides and high-spin metals, but an additional consideration must be made in these situations. Due to the possibility of the high-spin centre to change the magnetisation projection state m_S by more than one unit, we expect to observe higher harmonics of the dipolar coupling.^[163] The harmonics must be taken into account for data analysis, or otherwise they lead to artifact peaks in the distance distribution. If this can be successfully achieved we can use RIDME as an attractive alternative PDS method to the well-established nitroxide-high-spin metal ion DEER.

Scope of this chapter We first summarise the previously reported results with high-spin metal ion centres in RIDME, and we introduce shortly the theoretical models that have been proposed to describe the build-up of higher harmonics contributions in RIDME. We introduce an empirical modelling protocol for the build-up of harmonic overtones during the mixing time, with which we can generate harmonics-adapted kernels for the analysis of nitroxide-high-spin metal ion-RIDME. The analysis requires only knowledge of the (experimentally obtainable) longitudinal relaxation

rate of the metal ion spin, and no additional or external calibration is required. We demonstrate the robustness of the approach on several molecular rulers, and results obtained with spin-labelled oligo-proline peptide samples.

8.1 Introduction

Nitroxides, as well as high-spin metal ion centres are prominent examples of spin labels used for the characterisation of biomolecules by EPR.^[23,163,313] For example the DEER experiment between stable Gd(III) complexes and nitroxide spin labels for distance measurements in the nanometer regime has been developed.^[96,97,107,246,247] As we have described in Chapter 6, it is favourable in many situations to pump the nitroxide spins and detect the Gd(III) spin. Sensitivity of DEER with nitroxide-Gd(III) pairs is high in this experimental configuration, because large modulation depths can be achieved by pumping the comparatively narrow spectrum of the nitroxide spin and detecting the usually intense central transition of Gd(III)-complexes (as long as the zero-field splitting is small).^[96,162,163] It has been demonstrated that good sensitivity can be achieved with broadband inversion of the Gd(III) centre (as was demonstrated with Gd(III)-Gd(III) spin pairs^[75,78]), which should also translate to nitroxide-Gd(III) pairs, but this requires modern broadband or even ultra-wideband microwave pulse instrumentation.

In RIDME, the detection must, by design of the experiment, occur on the more slowly relaxing spin, which in this study is always a nitroxide spin. It is thus a complementary method to the conventional setup of nitroxide-metal ion DEER. In general, the benefit that RIDME experiments can have over DEER experiments is that MW pulses need only be applied at a single MW frequency, and therefore a high quality factor of the resonator can be used. It is expected, however, that this sensitivity benefit can get strongly reduced because the nitroxide transverse relaxation may be enhanced due to the presence of the high-spin metal ion spin (which is mostly relevant for short distances).^[195,313] The generally fast background decay in RIDME (especially in protonated solvents) is another issue for sensitivity.

The contributions of higher harmonics have been investigated in detail with several molecular rulers with Gd(III)-,^[162] and Mn(II)-complexes.^[161] In the case of metal ion-metal ion RIDME it was found that the relative contribution to the dipolar modulation of the higher harmonics is rather stable for a given complex of the metal ion, and in particular does not depend significantly on T_{mix} , or the experimental temperature.^[162,247]

In this chapter we report nitroxide-Gd(III) and nitroxide-Mn(II) RIDME experiments with molecular rulers (see Figure 8.1). The molecular rulers carry one nitroxide moiety and one metal-chelating moiety, separated by a variable length spacer. The length of the spacer is given by the number of repeating spacer units, which are functionalised with polyethylene-glycol chains to obtain water soluble rulers.^[250] The interspin distance between the molecular rulers is well-defined, as was shown with the Cu(II)-loaded variants. The intermediate stiffness of the spacer was found to result in moderate orientation selection at Q-band for RIDME performed with nitroxide detection.^[250] The orientation selection arises from the orientation of the nitroxide spin, and we thus also expect to observe it with the same ruler precursors loaded with other paramagnetic metal ions. In this study we use the following nomenclature for the high-spin metal ion-loaded rulers: rulers carrying the TAHA ligand moiety are denoted as ruler **1**, and rulers with the PyMTA moiety are denoted as rulers **2**, and the number of spacer units n is given as a subscript. The loaded metal is denoted explicitly. For example, the ruler **1**₁-Gd(III) is the [Gd(III)-TAHA] ruler with one spacer unit, which has an expected interspin distance of $R \approx 2.5$ nm. This is the only length of TAHA-based

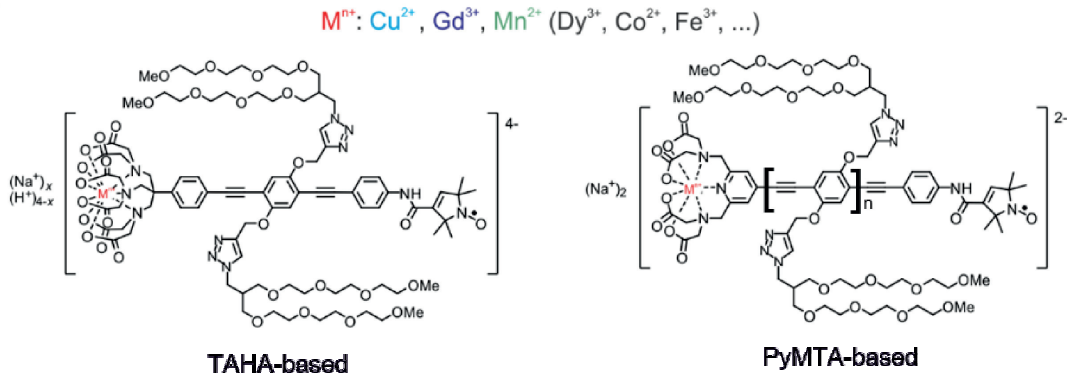


Figure 8.1: Chemical structures of the molecular rulers; left: TAHA-based ruler; right: PyMTA-based rulers with $n = 1$, or $n = 3$ spacer units;

ruler that we use in this work. For the PyMTA based rulers we use the ruler precursors (before metal ion loading) $\mathbf{2}_1$ ($R \approx 2.5$ nm), and $\mathbf{2}_3$ ($R \approx 3.7$ nm), which were then accordingly loaded with either Mn(II) or Gd(III). In contrast to what was presented for metal-metal RIDME, in the nitroxide detected RIDME we see a build-up of the higher harmonics contributions as a function of temperature and T_{mix} . This is an important finding both for the application of RIDME for distance measurements with nitroxide-high-spin metal ion pairs, as well as for fundamental studies on the processes that govern the time-evolution of the ensemble of spin states of the high-spin metal ions.

8.2 Theory

For the general considerations of dipolar coupling and pulsed dipolar spectroscopy please see Section 2.5.3 in Chapter 2. Here we introduce what additional considerations need to be made for RIDME experiment when the detected spin (A spin) is low-spin $S = 1/2$, and the inverted spin (B spin) is a high-spin centre $S > 1/2$. In the following R is the interspin distance, θ the dipolar angle of the interspin vector with the external magnetic field, and ω_{DD} is the dipolar coupling frequency.

8.2.1 Dipolar coupling with high-spin systems

We assume that both A and B spins are quantized along the same axis (by convention $\vec{B}_0 \parallel z$), which results in $m_S = -S, -S + 1, \dots, +S$ magnetic sublevel states (eigenstates of the respective \hat{S}_z operators). This condition is virtually always fulfilled for PDS at commonly used EPR bands with organic radicals, such as nitroxides or trityls, as well as low-spin transition metal ions like Cu(II), because the Zeeman interaction \mathcal{H}_Z is the dominating interaction of the EPR Hamiltonian. For high-spin metal ions the approximation may break down in cases when the zero-field splitting \mathcal{H}_{ZFS} is on the same scale or even larger than the Zeeman term. In the following we thus restrict the discussion to the important case of Kramers-type high-spin metal ions (which have half-integer

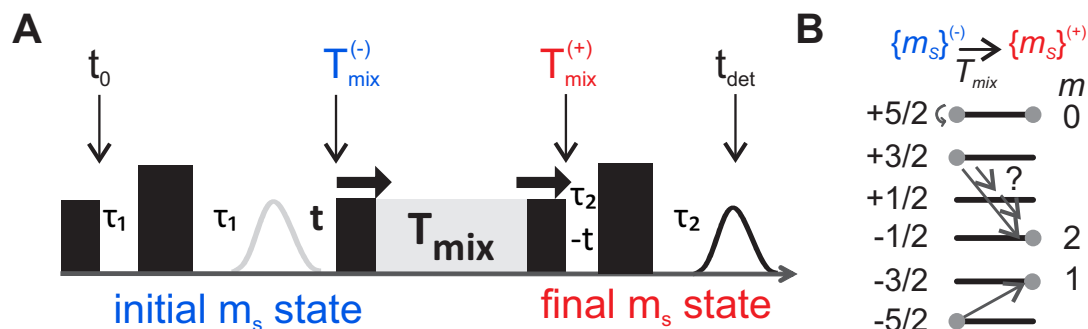


Figure 8.2: (A) 5-pulse RIDME sequence^[210] (B) schematic representation of magnetic sub-levels for an $S = 5/2$ spin; the initial spin state configuration $\{m_s\}^{(-)}$ is converted during T_{mix} to a new configuration $\{m_s\}^{(+)}$; three possible transitions are shown, but there may be many pathways and mechanisms that lead to the same effective change m .

spin) with a weak zero-field splitting ($\mathcal{H}_{\text{ZFS}} < \mathcal{H}_{\text{EZ}}$). Many Gd(III)-, and Mn(II)-complexes that were developed and used extensively for application in spin-labelling EPR are representatives of this class.

We furthermore assume that the dominating coupling between the nitroxide and the metal ion spin is dipolar coupling, and for the remainder of this chapter we furthermore assume that the weak coupling approximation is valid, i.e. only the secular terms of the dipolar coupling Hamiltonian is used (Equation (2.15) in Chapter 2). We furthermore neglect any (weak) electron spin exchange coupling contributions between the nitroxide and the high-spin metal ion (which are not expected to be relevant for most applications of RIDME as a distance measurement tool in structural biology). To be able to interpret dipolar data in the presence of the higher harmonics terms we want to know their relative contributions to the total dipolar modulation depth. This means that we have to find a description of the set of weighting factors $\{p_1, p_2, \dots\}$ of the harmonic overtones that quantify the distribution of the effective change of B spin magnetic state $m \equiv |\Delta m_S|$ in the sub-ensemble of B-spin that are coupled to the detected A spins (illustrated in Figure 8.3).

8.2.2 Harmonic overtones in dipolar spectroscopy

Because typical EPR spectrometers are only able to produce m.w. pulses frequencies at a certain microwave band and bandwidth, it is highly unlikely that spin inversion occurs with $|\Delta m_S| > 1$ in PDS experiments that use a microwave pulse for inversion of the B spin. An exception is when the B spin is a high-spin centre, and inversion by the microwave pulse occurs close to an avoided energy level crossing, where level mixing can mix states of different m_S . This has been experimentally observed in Gd(III)-Gd(III) distance measurements by DEER at short inter-spin distances ($R \lesssim 3$ nm), but can be neglected otherwise.^[60,61,67,162]

In RIDME the inversion occurs stochastically throughout the entire spectrum, and $|\Delta m_S| > 1$ is possible (illustrated in Figure 8.3). In principle it can occur also throughout the entire RIDME pulse sequence, but if B-spin relaxation events happen at random times during the transverse evolution period, the dipolar phase is not refocused at the RIDME zero-time. Instead this is

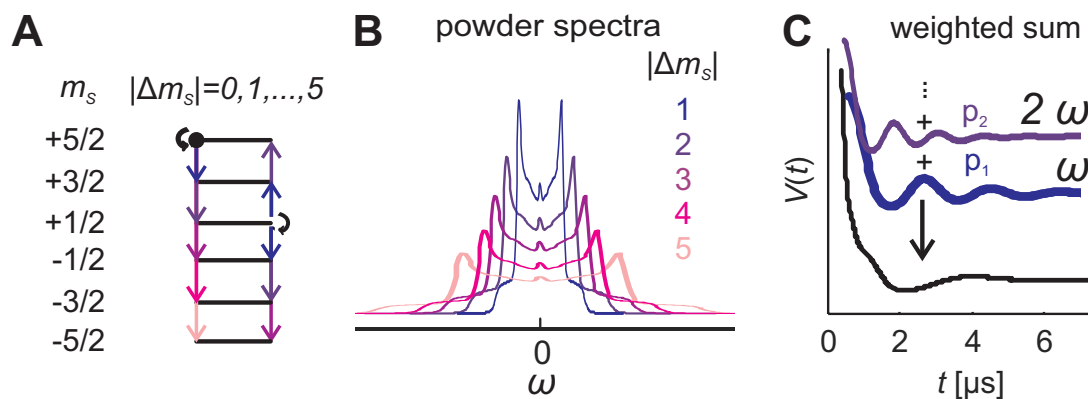


Figure 8.3: Dipolar coupling with $S > 1/2$; (A) schematic Zeeman energy level splitting for $S = 5/2$; two possible spin states and respective possible effective magnetic sublevel changes, and the range of $|\Delta m_s|$ for the two cases are indicated; (B) resulting effective stretching on the Pake dipolar coupling spectrum for spin transitions of order $m = |\Delta m_s|$; (C) expected dipolar evolution trace (black), and decomposition into the harmonic contributions with coupling frequency $m \cdot \omega_{DD}$ with weights $\{p_m\}$;

observed as a contribution to the background decay.^[164] RIDME typically still performs well, because usually the total transverse evolution time $t_{\text{trans}} = 2t_1 + 2t_2$ is short compared to the longitudinal relaxation time of the metal ion spin T_1 . In the following we assume that longitudinal relaxation of the high-spin metal ion B spin only occurs during T_{mix} . The dipolar coupling to the A spin thus effectively changes instantaneously upon conversion of the initial set of B spin states before the mixing block $\{m_s\}^{(-)}$ to the states after the mixing block $\{m_s\}^{(+)}$ (see Figure 8.2). In nitroxide-detected RIDME we (ideally) never excite any metal-ion spins with microwave pulses, and the total ensemble of metal-ion spins is thus considered to be constantly at thermal equilibrium, where the states are populated according to Boltzmann statistics. We also expect $\{m_s\}^{(-)}$ to be approximately Boltzmann distributed. However, the time-evolution of this sub-ensemble of B-spins may (transiently) adopt non-Boltzmann distributions of the magnetisation states.

Expected limiting values The maximum possible inversion of the B spin is given by $m^{(\text{max})} = 2S$, which corresponds to going from the lowest to the highest magnetic sub-level (or vice versa). All integer values of m in between are in principle possible, but note that the starting level matters for each particular spin (because m_s is bounded, see Figure 8.3). The effective maximum m that can be reached from a given starting level is $m^{(\text{max})}(m_s) = S \pm m_s$, where the negative sign is valid for starting levels $m_s < 0$, and the positive sign for $m_s > 0$. Inversely, we can count the combinations of initial/final state pairs that lead to the same effective m , which gives the number of effective pathways $N_m = 2(2S + 1 - m)$ that result in an effective change m (which is also valid for no effective change, $m = 0$). The factor 2 accounts for the 'up', resp. 'down' flips, which we cannot distinguish. At steady-state we expect the coefficients of m -th higher harmonic to be given

by

$$P_m^{(\text{lim})} = \frac{N_m}{N_{\text{total}}}, \quad (8.1)$$

which is normalised to the total number of possible initial/final state pairs $N_{\text{total}} = (2S + 1)^2$. Because we do not observe dipolar modulation from $m = 0$, we additionally define the relative contributions p_m , which are re-normalised to all observable contributions ($m > 0$) that contribute to the modulation depth, which we will later see can be used in the generation of kernels to fit dipolar evolution data

$$p_m = \frac{P_m}{\sum_{m>0} P_m}. \quad (8.2)$$

This treatment implies that the maximum attainable modulation depth is given by

$$\Delta^{\text{max}} = \sum_{m>0} N_m/N_{\text{total}} = 1 - N_0/N_{\text{total}} \quad (8.3)$$

$$= 1 - 1/(2S + 1). \quad (8.4)$$

It is possible that this value cannot be experimentally reached due to so-called 'flip-flop' events, which influence the relaxation of the detected A-spins, as was observed in RIDME with (low-spin) nitroxide-Cu(II) rulers.^[250] Also in metal-metal RIDME it was observed that a loss of modulation depth can occur, and this is also expected to have an influence on the build-up of the harmonic overtones.^[161,162]

Build-up of harmonic contributions So far we have not made any consideration on how the magnetic sub-level change occurs, and for the remainder of this chapter we will remain with this phenomenological description. Note that it has been described that in principle m can be reached either via direct processes (i.e. a spin state m_s directly converts to any other spin state $m_s \pm m$), or it can be reached via a chain of step-wise processes ($m_s \rightarrow m_s + 1 \rightarrow m_s + 2 \rightarrow \dots$).^[162,247] For either scenario (or a combination thereof) it is possible to design a set of differential equations that describe the changes of the populations of the B-spin magnetic moment states. A step-wise process was expected to be the better model, but the experimentally observed metal-metal RIDME coefficients could not directly be predicted.^[162,247] Together with the observation that the modulation depths were below the theoretically possible limit in metal-metal RIDME, the discrepancy points towards B-spin dependent relaxation of the A-spin via flip-flop events, or some degree of direct process occurring.^[162]

8.2.3 Kernel-based data analysis of RIDME experiments with harmonic overtones

Modification of the standard dipolar kernel function (see Equation (2.34) in Chapter 2) used to fit dipolar time-domain data with distance distributions have been reported successfully for metal-metal RIDME.^[162] In these cases the series of coefficients was truncated at order $m = 3$, because no higher orders were identified with significant intensity in the dipolar spectra. Furthermore,

and surprisingly, the coefficients were found to be largely independent of T_{mix} . Therefore the coefficients p_1 to p_3 (with $p_1 + p_2 + p_3 = 1$) could be calibrated with a set of molecular rulers, and data analysis can be performed with a modified kernel

$$K_{\text{mod}}(r, t) = \int [p_1 \cdot \cos(\omega(r, \theta) t) + p_2 \cdot \cos(2 \cdot \omega(r, \theta) t) + p_3 \cdot \cos(3 \cdot \omega(r, \theta) t)] \sin(\theta) d\theta. \quad (8.5)$$

It was reported that the coefficients varied between different metal ion chelators for the high-spin metal ions, but seemed to be stable after calibration. For example for Gd(III)-PyMTA the recommended contributions are $p_1 = 0.51$, $p_2 = 0.40$, and $p_3 = 0.09$.^[162]

Due to the different properties of the nitroxide and the high-spin metal ions (e.g. the significantly slower longitudinal relaxation of the nitroxide spin) we may be able to observe also experimentally the dipolar orders higher than $k = 3$ in nitroxide-metal ion RIDME. We therefore pre-emptively introduce a generalised kernel with an in principle arbitrary number of coefficients p_m

$$K_{\text{mod}}(r, t) = \int \left[\sum p_m \cdot \cos(m \cdot \omega(r, \theta) \cdot t) \right] \sin(\theta) d\theta, \quad (8.6)$$

$$(8.7)$$

where we assume that the relative coefficients are normalised ($\sum_m p_m = 1$). The ultimate goal is to find a general rule to derive the set of coefficients p_m for a given (orthogonal) RIDME experiment without any case-by-case calibration (which may not be possible). In the following sections we describe a framework how models for such sets of coefficients can be empirically constructed and tested.

Empirical coefficients build-up models For the moment we neglect flip-flop event, and we introduce an empirical framework to study the build-up of dipolar harmonics. We hypothesise that, independent of the exact mechanism, the coefficients for the higher harmonics build up to some limiting values $P_m^{(\text{lim})}$ (the 'plateaus') following an exponential law

$$P_m(T_{\text{mix}}) = P_m^{(\text{lim})} (1 - \exp(-k_{\text{eff},m} T_{\text{mix}})), \quad (8.8)$$

$$p_m = P_m / \sum_{m>0} P_m, \quad (8.9)$$

where $k_{\text{eff},m}$ is the effective build-up rate of the m -th harmonic. The build-up rates are expected to be proportional to the longitudinal relaxation rate of the metal ion spin ($k_{\text{eff},m} \propto 1/T_1$), but do not necessarily have to be the same for all m . The resulting variations of p_m (the relative fraction of the harmonic contributions to Δ , see Equation (8.9)) are highly non-intuitive, due to the constantly changing normalisation as a function of the total modulation depth ($\Delta(T_{\text{mix}}) = \sum_{m>0} P_m(T_{\text{mix}}) T_{\text{mix}}$). Numerical simulations for a simple model (all transitions in principle build up with $k_{\text{eff},m} = 1/T_1$, but build up to different levels $P_m^{(\text{lim})}$) can be found in Appendix E. In this numerical treatment it is also conveniently possible to include differences in the A-spin relaxation of the different harmonics due to flip-flop terms (an example is also shown in Appendix E).

8.3 Materials and Methods

All RIDME experiments were performed at Q-band (34-36 GHz). The EPR samples of the molecular rulers were prepared as 100 μM solutions in a mixture of D_2O and d_8 -glycerol in a 1:1 volume ratio. The spin labelled poly-proline samples were already available in the group, where the spin labels are nitroxide and Gd(III)-DOTA.^[97] The measurement temperature was varied between 10 K and 50 K, using an Oxford Instruments He-flow cryostat system. For each sample, the metal ion-nitroxide ruler solution was filled into a 3 mm outer diameter thin-wall quartz tube and shock frozen by quick immersion into liquid nitrogen.

For the RIDME experiments we used a home-built resonator, accommodating large-diameter samples,^[289] and a commercial Bruker E580 X/Q spectrometer upgraded to a high MW power.^[238] Unless stated otherwise the first inter-pulse delay t_1 was set to 5200 ns, which was used as a compromise between signal decay and background artifact intensity.^[250] The length of the second delay t_2 was set to 5000 ns for the long rulers (ruler **2**₃-Mn(II), results shown in Figure 8.4, resp. ruler **2**₃-Gd(III)), resp. 3500 ns for the short rulers (ruler **1**₁-Gd(III) and ruler **2**₁-Gd(III), and ruler **2**₁-Mn(II), results shown in Appendix E). The delays for the poly-proline samples were: $t_1 = 400$ ns for all measurements, and the second refocusing delay was adapted to the expected main distance, thus for the samples with expected distances $R_{\text{expect}} = \{2; 3; 4; 5\}$ μm , we used $t_2 = \{4; 4.4; 4; 5\}$ μs , respectively. The mixing time values were varied between different RIDME measurements, and are indicated in the text and in the figure captions. Unless stated otherwise the detection position was at the maximum of the nitroxide spectrum, and we used pulse lengths of 12 ns for $\pi/2$ pulses, and 24 ns for π pulses. For all RIDME measurements we used a deuterium ESEEM averaging scheme (8 times 16 ns steps).^[160] No orientation averaging was performed.

8.4 Results

In Figure 8.4 we show RIDME experiments measured on at 100 μM sample of ruler **2**₃-Mn(II) in deuterated buffer at 10 K. We clearly see that the modulation depth Δ strongly increases, and that the background decay becomes more steep as a function of mixing time. Note that indeed we found that the RIDME background decay is slightly distorted at early and late times if a short first refocusing delay t_1 is used (data not shown), as was reported with analogous nitroxide-Cu(II) rulers.^[250] An overlay of the form factors after stretched exponential background fit (scaled to unit modulation depth) is shown for early times in panel (D) of Figure 8.6. From the high modulation depths (almost up to the theoretical limit), and the appearance of the form factors it is apparent that in contrast to metal-metal RIDME, also high harmonics ($m > 4$) are observed. It furthermore appears that the relative dipolar contributions from higher harmonics are slightly changing with T_{mix} . We demonstrate in Figure 8.4(B,C) that if the higher harmonics are not accounted for in the dipolar kernel, we still get very good fits, but the fitted distance distribution contains strong artifact distance peaks, that correspond to a mis-interpretation of the intensity at $2\omega_{\text{DD}}, 3\omega_{\text{DD}}, \dots$ (true expected peak at $R \sim 3.9$ nm).

Without any fundamental explanation we report that very good fits and almost artifact-free dis-

tance distributions (Figure 8.4(E,F)) could be obtained with a fully empirical kernel model that takes all possible five harmonics (for $S^{\text{Mn(II)}} = 5/2$) in to account as

$$p_{m>0}(T_{\text{mix}}) = \frac{1}{2S} [1 - \exp(-T_{\text{mix}}/(mT_1))]. \quad (8.10)$$

This model assumes that the higher order contributions build up more slowly than the low order transitions, with rates $k_{\text{eff},m} = k_{\text{eff},1}/m = 1/(mT_1)$, and that the transitions build up to the same final values $P_{m>0}^{(\text{lim})} = 1/(2S)$. The latter is not expected from the theory, where higher order coefficients should converge to lower plateau values (see Equation (8.2)), which could in principle also be tested in the future. The analysis requires the knowledge of the experimentally used mixing time and the longitudinal relaxation time T_1 of the metal ion spin. The latter can for example be determined specifically for each sample by an inversion recovery experiment. Note that analysis with this kernel is expected to fail with this model, if T_1 of the high-spin species is strongly distributed. The first is not expected if the high-spin metal is in a stable complex with a chelator,^[163] unless a fraction of the metal-ion spins is aggregated in clusters, or exposed to severely different chemical environments. Note that no systematic comparison of kernel models was performed yet, and that it may well be that a better model than Equation (8.10) can be found to describe the build-up kinetics. Nonetheless, the fit of the dipolar data with this modified kernel is very good with all three fitted modulation depths, that span a large range of ratios of metal ion relaxation time and mixing time ($T_1(10\text{K}) = 88 \mu\text{s}$, and $T_{\text{mix}} = \{15, 50, 500\} \mu\text{s}$).

| T_{mix} | Δ | p_1 | p_2 | p_3 | p_4 | p_5 |
|-------------------|----------|-------|-------|-------|-------|-------|
| 15 μs | 0.165 | 0.42 | 0.22 | 0.15 | 0.11 | 0.09 |
| 50 μs | 0.255 | 0.40 | 0.23 | 0.16 | 0.12 | 0.10 |
| 500 μs | 0.662 | 0.24 | 0.22 | 0.20 | 0.18 | 0.16 |

Table 8.1: RIDME with ruler **2**₃-Mn(II) at 10 K, where the Mn(II) relaxation time was determined to be $T_1 = 88 \mu\text{s}$ (at the centre of the spectrum); modulation depth Δ , and empirically derived kernel coefficients for RIDME with Equation (8.10); an extended table including the measurements at 30 K and 50 K can be found in Appendix E.

Interestingly, the model was also able to recover almost artifact-free distance distributions for a range of mixing times at a different temperature (30 K, see Figure 8.5(B)), where the metal ion relaxation time is much faster ($T_1(30\text{K}) = 3 \mu\text{s}$). At an even higher temperature (50 K, see Figure 8.5(C)) the model seems to break down, and artifact peaks appear at both too short and too long distances (Figure 8.5(C)). At this temperature we also observe that the plateau modulation depth is lower than the maximum possible level (see Table 8.1), so either flip-flop events may become strong, or the metal ion spin relaxation is so fast that significant number of spin flips can also occur during the transverse evolution period.

We also measured RIDME data with Gd(III)-based molecular rulers, and the results with the long ruler **2**₃-Gd(III) are shown in Figure 8.6. Also in the case of this $S = 7/2$ spin we fitted the background corrected RIDME form factors with a kernel calculated using harmonic overtone coefficients according to Equation (8.10), including harmonics up to order $m = 7$. The resulting

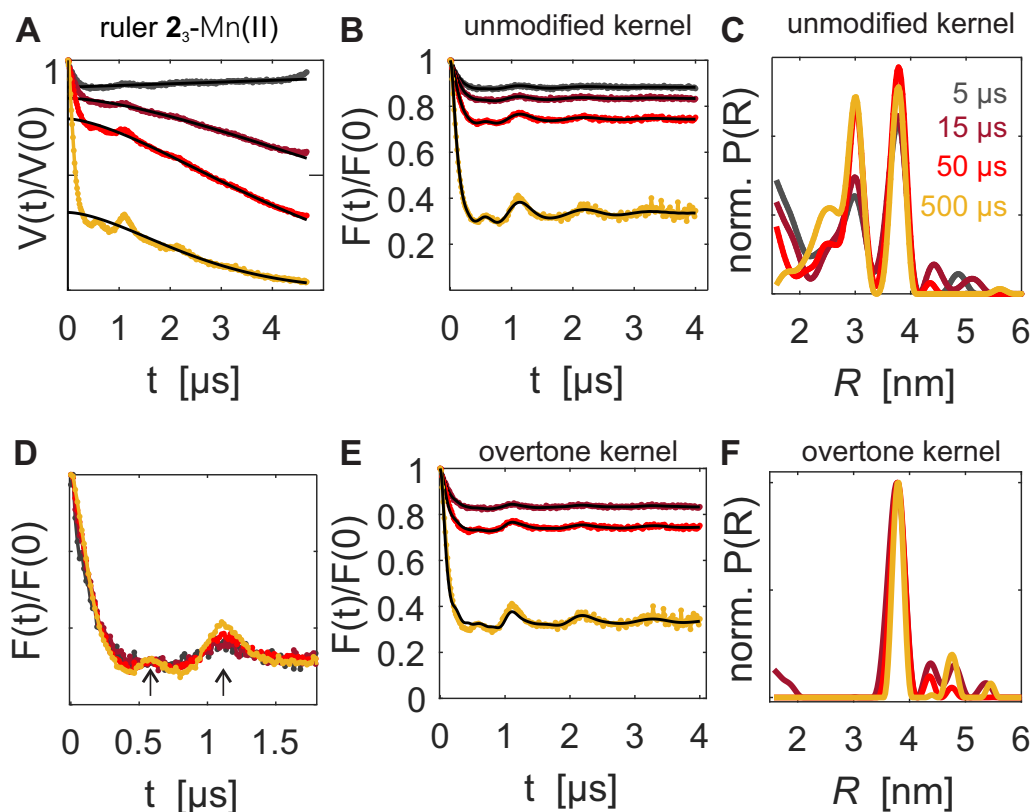


Figure 8.4: RIDME with ruler 2_3 -Mn(II) at 10K; (A) primary data and stretched exponential background fits for RIDME measured with increasing T_{mix} ; (B,C) data analysis with standard DeerAnalysis kernel without overtone correction, (B) form factors and fits (black), (C) distance distributions normalised to unit area; (D) overlay of form factors; (E-F) data analysis with high harmonics adapted kernel; (E) form factors and fits (F) distance distributions normalised to unit area;

distance distribution is a single narrow peak at the expected distance ($R = 3.9$ nm). We also performed measurement with the shorter molecular ruler 2_1 -Gd(III), as well as with the short linker with a different metal chelator (1_1 -Gd(III)) and the results can be found in Appendix E. All experiments with the shorter rulers were measured with short first refocusing delay $t_1 = 400$ ns, and thus we observed that the known low-frequency background artifact in nitroxide-detected RIDME at Q-band (compare Chapter 7) was comparatively strong and lead to a small artifact peak in the distance distribution at approximately 3 nm). Apart from this contamination, the adapted kernel fitting resulted in a narrow single peak at the expected distance ($R = 2.7$ nm) for ruler 2_1 -Gd(III) (PyMTA ligand), and a slightly shorter distance ($R = 2.5$ nm) for ruler 1_1 -Gd(III) (TAHA ligand). Interestingly, while the longitudinal relaxation time for Gd(III) in the two samples was very similar (e.g. at 20 K: $T_1(\text{ruler } 1_1\text{-Gd(III)}) = T_1(\text{ruler } 2_1\text{-Gd(III)}) = 7 \mu\text{s}$), the achievable modulation depths were rather different. This is summarised for all Gd(III)-based rulers in Figure 8.6. This suggests that Gd(III) loading of the TAHA complex was lower than of the PyMTA complex, but in fact the

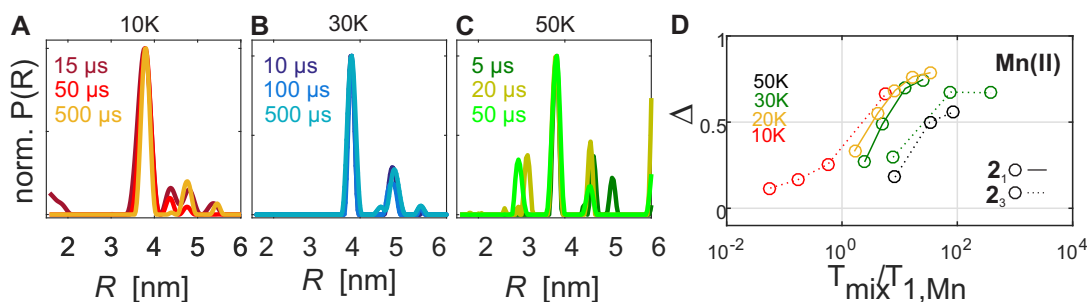


Figure 8.5: Kernel stability with RIDME with ruler 2_3 -Mn(II) at three different temperatures; (A) 10 K; same fit and conditions as in Figure 8.4 (B) 30 K; (C) 50 K; kernel coefficients are listed in Table 8.1; (D) modulation depth Δ as reported by DeerAnalysis after stretched exponential background correction with RIDME with rulers 2_1 -Mn(II) (solid lines), and 2_3 -Mn(II) (dashed lines); due to SNR limitations the series at 30 K and 50 K were measured with a first refocusing delay $t_1 = 400$ ns, which may slightly bias the fitted modulation depth due to a known background artifact.

opposite trend was observed in Gd(III)-nitroxide DEER (where the better modulation depth was found with the TAHA complex than with the PyMTA complex, see Appendix E). To some extent the modulation depth estimate can also be biased by the background artifact,^[250] which may explain why the extracted modulation depth for the TAHA-based ruler 1_1 -Gd(III) is unexpectedly higher at 30 K than at 20 K.

As a final proof of principle and outlook we show data obtained with another type of model system, the orthogonally spin labelled poly-proline samples reported in Garbuio et al.^[97] The samples were already available in the group, and provided with reference distance distributions from $R \approx 2$ nm to $R \approx 5$ nm, which are well-characterised by Gd(III)-nitroxide DEER.^[97] The results are shown in Figure 8.7. Because the data were measured before the RIDME optimisation with the molecular rulers was available (which allowed the systematic investigation of the background artifact and modulation depth build-up) the measurement conditions were not ideal for some poly-proline measurements, but we see that in general the adapted kernel-fitting procedure also seems to be a promising approach. For example, we used a short first refocusing delay $t_1 = 400$ ns, which is expected to lead to a small background artifact. Fortunately, the sample deuteration is much lower in the poly-proline samples (35 % d_8 -glycerol in H_2O) than in the molecular ruler samples (50 % d_8 -glycerol in D_2O), and the background artifact is thus not very strong, as expected (compare BG artifact section in Chapter 7).^[250] In all four tested cases we are able to identify the expected main distance peak in the RIDME experiment using the kernel adapted according to Equation (8.10). Both the shortest and the longest distance measurement by RIDME, however, we do not fully recover the shape of the distance distribution with DEER, which might be partially due to (weak) orientation selection (RIDME data measured only at the maximum of the nitroxide spectrum).

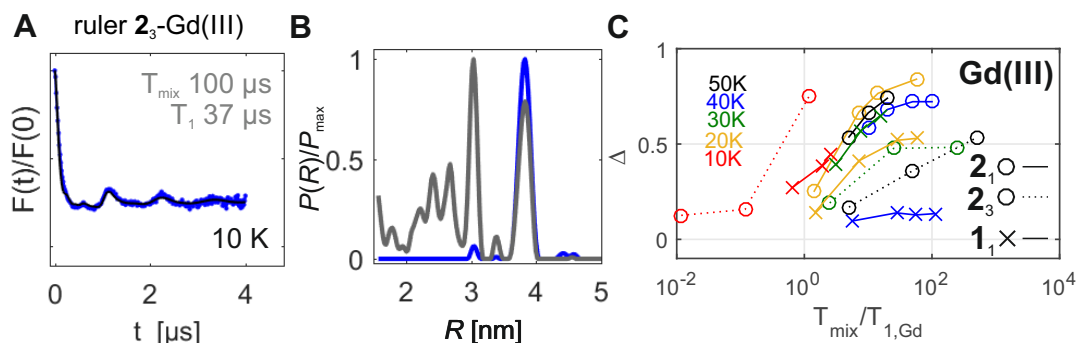


Figure 8.6: RIDME with Gd(III)-based rulers (A) form factor and adapted kernel fit with $\{p_1, p_2, \dots, p_7\} = \{0.31, 0.20, 0.14, 0.11, 0.09, 0.08, 0.07\}$ after stretched exponential background fit for RIDME with ruler 2_3 -Gd(III) at 10 K (B) modulation depth Δ as reported by DeerAnalysis after stretched exponential background correction;

8.5 Discussion and Outlook

Nitroxide-detected nitroxide-high-spin metal ion RIDME was tested as a method to accurately measure distances in the nanometer range in water soluble molecular rules, as well as poly-proline model compounds. It seems unlikely that Gd(III)-nitroxide RIDME will surpass DEER sensitivity in routine applications, due to the fast background decay, as well as the fast transverse relaxation of the nitroxide spins in the presence of the high-spin metal-ion spins. The sensitivity was not systematically compared, but for example in the measurement series with the poly-proline samples in mostly protonated solvent (see Figure 8.7) we systematically could measure only significantly shorter RIDME traces than the DEER traces reported in Garbuio et al.^[97] with exactly the same samples. Nonetheless RIDME can be a powerful complimentary tool to DEER, for example in situations where the Gd(III) ions are present in excess over the nitroxide spins. We clearly observed in all studied samples (Mn(II) and Gd(III) in different chelators) that higher harmonics contribute to high-spin metal ion-nitroxide RIDME, than were reported for the metal ion-metal ion RIDME.^[162,247] Furthermore, the coefficients of the higher harmonics were found to vary as a function of mixing time. If accounted for accurately, the presence of higher harmonics may in fact be beneficial for the sensitivity of RIDME, because in principle the same information is encoded multiple times already in the early part of the dipolar evolution trace. Of course this only helps if the background correction can be performed accurately, which may still require to measure long traces. We observed that the modulation depths that we could reach at low temperature (10 K) were close to the theoretical limit for Boltzmann statistics. At higher temperatures (30 K and above) we found lower plateau values for the modulation depth, as was already reported with low-spin molecular rulers (nitroxide-Cu(II), compare Chapter 7).^[250]

We performed distance analysis of the RIDME data using a modified kernel with higher harmonics terms up to the maximum possible transition for each spin type ($m = 7$ for Gd(III), resp. $m = 5$ for Mn(II)). We used a purely empirical model to determine the coefficients from just the experimentally used mixing time T_{mix} , and the experimentally determined longitudinal relaxation time

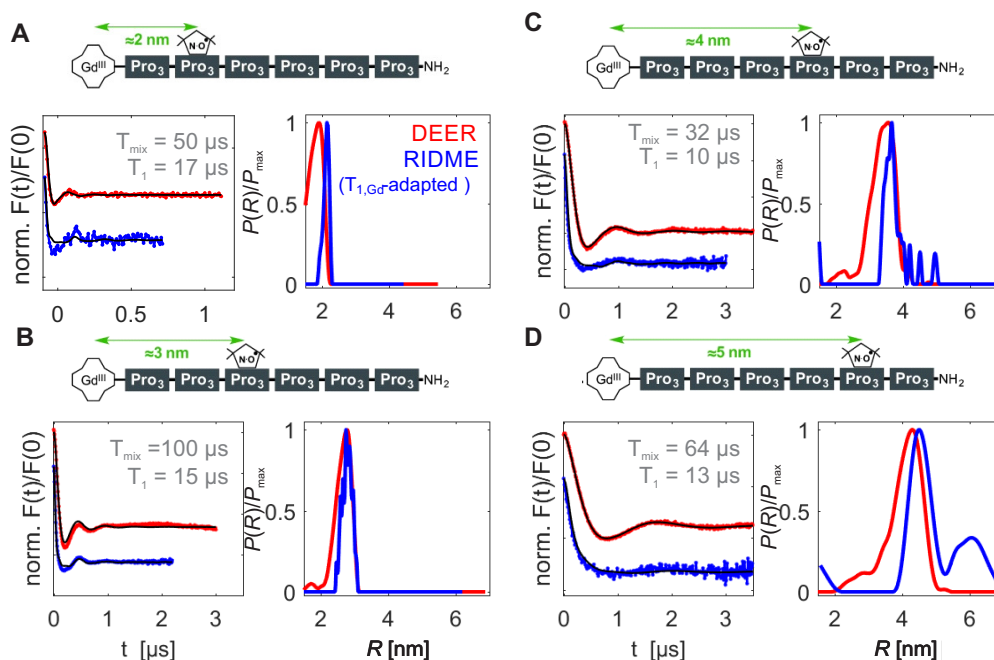


Figure 8.7: RIDME with Gd(III)-DOTA and nitroxide labelled poly-proline samples; samples were measured at 20 K, mixing times, and metal ion T_1 are indicated, kernel coefficients were calculated according to Equation (8.10); poly-proline schemes and DEER distance distributions adapted from Garbuio et al.^[97]; (A-D) left panels: form factors and fits for DEER (red) and RIDME (blue) scaled to unit modulation depth and shifted vertically by 0.1; right panels: distance distributions;

T_1 of the metal ion spin. The distance distributions obtained with this empirical kernel gave the expected narrow, single peak distance distributions for a large range of samples and experimental conditions, except when using experimental conditions where the modulation depth plateaus were attenuated. This study suggests that it may be possible to derive a basically calibration-free method to determine higher harmonics coefficients for nitroxide-high-spin RIDME experiments.



Conclusions and outlook

The probabilistic interpretation of experimental results for the analysis of EPR data is well-established, and we have demonstrated that it provides a powerful tool to study highly disordered biological systems at the molecular level.

To assess the aggregation state, we performed experiments with the partially disordered protein hnRNPA1, labelled at single sites, in apparently dispersed sample conditions. The DEER measurements on flash-frozen samples unexpectedly revealed that a small fraction of protein is constantly interacting. The interactions between molecules of hnRNPA1 must at least be partially reversible under the studied conditions, as was demonstrated by spin dilution experiments. Furthermore we found that the interactions do not occur in a single, fixed conformation, but rather in a broadly distributed manner. The protein-protein interactions are short-lived enough, that they could not, or only weakly be detected by ambient temperature measurements (CW X-band EPR, as well as paramagnetic relaxation enhancement NMR). The experiments with singly labelled hnRNPA1 also allowed us to define reference conditions where the protein is predominantly monomeric.

We consequently were able to systematically measure pair-wise distance distributions between sites in the RRM and the IDD of hnRNPA1 in the monomer-stabilised conditions. The observed distance distributions were broad, as expected with at least one spin labelling site in the disordered domain. Surprisingly, the observed distance distributions from the DEER experiments were centred at shorter distances than expected, suggesting a preference of the IDD to adopt rather compact conformations in the dispersed state. This was in agreement with intramolecular PRE experiments, where we observed PRE effects in the RRM of hnRNPA1 upon placing a spin label in the IDD.

Based on the DEER distance distribution restraints, we performed force-field free model generation of the full length hnRNPA1 protein. The resulting individual conformers in a DEER-restrained en-

semble model of full length hnRNPA1 in combination reproduce the DEER results, but are highly dissimilar from one another. The ensemble models could in addition to the DEER restraints be refined against experimental ensemble SAXS curves, which provided additional validation of the models. Analysis of the ensemble models in terms of known charge interactions revealed differences in ensemble models generated with or without experimental restraints, which could in the future be directly validated for example by mutation experiments. This in turn may reveal molecular mechanisms that are responsible for the comparatively compact conformation of the IDD of hnRNPA1 in the dispersed state.

In contrast to the dispersed state, we could define reference conditions under which solutions of hnRNPA1 undergo LLPS at ambient temperature *in vitro*, as was demonstrated by confocal microscopy. Characterisation of the protein conformations and interaction in the LD state was also investigated, and proved significantly more challenging than in the dispersed state. The major experimental challenge is fast relaxation of the spins in the LD state, due to high local spin densities.

We found that the addition of even small amounts of short RNAs with optimised binding sites for the RRM of hnRNPA1 strongly increased the LLPS propensity of solutions of hnRNPA1. This effect of RNA binding on LLPS of hnRNPA1 is of particular interest, due to the function of hnRNPA1 as splicing regulator. Characterisation by EPR of the RNA-induced LLPS state revealed very high local spin densities also in the RNA-induced LD state. No strong trends were observed, but we found weak indications that LLPS is slightly more enhanced by the short RNA with two optimal binding sites than the short RNA with mutated binding sites. This indicates that a specific RNA recognition mechanism may be relevant, in combination with a mechanism driven by unspecific RNA binding.

PDS methods with spectroscopically orthogonal spin labels were reviewed for their application towards identifying biomolecular interactions. We found that orthogonal spin labelling EPR can be used to investigate the diverse interactions observed in mixtures of RNA and hnRNPA1. To this end we performed DEER experiments in the LLPS state with a short RNA and hnRNPA1 labelled with the spectroscopically orthogonal spin labels nitroxide and Gd(III)-DOTA. In this particular case the Gd(III) spin label, however, was not the optimal choice, due to its known relaxation enhancement properties, which decreased the sensitivity. An alternative labelling strategy with a Cu(II)-based spin label was proposed. In future experiments one may also consider to place a spin label on the RNA. This may be particularly interesting because it has been proposed that RNAs have more compact conformations in cells when they are associated with stress granules, than when they are being translated.^[6]

As a relatively new addition to the distance measurement PDS toolbox we showed an in-depth analysis of the RIDME experiment with pairs of nitroxide and Cu(II)-ions based on experiments with molecular rulers. This 'low-spin' case (both spins $S=1/2$) can be analysed with standard kernel-based distance analysis methods, and has the advantage of potentially very high sensitivity in Cu(II)-nitroxide pairs with a large spectral separation. In the case of the studied molecular

rulers, the spin label attachment was sufficiently rigid to observe orientation selection at Q-band. For distance analysis this effect should be compensated, which could be achieved by a field-stepped, as well as by a novel broadband pulse setup. In addition, the orientation information could also be extracted from the EPR-correlated dipolar signals. The EPR-correlated dipolar information could be conveniently accessed with the broadband version of the RIDME experiment with coherent, AWG-synthesised broadband pulses.

Building on the 'low-spin' orthogonal RIDME, we performed benchmark experiments with Mn(II)-, resp. Gd(III)-loaded molecular rulers to extend the orthogonal RIDME method to distance measurements with nitroxide-high-spin metal ion pairs. Including a high-spin metal ion is a more complicated experiment than the low-spin case, due to the appearance of higher harmonics of the dipolar coupling in RIDME. Unlike with previously reported metal-metal RIDME, we found that a large range of harmonic overtones contribute to the dipolar signal in nitroxide-detected RIDME, which vary with the experimental mixing time. However, using an empirical kernel which includes all possible orders of harmonics for each metal ion, we were able to recover the expected distance distributions. The calibration of the kernel was based solely on the characteristic relaxation rate of the high-spin metal ion (which can be experimentally determined). The experiments with molecular rulers, and samples of spin-labelled oligo-proline peptides showed promising stability of the model.

In summary, in this thesis we have demonstrated that site-directed spin labelling in combination with pulsed dipolar EPR spectroscopy is a powerful tool to characterise disorder in biological systems. This is valid for both protein conformations, as well as protein-protein interaction or protein-RNA interactions. Orthogonal spin labelling strategies open the doors towards detailed analysis of multiple interactions in complex samples, and development of the RIDME experiment with orthogonal spin labels provides a sensitive method that is complimentary to the well-established DEER experiment.



Appendix A

Supplementary Information for Chapter 3

A.1 Purification of the LCD construct

Sequence of the LCD construct ('HTLCD') that was purified from *e. coli* (BL21, codon optimised, Agilent). The engineered TEV-cleavage site is indicated by ||:

```
MGSSHHHHHHSSGLVPRGSH  
MENLYFQ||GSRGRSGGNFG  
GGRGGGFGGNDNFGRGGNFS  
GRGGFGGSRGGGGYGGSGDG  
YNGFGNDGSNFGGGGSYNDF  
GNYNNQSSNFGPMKGGNFGG  
RSSGPYGGGGQYFAKPRNQG  
GYGGSSSSSYGSGRRF
```

Cells carrying the construct cloned into the vector pET28a with included kanamycin resistance were grown in LB-broth medium (Difco LB broth, Miller) supplemented with kanamycin (0.0005 % (w/v)) and induced at an O.D. \approx 0.8 with 0.5 mM IPTG. Overexpression was performed for 3-5 h at 37°C. Cells were lysed by 10 x sonification (sonic dismembrator, Thermo Fisher) cycles and cool-down cycles (in ice water bath). Lysate was pelleted and the supernatant was discarded. 15 %-SDS-PAGE results with aliquots of all following steps are shown in Figure A.1. The pellet from 1L culture was washed in 30 ml IB wash buffer (50 mM Tris, pH 8.0, 1 M NaCl, 0.1 % Triton-X) three times (intermediate pelleting in 50 ml falcon tubes at 20 °C, 5000 x rcf for 20 min). Supernatants were discarded. The detergent was then removed by washing three times with 30 mL Tris-wash

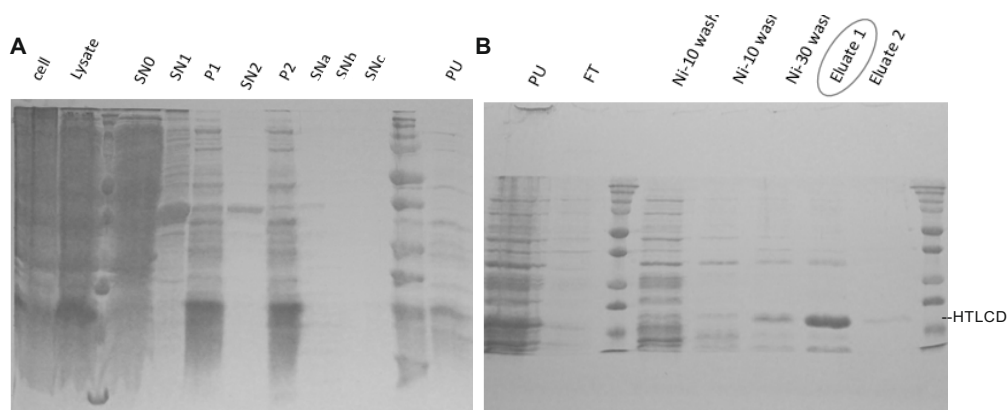


Figure A.1: SDS-PAGE of inclusion body purification protocol for LCD construct of hnRNPA1; 20 μ undiluted sample were loaded for each step, except for 'PU', where only 2 μ were loaded (A) cell lysis and IB wash steps: SN0-P2 IB wash buffer pellets (P) and supernatants (SN); SNa-SNc Tris-wash buffer steps; PU: Urea buffer (buffer list see text); (B) Ni-NTA affinity chromatography after IB wash steps; PU is the loaded sample, FT the flow-through during loading;

buffer (50 mM Tris, pH 8.0, 1 M NaCl, 0.1 % Triton-X), and the final pellet was dissolved in Urea buffer (50 mM Tris, pH 8.0, 1 M NaCl, 6M urea, 10 mM imidazole); The dissolved sample was loaded on a gravity flow Ni-NTA column, and the flow-through was discarded. After 10 ml washing with NTA-urea-wash buffer (50 mM Tris, pH 8.0, 1 M NaCl, 6 M urea, 30 mM imidazole), the protein was eluted with 5 ml NTA-urea-elution buffer (50 mM Tris, pH 8.0, 1 M NaCl, 6M urea, 300 mM imidazole).

A.2 Additional results for CW X-band lineshape fitting

The anisotropic g -, and A -tensor values of MTSL in high ionic strength dispersion buffer (50 mM sodium phosphate, pH 6.5, 100 mM R/E) were determined by fitting the solid state CW X-band spectrum acquired at 140K of MTSL (acquired at a Bruker Elexsys E500 spectrometer with a Bruker super high Q resonator ER4122SHQ at 48 dB MW attenuation, with a custom liquid nitrogen cooling and temperature stabilisation setup). The spectrum was fitted with the EasySpin^[280] `pepper` function, which an isotropic linewidth of $lw = 0.8$. The extracted parameters with an axially symmetric fit for the hyperfine tensor ($A_{xx} = A_{yy}$) are $g = [2.0109 \ 2.0083 \ 2.0050]$; $A(^{14}\text{N}) = [15.45, 15.45, 103]$ MHz; with an anisotropic strain of H -strain = $[32, 15, 20]$ MHz (also indicated in Figure A.2).

The ambient temperature lineshape analysis in the main text (Figure 3.4) was performed using these fitted spin label parameters with the EasySpin^[280] function `chili` (intermediate motion regime). Additional experimental conditions for the same spin mutant with MTSL are shown in Figure A.3. We observed only very minor differences for repeated measurements with the same spin labelling site (S231R1). Also the ^{15}N -isotope enriched version of hnRNPA1 which was used for the intramolecular PRE experiments shown in Figure 4.13 (Crefchap:ensemblesA1) are included,

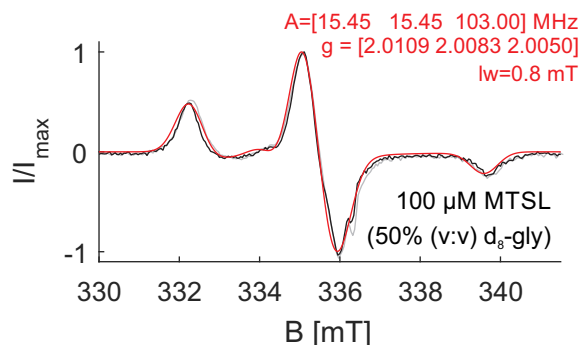


Figure A.2: CW X-band spectra of MTSL at 140 K frozen in dispersion buffer (100 mM R/E) with (black) an without (grey) 50 % (v/v) glycerol, and EasySpin^[280] powder spectrum simulations (red);

and show no significant difference. However, we clearly observed a difference when measuring in the low ionic strength (10 mM sodium phosphate) vs. the high ionic strength dispersion buffer (50 mM sodium phosphate). In the former we observe narrower lines (higher mobility) and a larger hyperfine splitting A_{zz} (only visual inspection, no fits available). In the low ionic strength buffer we furthermore observed narrower lineshapes at low labelling efficiency. We also include a series of spectra acquired with the same sample tube at lower temperatures (277 to 298 K). As expected we observe broadened lines at lower temperature.

A.3 Spin doping experiments

We here present experiments performed with 'spin-doping' conditions, where we added a small quantity (5 %) of spin-labelled protein to solutions of wild-type hnRNPA1. Due to sensitivity limitations these measurements were performed at a total protein concentration of 100 μ M. Spin-spin interactions should be significantly attenuated even for high-density aggregates at these ratios (effective 1:20 spin dilution). To have consistent conditions with the imaging we also admixed the low-melting agarose buffer. The results are shown in Figure A.4, which is an extended version of Figure 3.4 in Chapter 3. As we have discussed in the main text, the dispersed state is characterised by homogeneous samples in imaging, and comparatively high spin label mobility in MTSL-labelled hnRNPA1 S231C. In panel (F) of Figure A.4 we additionally show the CW X-band spectra obtained with spin labelled hnRNPA1 S231R1 into wild-type hnRNPA1. We observe very narrow lines that appear shifted to higher fields (small offsets due to spectrometer inaccuracy are possible, but smaller than the observed effect), and the hyperfine splitting is significantly smaller in the spin-doping experiments (see dashed lines). The shifting and smaller splitting is more pronounced in the low ionic strength buffer. Such narrow lines indicate very fast spin label mobility (see fits in Figure A.5), which is on the same order as expected for free spin label. It therefore seems very likely that the spin label was either cleaved off by residual reducing agent in the wild-type hnRNPA1 stock solution, or that the short exposure to elevated temperature during admixing of the low melting agarose buffer had an adverse effect on these particular protein samples.

We also performed DEER at Q-band with samples prepared in the same way as those for the CW

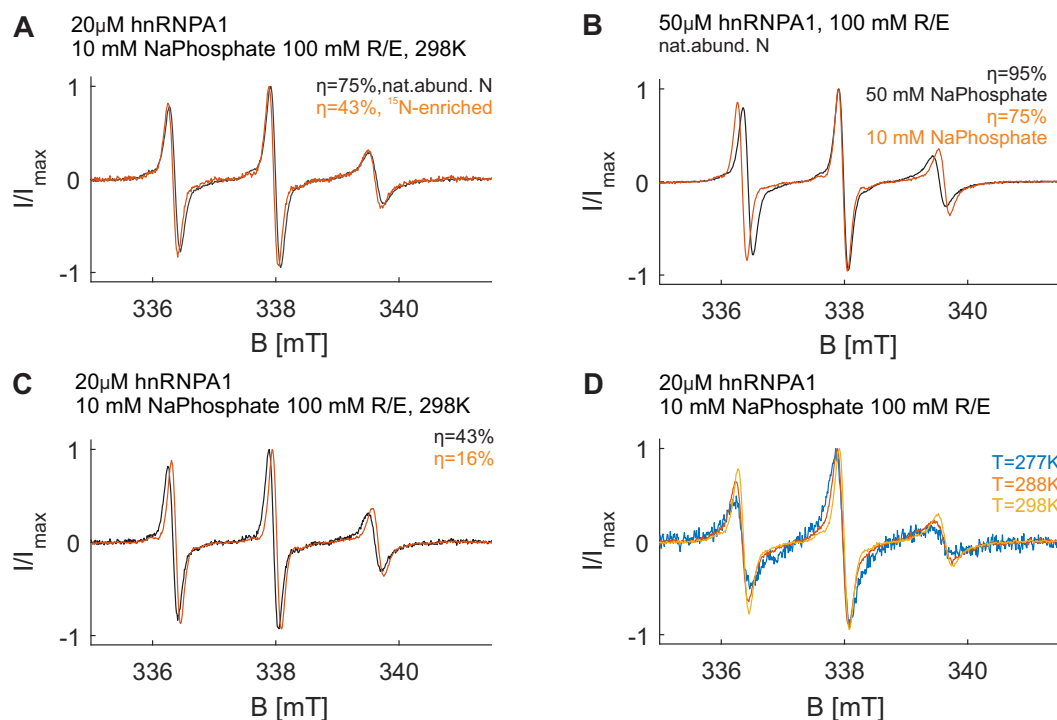


Figure A.3: CW X-band ambient temperature spectra of MTSL-labelled hnRNPA1 S231R1 in the dispersed state; (A) effect of labelling efficiency and isotope enrichment; (B) effect of ionic strength of dispersion buffer; (C) effect of labelling efficiency in low ionic strength buffer; (D) temperature dependence

X-band experiments. Interpretation of these experiments obtained with the spin-doping samples remains preliminary, because the CW X-band measurements suggest that the spin label attachment was not stable during the preparation of these samples. Thus, we unfortunately cannot directly relate the distance information and local spin label concentration from the DEER experiment to interactions of hnRNPA1.

The time-domain data (black) are shown in panel G of Figure A.4. DEER signal decay in these experiments can only arise from inter-molecular dipole-dipole coupling, and the background decay (coloured lines, colour consistent with sample conditions in panel (A)) can be used as a measure for local spin concentration. If protein-protein interactions bring the spin labels closer together, we expect higher local concentration and thus a faster decay. We find a low background density (3-dimensional exponential fit) for the dispersed state stabilised with glycerol of $k_{\text{dispersed}} = 0.082$, and high background densities for the high concentration samples $k_{100\text{ mMR/E}} = 0.170$, and $k_{50\text{ mMR/E}} = 0.323$. To understand better, in which distance range the additional couplings appear, we fitted the primary data directly with a single Gaussian fit (no background correction). Without glycerol, and at higher total protein concentrations (but same spin concentrations, i.e. for spin-diluted samples) we see a much faster decay (blue, 100 mM R/E). The short distance contribution from the 'dispersed' state measurement is still observed, but additional contribution from intermediate-range distances is observed. The effect is even stronger in the LD state (green, 50 mM R/E), where

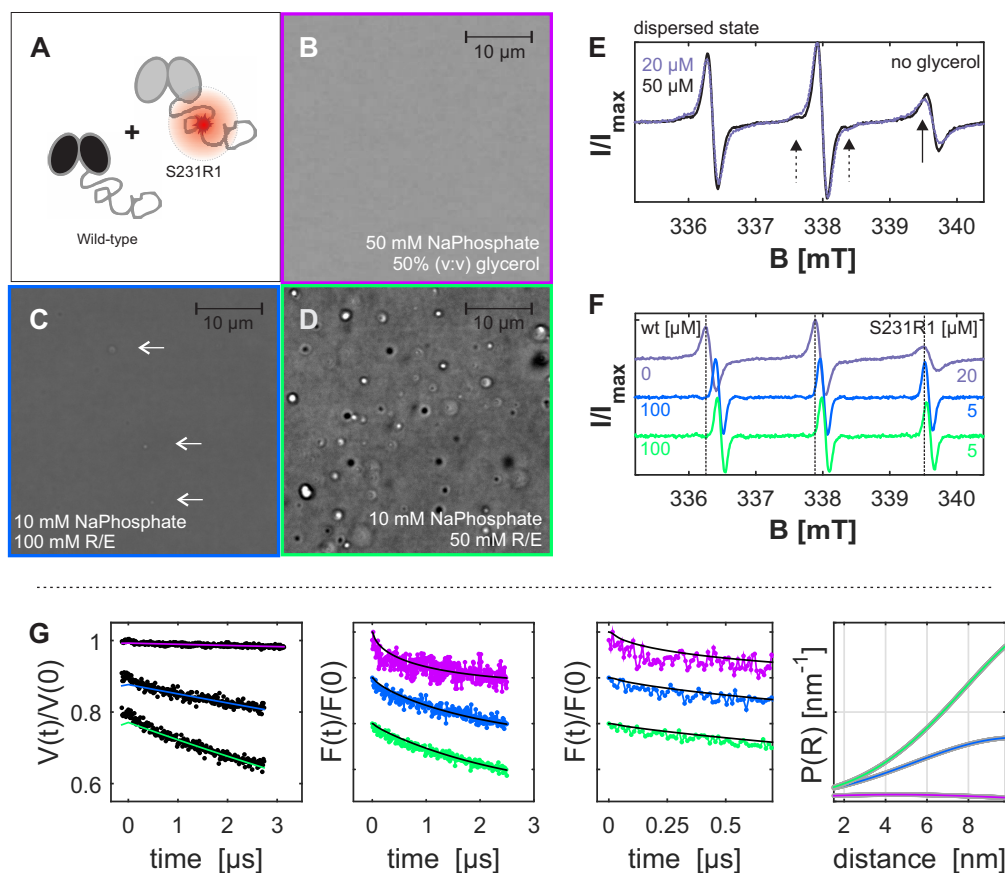


Figure A.4: Liquid-liquid phase separation of hnRNPA1; the sample conditions are persistently colour-coded in all panels. The CW X-band spectra are shifted to correspond to $\nu_{mw} = 9.5$ GHz. (A) EPR data in this figure were obtained with (spin diluted) MTSL-labelled S231C mutant. (B) Confocal transmission image (bright-field) of $20 \mu\text{M}$ hnRNPA1 at ambient temperature in high ionic strength dispersion buffer supplied with 50% (v:v) glycerol; (C) bright-field image of $100 \mu\text{M}$ hnRNPA1 at ambient temperature low ionic strength dispersion buffer stabilised with 0.2% agarose; the arrows highlight small droplets. (D) Bright-field image recorded at same conditions as (C) except for reduced concentration of amino acids in buffer: 50 mM R/E (i.e. LLPS buffer); (E) ambient temperature CW X-band spectra of MTSL-labelled hnRNPA1-S231C ($\eta = 75\%$) in high ionic strength dispersion buffer; (F) ambient temperature CW X-band spectra of the spin labelled mutant S231R1 in spin-doping experiments (1:20) with hnRNPA1-wildtype (blue: 100 mM resp. green: 50 mM R/E); (G) Primary DEER data $V(t)/V(0)$ (shifted vertically by 0.1) and 3-dimensional background fits (coloured lines), form factors $F(t)/F(0)$ and fits (black) of full and short-time range, and distance distributions $P(R)$ obtained with single Gaussian fit to form factors (area under distribution given by modulation depth);

even more and longer distances contribute to the decay.

We clearly observed that the local spin label densities obtained with these samples were very high, which indicates that, even if the spin label is cleaved off the protein chains, it is somehow

accumulating in clusters. We can hypothesise that the spin label is cleaved, but it is still (weakly) interacting with the protein, and thus accumulates in the high-density protein aggregates. More experimental evidence is required to test this hypothesis.

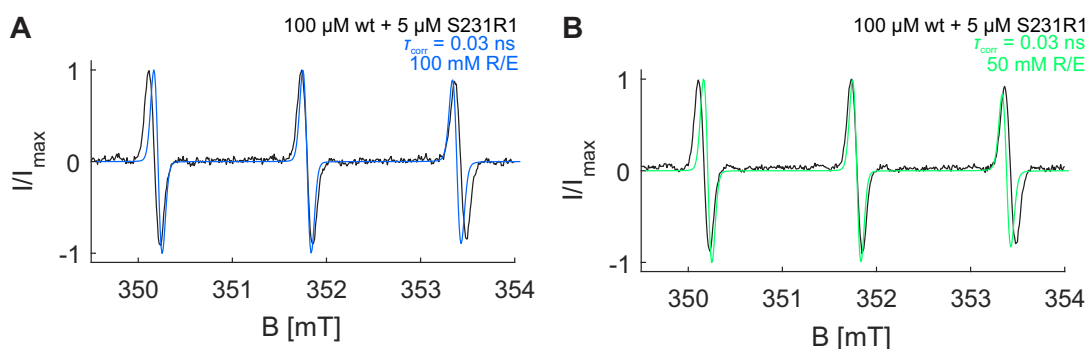


Figure A.5: EasySpin^[280] `chi1i` fits of the CW X-band spin doping results in low ionic strength dispersion buffer (left) and LLPS buffer (right)

A.4 Additional distance simulations with the dimer model of UP1

The simulation with the dimer model were performed in MMM.^[139] The starting structure file was obtained by generating the crystallographically related molecules of the pdb file 1U1Q in the Chimera^[234] protein visualisation studio and exporting only two directly interacting protein chains into a separate file (RNA coordinates were excluded). The reduced coordinate file was loaded into MMM and *in silico* spin labelled at the indicated sites with MTSL at 298 K.^[237] The results for intra-, and intermolecular distance distributions between the beacon sites are shown in Figure A.6. Except for the inter-molecular distance between beacons 182, all expected distances are rather long.

A.5 EDEPR spectra for spin dilution experiment with mutants 231 and 271

In the spin dilution experiment we observed some contribution of very short distances, which may fall into the exchange coupling regime (Figure 3.6). To exclude that large fractions of spins are actually in this distance regime we show the Q-band EDEPR spectra acquired at 50 K in Figure A.7. Some very minor spectral changes are observed upon spin dilution (indicated by arrows), but the lineshape and lineshape change do not suggest that the spectrum is dominated by strong exchange coupling for both spin labelling sites (231 and 271).

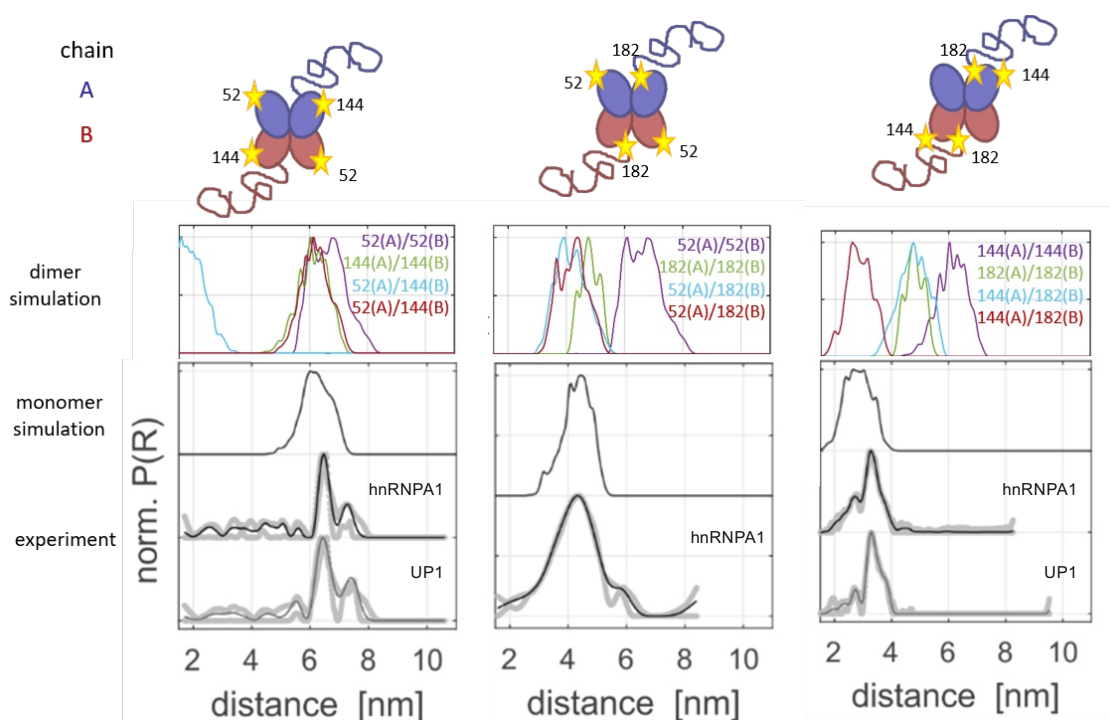


Figure A.6: Additional distance simulations between beacon sites in the context of the dimer structure of UP1 from crystallisation with short DNAs;^[223]

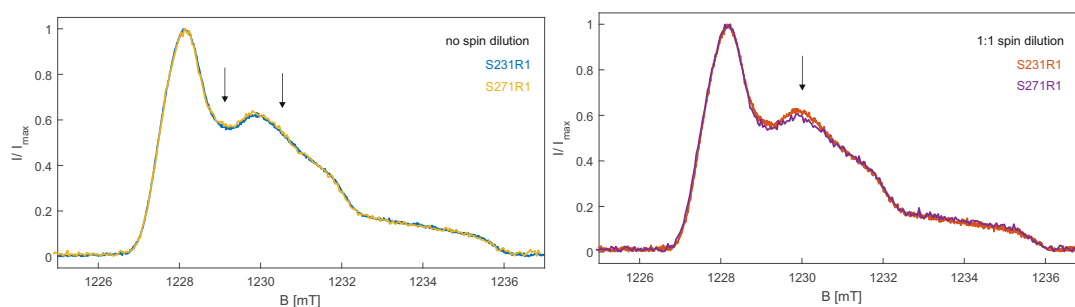


Figure A.7: EDEPR for single-Cys DEER experiment at 34.4 GHz, 50 K with 16/32 ns pulses and $\tau = 400$ ns; top: samples without spin dilution, bottom: samples with 1:1 spin dilution with Cys-free hnRNPA1; the arrows indicate regions that are slightly different in the mutant 271 compared to 231.

A.6 Additional CW X-band spectra for hnRNPA1, UP1 and circular dichroism results

A.7 Chemical shift differences for intermolecular PRE

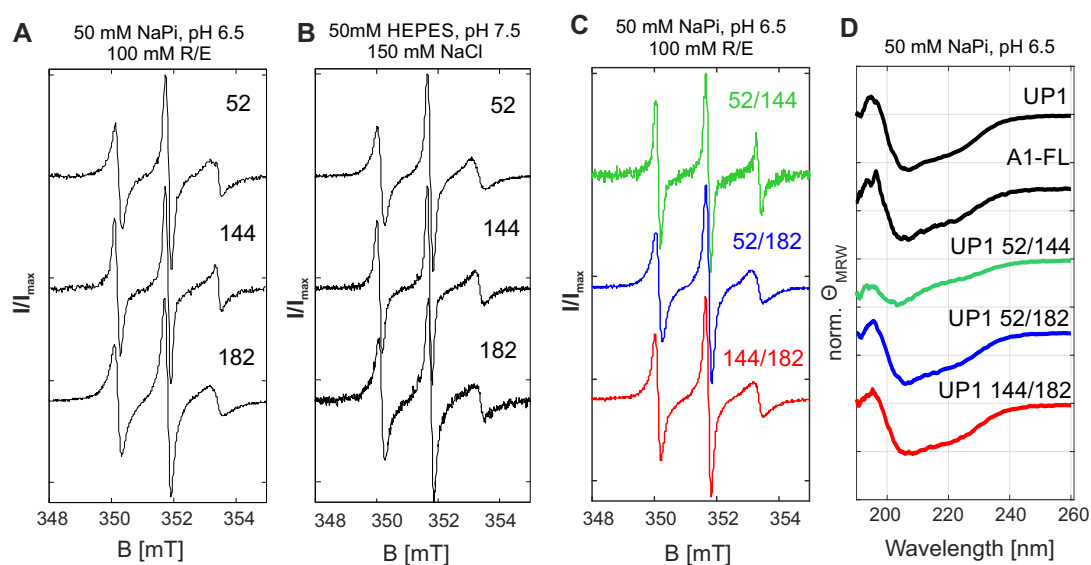


Figure A.8: (A) CW X-band spectra of MTSL-labelled hnRNPA1 at beacon sites in high ionic strength dispersion buffer; (B) CW X-band spectra of MTSL-labelled hnRNPA1 at beacon sites in HEPES buffer, as is often found in LLPS studies;^[218] (C) CW X-band spectra of double MTSL-labelled hnRNPA1 at beacon sites in high ionic strength dispersion buffer; (D) circular dichroism measurements with wild-type UP1 and wild-type hnRNPA1 (A1-FL), as well as double Cys-mutants of UP1;

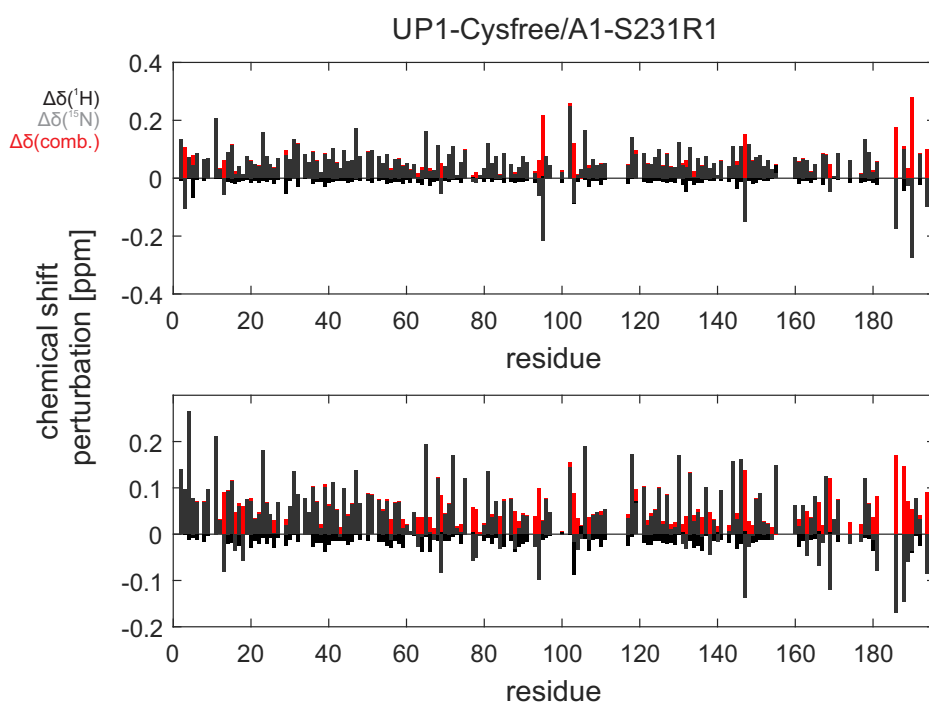


Figure A.9: Chemical shift differences $\Delta\delta$ between UP1 Cys-free in low ionic strength buffer (10 mM sodium phosphate, pH 6.5, 100 mM R/E) and hnRNPA1-C43S-C175A-S231R1 in low ionic strength buffer (top) resp. in high ionic strength buffer; black: $\Delta\delta$ of ^1H -chemical shift; grey: $\Delta\delta$ of ^{15}N -chemical shift; red: combined chemical shift difference $\sqrt{\Delta\delta(^1\text{H})^2 + \Delta\delta(^{15}\text{N})^2}$;

Appendix B

Supplementary Information for Chapter 4

B.1 Spin labelling

The labelling efficiency of each doubly spin labelled mutant of hnRNPA1 was determined by spin counting and referencing to a 100 μM solution of Tempo in HEPES buffer. All CW X-band spectra were acquired on a Bruker Elexsys E500 spectrometer including a Bruker super high Q resonator ER4122SHQ at 23 dB MW attenuation.

B.2 Random coil model fits for DEER

Two examples of fits of the DEER data with doubly spin labelled hnRNPA1 are shown in Figure B.2. The fit qualities are good, but in the two situations it is necessary to use a very different scaling factor ν . The short distance between 182/192 requires a scaling factor larger than 0.5, which indicates a more extended conformation than a fully ideal polymer.^[91] The opposite is encountered for the distance between sites 182 and 316, which is shorter than an ideal random peptide ($\nu < 0.5$).

B.3 Primary DEER data and analysis

Here we show the data analysis for the single Gaussian fit distance distributions shown in Figure 4.4, resp. Figure 4.5 in Chapter 4.

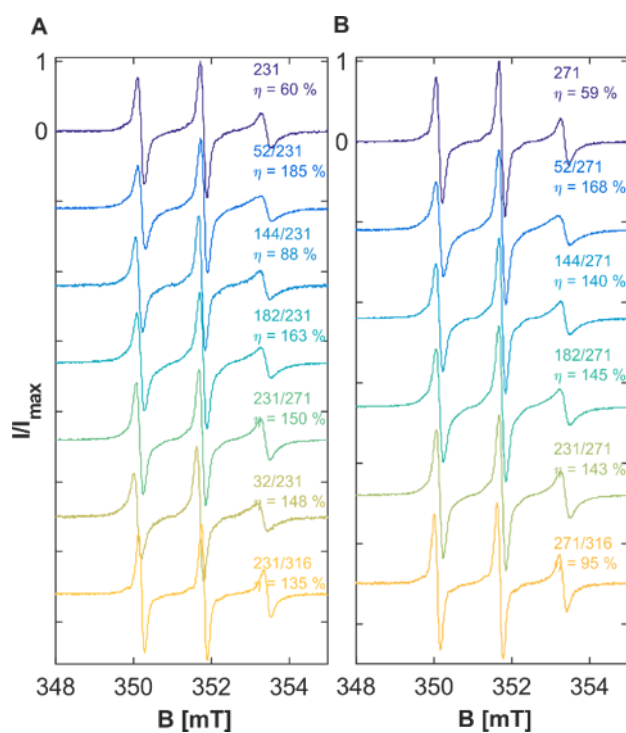


Figure B.1: CW X-band ambient temperature EPR spectra of $\sim 25 \mu\text{M}$ double Cys mutants of hnRNPA1 labelled with MTSL in dispersion buffer; labelling efficiencies η (per protein, not per site) are indicated

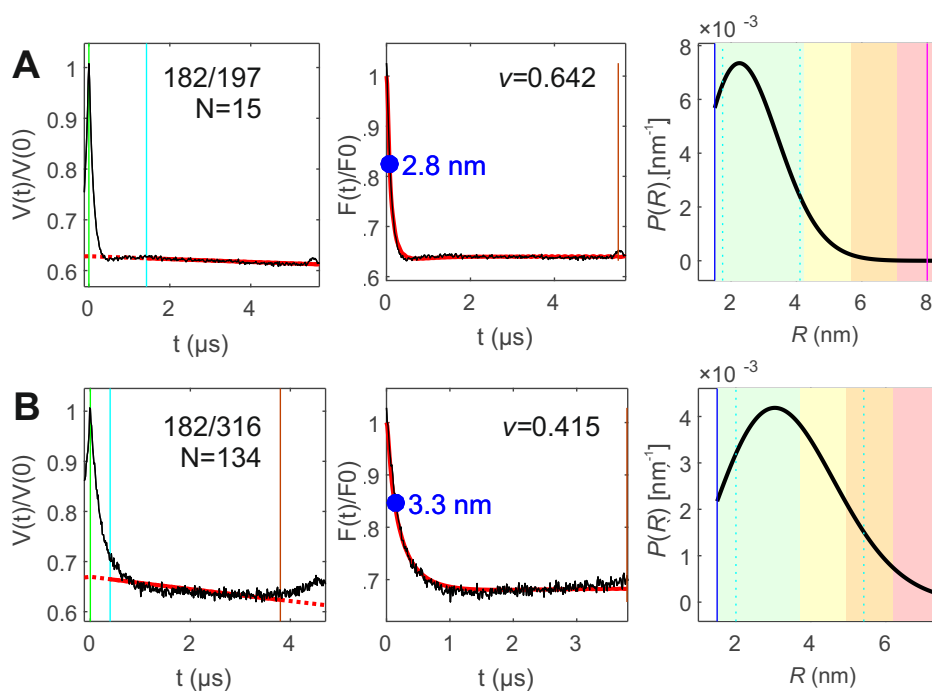


Figure B.2: DEER experiments fitted with random coil model; left to right: primary data and three dimensional background fit (red), form factors and random coil model fits (red), and distance distributions; labelling sites and distance in primary sequence are displayed in the primary data panel; (A) labelling sites 182/197; (B) labelling sites 182/316.

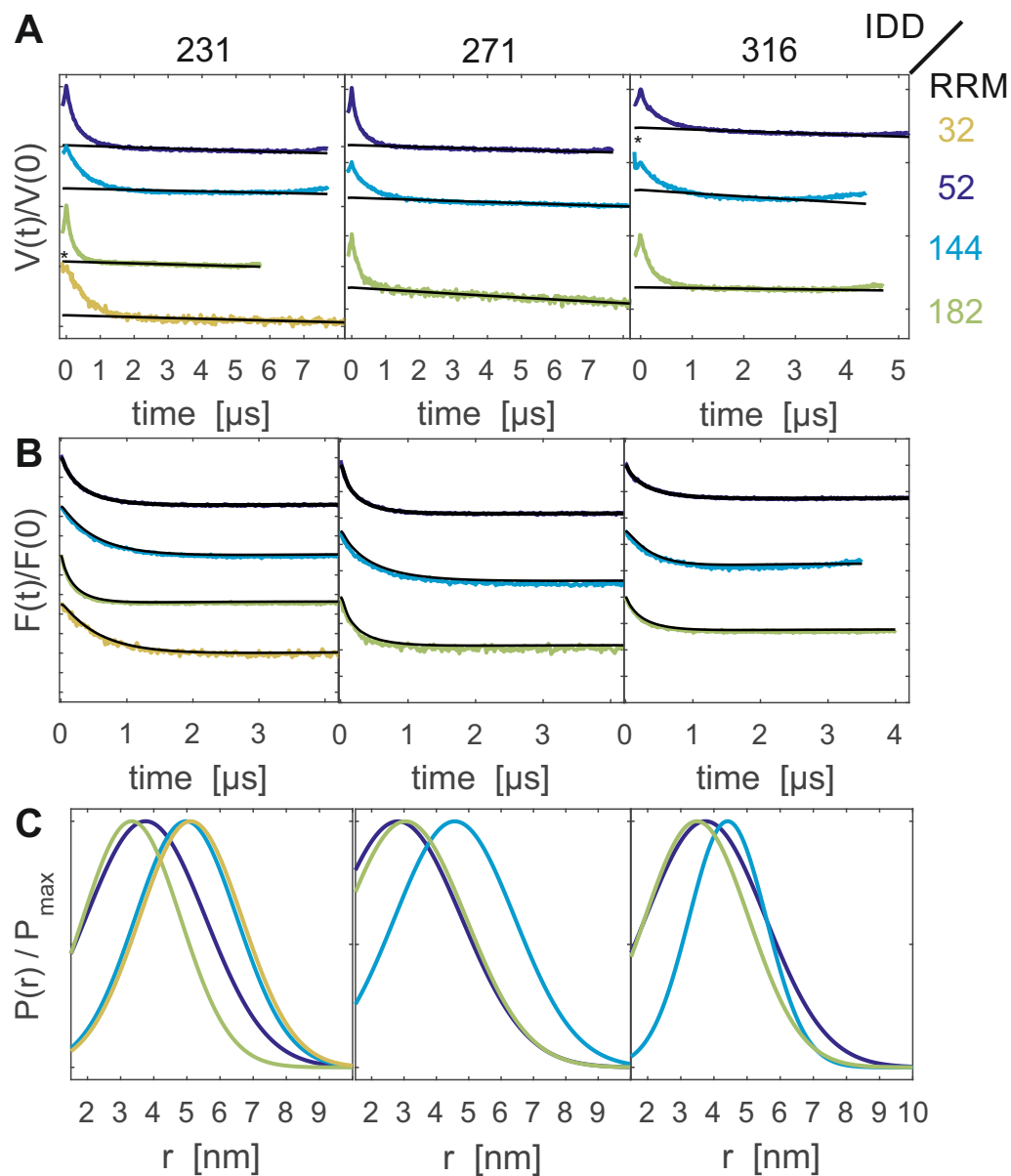


Figure B.3: DEER data analysis for trilateration of residues 231, 271 and 316 in the IDD from beacons 32, 52, 144 and 182 in the RRM; (A) normalised primary data $V(t)/V(0)$ and background fits (black lines); the spacing of the divisions corresponds to a difference of 0.5; (B) modulation depth scaled form factors $F(t)/F(0)$ obtained after background division; (C) single Gaussian fit distance distributions $P(r)/P_{\text{max}}$ normalised to unit intensity at the maximum of the distribution;

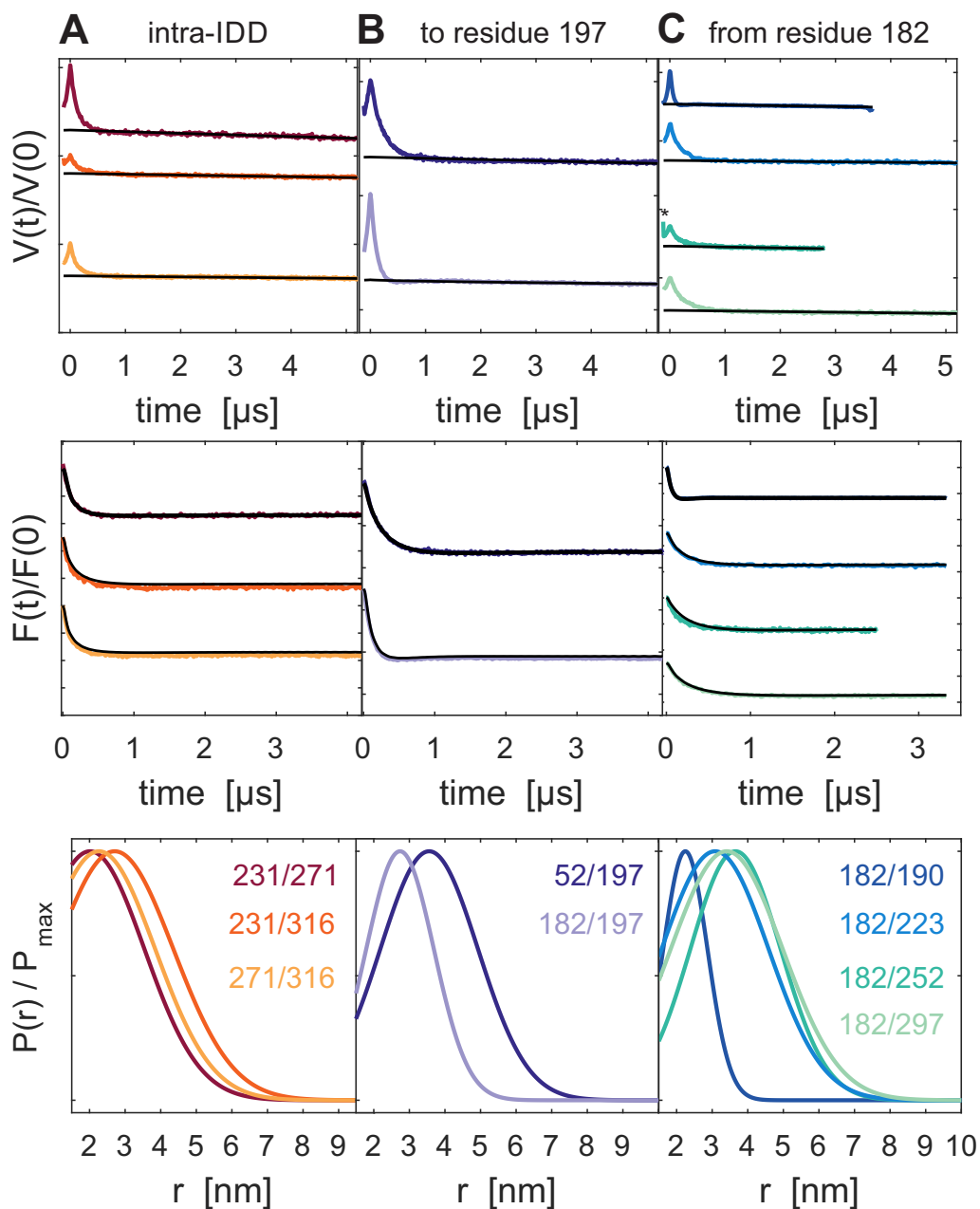


Figure B.4: Additional DEER experiments; top: normalised primary data $V(t)/V(0)$ and BG fits (black); middle: modulation depth scaled form factors $F(t)/F(0)$ and fits (black); bottom: normalised distance distributions $P(r)/P_{\text{max}}$; mutation positions are indicated in this row; (A) distances between two residues within the IDD ('intra-IDD'), (B) auxiliary distances to residue 197; (C) additional distances measured from position 182;

B.4 Input files for DEER restrained ensemble generation

The following input file was used for the generation of the ensembles 'A1 1' and 'A1 2' in the main text. For the generation of unrestrained ensembles the experimental DEER restraints were excluded from the file.

```

%%%%%%%%%%
% Generate Ensemble for C-terminal intrinsically disordered domain of hnRNP A1 188-320
# PDB mod1:A %first submodel of NMR ensemble [2LYV]
# DOMAIN 188 320
# NANCHOR [mod1](A)187
%A1wt 188-320
# SEQUENCE SASSSQRGRSGSGNFGGGRGGGFGGNDNFGRGGNFSGRGGFGGSRGGGGYGGSGDG-
YNGFG NDGSNFGGGGSYNDFGNYNQSSNFGPMKGGNFGGRSSGPYGGGGQYFAKPRNQGGYG-
GSSSSSSYGSGRRF
# ENSEMBLE 1000 0.5
# DEER MTSL 298

%trilateration
 52  231  3.75  1.81
144  231  4.97  1.54
182  231  3.33  1.48
 52  271  2.81  1.97
144  271  4.57  1.86
182  271  3.05  1.88
 52  316  3.75  1.81
144  316  4.41  1.17
182  316  3.48  1.57
% auxiliary
 32  231  5.12  1.55
 52  197  3.56  1.38
182  190  2.25  0.62
182  197  2.74  0.95
182  223  3.14  1.42
182  252  3.66  1.27
182  297  3.41  1.58
% intra-domain distances
231  271  2.01  1.53
231  316  2.71  1.65
271  316  2.26  1.58

# END
%%%%%%%%%%

```

B.5 Ensemble characteristics

Structure alignment

Here we shown plot of the restrained and unrestrained ensemble models of hnRNPA1 aligned to different sub-ranges. When aligned to the full chain, we see that the average conformations of the unrestrained ensembles adopt a more elongated shape than in the restrained ensembles. There is a slight trend for the 'M9' sequence to be more aligned in the restrained ensembles than in the reference ensembles, but it is weak compared to the differences between the ensembles of the same type. The aligned models are visualised for different alignment ranges (for details see figure caption) in Figure B.5. Clearly, no strongly preferred conformation is found. Nonetheless, to search for potential patterns in the chains we are currently developing analyses with different measures of local protein order.

End-to-end distances

In Figure B.6 we plot the histogram of two effective end-to-end distances of the restrained and the unrestrained ensemble model of hnRNPA1: (i) distance between residues 1 and 320, and (ii) distance between residues 188 and 320. The former can be seen as an effective end-to-end distance of full length hnRNPA1 R_{A1} , while the latter is the effective end-to-end distance for the IDD R_{IDD} . The two distances are very broadly distributed (standard deviation σ_R for both R_{A1} and R_{IDD} close to ~ 3 nm), and we find both very short ($R \sim 1$ nm), and very long ($R \sim 15$ nm) contributions. The maxima of both distributions (i.e. the most likely distance) is at approximately $R \sim 8-9$ nm. This value is in fact similar to what is expected for an RSA peptide chain model with ~ 130 amino acids (see Theory section). The average end-to-end distance of full-length hnRNPA1 R_{A1} is only slightly shifted to longer distances compared to R_{IDD} (see Table 4.4 in Chapter 4). This implies that in the unrestrained ensembles both residue 1 (N-ter) and residue 188 (start residue of the IDD) have very similar probabilities to be close to, or far away from the C-terminus of the full length protein.

Charge interactions

We analysed the full structure of hnRNPA1 for charge interactions within the IDD residues (188-320), as well as between the IDD residues and the RRM. This was performed with 'salt bridge' calculator in the 'timeline' tool in the vmd software package.^[128] The default definition of a salt bridge (with $R_{\text{threshold}} = 0.32$ nm) was used. The results for the unrestrained ensembles ('Ref 1' and 'Ref 2', see main text), and the restrained ensembles ('A1 1' and 'A1 2') are shown in ???. The frequency of each interaction is calculated as the number of chains in which the particular interaction is found, divided by the total number of chains. Note that arginine has two nitrogens for potential salt-bridge interactions, and it may happen that an individual salt-bridge is found twice within the same chain by the vmd routine, if both fall into the threshold range. In our calculation of the frequency of an interaction this was counted double.

Secondary structure

The secondary structure of the IDD residues (188-320) in the unrestrained ensemble models, resp. the DEER restrained ensemble models (19 distances) of full length hnRNPA1 are shown in Figure B.7. For each case we show two ensembles that were generated with different NMR structure sub-chains. The plots were generated with the 'timeline' tool in the vmd software package using the default definitions of the secondary structure classification.^[128] The colour-code for the secondary structure motifs is indicated in the figure captions. Note that because the ensemble generation happens in a stochastic manner, the chains are not sorted according to any criterion. We do not see extended secondary structure motifs in either the unrestrained, or the restrained ensemble. Note that short α -helical segments (pink) are found in all cases (also unrestrained ensembles), indicating that they may just be observed by coincidence (reflecting the Ramachandran statistics).

New ensemble alignment tools

In the course of the analysis to the IDD chains generated by the ensemble modeller we tried to identify if particular sub-range of the IDD chain adopted preferred conformations. To this end we did exhaustive RMSD analysis, by pair-wise chain comparison of variable length segments of the IDD models. The results of this 'sliding window' averaged RMSD analysis are shown in Figure B.8 and Figure B.9. Within a user specified range (here: the IDD of hnRNPA1, residues 188 to 320) the algorithm makes all possible pair-wise alignments. The best alignment is then chosen as the longest possible window that can be aligned with a resulting threshold RMSD.

B.6 SAXS data and analysis

Small angle X-ray scattering curves were measured on dilute samples of hnRNPA1 resp. UP1 (both wild-type constructs) in high ionic strength dispersion buffer (50 mM sodium phosphate, pH 6.5, 100 mM R/E). The results are shown in Figure B.10. The signal to noise is better for the sample of hnRNPA1 due to longer averaging (12 h, versus ~ 4 h for UP1). The data were analysed with the ATSAS software package^[92] to obtain a molecular distance distribution and the radius of gyration R_{gyr} . The fits are shown in Figure B.11.

B.7 Additional PRE results

Additional intramolecular PRE experiments were recorded with two more labelling sites in the IDD: 271 and 316. Both showed in the DEER still significant intensity below $R \approx 2.5$ nm for distances measurements to some of the beacons in the RRMS (see Figure B.3), which is approximately the cut-off distance to observe significant PRE effects. Indeed, we also saw intramolecular PRE effects with these additional labelling sites, which are mapped to the structure of the RRM in Figure B.12.

| ensemble | N_{chains} | amino acid pair | frequency [%] |
|----------|---------------------|-----------------|---------------|
| Ref 1 | 200 | 'ASP214-ARG140' | 1 |
| | | 'ASP214-ARG206' | 2.5 |
| | | 'ASP214-ARG218' | 3.5 |
| | | 'ASP214-ARG225' | 0.5 |
| | | 'ASP242-ARG232' | 0.5 |
| | | 'ASP262-ARG218' | 1 |
| | | 'ASP262-LYS277' | 0.5 |
| Ref 2 | 200 | 'ASP214-ARG194' | 0.5 |
| | | 'ASP214-ARG225' | 1.5 |
| | | 'ASP242-ARG232' | 0.5 |
| | | 'ASP250-ARG218' | 0.5 |
| | | 'ASP262-HIS33' | 1 |
| | | 'ASP262-LYS277' | 0.5 |
| | | 'GLU132-ARG194' | 0.5 |
| | | 'GLU24-ARG218' | 1.5 |
| | | 'GLU85-ARG194' | 0.5 |

Table B.1: Salt bridges by standard definition in vmd in unrestrained ensembles (background);

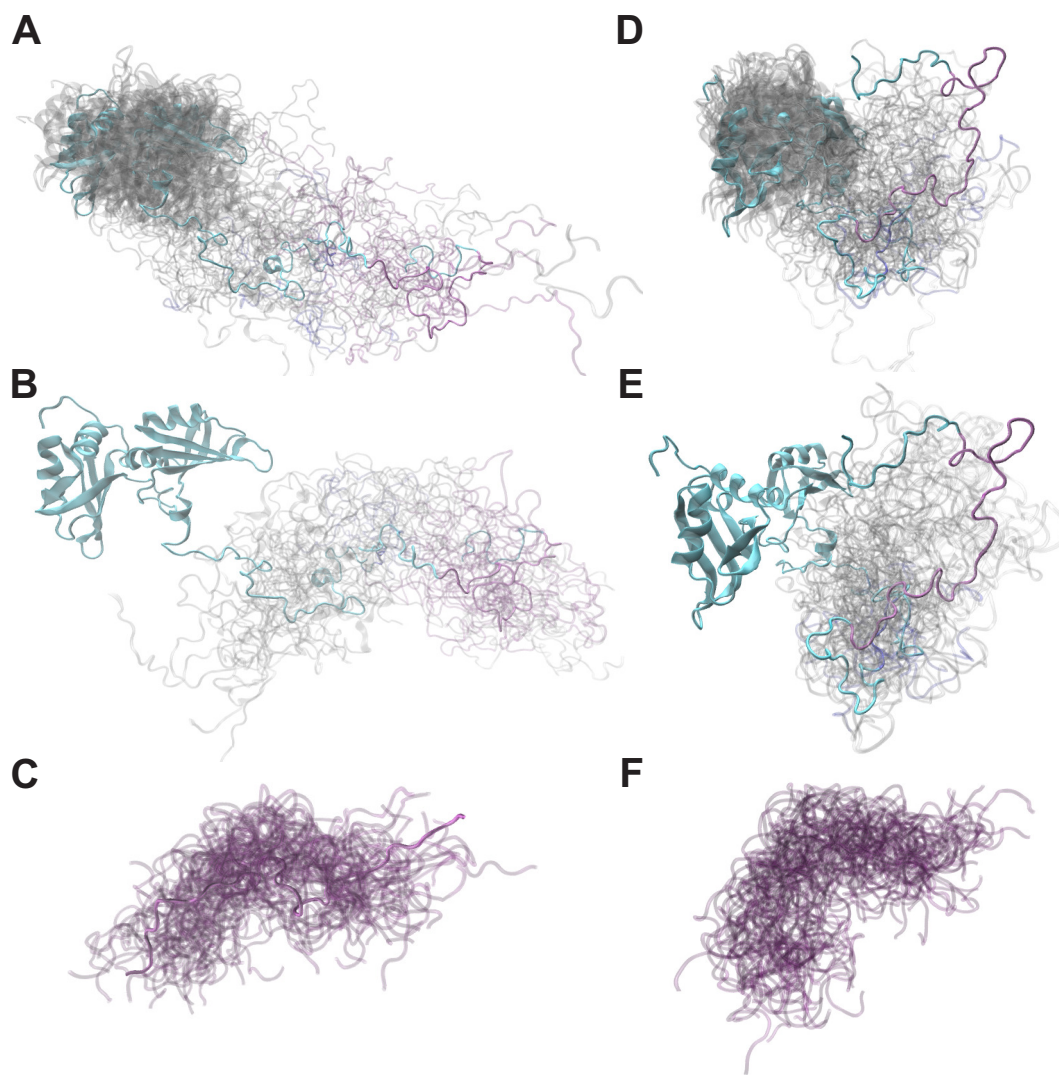


Figure B.5: Partially aligned ensemble models of hnRNPA1; purple: M9 sequence; dark blue: steric zipper sequence; (A-C) unrestrained ensemble 'Ref 1'; (D-F) DEER restrained ensemble 'A1 1'; (A,D) full chain alignment (residues 1-320); 20 chains are visualised; (B,E) partial alignment of the IDD (residues 188 to 320), 20 chains are visualised, the RRM is shown for only one chain; (C,F) partial alignment of 'M9' sequence (residues 257-305), 50 chains are visualised, only the aligned residues are shown;

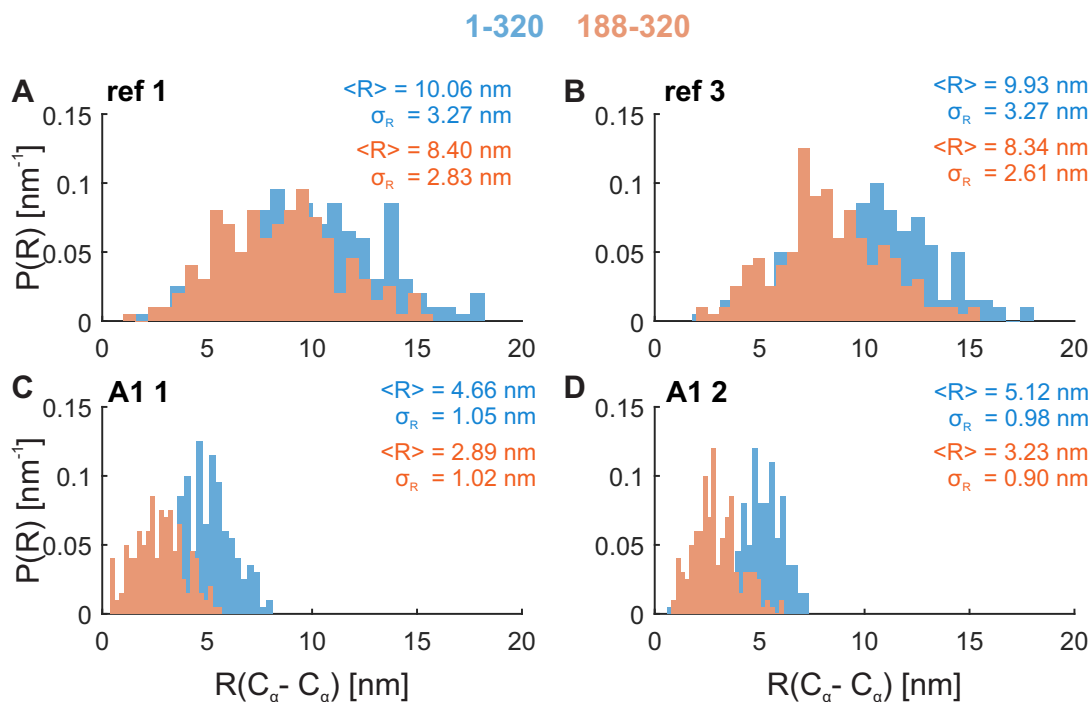


Figure B.6: Histograms of the end-to-end distance distribution for two end-point definitions with four different ensemble models; the mean distance $\langle R \rangle$ and standard deviation $\sigma(R)$ for two residue pairs (residue 1 to 320, resp. residue 188 to 320) are indicated. (A,B) Unrestrained reference ensembles; (C,D) ensembles generated with 19 DEER distance restraints;

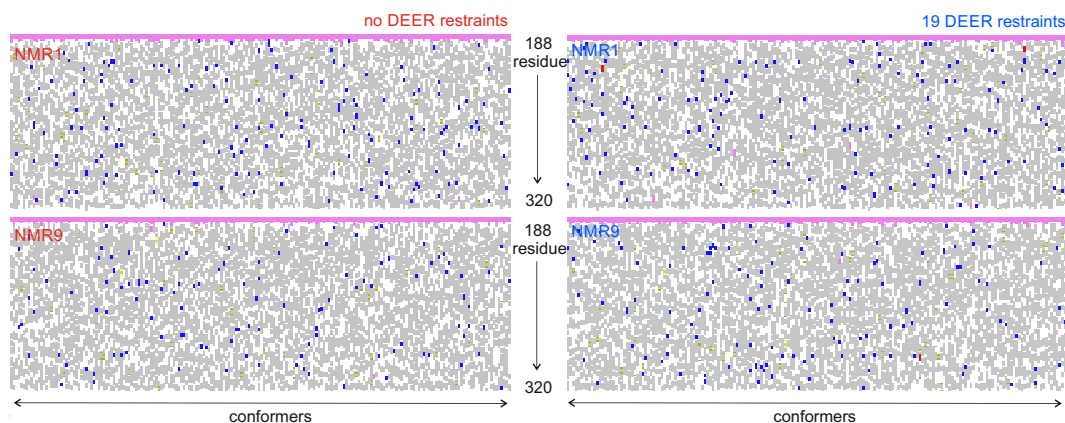


Figure B.7: Secondary structure classification (default values of vmd) of the IDD residues in the restrained ensembles ('A1 1', and 'A1 2' (see main text)); colour code is as follows: turn (grey), extended conformation (yellow), isolated bridge (green) α -helix (pink), 3_{10} -helix (blue), π -helix (red), random coil (white); two different NMR structure sub-chains were used as starting structures for the unrestrained (left), resp. DEER restrained (right) ensemble generation, top: NMR1, bottom: NMR9

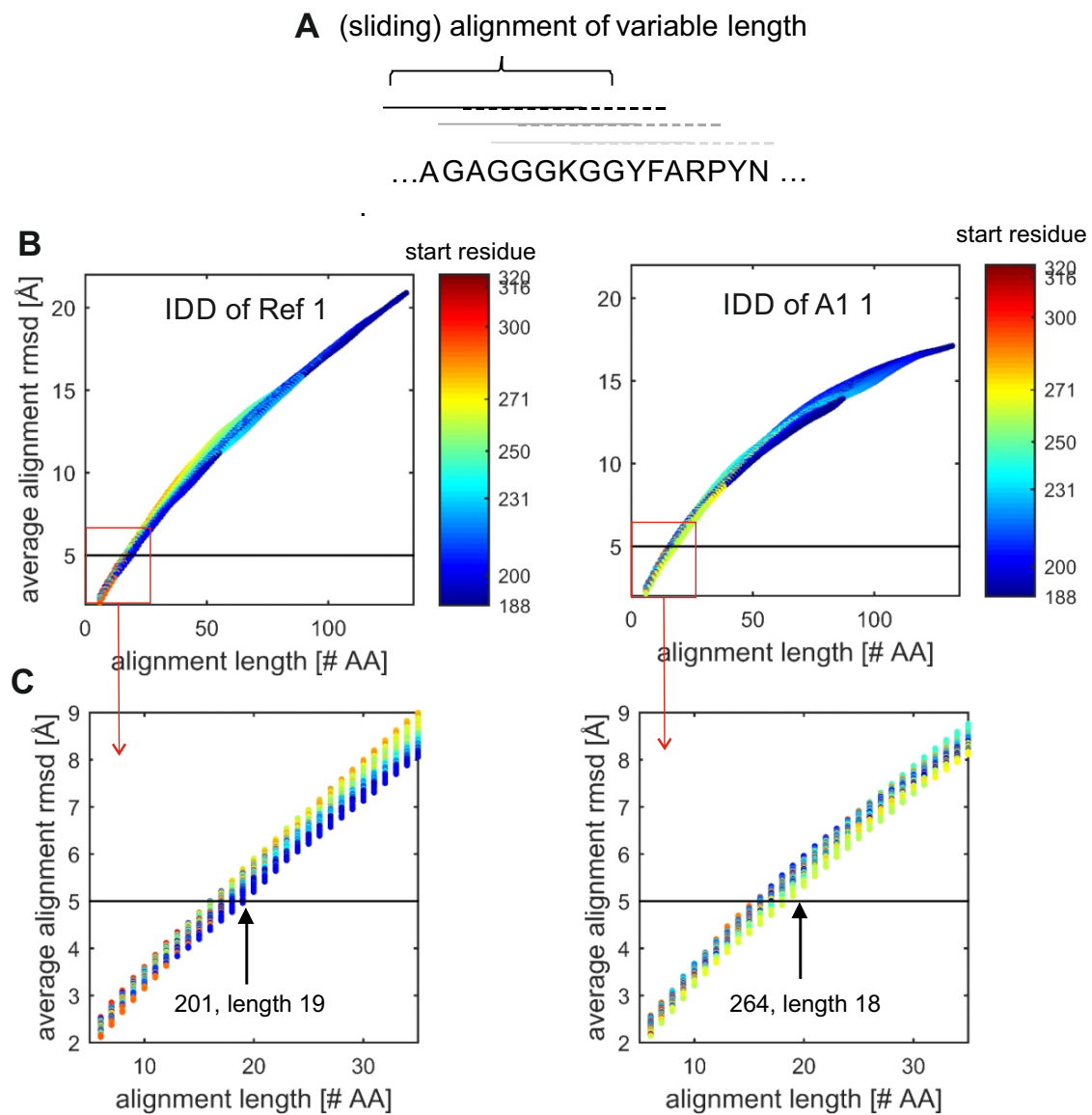


Figure B.8: Sliding window alignment (A) representation of the algorithm (exhaustive alignment search); (B) alignment length vs. average inter-conformer RMSD; the number of the first residue of each alignment window is colour-coded; the horizontal line indicates a possible RMSD cutoff (C) zoom-in on short alignment window size; the arrow indicates the longest possible alignment window that results in a user-chosen RMSD;

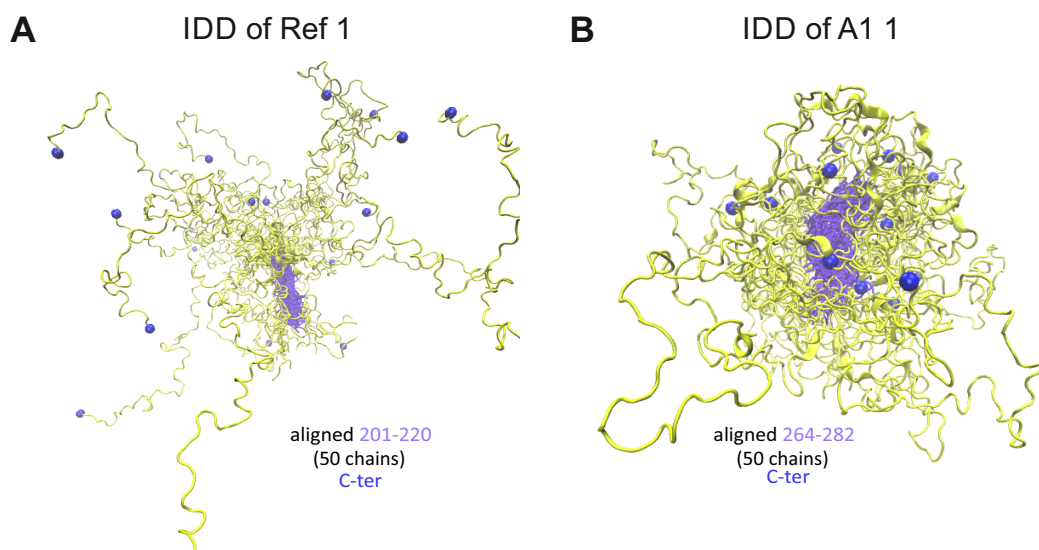


Figure B.9: Final alignment after sliding window alignment analysis of unrestrained (A), resp. DEER restrained (B) ensembles; the alignment range was automatically determined for a threshold RMSD of 5 Å (see arrow in Figure B.8) (A) representation of the chain selection scheme during exhaustive alignment search; aligned to longest possible window that produces a user-chosen average RMSD cutoff; full IDD (yellow) was aligned with the transformation matrix identified for the optimal window range (purple)

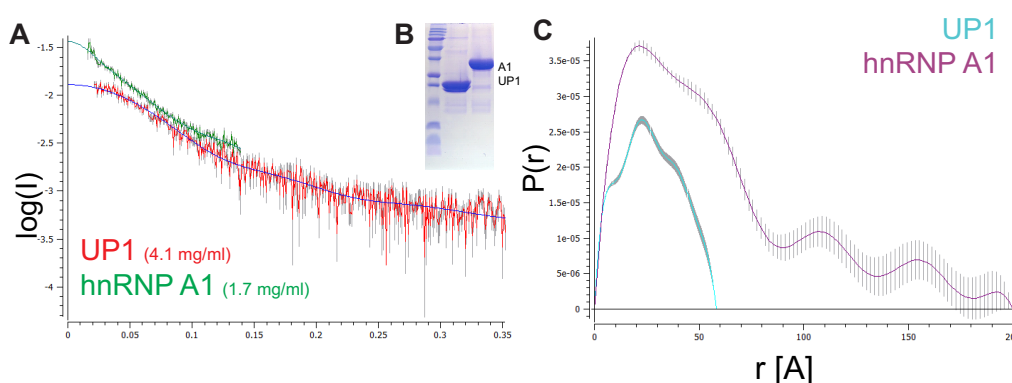


Figure B.10: Experimental SAXS curves obtained with hnRNPA1 resp. UP1 in dispersion buffer; (A) scattering curves after subtraction of the buffer baseline and fits with distance distributions; (B) SDS-PAGE of the purified proteins; (C) calculated distance distributions;

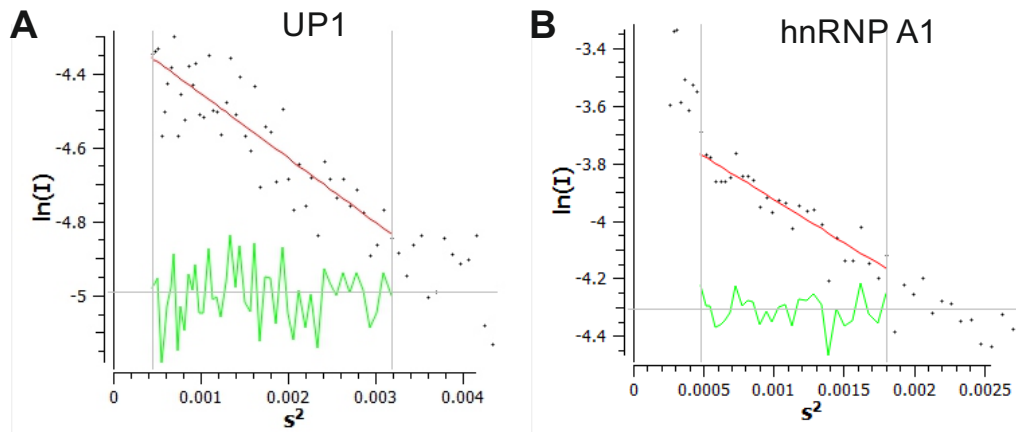


Figure B.11: fitting of R_{gyr} with ATSAS^[92]; (A) for UP1; (B) for hnRNP A1

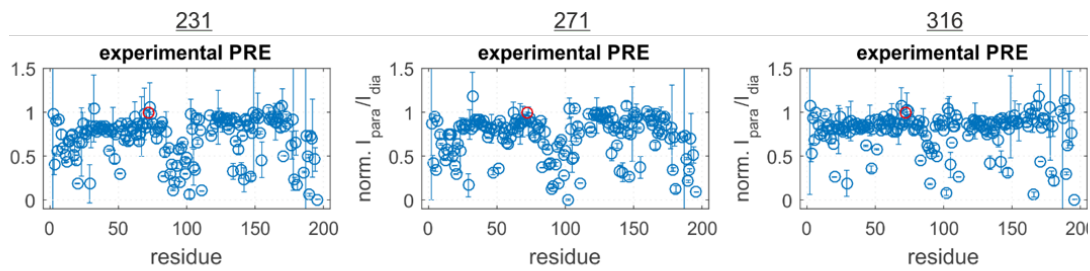


Figure B.12: Additional PRE results with the MTSL spin label at sites 231, 271 and 316; the plot in 231 corresponds to a repetition of the experiment shown in the main text.

| ensemble | N_{chains} | amino acid pair | frequency [%] |
|-----------------|---------------------|-----------------|---------------|
| A1 1 | 186 | 'ASP214-ARG194' | 1.1 |
| | | 'ASP214-ARG206' | 1.1 |
| | | 'ASP214-ARG218' | 2.7 |
| | | 'ASP214-ARG284' | 0.5 |
| | | 'ASP242-ARG232' | 1.6 |
| | | 'ASP250-ARG225' | 1.6 |
| | | 'ASP250-ARG319' | 1.1 |
| | | 'ASP262-ARG194' | 0.5 |
| | | 'ASP262-ARG206' | 0.5 |
| | | 'ASP42-ARG318' | 1.1 |
| | | 'ASP48-ARG300' | 0.5 |
| | | 'GLU132-LYS277' | 0.5 |
| | | 'GLU85-ARG319' | 0.5 |
| | | A1 2 | 186 |
| 'ASP214-ARG196' | 1.1 | | |
| 'ASP214-ARG206' | 2.2 | | |
| 'ASP214-ARG218' | 4.8 | | |
| 'ASP214-ARG225' | 0.5 | | |
| 'ASP214-LYS105' | 0.5 | | |
| 'ASP242-ARG218' | 1.1 | | |
| 'ASP242-ARG225' | 0.5 | | |
| 'ASP242-ARG232' | 2.7 | | |
| 'ASP242-ARG319' | 0.5 | | |
| 'ASP250-ARG232' | 0.5 | | |
| 'ASP262-ARG225' | 0.5 | | |
| 'ASP262-ARG232' | 0.5 | | |
| 'ASP48-ARG194' | 0.5 | | |
| 'GLU11-LYS277' | 1.1 | | |
| 'GLU185-ARG194' | 2.2 | | |
| 'GLU85-ARG194' | 1.1 | | |

Table B.2: Salt bridges by standard definition in vmd in restrained ensembles;

B

Appendix C

Supplementary Information for Chapter 5

C.1 Additional EMSA results

Additional EMSA assays were performed in TBE-buffered acrylamide gels at pH 7.5 under reducing conditions (1 mM DTT). The RNA binding was performed in 50 mM sodium phosphate, pH 6.5, 100 mM arginine/glutamate (R/E), 1 mM DTT, unless stated otherwise. In Figure C.1 we show that all RNAs (RNA_{aaa}, RNA_{aag}, RNA_{aga}, RNA_{agg}, for sequences and definitions of abbreviations see main text) are able to interact with UP1 and hnRNPA1.

In Figure C.2 we show that the absolute concentration of hnRNPA1, as well as the concentration of the buffer additives R/E matter. The central panel of Figure C.2 is the same as shown in the main text, for comparison. Interestingly, the cooperative binding of RNA_{aaa} and RNA_{agg} was not observed with a lower concentration of hnRNPA1 (18 μ M), but more resolved bands of low mobility are observed instead. Free RNA is still encountered in this assay. At higher hnRNPA1 concentration (36 μ M) we see a sequestering of the RNAs. This is observed even more strongly at three times higher concentration of R/E (100 mM vs. 300 mM).

C.2 Additional confocal imaging results

C.3 Additional DEER results with spin dilution and single Cys hnRNPA1

In Figure C.5(A-B) we show DEER results obtained with free hnRNPA1, which were already mentioned briefly in Chapter 3). Even in the absence of RNA in dispersion buffer (100 mM amino

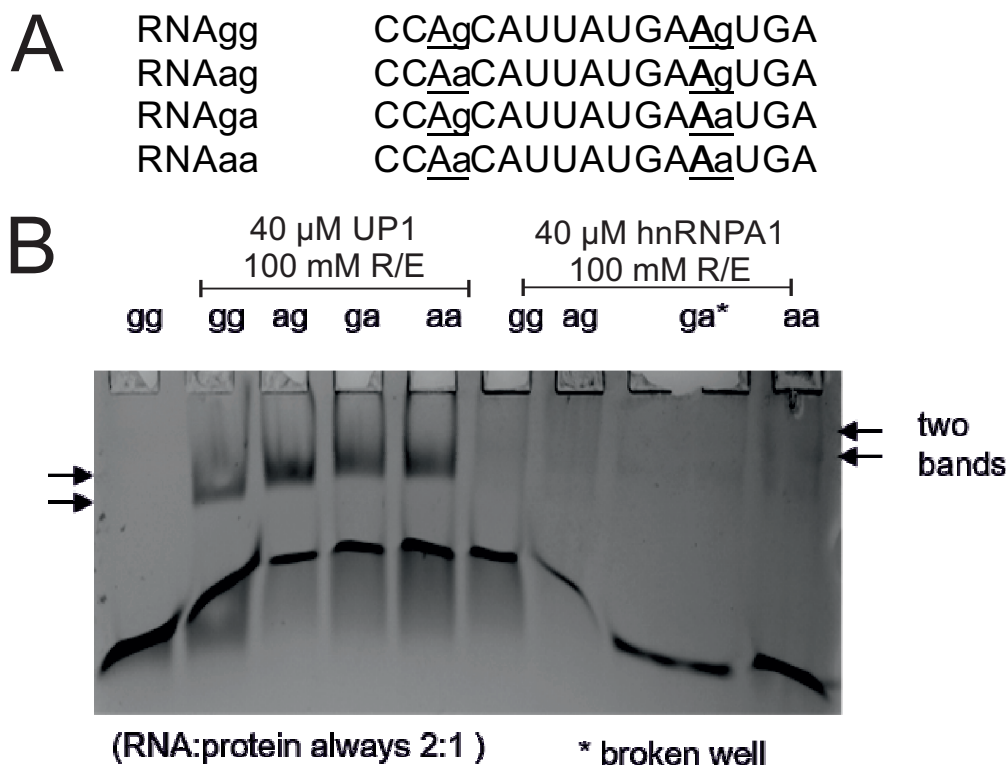


Figure C.1: RNA binding by UP1 and hnRNPA1 with the four studied RNAs; (A) RNA sequences; (B) EMSA at low RNA excess; lane to the left is free RNA;

acids R/E) frozen without glycerol the background decay was comparatively fast, given that the spin concentration was only $5 \mu\text{M}$. Note that these are conditions where almost no LDs were observed by imaging. The DEER signal decay was even faster in conditions of free hnRNPA1 where many small droplets were observed (50 mM amino acids R/E). This indicates that the (bound or potentially cleaved) spin label is found at higher local concentrations when we observe LLPS. The distance fits of the short-distance range (form factor fit after background correction) give more intensity (higher modulation depth) in the LD state. The fitted mean distance of the single Gaussian fit R_m is shifted to slightly larger distances, and the fitted distribution is narrower (smaller width σ_R) in the LD state than in the dispersed state.

In the presence of approximately 1:1 molar ratio of RNA_{gg} in dispersion buffer (100 mM amino acids R/E), we observe a less steep background decay than with the free protein. This is consistent with a lower local spin density than in the absence of RNA. The effect is even stronger with RNA_{aa}, where we observed the slowest decay in the series. The form factor fits with a single Gaussian model of the data with RNA are not very good, indicating that this is not a very good model. Unfortunately, with the given SNR we observed that model free analysis with Tikhonov regularisation tended to lead to very fragmented distance distributions with the automatic choice of regularisation parameter (results not shown), which did not allow more detailed interpretation.

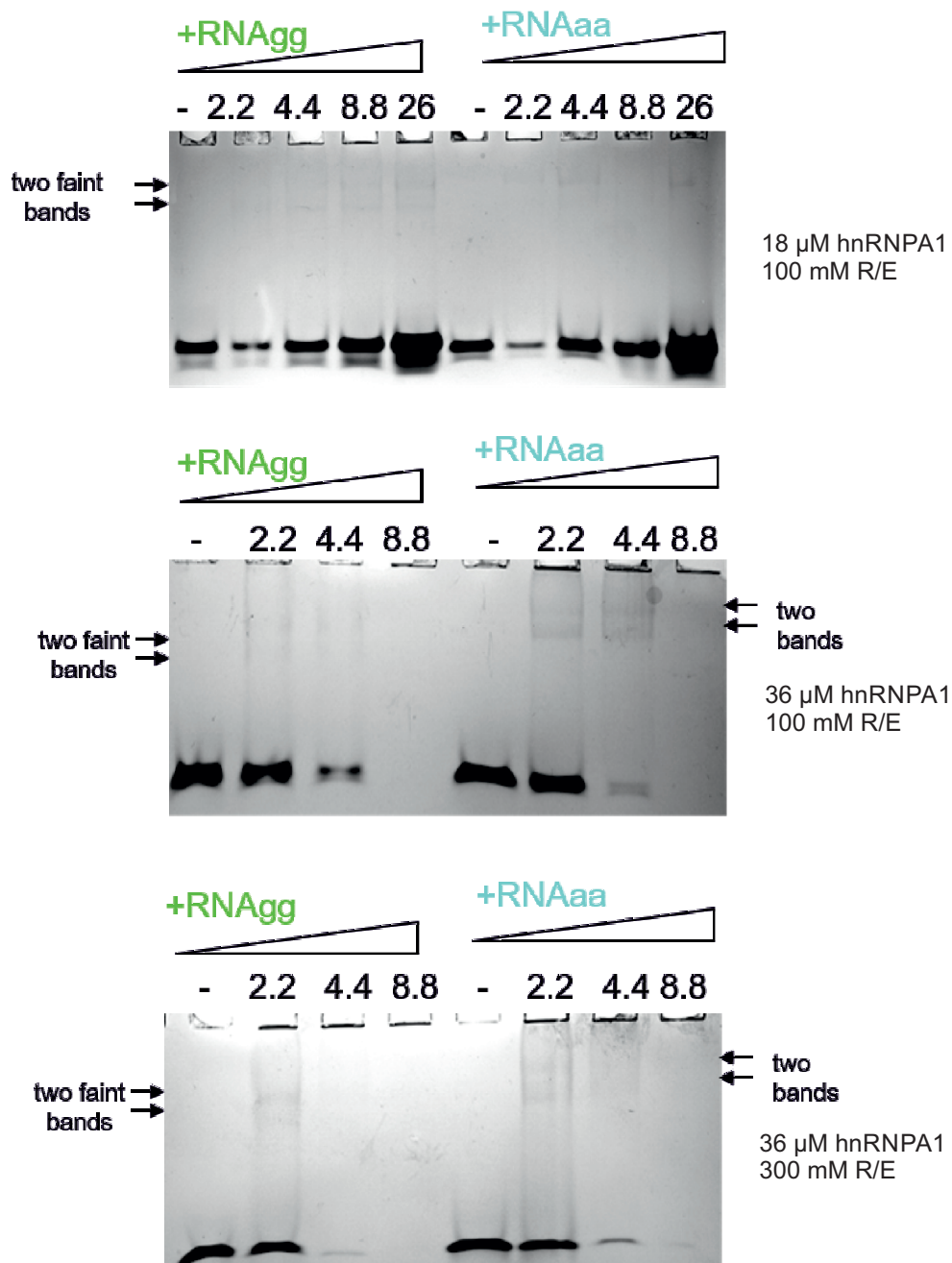


Figure C.2: EMSA of hnRNPA1 with RNAGg and RNAaa concentration ramp in dispersion buffer; (A) 'low' hnRNPA1 concentration; (B) 'high' hnRNPA1 concentration; (C) with 3 x increased amount of R/E in buffer

C.4 Relaxation measurements with singly spin-labelled hnRNPA1

Relaxation measurements were performed with 16 ns $\pi/2$, and 32 ns π pulse lengths. Transverse relaxation was quantified with the Hahn echo decay experiment, and longitudinal relaxation with

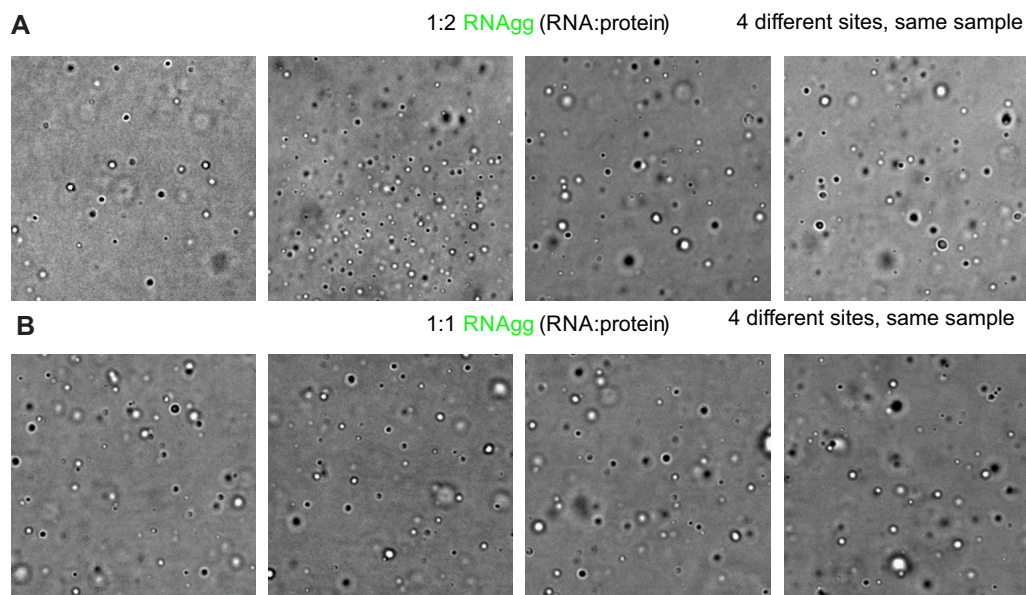


Figure C.3: Confocal imaging with RNA-induced LLPS of hnRNPA1 (dispersion buffer, 0.2% agarose); images are $41 \times 41 \mu\text{m}$; four different sites of the same sample are shown per condition; (A) RNA:protein over hnRNPA1 excess; (B) approximately same concentration;

the inversion recovery experiment (see Chapter 2). Unless stated otherwise, data were acquired at the maximum of the nitroxide Q-band spectrum. The data were phase-corrected to minimise the norm (sum of absolute values) of the imaginary part, and the constant plotting (see Figure C.6). Data fitting was performed with a single exponential, a bi-exponential, and a stretched exponential model:

$$S(t) = c \exp(-kt) \quad (\text{C.1})$$

$$S(t) = c_1 \exp(-k_1 t) + c_2 \exp(-k_2 t) \quad (\text{C.2})$$

$$S(t) = c \exp(-kt)^n \quad (\text{C.3})$$

The results for $5 \mu\text{M}$ hnRNPA1-S231R1 added to $100 \mu\text{M}$ wild-type hnRNPA1 are shown in Figure C.5 and summarised in Table C.1. We have previously presented results with droplet formation assays by confocal imaging at these total protein concentrations and buffer conditions. Note that recently we discovered that these results are possibly biased by spin label cleavage due to residual traces of reducing agent in the stock of wild-type hnRNPA1 (compare Chapter 3). This naturally affects the interpretation of the observed spin label distribution with respect to protein-protein interactions, and we are thus currently running control experiments. In this section we will nonetheless present the differences we found in spin relaxation and spin label distribution in samples prepared with singly-spin labelled hnRNPA1 under different sample conditions.

We first characterised relaxation properties in the samples frozen with low-melting agarose. Note that in all four samples we got slightly better results for fitting the longitudinal relaxation data with a bi-exponential or stretched exponential fit model than with a single exponential fit model.

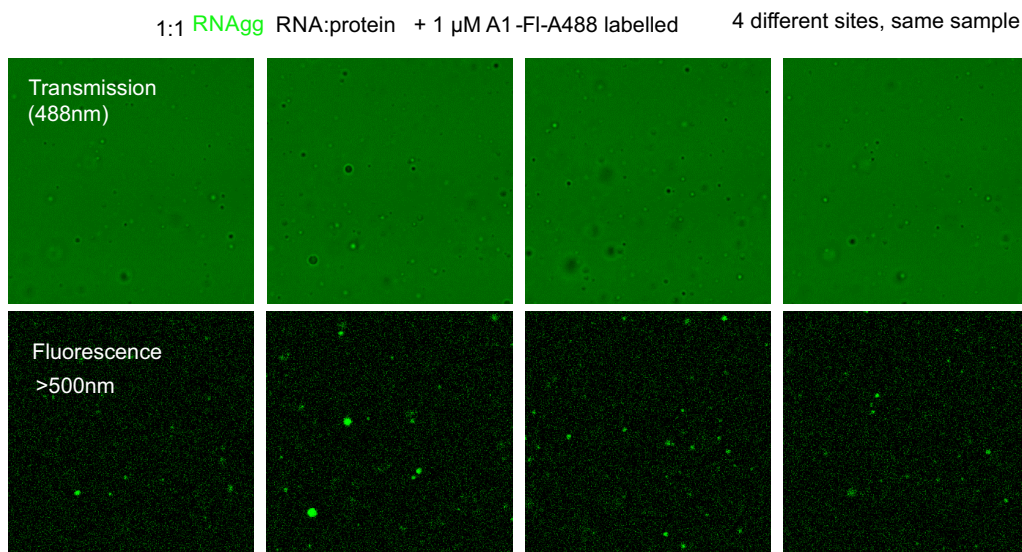


Figure C.4: Confocal imaging with RNA-induced LLPS of hnRNPA1 doped with Alexa-488 labelled hnRNPA1 (dispersion buffer, 0.2 % agarose); images are $41 \times 41 \mu\text{m}$; four different sites of the same sample are shown top: transmission images, bottom: fluorescent images;

| 231 [μM] | RNA [μM] | conditions | t_2 [μs] | BG dens. | Δ | $\langle N_{\text{spin}} \rangle$ | R_m [nm] | σ_R [nm] |
|--------------------------|--------------------------|--------------------|----------------------------|----------|----------|-----------------------------------|---------------|--------------------|
| 5 | 0 | 100 mM R/E | 3.5 | 0.170 | 0.028 | 1.05 | 3.371 | 1.415 |
| 5 | 0 | 50 mM R/E | 3.5 | 0.323 | 0.030 | 1.06 | 4.258 | 0.9354 |
| 5 | 45 | RNAagg, 100 mM R/E | 3.5 | 0.261 | 0.021 | 1.05 | 3.655 | 1.405 |
| 5 | 45 | RNAaaa, 100 mM R/E | 3.5 | 0.216 | 0.027 | 1.05 | 4.062 | 1.167 |

Table C.1: Measurement conditions and fit parameters from single-Cys DEER (S231R1) spin doping experiments shown in Figure C.5; for parameter definition see main text; hnRNPA1 wild-type concentration was $100 \mu\text{M}$ in all measurements.

It is tempting to assign the two fitted components to two different populations of spins in the sample which are exposed to different micro-environments (like dispersed and LD state), but note that similar behaviour is also observed for spin labels in homogeneous environments, which is usually explained by local inhomogeneities in the glassy frozen solvent. Nonetheless, we observed significant differences for the longitudinal relaxation between the samples without RNA and with RNAagg (values shown in Figure C.5). Significantly slower longitudinal relaxation than in the absence of RNA was observed with RNAagg. This was not the case with RNAaaa, where longitudinal relaxation was similar to that of the free hnRNPA1 samples. We currently have no explanation for the difference between the two types of RNA, and cannot exclude an artifact of e.g. sample preparation. In all measurements, except for the one with RNAagg, the fitted T_1 is rather short for a nitroxide at 50 K. For the transverse relaxation data the stretched exponential fit model gave the best results. Interestingly, the fitted transverse relaxation time was approximately the same in all

samples. In all cases it allowed detection of DEER traces with a total transverse evolution time of at least $\tau_{\text{tot}} = \tau_1 + \tau_2 = 4.4 \mu\text{s}$ (for ~ 12 h acquisition time per trace).

With the bi-exponential fit model the samples without RNA we observed in roughly equal fractions a fast relaxing ($T_1 \approx 0.6$ ms) and a more slowly relaxing component ($T_1 \approx 2$ ms). In the samples with RNA we find in general slower longitudinal relaxation than in the samples without RNA. The fractions of the fast and slow relaxing components in the bi-exponential fit are inverted for the sample with RNA_{agg} resp. RNA_{aaa}. With RNA_{agg} the slowly relaxing component dominates, whereas with RNA_{aaa} the fast relaxing component dominates. Both are comparatively short for typically observed nitroxides.

Nonetheless, we did clearly observe better relaxation times than in the samples without spin dilution, and we found that there were small differences observed in the samples prepared with and without RNA in terms of the steepness of the DEER signal decays. The fastest DEER signal decay in the series with singly spin labelled hnRNPA1 was observed in the LLPS sample without RNA, which also featured the smallest LDs in imaging. Assuming a homogeneous distribution of material in an LD this implies that the spin label density of the LD is decreased in the presence of RNA, but keep in mind that we may be partially observing cleaved spin label in the experiment. Another possible factor contributing to fast spin relaxation may be effects from the freezing procedure without glycerol as cryo-protectant, which could lead to partial crystallisation, and strong sample inhomogeneity.^[42] This could in future experiments be checked by spin probing with nitroxides in LLPS samples, and by freezing reference mixtures of spin label in dispersed conditions.

C.5 Additional DEER results with a double Cys mutant

We performed DEER experiments with the MTSL-labelled double Cys mutant 182/223, which was found to have an intermediate mean distance in the dispersed state (see ?? in Chapter 4). The results for spin doping experiments of this mutant into wild-type hnRNPA1 samples are shown in Figure 4.5. Note that partial spin label cleavage might have occurred in these samples due to residual reducing agent (see discussion in main text). Upon freezing in agarose stabilised conditions we found a steeper background decay than in the dispersed state with glycerol. This is in agreement with the single Cys-mutant experiments. Upon addition of RNA_{agg} we see an enhanced modulation depth, and a slightly larger contribution of longer distances compared to the free state. The effect of RNA_{aaa} is weaker, but similar to that of RNA_{agg}.

| 182/223 [μM] | wt [μM] | RNA [μM] | conditions | t_2 [μs] | BG dens. | Δ | $\langle N_{\text{spin}} \rangle$ | R_m [nm] | σ_R [nm] |
|------------------------------|-------------------------|--------------------------|--------------------------------------|----------------------------|-------------|----------|-----------------------------------|---------------|--------------------|
| 10 | 0 | 0 | 100 mM R/E, d ₈ -glycerol | 6.5 | 0.000 | 0.246 | 1.50 | 3.207 | 1.334 |
| 5 | 100 | 0 | 100 mM R/E | 4 | 0.353 | 0.190 | 1.40 | 3.308 | 1.525 |
| 5 | 100 | 100 | RNA _{agg} , 100 mM R/E | 4 | 0.601 | 0.276 | 1.58 | 3.763 | 1.229 |
| 5 | 100 | 100 | RNA _{aaa} , 100 mM R/E | 4 | 0.509 | 0.222 | 1.45 | 3.963 | 1.085 |

Table C.2: Fit parameters from double-Cys (S182R1/S223R1) DEER spin doping experiments shown in Figure C.8;

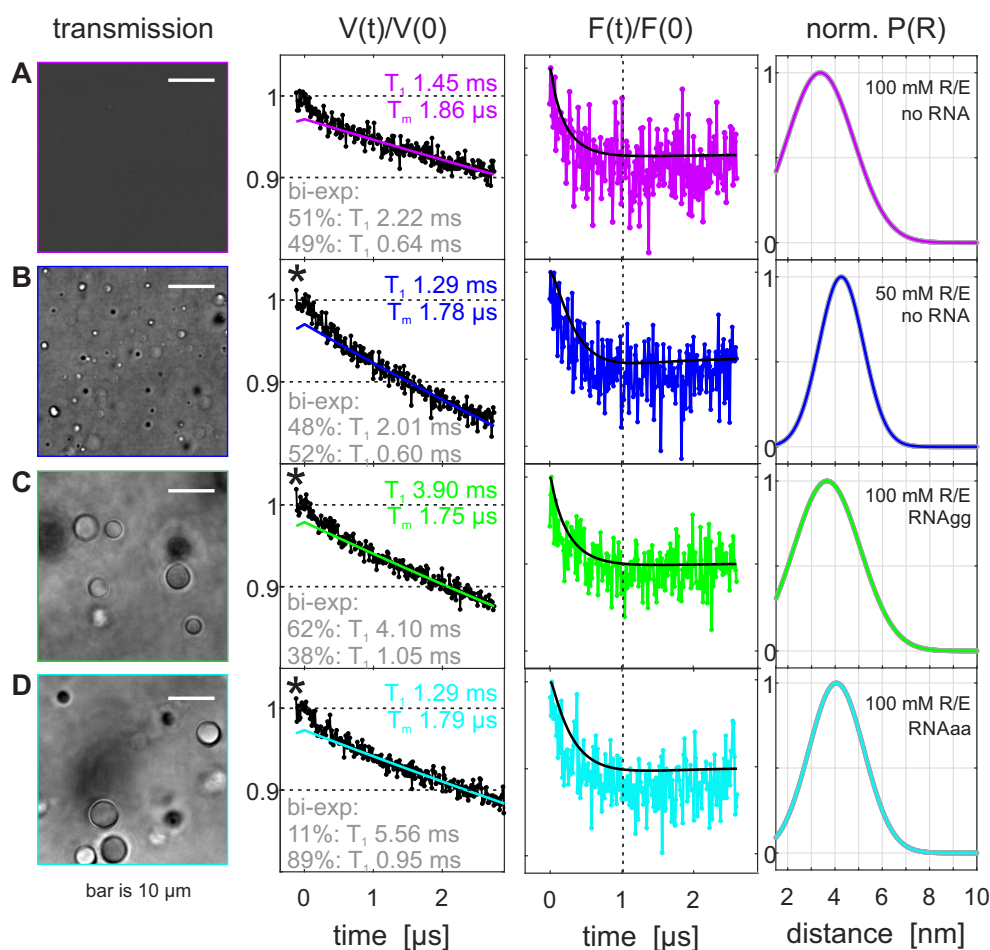


Figure C.5: Comparing droplet images to DEER data measured with single-Cys mutants of hnRNPA1; DEER data were obtained with 5 μM MTSL-labelled hnRNPA1-S231C doped into 100 μM wild-type hnRNPA1, left to right: agarose-stabilised confocal images obtained with 100 μM wild-type hnRNPA1; primary DEER data and background fit (coloured lines), in this panel we also give the independently determined relaxation rates (mono-exponential and bi-exponential fits). Form factors and Gaussian fit (black); fitted Gaussian distance distributions; (A) no RNA, 100 mM R/E; (B) no RNA, 50 mM R/E; (C) + RNA_{agg}, 100 mM R/E; (D) + RNA_{aa}, 100 mM R/E;

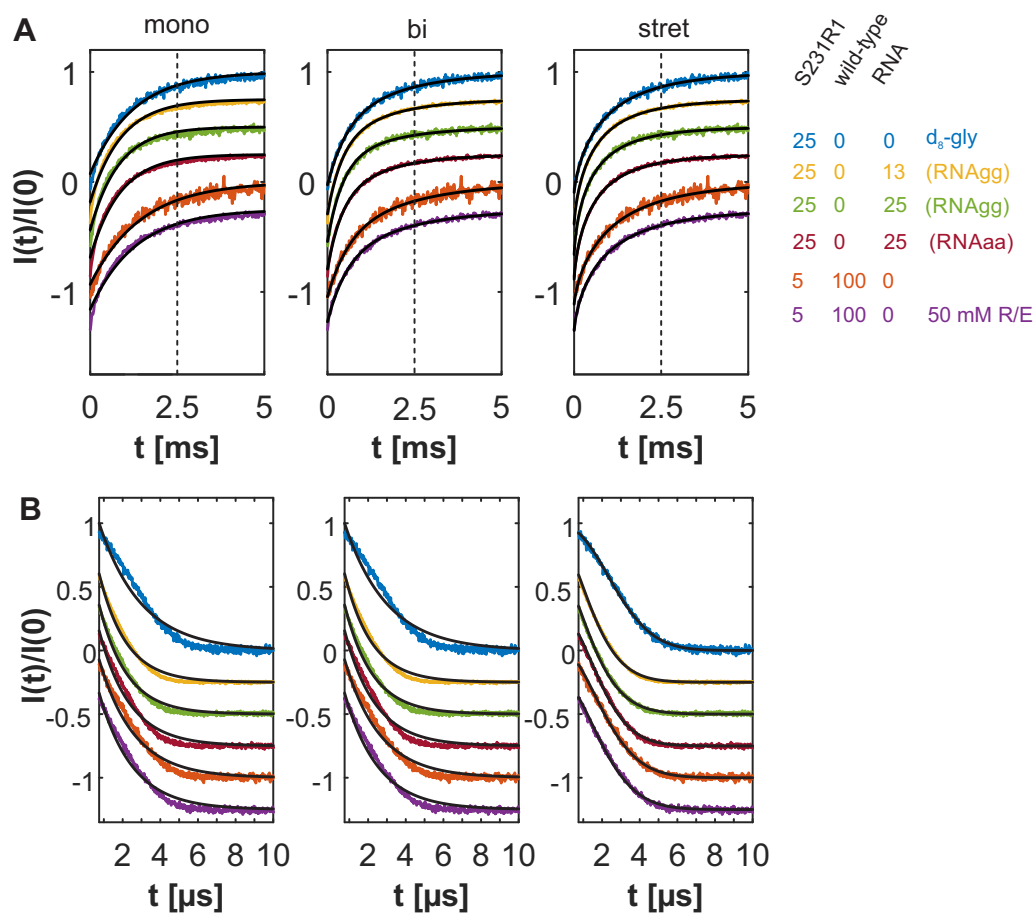


Figure C.6: Relaxation properties of the LLPS samples at 50 K; (A) inversion recovery traces, normalised to unit intensity at the plateau and shifted vertically for visibility by 0.25; shot repetition time $srt = 16$ ms, refocusing delay $\tau = 400$ ns; (B) Hahn echo decay ($srt = 4$ ms); traces were normalised to unit intensity at $\tau = 400$ ns and shifted vertically for visibility by 0.25; The experiments were performed with 16, resp. 32 ns ($\pi/2$, resp. π) pulses on the maximum of the nitroxide Q-band spectrum. Sample conditions are indicated in the legend. From left to right: fits (black) with one exponential component; or two exponential components; or one stretched exponential component;

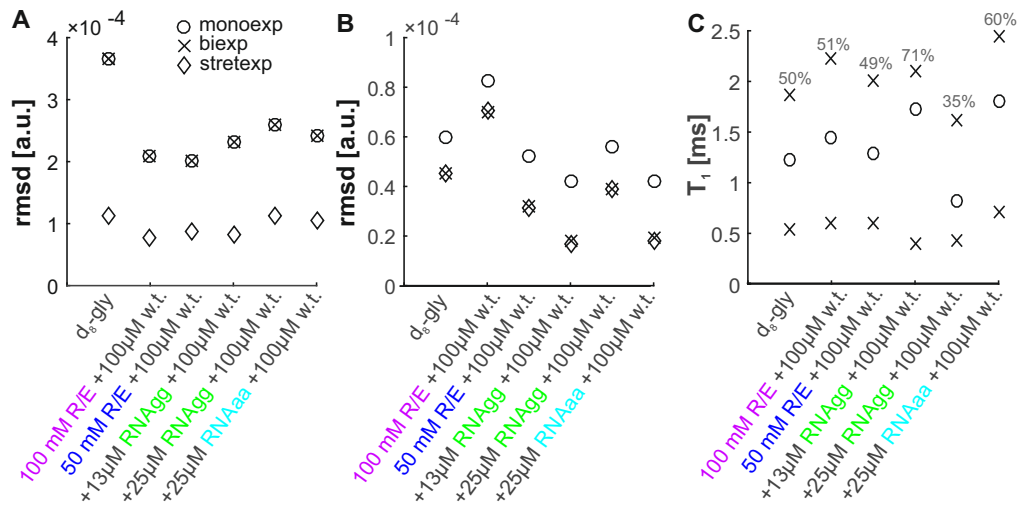


Figure C.7: Fit qualities and relaxation parameters; (A) rmsd of T_m fits with the mono-, resp. bi-, resp. stretched exponential fit model; (B) RMSD of IR fits with same models; (C) fitted longitudinal relaxation times T_1 for IR experiments with mono-exponential fit, and the two components of the bi-exponential fit (fraction indicated for slow relaxing component);

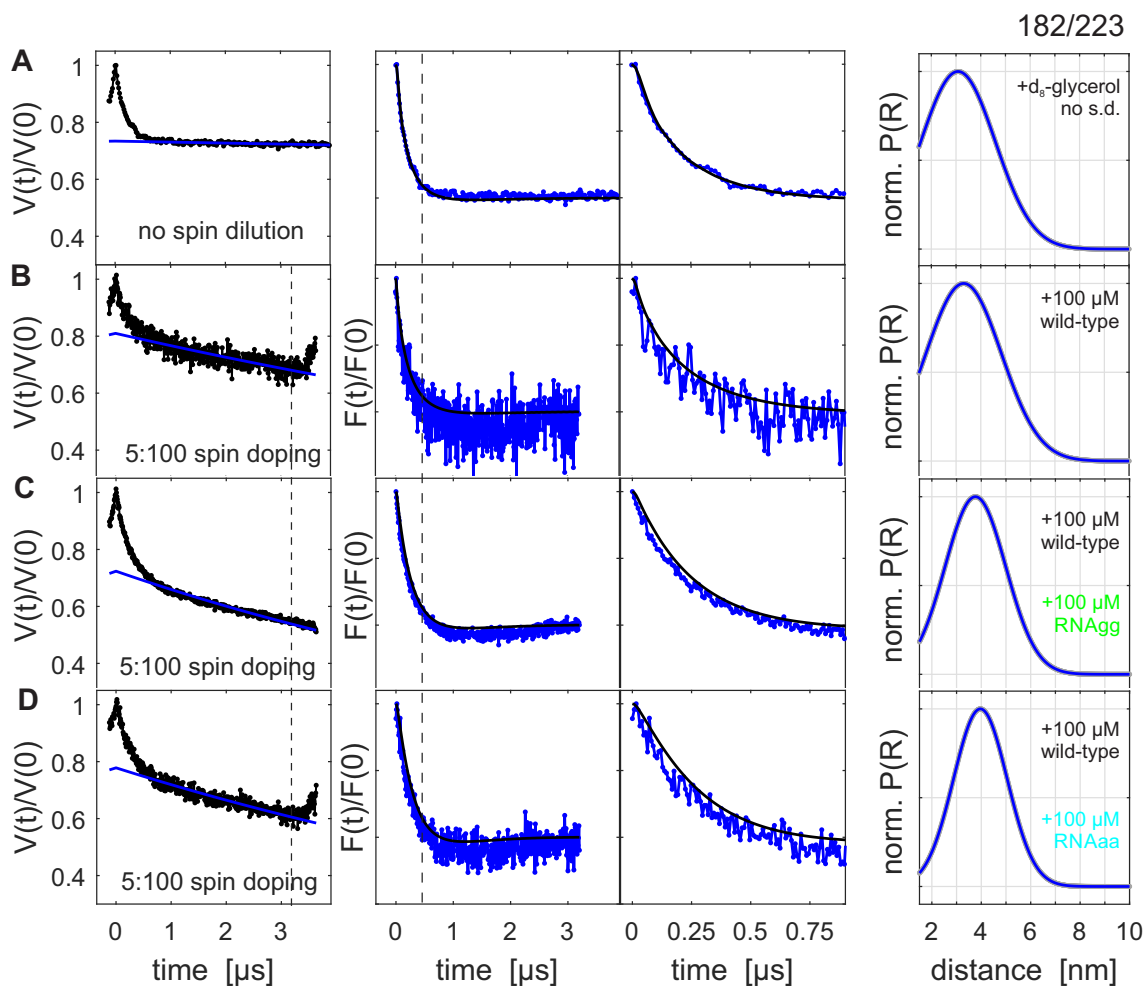


Figure C.8: Monitoring conformational changes of the IDD by intramolecular distance distributions with the MTSL-labelled site pair 182/223; left to right: primary DEER data $V(t)/V(0)$, data were truncated at the dashed line prior to further analysis; form factors after 3-dimensional background correction $F(t)/F(0)$ and zoom on short t ; normalised Gaussian distance distributions $P(R)/P_{\max}$ fitted to the form factor contribution; (A) 20 μM double labelled hnRNPA1 mutant, no spin dilution, dispersed state (50 mM sodium phosphate, pH 6.5, 100 mM R/E, 50 % (v:v) d_8 -glycerol); (B-D) 5 μM double labelled hnRNPA1 mutant doped into 100 μM wild-type hnRNPA1; in dispersion buffer 50 mM sodium phosphate, pH 6.5, 100 mM R/E/0.2 % (w:v) agarose; (B) no RNA (C) +RNAgg (1:1 molar) (D) +RNAaa (1:1 molar)

Appendix D

Supplementary Information for Chapter 7

D.1 RIDME background measurements for nitroxide detected RIDME

We found that the stretched exponential fit of the RIDME background (BG) is often not a good model for nitroxide-detected RIDME. This we observed not only for our model compounds, but also on reference samples. In Figure D.1 we show RIDME background measurements on a mixture of tempol with [Cu(II)-TAHA] in fully deuterated solvent at different temperatures and varying T_{mix} . Along the vertical axis we increased the length of the first refocusing delay t_1 , while keeping t_2 fixed. The dashed lines are a guide to the eye for a 'ridge'-like feature in the background shape that leads to a deviation from the stretched exponential decay. This feature is present in a large range of conditions, and moves with t_1 , until it disappears after $t_1 \approx t_2$ in this case. This may be a coincidence for this particular choice of t_2 . Note, that ESEEM modulations generally are strongly suppressed when increasing t_1 . The same artifact is observed in samples of only tempol (Figure D.2). Here we measured a series with different solvent compositions with varying mixtures of D_2O and H_2O . The percentage of H_2O written in the figure is given as the volume fraction of total sample volume. In each vertically shifted trace we increased t_1 . The experimental temperature of 50 K is not optimal for nitroxide-detected RIDME, but was chosen for convenient sample exchange during the measurement session. We observed that with higher degree of protonation, it is still possible (if more challenging) to find a choice of t_1 where the background is well approximated by a single stretched exponential while maintaining a reasonable SNR (which decreases due to transverse relaxation with longer t_1). Although more rigorous testing is required to understand this background issue, we observed that the t_1 required to obtain a stretched exponential-type

background shape coincides with the time t , after which the 3p-echo decay is a monotonously decaying function. For this particular sample this happens at $\sim 4 \mu\text{s}$ (Figure D.3). The background fitting with a stretched exponential is empirically found to be much more stable with respect to the fitting range when a sufficiently long t_1 is used. We observed that in RIDME time-evolution during t_1 and t_2 is not strictly equivalent. Even just using $t_1 > t_2$ with a constant t_{max} can slightly suppress the unwanted background shape at early times in the trace.^[250]

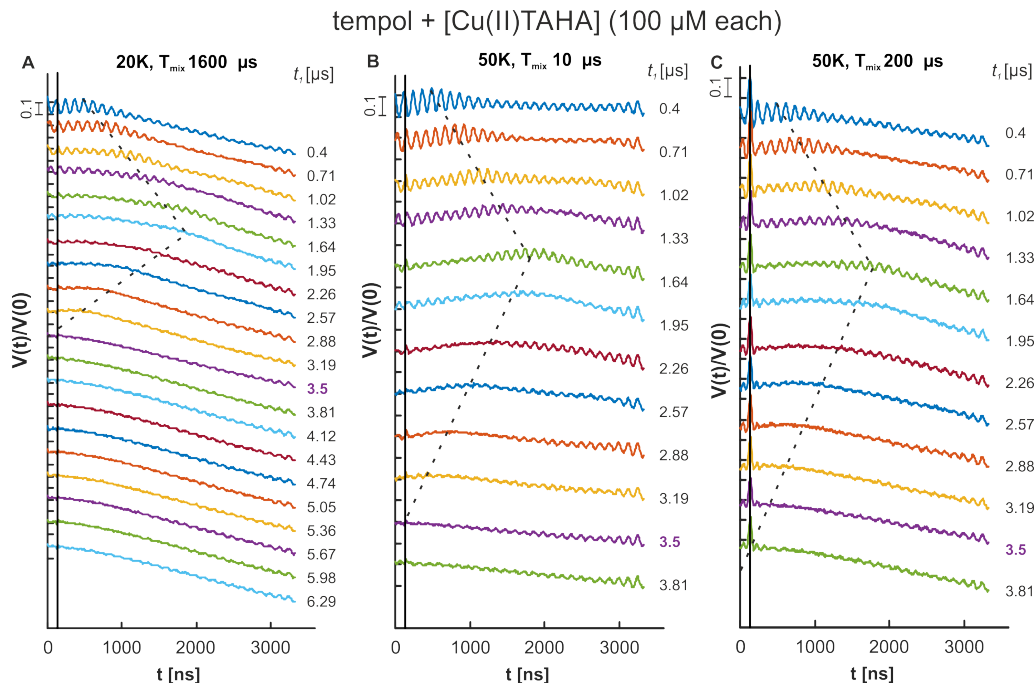


Figure D.1: RIDME background measurements on a mixture of tempol with [Cu(II)-TAHA] (20) in aqueous deuterated solvent at different temperatures and mixing times. The second refocusing delay in all traces was $t_2 = 3500$ ns. At 20 K (A) we used an initial t_1 of $t_1 = 400$ ns, which was incremented in steps of 310 ns to a final value of $t_1^{\text{max}} = 6290$ ns. For the measurements at 50 K (B,C) the same initial delay and increment was used, but we recorded traces only up to $t_1^{\text{max}} = 3810$ ns. The dashed lines are a guide to the eye for a 'ridge'-like feature in the shape of the background trace, which appears in all three tested conditions. The position of this component moves with t_1 .

We tested the ESEEM-removal by division approach,^[3] and found that this method, too, is able to suppress the background artifact. The suppression, however, comes at the cost of modulation depth, and thus sensitivity. In samples with high modulation depth, and fast transverse relaxation, however, this approach may perform better than the increased t_1 time method.

D.1.1 Orientation-Dependent Relaxation Measurements for Cu(II)

As is pointed out in the main text we can assume to average the RIDME contributions from all orientations of the Cu(II) spins in nitroxide-detected RIDME as long as the mixing time exceeds the

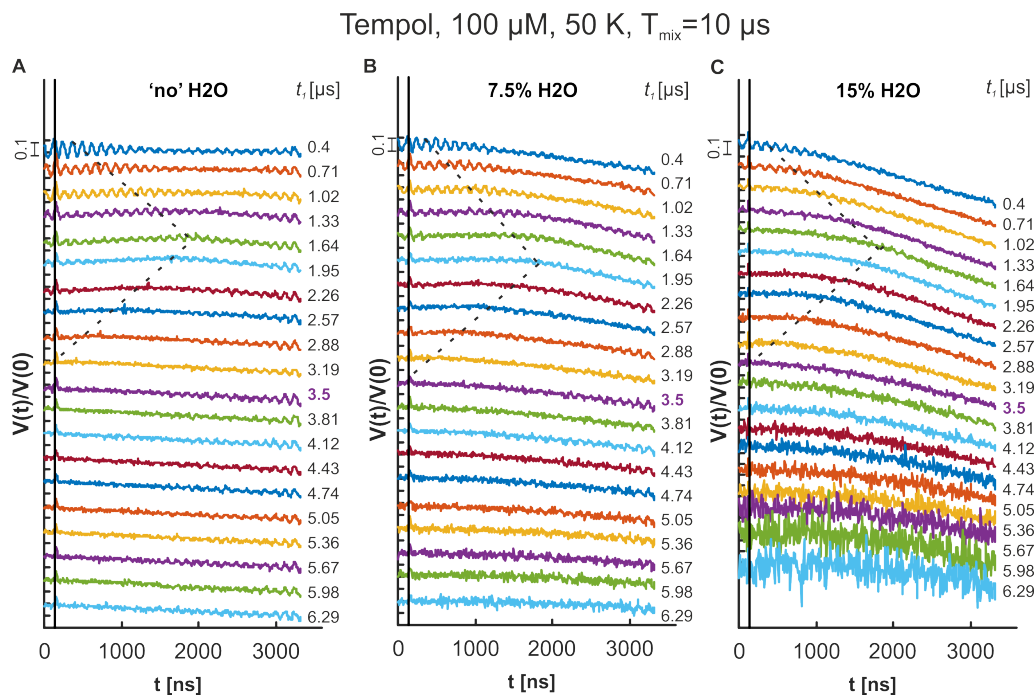


Figure D.2: RIDME background measurements on tempol in aqueous solvents of varying $\text{D}_2\text{O}:\text{H}_2\text{O}$ ratios. The percentage given for each panel is the approximate volume concentration of H_2O in the total sample volume. In the traces from top to bottom the delay t is incremented from the starting value of $t_1 = 400$ ns in steps of 310 ns to a final value of $t_1 = 6290$ ns. t_2 is fixed at 3500 ns in all traces. The dashed lines are a guide to the eye for a 'ridge'-like feature in the shape of the background trace. In the case of lowest degree of protonation (A) an additional dotted line indicates where a spike-like feature appears in the traces. SNR decreases in each series, since also $t_{\text{tot}} = t_1 + t_2$ increases. This is most strongly observed in the case of highest solvent protonation (C).

characteristic longitudinal relaxation time of all possible orientations of $\text{Cu}(\text{II})$. In SI1 Figure D.5 we demonstrate that, while there are differences in longitudinal relaxation at different positions in the $\text{Cu}(\text{II})$ spectrum, these are small compared to the mixing times that can be used in nitroxide-detected RIDME. This is both the case for $\text{Cu}(\text{II})$ in model compound **1**, and $\text{Cu}(\text{II})$ in the same ligand environment, but not covalently linked to the nitroxide-spacer moiety.

D.1.2 Comparison of $\text{Cu}(\text{II})$ -nitroxide DEER and RIDME measurements at Q-band

We compared RIDME and DEER measurements on the $[\text{Cu}(\text{II})\text{-TAHA}]$ -nitroxide ruler **1**, for which the dipole-dipole interaction is dominant and the shape of the dipolar spectrum has clear features of the canonical Pake pattern. For this ruler the separation between EPR absorption maxima of the nitroxide spins and the $\text{Cu}(\text{II})$ ions is $\Delta B = 33$ mT, which approximately translates to the resonance frequency difference $\Delta\nu \approx 920$ MHz. Even with the recent major improvements in

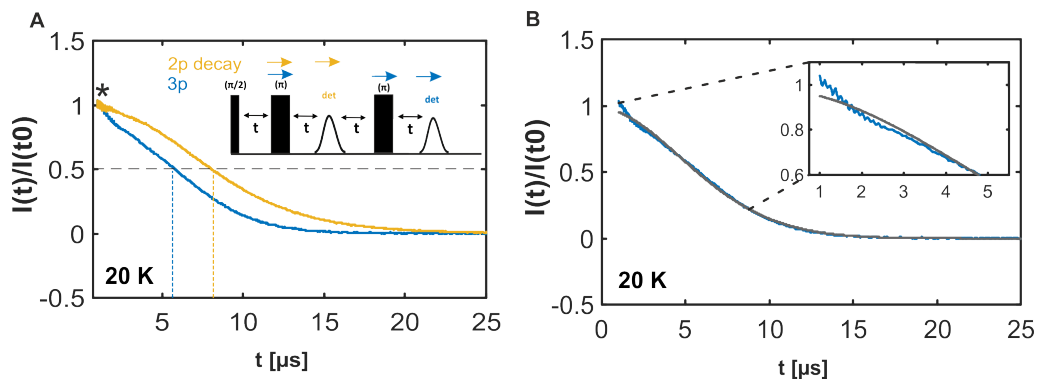


Figure D.3: RIDME background measurements on tempol in aqueous solvents of varying $D_2O:H_2O$ ratios. The percentage given for each panel is the approximate volume concentration of H_2O in the total sample volume. In the traces from top to bottom the delay t is incremented from the starting value of $t_1 = 400$ ns in steps of 310 ns to a final value of $t_1 = 6290$ ns. t_2 is fixed at 3500 ns in all traces. The dashed lines are a guide to the eye for a 'ridge'-like feature in the shape of the background trace. In the case of lowest degree of protonation (**A**) an additional dotted line indicates where a spike-like feature appears in the traces. SNR decreases in each series, since also $t_{tot} = t_1 + t_2$ increases. This is most strongly observed in the case of highest solvent protonation (**C**).

EPR-resonator technology^[290] and UWB excitation^[75,278] this large resonance frequency offset remains challenging for DEER spectroscopy. It is not a unique case: maximum absorption in the Cu(II) EPR spectrum is observed at a similar field for [Cu(II)-PyMTA]-nitroxide **2** as well as for [Cu(II)-terpyridine]-nitroxide.^[208] At X-band frequencies, DEER measurements between the maxima of the nitroxide and Cu(II) spectra are facile with commercial resonators and hardware, but orientation averaging is challenging.^[227]

In order to qualitatively compare the performance of the DEER and RIDME experiments in this case, we conducted the following two measurements. Both experiments were set up in the same spectrometer session on a 200 μM sample of [Cu(II)-TAHA]-nitroxide **1**. First, we set up a DEER experiment with the shortest achievable 48/96 ns pulses for detection on the maximum of the Cu(II) spectrum. For pumping the nitroxide spins we used a chirp pulse of duration $t_p = 150$ ns and of bandwidth 450 MHz. To have a pump pulse that is approximately centred in the nitroxide EPR spectrum we used an offset of pump and detection pulse of +900 MHz. The refocusing delays were set to $t_1 = 400$ ns and $t_2 = 3500$ ns. Due to the strong resonator over-coupling, the critical adiabaticity of the chirp pulse was small, and the experimentally observed inversion efficiency was only 1% (Figure D.6). Note that higher resonator bandwidth and better power conversion could have been achieved with a loop-gap resonator for 1.6 mm samples,^[290] albeit at the expense of a reduction of the echo amplitude by about a factor of two.

Second, we performed a RIDME experiment in the following way. The resonator mode was changed to a narrow profile (as seen in the tune picture). The detection frequency was set in the centre of the resonator, to have maximum sensitivity. With such a setup, the detection $(\pi/2)/(\pi)$ pulses of the

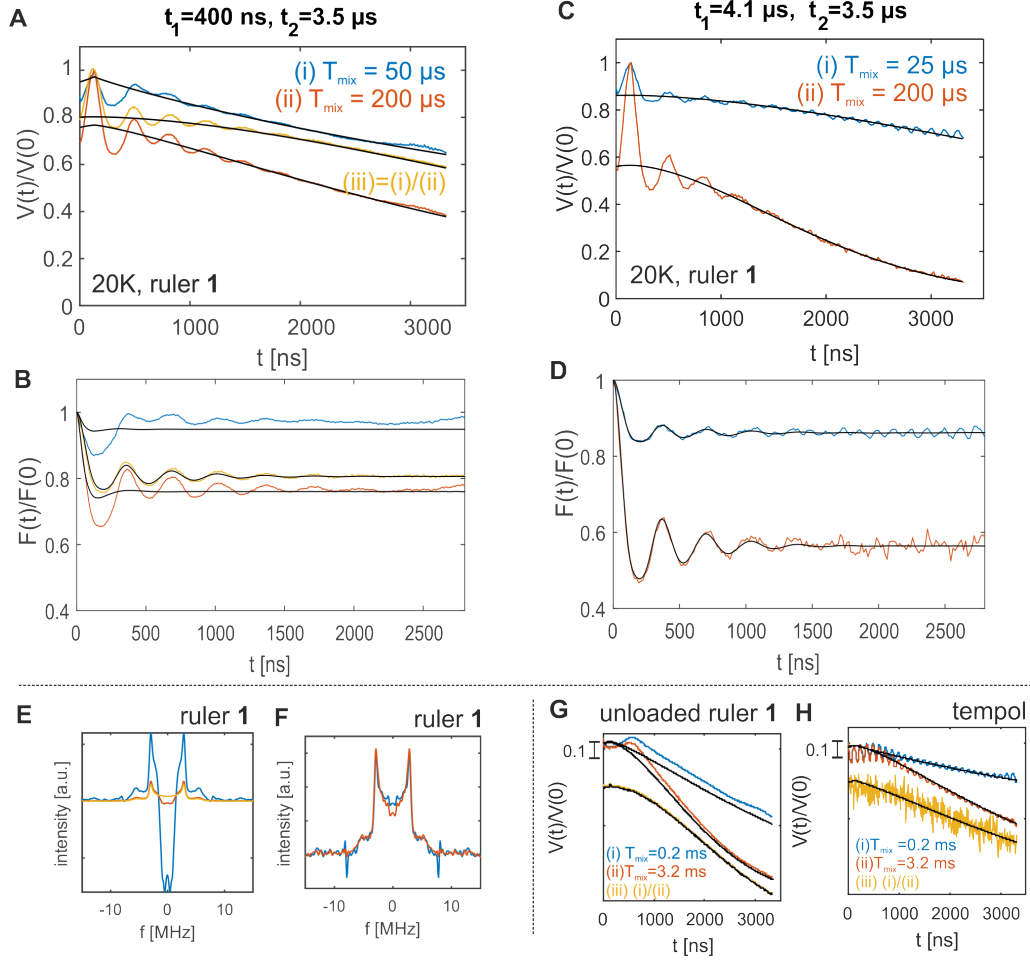


Figure D.4: Removal of background artifact including division approach; all data measured at 20 K with $t_2 = 3.5 \mu\text{s}$; (A-F) ruler 1; (A) normalised primary RIDME data with $t_1 = 0.4 \mu\text{s}$ and (C) with $t_1 = 4.1 \mu\text{s}$; mixing times are indicated in the legend. Blue traces correspond to the measurement at short T_{mix} , red traces at long T_{mix} , yellow traces are obtained by division of the complex signals after normalisation at the zero-time (to account for different signal intensities); (A,C) black traces are the background fit with a single stretched exponential function. Better fits can be obtained after division, or by measuring with long t_1 . (B,D) Experimental form factors (colored), and fit (black) after background division; note that a longer T_{mix} than reported in the original study^[3] is used for division. We observe good removal of the BG artifact, but a significant loss of modulation depth. (E) spectra of traces with $t_1 = 0.4 \mu\text{s}$; (F) spectra of traces with $t_1 = 4.1 \mu\text{s}$; (G) RIDME background measurement with unloaded ruler 1, resp. (H) tempol; T_{mix} indicated in legend, yellow traces obtained by division, and shifted by 0.25 for visibility; background fit with single stretched exponential in black

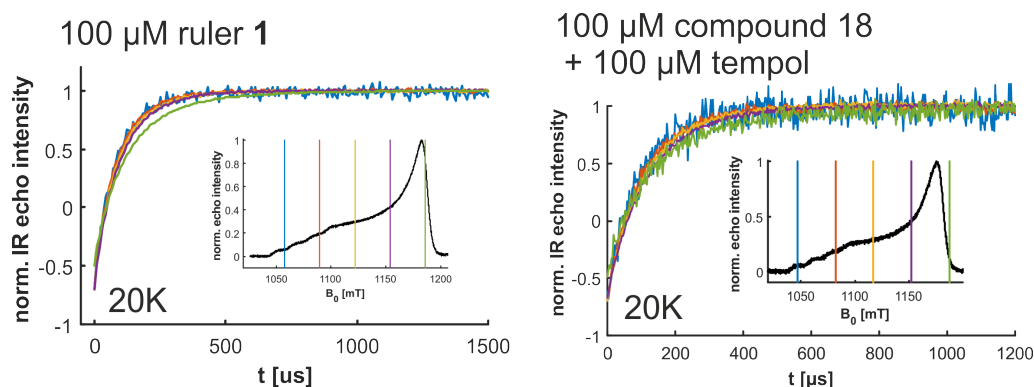


Figure D.5: Orientation dependent longitudinal relaxation of Cu(II) in ruler **1** (left), and in a reference sample (1:1 mixture of compound **18** and tempol) (right) at 20 K; Cu(II) oriented with the x/y -components of the hyperfine-, and g -tensor along B_0 (green curves) relaxes slightly more slowly than when oriented along the z -component (dark blue and orange).

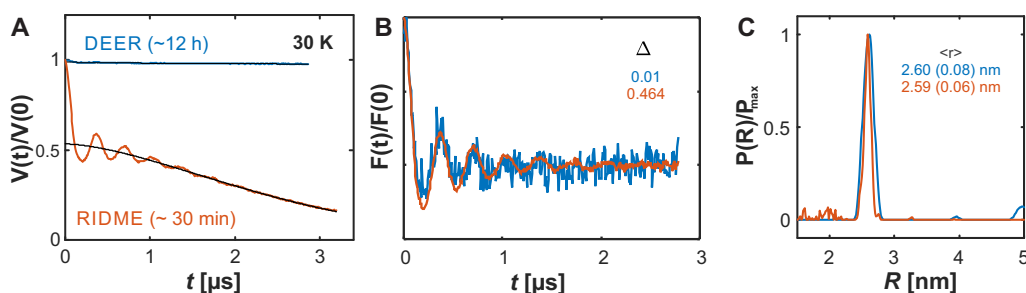


Figure D.6: PDS on 200 μM ruler **1** in deuterated solvent; (A) primary data; (B) form factors scaled by modulation depth (C) distance distributions;

length of 12/24 ns could be used. The magnetic field was set to the maximum of the nitroxide EPR spectrum at the detection frequency. The transverse evolution delays were set to $t_1 = t_2 = 3500$ ns, in order to avoid the background shape problem, which at the same time removed the ESEEM artefacts from the RIDME trace. The mixing time of $T_{\text{mix}} = 400$ μs was used.

The time-increment for shifting the position of both pump pulse (in DEER) and the mixing block (in RIDME) was set to 8 ns. In the DEER experiment, a reduced number of data points was detected, so that not the full range of available transverse evolution period was measured and thus a small additional increase in SNR could be achieved.

The detected RIDME modulation depth was 46% against 1% in DEER, which ensured a major SNR advantage for RIDME in the comparison of the form factor traces. Both measurements revealed a sharp peak at 2.6 nm (2.59 nm for DEER), which was slightly broader in the DEER case (FWHM of 0.08 nm) as compared to the RIDME data (FWHM of 0.06 nm). The small differences in position and width of the distance peak from the DEER data are likely due to the higher noise level in those data, but could be as well related to a stronger orientation selection effect in this measurement. Furthermore, a smearing of the DEER time trace, due to the 150 ns

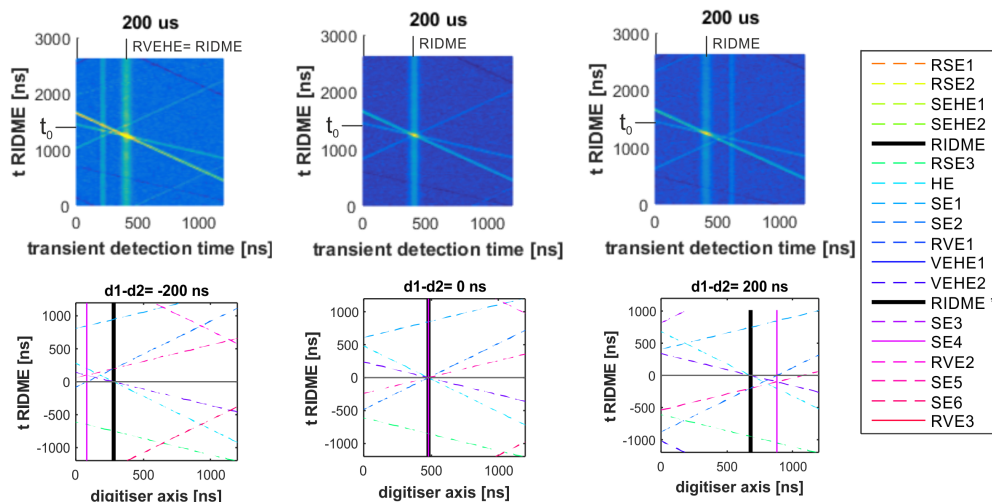


Figure D.7: Calculated and experimental echo pathways (echo transient plots) in 5-pulse RIDME

long pump pulse is expected, which would also affect the shape of the distance distribution.^[76] Although a DEER experiment with a dedicated ultra-wideband resonator for 1.6 mm sample tubes and systematic chirp pulse optimisation is expected to perform better, the comparison is still representative for a large resonance offset between the pumped and detected species. The RIDME experiment outperforms DEER in this regime. Only the use of bimodal resonators with tunable frequency offset between the two modes could be expected to change this.

D.2 Echo crossing

For $N_p=5$ -pulse RIDME this amounts to $3^{N_p-1}=81$ pathways. By nature of the detection method, however, we only needed to consider pathways that end up in coherence order -1 after the final pulse. In addition, we assumed that all coherence pathways, which are not in coherence order 0 during the mixing block, are strongly attenuated due to transverse relaxation, and can be neglected. With this approximation we arrived at 27 relevant pathways, for which the full list is given in Table 3. The refocusing condition as well as the time-step with which the echo moves with respect to the stationary RIDME RVE echo for all identified echos is also given. Note that from these values it is possible to calculate the echo-crossing point for an arbitrary choice of delays t_1 , t_2 and time step dt , which may be useful in the identification of echo crossing artefacts in general for 5-pulse RIDME experiments. To determine which echo pathways are relevant in a real RIDME experiment we detected echo transients (without phase cycling) for several time-points. We found that for mixing times in the recommended range (see next section) we can assign all experimentally relevant echo traces in the detection window to our calculated echo pathways, which validates our assumption that the remaining pathways are strongly attenuated in nitroxide-Cu(II) RIDME during T_{mix} (compare Figure D.7). Importantly, we can see that an echo-crossing is not the cause for the low-frequency artifact reported above.

Table D.1: Relaxation properties of [Cu(II)-TAHA]-nitroxide **1** in the temperature range 10 K-50 K; fits of the data with different models can be found in the †SI1. Here we report the delays until a given fraction of spins has relaxed towards equilibrium (indicated as dashed lines in †SI1 Figures 3-6).

| | 10 K | 20 K | 30 K | 40 K | 50 K |
|--|-----------------------------|------|------|------|------|
| (IR) signal recovered to | nitroxide [ms] | | | | |
| 1-1/e \approx 0.63 | 31.3 | 4.3 | 1.3 | 0.5 | 0.4 |
| | Cu(II) (maximum) [μ s] | | | | |
| 1-1/e | 2022 | 57 | 18 | 2 | 1 |
| (T_m) signal decayed to | nitroxide [μ s] | | | | |
| 1/e \approx 0.37 | 8.7 | 9.1 | 7.3 | 4.4 | 3.2 |
| | Cu(II) (maximum) [μ s] | | | | |
| 1/e | 7.7 | 6.7 | 4.2 | 2.4 | 1.7 |

D.2.1 Sensitivity

We determine the optimal measurement temperature for a sample given its relaxation properties following the argumentation for the optimisation of nitroxide-nitroxide DEER in Jeschke and Polyhach^[140] Note that we expect this optimisation to hold for a wide range of samples, if the relevant relaxation properties are known. We define the quantity $S_{r_{\max}}$

$$S_{r_{\max}}(T) \approx \frac{1}{T} \cdot \exp(-5 T_{1,\text{Cu}}/T_{1,\text{NO}}) \cdot \exp(-2 t_{r_{\max}}/T_{m,\text{NO}}) \cdot \sqrt{T_{\text{ref}}/T_{1,\text{NO}}} \cdot \lambda_{\max}(T) \quad (\text{D.1})$$

which takes into account that the expected optimal experimental conditions depend on the longest expected distance r_{\max} , which manifests in a required minimum dipolar evolution trace length $t_{r_{\max}}$. The optimisation is in terms of the temperature T , the longitudinal relaxation times of the two spins $T_{1,\text{Cu}}$ and $T_{1,\text{NO}}$, the transverse relaxation of time of the detected nitroxide spins $T_{m,\text{NO}}$, and the empirical maximal modulation depth plateau value $\lambda_{\max}(T)$. The factor $\sqrt{T_{\text{ref}}/T_{1,\text{NO}}}$ accounts for the fact that at lower temperatures it is necessary to use lower shot repetition rates to avoid saturation of the detected spin, and T_{ref} is an arbitrary reference time to obtain a dimensionless parameter. In eq. (D.1) we have already inserted $T_{\text{mix}} = 5 \cdot T_{1,\text{Cu}}$, which corresponds to the point where the modulation depth plateau is reached at all tested temperatures. The experimental 1/e times for transverse relaxation resp. the $(1 - 1/e)$ times for inversion recovery are summarised in Table D.1. Note that Cu(II) complexes feature weak anisotropy of the longitudinal relaxation time (Figure D.5), which we neglect in the following.

The $S_{r_{\max}}$ reported in Chapter 7 for the tested temperature range was calculated using this equation from the values reported in Table D.1.

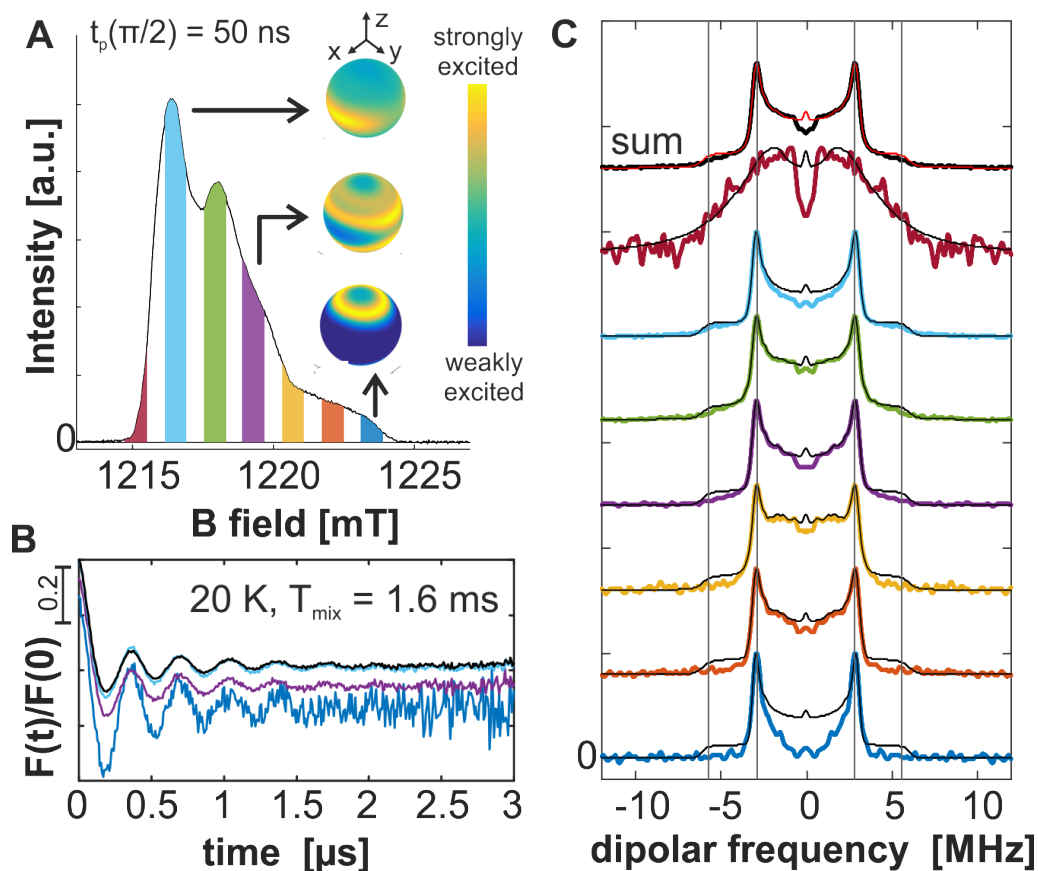


Figure D.8: Orientation selective RIDME at Q-band with ruler 1; experimental conditions are indicated; (A) experimental resonance field positions within the nitroxide spectrum; (B) selection of two dipolar evolution traces (C) dipolar coupling spectra for all detected resonance fields, and summed spectrum;

D.3 Classical orientation selection

We used a $\pi/2$ pulse length of 50 ns and a π pulse length of 100 ns in these experiments in order to have sufficient spectral resolution within the nitroxide spectrum, but still enough excitation bandwidth to cover all dipolar frequencies, estimated from the single-position RIDME experiments with hard MW pulses (12/24 ns). The RIDME detection positions within the nitroxide spectrum are shown in Figure D.8(A).

RIDME time traces were measured with a long t_1 delay, in order to obtain single stretched exponential background. The primary time traces were background corrected with the DeerAnalysis 2016 software, using a stretched exponential fit with varying dimension parameter n_{BG} . The form factor traces and corresponding dipolar spectra are shown in Figure D.8(B,C). All the obtained form factor traces have nearly the same modulation depth, which was equal to the corresponding modulation depth in single-position RIDME measurements with hard MW pulses with the same mixing time. First, this confirms that our single-position measurements of the dipolar modulation buildup

kinetics were accurate. Second, it confirms that for long mixing times we obtain nearly isotropic flip probability over the entire Cu(II) spectrum and accordingly achieve the full modulation depth also in the orientation-selective RIDME measurements.

Appendix E

Supplementary Information for Chapter 8

E.1 Numerical simulation of coefficients build-up

In Figure E.1 we show an example of a numerical simulation for a range of mixing times relative to the transverse relaxation time T_1 for a $S = 5/2$ system, where we have used the build-up model for harmonics

$$P_{m>0}(T_{\text{mix}}) = p_{\text{nf}}^m P_{m>0}^{(\text{lim})} [1 - \exp(-(T_{\text{mix}}/T_1))], \quad (\text{E.1})$$

$$p_m = P_m / \sum_{m>0} P_m. \quad (\text{E.2})$$

This model assumes that all transitions in principle build up with $1/T_1$, but build up to different levels. Compared to the equations given in the main text we have added an empirical term p_{nf}^m to account for flip-flops, where p_{nf} is the probability that the detected spin has undergone no flip-flop event for an effective spin inversion of m . For $p_{\text{nf}} = 1$ no flip flops are observed. The exponent m signifies that increasingly high m has an increasingly higher probability of inducing a flip-flop event on the detected spin.

Effectively, the flip-flop terms in this model attenuate the plateau levels of the higher order spin transition coefficients faster than those of the lower harmonics. Because we also consider terms with no flip ($m = 0$) we see that also the modulation depth is attenuated, as can be seen in Figure E.1.

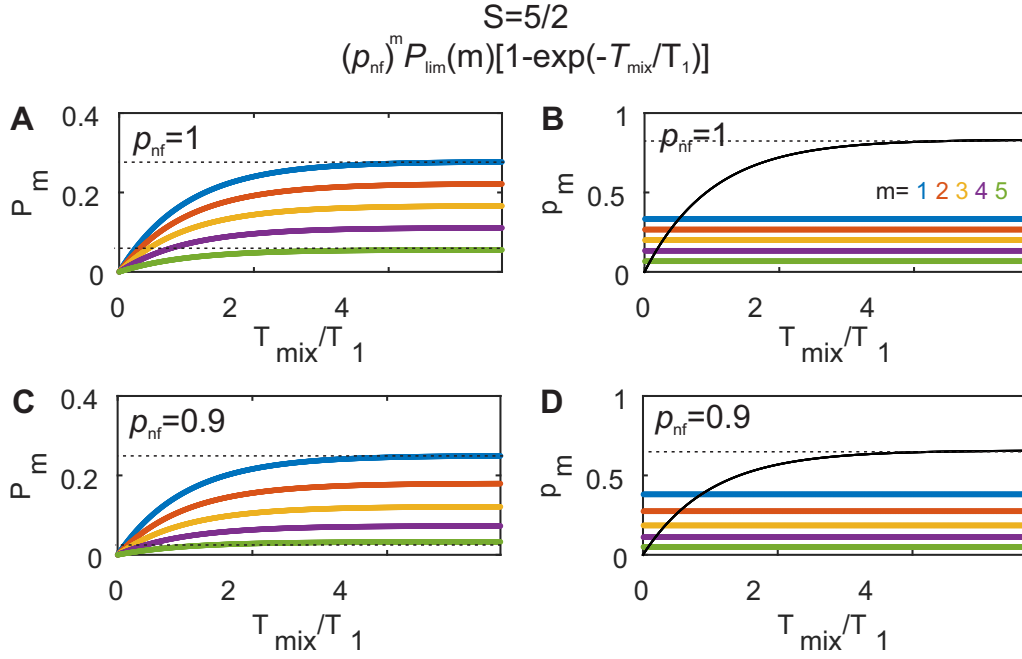


Figure E.1: Simulation for a simple model of coefficients build-up in high-spin $S = 5/2$ RIDME according to Equation (E.1), resp. Equation (E.2). (A,C) build-up of contributions P_M (B,C) build-up of the relative contributions p_m to the modulation depth Δ ; (A,B)

E.2 Extended coefficients table for Mn(II)-ruler temperatures series

The coefficients for the temperature series in Figure 8.5 in the main text are reported in Table 8.1.

| T K | T_{mix} [μs] | T_1 [μs] | Δ | p_1 | p_2 | p_3 | p_4 | p_5 |
|----------|---------------------------------------|----------------------------|----------|-------|-------|-------|-------|-------|
| 10 | 88 | 15 | 0.165 | 0.42 | 0.22 | 0.15 | 0.11 | 0.09 |
| | 88 | 50 | 0.255 | 0.40 | 0.23 | 0.16 | 0.12 | 0.10 |
| | 88 | 500 | 0.662 | 0.24 | 0.22 | 0.20 | 0.18 | 0.16 |
| 30 | 3 | 10 | 0.367 | 0.28 | 0.23 | 0.19 | 0.16 | 0.14 |
| | 3 | 100 | 0.638 | 0.20 | 0.20 | 0.20 | 0.20 | 0.20 |
| | 3 | 500 | 0.649 | 0.20 | 0.20 | 0.20 | 0.20 | 0.20 |
| 50 | 1 | 5 | 0.181 | 0.24 | 0.22 | 0.20 | 0.18 | 0.16 |
| | 1 | 20 | 0.500 | 0.20 | 0.20 | 0.20 | 0.20 | 0.20 |
| | 1 | 50 | 0.557 | 0.20 | 0.20 | 0.20 | 0.20 | 0.20 |

Table E.1: Overtone coefficients used in the analysis of RIDME with ruler ${}^2_3\text{-Mn(II)}$ at different temperatures calculated with Equation (8.10);

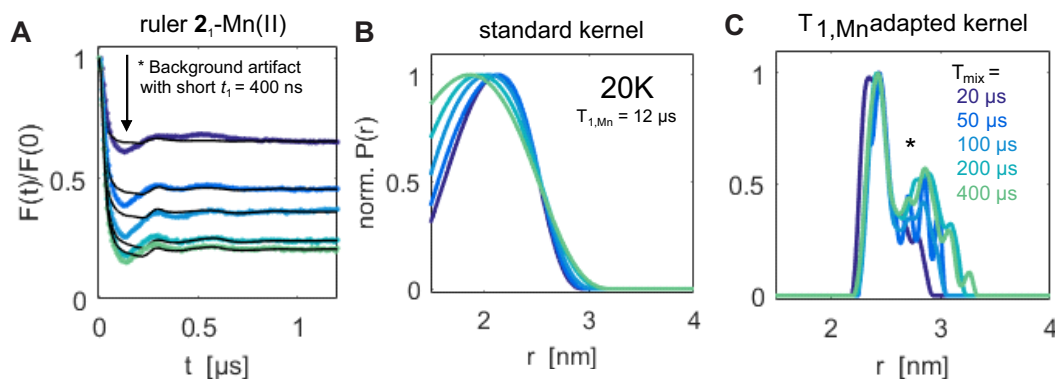


Figure E.2: RIDME with ruler $\mathbf{2}_1\text{-Mn(II)}$ at 20K; (A) primary data and stretched exponential background fit; (B) distance distribution with direct conversion of the form factor with the standard kernel; (C) distance analysis with a higher harmonics adapted kernel according to Equation (8.10) in Chapter 8;

E.3 RIDME with an additional Mn(II)-based ruler

In Figure E.2 we show RIDME results with ruler $\mathbf{2}_1\text{-Mn(II)}$. The distance distribution with direct conversion of the form factor with the standard kernel is artificially broadened due to artifact contributions at short distances. The adapted kernel gives the expected distance. Because a short $t_1=400\text{ ns}$ was used we observed a known background-artifact which leads to an artifact peak indicated by an asterisk in the distance distribution. The longitudinal relaxation time of Mn(II) in this sample was $T_{1,\text{Mn}} = 12\ \mu\text{s}$ at 20 K.

E.4 RIDME with additional Gd(III)-based rulers

As a proof of principle we also show RIDME data measured on rulers $\mathbf{1}_1\text{-Gd(III)}$ and $\mathbf{2}_1\text{-Gd(III)}$ in Figure E.3. The difference between the two rulers is the Gd(III) ligand. The RIDME experiment was measured at the maximum of the nitroxide spectrum without orientation averaging. The data could be fitted with the same model for the overtone coefficients as for the Mn(II) ruler (see Equation (8.10)), including harmonics up to order $m = 7$.

E.5 DEER with the molecular rulers Gd(III)-based rulers

DEER was measurement for comparison with the RIDME experiments on the molecular rulers. The results with the two short Gd(III)-based rulers are shown in Figure E.4, the result with the short Mn(II)-based ruler is shown in Figure E.5.

The Gd(III)-based rulers we measured DEER at 10 K with detection on the maximum of the Gd(III) spectrum and a pump pulse on the nitroxide at 300 MHz offset. A slightly longer pump pulse had to be used in the measurement with ruler $\mathbf{1}_1\text{-Gd(III)}$ than with ruler $\mathbf{2}_1\text{-Gd(III)}$ due to a worse resonator profile quality in the measurement session. The longer pump pulse is expected

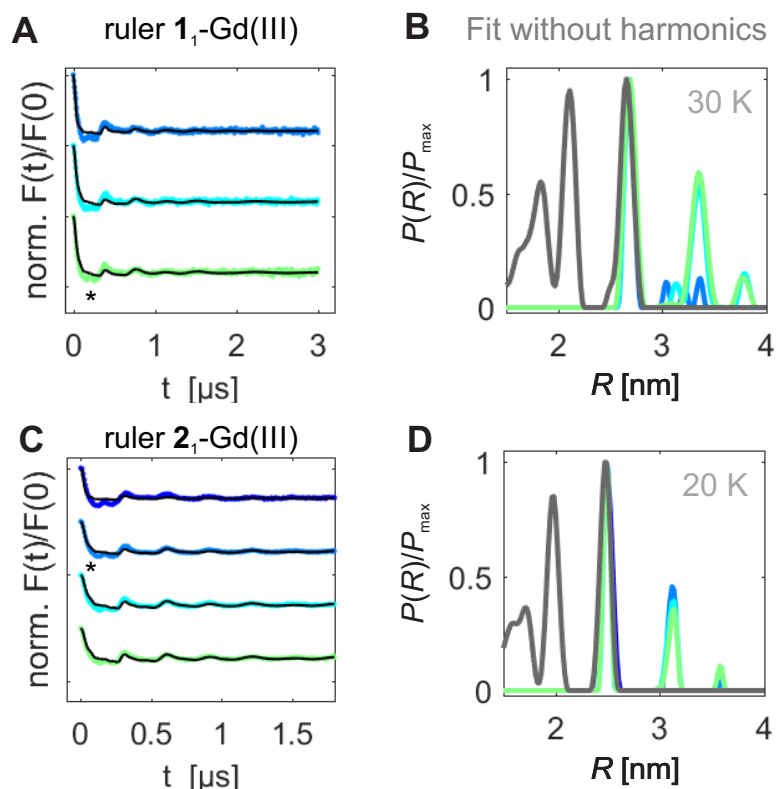


Figure E.3: (A,B) RIDME with ruler 1_1 -Gd(III) at 30K; (A,B) RIDME with ruler 2_1 -Gd(III) at 20K; (A,C) form factor after stretched exponential background fit and adapted kernel fit; (B,D) distance distribution with a higher harmonics adapted kernel according to Equation (8.10) in Chapter 8 in color, and without kernel adaptation (grey)

to have a slightly reduced pulse bandwidth, which may slightly reduce the modulation depth. The resulting modulation depths are indicated in the figures, and it is significantly larger for the TAHA-based ruler than for the PyMTA-based rulers. In both cases the modulation depth is low. The distance observed with the TAHA-based ruler is slightly longer than the distance with the PyMTA-based ruler.

For the Mn(II)-based rulers we measured DEER at 20K with a pump pulse on the maximum of the nitroxide spectrum, and detection on Mn(II) with an offset of 300 MHz (no clear maximum observed in the spectrum). The distance agrees well with the analogous Gd(III)-based ruler.

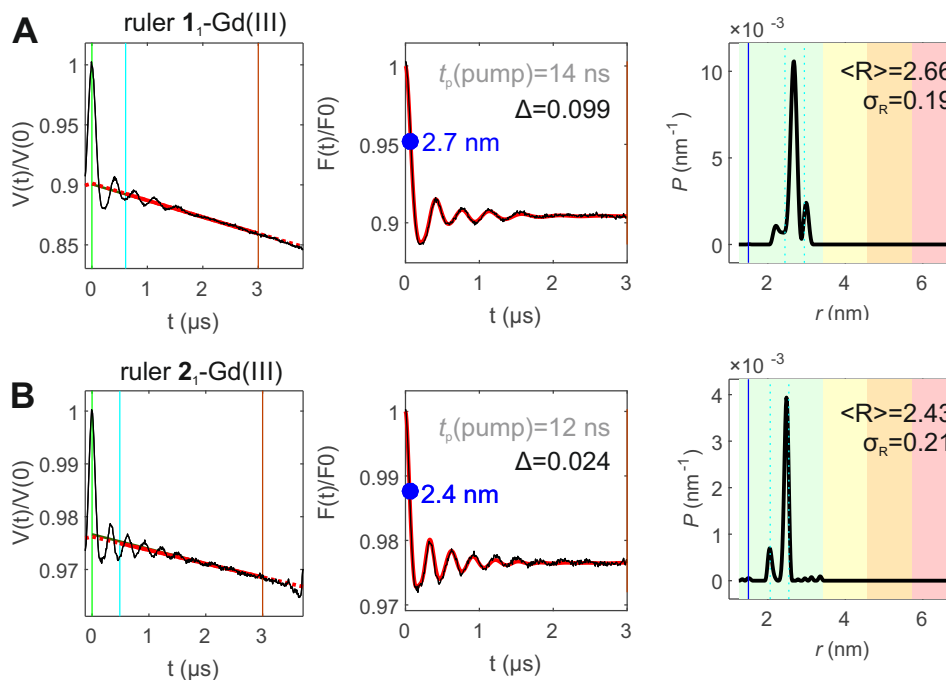


Figure E.4: DEER measurements with the rulers at 10 K; (A) 1_1 -Gd(III), and 2_1 -Gd(III); left to right: primary data and background fits, form factors and fits, and distance distributions.

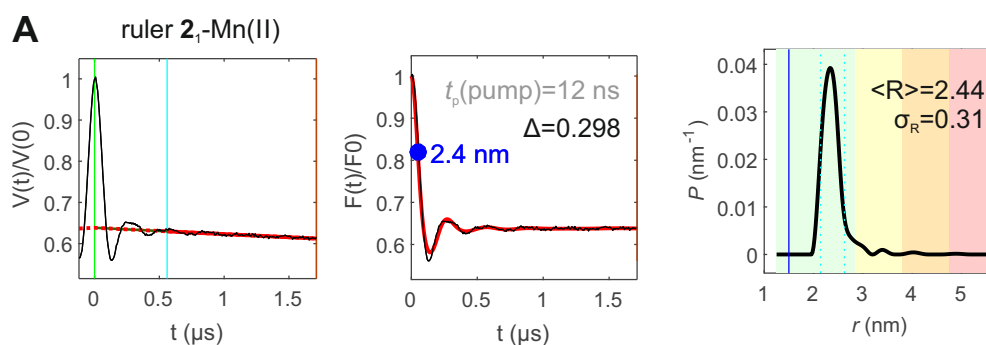


Figure E.5: DEER measurements with the rulers at 20 K; 2_1 -Mn(II); left to right: primary data and background fit, form factor and fit, and distance distributions.

E

Bibliography

- [1] CARA - Computer Aided Resonance Assignment. URL <http://cara.nmr-software.org/portal/>.
- [2] C. Abé, D. Klose, F. Dietrich, W. H. Ziegler, Y. Polyhach, G. Jeschke, and H.-J. Steinhoff. Orientation selective DEER measurements on vinculin tail at X-band frequencies reveal spin label orientations. *Journal of Magnetic Resonance (San Diego, Calif.: 1997)*, 216:53–61, Mar. 2012. ISSN 1096-0856. doi: 10.1016/j.jmr.2011.12.024.
- [3] D. Abdullin, F. Duthie, A. Meyer, E. S. Müller, G. Hagelueken, and O. Schiemann. Comparison of PELDOR and RIDME for Distance Measurements between Nitroxides and Low-Spin Fe(III) Ions. *The Journal of Physical Chemistry B*, 119(43):13534–13542, Oct. 2015. ISSN 1520-6106. doi: 10.1021/acs.jpbc.5b02118. URL <http://dx.doi.org/10.1021/acs.jpbc.5b02118>.
- [4] D. Abdullin, N. Florin, G. Hagelueken, and O. Schiemann. EPR-Based Approach for the Localization of Paramagnetic Metal Ions in Biomolecules. *Angewandte Chemie*, 127(6):1847–1851, 2015. ISSN 1521-3757. doi: 10.1002/ange.201410396. URL <https://onlinelibrary.wiley.com/doi/abs/10.1002/ange.201410396>.
- [5] K. Ackermann, C. Pliotas, S. Valera, J. H. Naismith, and B. E. Bode. Sparse Labeling PELDOR Spectroscopy on Multimeric Mechanosensitive Membrane Channels. *Biophysical Journal*, 113(9):1968–1978, Nov. 2017. ISSN 1542-0086. doi: 10.1016/j.bpj.2017.09.005.
- [6] S. Adivarahan, N. Livingston, B. Nicholson, S. Rahman, B. Wu, O. S. Rissland, and D. Zenklusen. Spatial Organization of Single mRNPs at Different Stages of the Gene Expression Pathway. *Molecular Cell*, 72(4):727–738.e5, Nov. 2018. ISSN 1097-2765. doi: 10.1016/j.molcel.2018.10.010. URL <http://www.sciencedirect.com/science/article/pii/S1097276518308426>.

- [7] D. Akhmetzyanov, P. Schöps, A. Marko, N. C. Kunjir, S. T. Sigurdsson, and T. F. Prisner. Pulsed EPR dipolar spectroscopy at Q- and G-band on a trityl biradical. *Physical chemistry chemical physics: PCCP*, 17(37):24446–24451, Oct. 2015. ISSN 1463-9084. doi: 10.1039/c5cp03671b.
- [8] S. Alberti, S. Saha, J. B. Woodruff, T. M. Franzmann, J. Wang, and A. A. Hyman. A User’s Guide for Phase Separation Assays with Purified Proteins. *Journal of Molecular Biology*, June 2018. ISSN 0022-2836. doi: 10.1016/j.jmb.2018.06.038. URL <http://www.sciencedirect.com/science/article/pii/S0022283618306673>.
- [9] S. Alberti, A. Gladfelter, and T. Mittag. Considerations and Challenges in Studying Liquid-Liquid Phase Separation and Biomolecular Condensates. *Cell*, 176(3):419–434, Jan. 2019. ISSN 00928674. doi: 10.1016/j.cell.2018.12.035. URL <https://linkinghub.elsevier.com/retrieve/pii/S0092867418316490>.
- [10] N. Alonso-García, I. García-Rubio, J. A. Manso, R. M. Buey, H. Urien, A. Sonnenberg, G. Jeschke, and J. M. de Pereda. Combination of X-ray crystallography, SAXS and DEER to obtain the structure of the FnIII-3,4 domains of integrin alpha-6-beta-4. *Acta Crystallographica. Section D, Biological Crystallography*, 71(Pt 4):969–985, Apr. 2015. ISSN 1399-0047. doi: 10.1107/S1399004715002485.
- [11] C. Altenbach, C. J. López, K. Hideg, and W. L. Hubbell. Chapter Three - Exploring Structure, Dynamics, and Topology of Nitroxide Spin-Labeled Proteins Using Continuous-Wave Electron Paramagnetic Resonance Spectroscopy. In P. Z. Qin and K. Warncke, editors, *Methods in Enzymology*, volume 564 of *Electron Paramagnetic Resonance Investigations of Biological Systems by Using Spin Labels, Spin Probes, and Intrinsic Metal Ions, Part B*, pages 59–100. Academic Press, Jan. 2015. doi: 10.1016/bs.mie.2015.08.006. URL <http://www.sciencedirect.com/science/article/pii/S0076687915004589>.
- [12] S. Ambadipudi, J. Biernat, D. Riedel, E. Mandelkow, and M. Zweckstetter. Liquid-liquid phase separation of the microtubule-binding repeats of the Alzheimer-related protein Tau. *Nature Communications*, 8, Aug. 2017. ISSN 2041-1723. doi: 10.1038/s41467-017-00480-0. URL <https://www.ncbi.nlm.nih.gov/pmc/articles/PMC5561136/>.
- [13] J. Andrecka, R. Lewis, F. Brückner, E. Lehmann, P. Cramer, and J. Michaelis. Single-molecule tracking of mRNA exiting from RNA polymerase II. *Proceedings of the National Academy of Sciences*, 105(1):135–140, Jan. 2008. ISSN 0027-8424, 1091-6490. doi: 10.1073/pnas.0703815105. URL <https://www.pnas.org/content/105/1/135>.
- [14] A. V. Astashkin. Chapter Ten - Mapping the Structure of Metalloproteins with RIDME. In Peter Z. Qin and Kurt Warncke, editor, *Methods in Enzymology*, volume Volume 563, pages 251–284. Academic Press, 2015. ISBN 0076-6879. bibtex: Astashkin2015.
- [15] A. V. Astashkin. Mapping the Structure of Metalloproteins with RIDME. *Methods in enzymology*, 563:251–84, Aug. 2015. ISSN 1557-7988. doi: 10.1016/bs.mie.2015.06.031. MEDLINE:26478488.

- [16] M. Azarkh, O. Okle, V. Singh, I. T. Seemann, J. S. Hartig, D. R. Dietrich, and M. Drescher. Long-Range Distance Determination in a DNA Model System inside *Xenopus laevis* Oocytes by In-Cell Spin-Label EPR. *ChemBioChem*, 12(13):1992–1995, Sept. 2011. ISSN 1439-7633. doi: 10.1002/cbic.201100281. URL <https://onlinelibrary.wiley.com/doi/abs/10.1002/cbic.201100281>.
- [17] J. L. Baber, J. M. Louis, and G. M. Clore. Dependence of Distance Distributions Derived from Double Electron–Electron Resonance Pulsed EPR Spectroscopy on Pulse-Sequence Time. *Angewandte Chemie*, 127(18):5426–5429, Apr. 2015. ISSN 1521-3757. doi: 10.1002/ange.201500640. URL <http://onlinelibrary.wiley.com/doi/10.1002/ange.201500640/abstract>.
- [18] J. E. Banham, C. M. Baker, S. Ceola, I. J. Day, G. H. Grant, E. J. J. Groenen, C. T. Rodgers, G. Jeschke, and C. R. Timmel. Distance measurements in the borderline region of applicability of CW EPR and DEER: A model study on a homologous series of spin-labelled peptides. *Journal of Magnetic Resonance*, 191(2):202–218, Apr. 2008. ISSN 1090-7807. doi: 10.1016/j.jmr.2007.11.023. URL <http://www.sciencedirect.com/science/article/pii/S1090780707003631>.
- [19] P. Barraud and F. H.-T. Allain. Solution structure of the two RNA recognition motifs of hnRNP A1 using segmental isotope labeling: how the relative orientation between RRM5 influences the nucleic acid binding topology. *Journal of Biomolecular NMR*, 55(1):119–138, Dec. 2012. ISSN 0925-2738, 1573-5001. doi: 10.1007/s10858-012-9696-4. URL <http://link.springer.com/article/10.1007/s10858-012-9696-4>.
- [20] J. L. Battiste and G. Wagner. Utilization of Site-Directed Spin Labeling and High-Resolution Heteronuclear Nuclear Magnetic Resonance for Global Fold Determination of Large Proteins with Limited Nuclear Overhauser Effect Data. *Biochemistry*, 39(18):5355–5365, 2000. ISSN 0006-2960. doi: 10.1021/bi000060h. URL <http://dx.doi.org/10.1021/bi000060h>.
- [21] J. Baum, R. Tycko, and A. Pines. Broadband and adiabatic inversion of a two-level system by phase-modulated pulses. *Physical Review A*, 32(6):3435–3447, Dec. 1985. doi: 10.1103/PhysRevA.32.3435. URL <https://link.aps.org/doi/10.1103/PhysRevA.32.3435>.
- [22] J. S. Becker and S. Saxena. Double quantum coherence electron spin resonance on coupled Cu(II)-Cu(II) electron spins. *Chemical Physics Letters*, 414(1-3):248–252, Oct. 2005. ISSN 0009-2614. doi: 10.1016/j.cplett.2005.08.072. WOS:000232460400047.
- [23] L. J. Berliner. *Spin Labeling: Theory and Applications*. Academic Press, Oct. 2013. ISBN 978-1-4832-1641-6.
- [24] L. J. Berliner and J. Reuben. *Spin Labeling: Theory and Applications*. Springer Science & Business Media, Dec. 2012. ISBN 978-1-4613-0743-3. Google-Books-ID: BSzUBwAAQBAJ.
- [25] L. J. Berliner, S. S. Eaton, and G. R. Eaton. *Distance Measurements in Biological Systems by EPR*. Springer Science & Business Media, Apr. 2006. ISBN 978-0-306-47109-4. Google-Books-ID: pvrqBwAAQBAJ.

- [26] I. Beusch, P. Barraud, A. Moursy, A. Cléry, and F.-T. Allain. Tandem hnRNP A1 RNA recognition motifs act in concert to repress the splicing of survival motor neuron exon 7. *eLife*, 6, 2017. doi: 10.7554/eLife.25736.
- [27] J. R. Biller, V. Meyer, H. Elajaili, G. M. Rosen, J. P. Y. Kao, S. S. Eaton, and G. R. Eaton. Relaxation times and line widths of isotopically-substituted nitroxides in aqueous solution at X-band. *Journal of Magnetic Resonance*, 212(2):370–377, Oct. 2011. ISSN 1090-7807. doi: 10.1016/j.jmr.2011.07.018. URL <http://www.sciencedirect.com/science/article/pii/S1090780711002503>.
- [28] S. Bleicken, G. Jeschke, C. Stegmüller, R. Salvador-Gallego, A. J. García-Sáez, and E. Bordignon. Structural Model of Active Bax at the Membrane. *Molecular Cell*, 56(4):496–505, Nov. 2014. ISSN 1097-2765. doi: 10.1016/j.molcel.2014.09.022. URL <http://www.sciencedirect.com/science/article/pii/S1097276514007795>.
- [29] J. Blobel, S. Schmidl, D. Vidal, L. Nisius, P. Bernadó, O. Millet, E. Brunner, and M. Pons. Protein Tyrosine Phosphatase Oligomerization Studied by a Combination of ^{15}N NMR Relaxation and ^{129}Xe NMR. Effect of Buffer Containing Arginine and Glutamic Acid. *Journal of the American Chemical Society*, 129(18):5946–5953, May 2007. ISSN 0002-7863. doi: 10.1021/ja069144p. URL <https://doi.org/10.1021/ja069144p>.
- [30] J. Blobel, U. Brath, P. Bernadó, C. Diehl, L. Ballester, A. Sornosa, M. Akke, and M. Pons. Protein loop compaction and the origin of the effect of arginine and glutamic acid mixtures on solubility, stability and transient oligomerization of proteins. *European Biophysics Journal*, 40(12):1327–1338, Dec. 2011. ISSN 1432-1017. doi: 10.1007/s00249-011-0686-3. URL <https://doi.org/10.1007/s00249-011-0686-3>.
- [31] B. E. Bode, D. Margraf, J. Plackmeyer, G. Dürner, T. F. Prisner, and O. Schiemann. Counting the Monomers in Nanometer-Sized Oligomers by Pulsed Electron Double Resonance. *Journal of the American Chemical Society*, 129(21):6736–6745, May 2007. ISSN 0002-7863. doi: 10.1021/ja065787t. URL <https://doi.org/10.1021/ja065787t>.
- [32] B. E. Bode, J. Plackmeyer, T. F. Prisner, and O. Schiemann. PELDOR Measurements on a Nitroxide-Labeled Cu(II) Porphyrin: Orientation Selection, Spin-Density Distribution, and Conformational Flexibility. *The Journal of Physical Chemistry A*, 112(23):5064–5073, June 2008. ISSN 1089-5639. doi: 10.1021/jp710504k. URL <https://doi.org/10.1021/jp710504k>.
- [33] B. E. Bode, J. Plackmeyer, M. Bolte, T. F. Prisner, and O. Schiemann. PELDOR on an exchange coupled nitroxide copper(II) spin pair. *Journal of Organometallic Chemistry*, 694(7):1172–1179, Apr. 2009. ISSN 0022-328X. doi: 10.1016/j.jorganchem.2008.11.029. URL <http://www.sciencedirect.com/science/article/pii/S0022328X08007675>.
- [34] S. Boeynaems, S. Alberti, N. L. Fawzi, T. Mittag, M. Polymenidou, F. Rousseau, J. Schymkowitz, J. Shorter, B. Wolozin, L. Van Den Bosch, P. Tompa, and M. Fuxreiter. Protein Phase Separation: A New Phase in Cell Biology. *Trends in Cell Biol-*

- ogy*, 28(6):420–435, June 2018. ISSN 09628924. doi: 10.1016/j.tcb.2018.02.004. URL <https://linkinghub.elsevier.com/retrieve/pii/S096289241830028X>.
- [35] S. Boeynaems, A. S. Holehouse, V. Weinhardt, D. Kovacs, J. V. Lindt, C. Larabell, L. V. D. Bosch, R. Das, P. S. Tompa, R. V. Pappu, and A. D. Gitler. Spontaneous driving forces give rise to protein RNA condensates with coexisting phases and complex material properties. *Proceedings of the National Academy of Sciences*, 116(16):7889–7898, Apr. 2019. ISSN 0027-8424, 1091-6490. doi: 10.1073/pnas.1821038116. URL <https://www.pnas.org/content/116/16/7889>.
- [36] S. Bonomi, A. di Matteo, E. Buratti, D. S. Cabianca, F. E. Baralle, C. Ghigna, and G. Biamenti. HnRNP A1 controls a splicing regulatory circuit promoting mesenchymal-to-epithelial transition. *Nucleic Acids Research*, 41(18):8665–8679, Oct. 2013. ISSN 0305-1048. doi: 10.1093/nar/gkt579. URL <https://www.ncbi.nlm.nih.gov/pmc/articles/PMC3794575/>.
- [37] P. P. Borbat and J. H. Freed. Multiple-quantum ESR and distance measurements. *Chemical Physics Letters*, 313(1):145–154, Nov. 1999. ISSN 0009-2614. doi: 10.1016/S0009-2614(99)00972-0. URL <http://www.sciencedirect.com/science/article/pii/S0009261499009720>.
- [38] P. P. Borbat and J. H. Freed. Pulse Dipolar Electron Spin Resonance: Distance Measurements. In C. R. Timmel and J. R. Harmer, editors, *Structural Information from Spin-Labels and Intrinsic Paramagnetic Centres in the Biosciences*, number 152 in Structure and Bonding, pages 1–82. Springer Berlin Heidelberg, 2013. ISBN 978-3-642-39124-8 978-3-642-39125-5. doi: 10.1007/430_2012_82. URL http://link.springer.com/chapter/10.1007/430_2012_82.
- [39] E. Bordignon. EPR Spectroscopy of Nitroxide Spin Probes. In *eMagRes*. John Wiley & Sons, Ltd, 2007. ISBN 978-0-470-03459-0. doi: 10.1002/9780470034590.emrstm1513. URL <http://onlinelibrary.wiley.com/doi/10.1002/9780470034590.emrstm1513/abstract>.
- [40] E. Bordignon. Site-Directed Spin Labeling of Membrane Proteins. In *EPR Spectroscopy*, Topics in Current Chemistry, pages 121–157. Springer, Berlin, Heidelberg, 2011. ISBN 978-3-642-28346-8 978-3-642-28347-5. doi: 10.1007/128_2011_243. URL https://link.springer.com/chapter/10.1007/128_2011_243.
- [41] E. Bordignon, H. Brutlach, L. Urban, K. Hideg, A. Savitsky, A. Schnegg, P. Gast, M. Engelhard, E. J. J. Groenen, K. Möbius, and H.-J. Steinhoff. Heterogeneity in the Nitroxide Micro-Environment: Polarity and Proticity Effects in Spin-Labeled Proteins Studied by Multi-Frequency EPR. *Applied Magnetic Resonance*, 37(1):391, Nov. 2009. ISSN 1613-7507. doi: 10.1007/s00723-009-0072-9. URL <https://doi.org/10.1007/s00723-009-0072-9>.
- [42] E. Bordignon, A. I. Nalepa, A. Savitsky, L. Braun, and G. Jeschke. Changes in the Microenvironment of Nitroxide Radicals around the Glass Transition Temperature. *The Journal of Physical Chemistry B*, 119(43):13797–13806, Oct. 2015. ISSN 1520-6106. doi: 10.1021/acs.jpcc.5b04104. URL <http://dx.doi.org/10.1021/acs.jpcc.5b04104>.

- [43] A. Borgia, M. B. Borgia, K. Bugge, V. M. Kissling, P. O. Heidarsson, C. B. Fernandes, A. Sottini, A. Soranno, K. J. Buholzer, D. Nettels, B. B. Kragelund, R. B. Best, and B. Schuler. Extreme disorder in an ultra-high-affinity protein complex. *Nature*, 555(7694):61–66, Mar. 2018. ISSN 0028-0836. doi: 10.1038/nature25762. URL <https://www.ncbi.nlm.nih.gov/pmc/articles/PMC6264893/>.
- [44] A. M. Bowen, C. E. Tait, C. R. Timmel, and J. R. Harmer. Orientation-Selective DEER Using Rigid Spin Labels, Cofactors, Metals, and Clusters. In *Structural Information from Spin-Labels and Intrinsic Paramagnetic Centres in the Biosciences*, Structure and Bonding, pages 283–327. Springer, Berlin, Heidelberg, 2013. ISBN 978-3-642-39124-8 978-3-642-39125-5. doi: 10.1007/430_2013_115. URL https://link.springer.com/chapter/10.1007/430_2013_115.
- [45] A. M. Bowen, M. W. Jones, J. E. Lovett, T. G. Gaule, M. J. McPherson, J. R. Dilworth, C. R. Timmel, and J. R. Harmer. Exploiting orientation-selective DEER: determining molecular structure in systems containing Cu(II) centres. *Physical Chemistry Chemical Physics*, 18(8):5981–5994, Feb. 2016. ISSN 1463-9084. doi: 10.1039/C5CP06096F. URL <http://pubs.rsc.org/en/content/articlelanding/2016/cp/c5cp06096f>.
- [46] J. P. Brady, P. J. Farber, A. Sekhar, Y.-H. Lin, R. Huang, A. Bah, T. J. Nott, H. S. Chan, A. J. Baldwin, J. D. Forman-Kay, and L. E. Kay. Structural and hydrodynamic properties of an intrinsically disordered region of a germ cell-specific protein on phase separation. *Proceedings of the National Academy of Sciences*, 114(39):E8194–E8203, Sept. 2017. ISSN 0027-8424, 1091-6490. doi: 10.1073/pnas.1706197114. URL <https://www.pnas.org/content/114/39/E8194>.
- [47] F. D. Breitgoff, J. Soetbeer, A. Doll, G. Jeschke, and Y. O. Polyhach. Artefact suppression in 5-pulse double electron electron resonance for distance distribution measurements. *Physical chemistry chemical physics: PCCP*, 19(24):15766–15779, June 2017. ISSN 1463-9084. doi: 10.1039/c7cp01488k.
- [48] F. D. Breitgoff, K. Keller, M. Qi, D. Klose, M. Yulikov, A. Godt, and G. Jeschke. UWB DEER and RIDME distance measurements in Cu(II)–Cu(II) spin pairs. *Journal of Magnetic Resonance*, page 106560, July 2019. ISSN 1090-7807. doi: 10.1016/j.jmr.2019.07.047. URL <http://www.sciencedirect.com/science/article/pii/S1090780719301715>.
- [49] V. Brumas, N. Alliey, and G. Berthon. A new investigation of copper(II)-serine, copper(II)-histidine-serine, copper(II)-asparagine, and copper(II)-histidine-asparagine equilibria under physiological conditions, and implications for simulation models relative to blood plasma. *Journal of Inorganic Biochemistry*, 52(4):287–296, Dec. 1993. ISSN 0162-0134.
- [50] H. Y. Carr and E. M. Purcell. Effects of Diffusion on Free Precession in Nuclear Magnetic Resonance Experiments. *Physical Review*, 94(3):630–638, May 1954. doi: 10.1103/PhysRev.94.630. URL <https://link.aps.org/doi/10.1103/PhysRev.94.630>.

- [51] J. Cattani, V. Subramaniam, and M. Drescher. Room-temperature in-cell EPR spectroscopy: alpha-Synuclein disease variants remain intrinsically disordered in the cell. *Physical chemistry chemical physics: PCCP*, 19(28):18147–18151, July 2017. ISSN 1463-9084. doi: 10.1039/c7cp03432f.
- [52] Y.-W. Chiang, P. P. Borbat, and J. H. Freed. The determination of pair distance distributions by pulsed ESR using Tikhonov regularization. *Journal of Magnetic Resonance*, 172(2):279–295, Feb. 2005. ISSN 1090-7807. doi: 10.1016/j.jmr.2004.10.012. URL <http://www.sciencedirect.com/science/article/pii/S1090780704003532>.
- [53] M.-K. Cho, G. Nodet, H.-Y. Kim, M. R. Jensen, P. Bernado, C. O. Fernandez, S. Becker, M. Blackledge, and M. Zweckstetter. Structural characterization of alpha-synuclein in an aggregation prone state. *Protein Science: A Publication of the Protein Society*, 18(9):1840–1846, Sept. 2009. ISSN 1469-896X. doi: 10.1002/pro.194.
- [54] P. A. Chong, R. M. Vernon, and J. D. Forman-Kay. RGG/RG Motif Regions in RNA Binding and Phase Separation. *Journal of Molecular Biology*, 430(23):4650–4665, 2018. ISSN 1089-8638. doi: 10.1016/j.jmb.2018.06.014.
- [55] J. A. Clayton, M. Qi, A. Godt, D. Goldfarb, S. Han, and M. S. Sherwin. Gd³⁺–Gd³⁺ distances exceeding 3 nm determined by very high frequency continuous wave electron paramagnetic resonance. *Physical Chemistry Chemical Physics*, 19(7):5127–5136, Feb. 2017. ISSN 1463-9084. doi: 10.1039/C6CP07119H. URL <http://pubs.rsc.org/en/content/articlelanding/2017/cp/c6cp07119h>.
- [56] J. A. Clayton, K. Keller, M. Qi, J. Wegner, V. Koch, H. Hintz, A. Godt, S. Han, G. Jeschke, M. S. Sherwin, and M. Yulikov. Quantitative analysis of zero-field splitting parameter distributions in Gd(III) complexes. *Physical Chemistry Chemical Physics*, 20(15):10470–10492, Apr. 2018. ISSN 1463-9084. doi: 10.1039/C7CP08507A. URL <http://pubs.rsc.org/en/content/articlelanding/2018/cp/c7cp08507a>.
- [57] G. M. Clore. Practical Aspects of Paramagnetic Relaxation Enhancement in Biological Macromolecules. *Methods in Enzymology*, 564:485–497, 2015. ISSN 1557-7988. doi: 10.1016/bs.mie.2015.06.032.
- [58] G. M. Clore and J. Iwahara. Theory, practice, and applications of paramagnetic relaxation enhancement for the characterization of transient low-population states of biological macromolecules and their complexes. *Chemical Reviews*, 109(9):4108–4139, Sept. 2009. ISSN 1520-6890. doi: 10.1021/cr900033p.
- [59] G. M. Clore, C. Tang, and J. Iwahara. Elucidating transient macromolecular interactions using paramagnetic relaxation enhancement. *Current Opinion in Structural Biology*, 17(5):603–616, Oct. 2007. ISSN 0959-440X. doi: 10.1016/j.sbi.2007.08.013. URL <http://www.sciencedirect.com/science/article/pii/S0959440X07001200>.

- [60] M. R. Cohen, V. Frydman, P. Milko, M. A. Iron, E. H. Abdelkader, M. D. Lee, J. D. Swarbrick, A. Raitsimring, G. Otting, B. Graham, A. Feintuch, and D. Goldfarb. Overcoming artificial broadening in Gd³⁺–Gd³⁺ distance distributions arising from dipolar pseudo-secular terms in DEER experiments. *Physical Chemistry Chemical Physics*, 18(18):12847–12859, May 2016. ISSN 1463-9084. doi: 10.1039/C6CP00829A. URL <https://pubs.rsc.org/en/content/articlelanding/2016/cp/c6cp00829a>.
- [61] A. Collauto, V. Frydman, M. Lee, E. Abdelkader, A. Feintuch, J. Swarbrick, B. Graham, G. Otting, and D. Goldfarb. RIDME distance measurements using Gd(III) tags with a narrow central transition. *Physical Chemistry Chemical Physics*, 18(28):19037–19049, 2016. ISSN 1463-9076. doi: 10.1039/c6cp03299k.
- [62] L. Columbus and B. Kroncke. Chapter Sixteen - Solution NMR Structure Determination of Polytropic α -Helical Membrane Proteins: A Guide to Spin Label Paramagnetic Relaxation Enhancement Restraints. In A. K. Shukla, editor, *Methods in Enzymology*, volume 557 of *Membrane Proteins—Engineering, Purification and Crystallization*, pages 329–348. Academic Press, Jan. 2015. doi: 10.1016/bs.mie.2014.12.005. URL <http://www.sciencedirect.com/science/article/pii/S0076687914001190>.
- [63] A. E. Conicella, G. H. Zerze, J. Mittal, and N. L. Fawzi. ALS Mutations Disrupt Phase Separation Mediated by α -Helical Structure in the TDP-43 Low-Complexity C-Terminal Domain. *Structure (London, England: 1993)*, 24(9):1537–1549, 2016. ISSN 1878-4186. doi: 10.1016/j.str.2016.07.007.
- [64] V. W. Cornish, D. R. Benson, C. A. Altenbach, K. Hideg, W. L. Hubbell, and P. G. Schultz. Site-specific incorporation of biophysical probes into proteins. *Proceedings of the National Academy of Sciences*, 91(8):2910–2914, Apr. 1994. ISSN 0027-8424, 1091-6490. doi: 10.1073/pnas.91.8.2910. URL <http://www.pnas.org/content/91/8/2910>.
- [65] T. F. Cunningham, M. R. Putterman, A. Desai, W. S. Horne, and S. Saxena. The double-histidine Cu²⁺-binding motif: a highly rigid, site-specific spin probe for electron spin resonance distance measurements. *Angewandte Chemie (International Ed. in English)*, 54(21):6330–6334, May 2015. ISSN 1521-3773. doi: 10.1002/anie.201501968.
- [66] T. F. Cunningham, M. D. Shannon, M. R. Putterman, R. J. Arachchige, I. Sengupta, M. Gao, C. P. Jaroniec, and S. Saxena. Cysteine-Specific Cu²⁺ Chelating Tags Used as Paramagnetic Probes in Double Electron Electron Resonance. *The Journal of Physical Chemistry B*, 119(7):2839–2843, Feb. 2015. ISSN 1520-6106, 1520-5207. doi: 10.1021/jp5103143. URL <http://pubs.acs.org/doi/abs/10.1021/jp5103143>.
- [67] A. Dalaloyan, M. Qi, S. Ruthstein, S. Vega, A. Godt, A. Feintuch, and D. Goldfarb. Gd(III)–Gd(III) EPR distance measurements – the range of accessible distances and the impact of zero field splitting. *Physical Chemistry Chemical Physics*, 17(28):18464–18476, July 2015. ISSN 1463-9084. doi: 10.1039/C5CP02602D. URL <http://pubs.rsc.org/en/content/articlelanding/2015/cp/c5cp02602d>.

- [68] M. M. Dedmon, K. Lindorff-Larsen, J. Christodoulou, M. Vendruscolo, and C. M. Dobson. Mapping Long-Range Interactions in alpha-Synuclein using Spin-Label NMR and Ensemble Molecular Dynamics Simulations. *Journal of the American Chemical Society*, 127(2):476–477, Jan. 2005. ISSN 0002-7863. doi: 10.1021/ja044834j. URL <https://doi.org/10.1021/ja044834j>.
- [69] V. P. Denysenkov, T. F. Prisner, J. Stubbe, and M. Bennati. High-field pulsed electron–electron double resonance spectroscopy to determine the orientation of the tyrosyl radicals in ribonucleotide reductase. *Proceedings of the National Academy of Sciences*, 103(36):13386–13390, Sept. 2006. ISSN 0027-8424, 1091-6490. doi: 10.1073/pnas.0605851103. URL <http://www.pnas.org/content/103/36/13386>.
- [70] J.-E. Deshaies, L. Shkreta, A. Moszczynski, H. Sidibé, S. Semmler, A. Fouillen, E. Bennett, U. Bekenstein, L. Destroismaisons, J. Toutant, Q. Delmotte, K. Volkening, S. Stabile, A. Aulas, Y. Khalfallah, H. Soreq, A. Nanci, M. Strong, B. Chabot, and V. Vande. TDP-43 regulates the alternative splicing of hnRNP A1 to yield an aggregation-prone variant in amyotrophic lateral sclerosis. *Brain*, 141(5):1320–1333, 2018. doi: 10.1093/brain/awy062.
- [71] I. Dhimitruka, O. Grigorieva, J. L. Zweier, and V. V. Khramtsov. Synthesis, structure, and EPR characterization of deuterated derivatives of Finland trityl radical. *Bioorganic & Medicinal Chemistry Letters*, 20(13):3946–3949, July 2010. ISSN 0960-894X. doi: 10.1016/j.bmcl.2010.05.006. URL <http://www.sciencedirect.com/science/article/pii/S0960894X10006335>.
- [72] J. Ding, M. K. Hayashi, Y. Zhang, L. Manche, A. R. Krainer, and R. M. Xu. Crystal structure of the two-RRM domain of hnRNP A1 (UP1) complexed with single-stranded telomeric DNA. *Genes & Development*, 13(9):1102–1115, May 1999. ISSN 0890-9369. doi: 10.1101/gad.13.9.1102.
- [73] A. Doll and G. Jeschke. Fourier-transform electron spin resonance with bandwidth-compensated chirp pulses. *Journal of Magnetic Resonance (San Diego, Calif.: 1997)*, 246:18–26, Sept. 2014. ISSN 1096-0856. doi: 10.1016/j.jmr.2014.06.016.
- [74] A. Doll and G. Jeschke. EPR-correlated dipolar spectroscopy by Q-band chirp SIFTER. *Physical Chemistry Chemical Physics*, 18(33):23111–23120, 2016. doi: 10.1039/C6CP03067J. URL <http://pubs.rsc.org/en/Content/ArticleLanding/2016/CP/C6CP03067J>.
- [75] A. Doll and G. Jeschke. Wideband frequency-swept excitation in pulsed EPR spectroscopy. *Journal of Magnetic Resonance*, 280(Supplement C):46–62, July 2017. ISSN 1090-7807. doi: 10.1016/j.jmr.2017.01.004. URL <http://www.sciencedirect.com/science/article/pii/S1090780717300046>.
- [76] A. Doll, S. Pribitzer, R. Tschaggelar, and G. Jeschke. Adiabatic and fast passage ultra-wideband inversion in pulsed EPR. *Journal of Magnetic Resonance*, 230:27–39, May 2013. ISSN 1090-7807. doi: 10.1016/j.jmr.2013.01.002. URL <http://www.sciencedirect.com/science/article/pii/S1090780713000153>.

- [77] A. Doll, M. Qi, S. Pribitzer, N. Wili, M. Yulikov, A. Godt, and G. Jeschke. Sensitivity enhancement by population transfer in Gd(III) spin labels. *Physical Chemistry Chemical Physics*, 17(11):7334–7344, Mar. 2015. ISSN 1463-9084. doi: 10.1039/C4CP05893C. URL <http://pubs.rsc.org/en/content/articlelanding/2015/cp/c4cp05893c>.
- [78] A. Doll, M. Qi, N. Wili, S. Pribitzer, A. Godt, and G. Jeschke. Gd(III)-Gd(III) distance measurements with chirp pump pulses. *Journal of Magnetic Resonance (San Diego, Calif.: 1997)*, 259:153–162, Oct. 2015. ISSN 1096-0856. doi: 10.1016/j.jmr.2015.08.010.
- [79] M. Drescher. EPR in protein science : intrinsically disordered proteins. *Topics in Current Chemistry*, 321:91–119, 2012. ISSN 0340-1022. doi: 10.1007/128_2011_235.
- [80] S. A. Dzuba, E. P. Kirilina, E. S. Salnikov, and L. V. Kulik. Restricted orientational motion of nitroxides in molecular glasses: Direct estimation of the motional time scale basing on the comparative study of primary and stimulated electron spin echo decays. *The Journal of Chemical Physics*, 122(9):094702, Mar. 2005. ISSN 0021-9606, 1089-7690. doi: 10.1063/1.1856926. URL <http://scitation.aip.org/content/aip/journal/jcp/122/9/10.1063/1.1856926>.
- [81] M. Dzuricky, S. Roberts, and A. Chilkoti. Convergence of Artificial Protein Polymers and Intrinsically Disordered Proteins. *Biochemistry*, 57(17):2405–2414, May 2018. ISSN 0006-2960. doi: 10.1021/acs.biochem.8b00056. URL <https://doi.org/10.1021/acs.biochem.8b00056>.
- [82] G. R. Eaton and S. S. Eaton. Solvent and Temperature Dependence of Spin Echo Dephasing for Chromium(V) and Vanadyl Complexes in Glassy Solution. *Journal of Magnetic Resonance*, 136(1):63–68, Jan. 1999. ISSN 1090-7807. doi: 10.1006/jmre.1998.1610. URL <http://www.sciencedirect.com/science/article/pii/S109078079891610X>.
- [83] S. S. Eaton and G. R. Eaton. Relaxation Times of Organic Radicals and Transition Metal Ions. In *Distance Measurements in Biological Systems by EPR*, Biological Magnetic Resonance, pages 29–154. Springer, Boston, MA, 2002. ISBN 978-1-4757-0575-1 978-0-306-47109-4. doi: 10.1007/0-306-47109-4_2. URL https://link.springer.com/chapter/10.1007/0-306-47109-4_2.
- [84] T. E. Edwards, T. M. Okonogi, B. H. Robinson, and S. T. Sigurdsson. Site-specific incorporation of nitroxide spin-labels into internal sites of the TAR RNA; structure-dependent dynamics of RNA by EPR spectroscopy. *Journal of the American Chemical Society*, 123(7):1527–1528, Feb. 2001. ISSN 0002-7863. doi: 10.1021/ja005649i. WOS:000167031300043.
- [85] T. H. Edwards and S. Stoll. Optimal Tikhonov regularization for DEER spectroscopy. *Journal of Magnetic Resonance*, 288:58–68, Mar. 2018. ISSN 1090-7807. doi: 10.1016/j.jmr.2018.01.021. URL <http://www.sciencedirect.com/science/article/pii/S1090780718300442>.

- [86] B. Endeward, J. A. Butterwick, R. MacKinnon, and T. F. Prisner. Pulsed Electron Double Resonance Determination of Spin Label Distances and Orientations on the Tetrameric Potassium Ion Channel KcsA. *Journal of the American Chemical Society*, 131(42):15246–15250, Oct. 2009. ISSN 0002-7863. doi: 10.1021/ja904808n. URL <https://doi.org/10.1021/ja904808n>.
- [87] M. Ezhevskaya, E. Bordignon, Y. Polyhach, L. Moens, S. Dewilde, G. Jeschke, and S. V. Doorslaer. Distance determination between low-spin ferric haem and nitroxide spin label using DEER: the neuroglobin case. *Molecular Physics*, 111(18-19):2855–2864, Oct. 2013. ISSN 0026-8976. doi: 10.1080/00268976.2013.813592. URL <https://doi.org/10.1080/00268976.2013.813592>.
- [88] N. L. Fawzi, M. R. Fleissner, N. J. Anthis, T. Kalai, K. Hideg, W. L. Hubbell, and G. M. Clore. A rigid disulfide-linked nitroxide side chain simplifies the quantitative analysis of PRE data. *Journal of Biomolecular Nmr*, 51(1-2):105–114, Sept. 2011. ISSN 0925-2738. doi: 10.1007/s10858-011-9545-x. WOS:000295988100011.
- [89] J. B. Feix and C. S. Klug. Site-Directed Spin Labeling of Membrane Proteins and Peptide-Membrane Interactions. In L. J. Berliner, editor, *Biological Magnetic Resonance*, number 14 in Biological Magnetic Resonance, pages 251–281. Springer US, 2002. ISBN 978-0-306-45644-2 978-0-306-47072-1. doi: 10.1007/0-306-47072-1_6. URL http://link.springer.com/chapter/10.1007/0-306-47072-1_6.
- [90] J.-F. Fiset, J. Toutant, S. Dugré-Brisson, L. Desgroseillers, and B. Chabot. hnRNP A1 and hnRNP H can collaborate to modulate 5-prime splice site selection. *RNA*, 16(1):228–238, Jan. 2010. ISSN 1355-8382, 1469-9001. doi: 10.1261/rna.1890310. URL <http://rnajournal.cshlp.org/content/16/1/228>.
- [91] N. C. Fitzkee and G. D. Rose. Reassessing random-coil statistics in unfolded proteins. *Proceedings of the National Academy of Sciences*, 101(34):12497–12502, Aug. 2004. ISSN 0027-8424, 1091-6490. doi: 10.1073/pnas.0404236101. URL <https://www.pnas.org/content/101/34/12497>.
- [92] D. Franke, M. V. Petoukhov, P. V. Konarev, A. Panjkovich, A. Tuukkanen, H. D. T. Mertens, A. G. Kikhney, N. R. Hajizadeh, J. M. Franklin, C. M. Jeffries, and D. I. Svergun. ATSAS 2.8: a comprehensive data analysis suite for small-angle scattering from macromolecular solutions. *Journal of Applied Crystallography*, 50(4):1212–1225, Aug. 2017. ISSN 1600-5767. doi: 10.1107/S1600576717007786. URL <http://scripts.iucr.org/cgi-bin/paper?ge5042>.
- [93] J. H. Freed. 3 - Theory of Slow Tumbling ESR Spectra for Nitroxides. In L. J. Berliner, editor, *Spin Labeling*, Molecular Biology: An International Series of Monographs and Textbooks, pages 53–132. Academic Press, Amsterdam, Jan. 1976. ISBN 978-0-12-092350-2. doi: 10.1016/B978-0-12-092350-2.50008-4. URL <http://www.sciencedirect.com/science/article/pii/B9780120923502500084>.

- [94] P. G. Vekilov. Phase transitions of folded proteins. *Soft Matter*, 6(21):5254–5272, 2010. doi: 10.1039/C0SM00215A. URL <http://pubs.rsc.org/en/Content/ArticleLanding/2010/SM/C0SM00215A>.
- [95] B. J. Gaffney, M. D. Bradshaw, S. D. Frausto, F. Wu, J. H. Freed, and P. Borbat. Locating a Lipid at the Portal to the Lipoxygenase Active Site. *Biophysical Journal*, 103(10):2134–2144, Nov. 2012. ISSN 0006-3495. doi: 10.1016/j.bpj.2012.10.002. URL <http://www.sciencedirect.com/science/article/pii/S0006349512011058>.
- [96] L. Garbuio, E. Bordignon, E. K. Brooks, W. L. Hubbell, G. Jeschke, and M. Yulikov. Orthogonal Spin Labeling and Gd(III)–Nitroxide Distance Measurements on Bacteriophage T4-Lysozyme. *The Journal of Physical Chemistry B*, 117(11):3145–3153, Mar. 2013. ISSN 1520-6106. doi: 10.1021/jp401806g. URL <https://doi.org/10.1021/jp401806g>.
- [97] L. Garbuio, B. Lewandowski, P. Wilhelm, L. Ziegler, M. Yulikov, H. Wennemers, and G. Jeschke. Shape Persistence of Polyproline II Helical Oligoprolines. *Chemistry – A European Journal*, 21(30):10747–10753, July 2015. ISSN 1521-3765. doi: 10.1002/chem.201501190. URL <http://onlinelibrary.wiley.com/doi/10.1002/chem.201501190/abstract>.
- [98] E. Gasteiger, A. Gattiker, C. Hoogland, I. Ivanyi, R. D. Appel, and A. Bairoch. ExpASY: the proteomics server for in-depth protein knowledge and analysis. *Nucleic Acids Research*, 31(13):3784–3788, July 2003. ISSN 0305-1048. doi: 10.1093/nar/gkg563. URL <https://academic.oup.com/nar/article/31/13/3784/2904185>.
- [99] C. Gemperle, G. Aebli, A. Schweiger, and R. R. Ernst. Phase cycling in pulse EPR. *Journal of Magnetic Resonance (1969)*, 88(2):241–256, June 1990. ISSN 0022-2364. doi: 10.1016/0022-2364(90)90181-8. URL <http://www.sciencedirect.com/science/article/pii/0022236490901818>.
- [100] M. Ghosh and M. Singh. RGG-box in hnRNPA1 specifically recognizes the telomere G-quadruplex DNA and enhances the G-quadruplex unfolding ability of UP1 domain. *Nucleic Acids Research*, 46(19):10246–10261, Nov. 2018. ISSN 0305-1048. doi: 10.1093/nar/gky854. URL <https://academic.oup.com/nar/article/46/19/10246/5105846>.
- [101] S. Ghosh, M. J. Lawless, G. S. Rule, and S. Saxena. The Cu²⁺-nitrilotriacetic acid complex improves loading of α -helical double histidine site for precise distance measurements by pulsed ESR. *Journal of Magnetic Resonance*, 286:163–171, Jan. 2018. ISSN 1090-7807. doi: 10.1016/j.jmr.2017.12.005. URL <http://www.sciencedirect.com/science/article/pii/S1090780717302975>.
- [102] A. Giannoulis, M. Oranges, and B. E. Bode. Monitoring Complex Formation by Relaxation-Induced Pulse Electron Paramagnetic Resonance Distance Measurements. *ChemPhysChem*, 18(17):2318–2321, Sept. 2017. ISSN 1439-7641. doi: 10.1002/cphc.201700666. URL <http://onlinelibrary.wiley.com/doi/10.1002/cphc.201700666/abstract>.

- [103] A. Giannoulis, C. L. Motion, M. Oranges, M. Buhl, G. M. Smith, and B. E. Bode. Orientation selection in high-field RIDME and PELDOR experiments involving low-spin Co-II ions. *Physical Chemistry Chemical Physics*, 20(4):2151–2154, Jan. 2018. ISSN 1463-9076. doi: 10.1039/c7cp07248a. WOS:000423505500002.
- [104] J. R. Gillespie and D. Shortle. Characterization of long-range structure in the denatured state of staphylococcal nuclease. I. paramagnetic relaxation enhancement by nitroxide spin labels1. *Journal of Molecular Biology*, 268(1):158–169, Apr. 1997. ISSN 0022-2836. doi: 10.1006/jmbi.1997.0954. URL <http://www.sciencedirect.com/science/article/pii/S0022283697909542>.
- [105] C. Gmeiner, G. Dorn, F. Allain, G. Jeschke, and M. Yulikov. Spin labelling for integrative structure modelling: A case study of the polypyrimidine-tract binding protein 1 domains in complexes with short RNAs. *Physical Chemistry Chemical Physics*, 19(41):28360–28380, 2017. doi: 10.1039/c7cp05822e.
- [106] C. Gmeiner, D. Klose, E. Mileo, V. Belle, S. Marque, G. Dorn, F. Allain, B. Guigliarelli, G. Jeschke, and M. Yulikov. Orthogonal tyrosine and cysteine site-directed spin labeling for dipolar pulse EPR spectroscopy on proteins. *Journal of Physical Chemistry Letters*, 8(19):4852–4857, 2017. doi: 10.1021/acs.jpcclett.7b02220.
- [107] D. Goldfarb. Gd3+ spin labeling for distance measurements by pulse EPR spectroscopy. *Physical Chemistry Chemical Physics*, 16(21):9685–9699, May 2014. ISSN 1463-9084. doi: 10.1039/C3CP53822B. URL <http://pubs.rsc.org/en/content/articlelanding/2014/cp/c3cp53822b>.
- [108] O. H. Griffith, D. W. Cornell, and H. M. McConnell. Nitrogen Hyperfine Tensor and g Tensor of Nitroxide Radicals. *The Journal of Chemical Physics*, 43(8):2909–2910, Oct. 1965. ISSN 0021-9606, 1089-7690. doi: 10.1063/1.1697233. URL <http://scitation.aip.org/content/aip/journal/jcp/43/8/10.1063/1.1697233>.
- [109] D. Grohmann, A. Hirtreiter, and F. Werner. RNAP subunits F/E (RBP4/7) are stably associated with archaeal RNA polymerase: using fluorescence anisotropy to monitor RNAP assembly in vitro. *Biochemical Journal*, 421(3):339–343, Aug. 2009. ISSN 0264-6021, 1470-8728. doi: 10.1042/BJ20090782. URL <http://www.biochemj.org/content/421/3/339>.
- [110] X. Gui, F. Luo, Y. Li, H. Zhou, Z. Qin, Z. Liu, J. Gu, M. Xie, K. Zhao, B. Dai, W. S. Shin, J. He, L. He, L. Jiang, M. Zhao, B. Sun, X. Li, C. Liu, and D. Li. Structural basis for reversible amyloids of hnRNPA1 elucidates their role in stress granule assembly. *Nature Communications*, 10(1):2006, 2019. ISSN 2041-1723. doi: 10.1038/s41467-019-09902-7.
- [111] T. v. Hagens, Y. Polyhach, M. Sajid, A. Godt, and G. Jeschke. Suppression of ghost distances in multiple-spin double electron–electron resonance. *Physical Chemistry Chemical Physics*, 15(16):5854–5866, Mar. 2013. ISSN 1463-9084. doi: 10.1039/C3CP44462G. URL <https://pubs.rsc.org/en/content/articlelanding/2013/cp/c3cp44462g>.

- [112] G. Hanson and L. Berliner, editors. *Metals in Biology: Applications of High-Resolution EPR to Metalloenzymes*. Biological Magnetic Resonance. Springer-Verlag, New York, 2010. ISBN 978-1-4419-1139-1. URL <https://www.springer.com/gp/book/9781441911391>.
- [113] M. M. Haugland, J. E. Lovett, and E. A. Anderson. Advances in the synthesis of nitroxide radicals for use in biomolecule spin labelling. *Chemical Society Reviews*, 47(3):668–680, Feb. 2018. ISSN 0306-0012. doi: 10.1039/c6cs00550k. WOS:000424136900002.
- [114] J. M. Hays, M. K. Kieber, J. Z. Li, J. I. Han, L. Columbus, and P. M. Kasson. Refinement of Highly Flexible Protein Structures using Simulation-Guided Spectroscopy. *Angewandte Chemie International Edition*, 57(52):17110–17114, 2018. ISSN 1521-3773. doi: 10.1002/anie.201810462. URL <https://onlinelibrary.wiley.com/doi/abs/10.1002/anie.201810462>.
- [115] J. M. Hays, D. S. Cafiso, and P. M. Kasson. Hybrid Refinement of Heterogeneous Conformational Ensembles Using Spectroscopic Data. *The Journal of Physical Chemistry Letters*, 10(12):3410–3414, June 2019. doi: 10.1021/acs.jpcclett.9b01407. URL <https://doi.org/10.1021/acs.jpcclett.9b01407>.
- [116] G. Herrick and B. Alberts. Purification and physical characterization of nucleic acid helix-unwinding proteins from calf thymus. *Journal of Biological Chemistry*, 251(7):2124–2132, Apr. 1976. ISSN 0021-9258, 1083-351X. URL <http://www.jbc.org/content/251/7/2124>.
- [117] D. Hilger, H. Jung, E. Padan, C. Wegener, K.-P. Vogel, H.-J. Steinhoff, and G. Jeschke. Assessing Oligomerization of Membrane Proteins by Four-Pulse DEER: pH-Dependent Dimerization of NhaA Na⁺/H⁺ Antiporter of *E. coli*. *Biophysical Journal*, 89(2):1328–1338, Aug. 2005. ISSN 0006-3495. doi: 10.1529/biophysj.105.062232. URL <http://www.sciencedirect.com/science/article/pii/S0006349505727806>.
- [118] A. Hirtreiter, D. Grohmann, and F. Werner. Molecular mechanisms of RNA polymerase—the F/E (RPB4/7) complex is required for high processivity in vitro. *Nucleic Acids Research*, 38(2):585–596, Jan. 2010. ISSN 0305-1048. doi: 10.1093/nar/gkp928. URL <https://academic.oup.com/nar/article/38/2/585/2409603>.
- [119] R. Hänsel, L. M. Luh, I. Corbeski, L. Trantirek, and V. Dötsch. In-Cell NMR and EPR Spectroscopy of Biomacromolecules. *Angewandte Chemie International Edition*, 53(39):10300–10314, Sept. 2014. ISSN 1521-3773. doi: 10.1002/anie.201311320. URL <http://onlinelibrary.wiley.com/doi/10.1002/anie.201311320/abstract>.
- [120] A. S. Holehouse, R. K. Das, J. N. Ahad, M. O. G. Richardson, and R. V. Pappu. CIDER: Resources to Analyze Sequence-Ensemble Relationships of Intrinsically Disordered Proteins. *Biophysical Journal*, 112(1):16–21, Jan. 2017. ISSN 0006-3495. doi: 10.1016/j.bpj.2016.11.3200. URL <http://www.sciencedirect.com/science/article/pii/S0006349516342692>.
- [121] S. Hovmöller, T. Zhou, and T. Ohlson. Conformations of amino acids in proteins. *Acta Crystallographica Section D: Biological Crystallography*, 58(5):768–776, May 2002. ISSN

- 0907-4449. doi: 10.1107/S0907444902003359. URL <http://scripts.iucr.org/cgi-bin/paper?gr2189>.
- [122] P. Hu and S. R. Hartmann. Theory of spectral diffusion decay using an uncorrelated-sudden-jump model. *Physical Review B*, 9(1):1–13, Jan. 1974. doi: 10.1103/PhysRevB.9.1. URL <https://link.aps.org/doi/10.1103/PhysRevB.9.1>.
- [123] Y. Hua, T. A. Vickers, B. F. Baker, C. F. Bennett, and A. R. Krainer. Enhancement of SMN2 Exon 7 Inclusion by Antisense Oligonucleotides Targeting the Exon. *PLOS Biology*, 5(4):e73, Mar. 2007. ISSN 1545-7885. doi: 10.1371/journal.pbio.0050073. URL <https://journals.plos.org/plosbiology/article?id=10.1371/journal.pbio.0050073>.
- [124] J. Huang, S. Rauscher, G. Nawrocki, T. Ran, M. Feig, B. L. d. Groot, H. Grubmüller, and A. D. MacKerell. CHARMM36m: an improved force field for folded and intrinsically disordered proteins. *Nature Methods*, 14(1):71–73, Jan. 2017. ISSN 1548-7105. doi: 10.1038/nmeth.4067. URL <https://www.nature.com/articles/nmeth.4067>.
- [125] W. L. Hubbell, H. S. Mchaourab, C. Altenbach, and M. A. Lietzow. Watching proteins move using site-directed spin labeling. *Structure*, 4(7):779–783, July 1996. ISSN 0969-2126. doi: 10.1016/S0969-2126(96)00085-8. URL <http://www.sciencedirect.com/science/article/pii/S0969212696000858>.
- [126] W. L. Hubbell, C. J. López, C. Altenbach, and Z. Yang. Technological advances in site-directed spin labeling of proteins. *Current Opinion in Structural Biology*, 23(5):725–733, Oct. 2013. ISSN 1879-033X. doi: 10.1016/j.sbi.2013.06.008.
- [127] M. P. Hughes, M. R. Sawaya, D. R. Boyer, L. Goldschmidt, J. A. Rodriguez, D. Cascio, L. Chong, T. Gonen, and D. S. Eisenberg. Atomic structures of low-complexity protein segments reveal kinked β sheets that assemble networks. *Science*, 359(6376):698–701, Feb. 2018. ISSN 0036-8075, 1095-9203. doi: 10.1126/science.aan6398. URL <https://science.sciencemag.org/content/359/6376/698>.
- [128] W. Humphrey, A. Dalke, and K. Schulten. VMD: Visual molecular dynamics. *Journal of Molecular Graphics*, 14(1):33–38, Feb. 1996. ISSN 0263-7855. doi: 10.1016/0263-7855(96)00018-5. URL <http://www.sciencedirect.com/science/article/pii/0263785596000185>.
- [129] J. Iwahara and G. M. Clore. Detecting transient intermediates in macromolecular binding by paramagnetic NMR. *Nature*, 440(7088):1227–1230, Apr. 2006. ISSN 1476-4687. doi: 10.1038/nature04673.
- [130] J. Iwahara, C. D. Schwieters, and G. M. Clore. Ensemble Approach for NMR Structure Refinement against 1h Paramagnetic Relaxation Enhancement Data Arising from a Flexible Paramagnetic Group Attached to a Macromolecule. *Journal of the American Chemical Society*, 126(18):5879–5896, May 2004. ISSN 0002-7863. doi: 10.1021/ja031580d. URL <https://doi.org/10.1021/ja031580d>.

- [131] A. P. Jagtap, I. Krstic, N. C. Kunjir, R. Hänsel, T. F. Prisner, and S. T. Sigurdsson. Sterically shielded spin labels for in-cell EPR spectroscopy: Analysis of stability in reducing environment. *Free Radical Research*, 49(1):78–85, Jan. 2015. ISSN 1071-5762. doi: 10.3109/10715762.2014.979409. URL <https://doi.org/10.3109/10715762.2014.979409>.
- [132] J. J. Jassoy, A. Berndhäuser, F. Duthie, S. P. Kühn, G. Hagelueken, and O. Schiemann. Versatile Trityl Spin Labels for Nanometer Distance Measurements on Biomolecules In Vitro and within Cells. *Angewandte Chemie International Edition*, 56(1):177–181, Jan. 2017. ISSN 1521-3773. doi: 10.1002/anie.201609085. URL <http://onlinelibrary.wiley.com/doi/10.1002/anie.201609085/abstract>.
- [133] J. Jean-Philippe, S. Paz, and M. Caputi. hnRNP A1: The Swiss Army Knife of Gene Expression. *International Journal of Molecular Sciences*, 14(9):18999–19024, Sept. 2013. doi: 10.3390/ijms140918999. URL <http://www.mdpi.com/1422-0067/14/9/18999>.
- [134] M. R. Jensen, R. W. Ruigrok, and M. Blackledge. Describing intrinsically disordered proteins at atomic resolution by NMR. *Current Opinion in Structural Biology*, 23(3):426–435, June 2013. ISSN 0959-440X. doi: 10.1016/j.sbi.2013.02.007. URL <http://www.sciencedirect.com/science/article/pii/S0959440X13000365>.
- [135] G. Jeschke. Determination of the Nanostructure of Polymer Materials by Electron Paramagnetic Resonance Spectroscopy. *Macromolecular Rapid Communications*, 23(4):227–246, 2002. ISSN 1521-3927. doi: 10.1002/1521-3927(20020301)23:4<227::AID-MARC227>3.0.CO;2-D. URL <https://onlinelibrary.wiley.com/doi/abs/10.1002/1521-3927%2820020301%2923%3A4%3C227%3A%3AAID-MARC227%3E3.0.CO%3B2-D>.
- [136] G. Jeschke. DEER Distance Measurements on Proteins. In M. A. Johnson and T. J. Martinez, editors, *Annual Review of Physical Chemistry, Vol 63*, volume 63, pages 419–446. Annual Reviews, Palo Alto, 2012. ISBN 978-0-8243-1063-9. WOS:000304203500020.
- [137] G. Jeschke. Conformational dynamics and distribution of nitroxide spin labels. *Progress in Nuclear Magnetic Resonance Spectroscopy*, 72:42–60, July 2013. ISSN 0079-6565. doi: 10.1016/j.pnmrs.2013.03.001. URL <http://www.sciencedirect.com/science/article/pii/S0079656513000393>.
- [138] G. Jeschke. Ensemble models of proteins and protein domains based on distance distribution restraints. *Proteins: Structure, Function, and Bioinformatics*, 84(4):544–560, Apr. 2016. ISSN 1097-0134. doi: 10.1002/prot.25000. URL <http://onlinelibrary.wiley.com/doi/10.1002/prot.25000/abstract>.
- [139] G. Jeschke. MMM: A toolbox for integrative structure modeling. *Protein Science*, 27(1):76–85, 2018. ISSN 1469-896X. doi: 10.1002/pro.3269. URL <https://onlinelibrary.wiley.com/doi/abs/10.1002/pro.3269>.
- [140] G. Jeschke and Y. Polyhach. Distance measurements on spin-labelled biomacromolecules by pulsed electron paramagnetic resonance. *Physical Chemistry Chemical Physics*, 9(16):

- 1895–1910, Apr. 2007. ISSN 1463-9084. doi: 10.1039/B614920K. URL <http://pubs.rsc.org/en/content/articlelanding/2007/cp/b614920k>.
- [141] G. Jeschke, M. Pannier, A. Godt, and H. W. Spiess. Dipolar spectroscopy and spin alignment in electron paramagnetic resonance. *Chemical Physics Letters*, 331(2-4):243–252, Dec. 2000. ISSN 0009-2614. doi: 10.1016/S0009-2614(00)01171-4. WOS:000165721400021.
- [142] G. Jeschke, A. Koch, U. Jonas, and A. Godt. Direct Conversion of EPR Dipolar Time Evolution Data to Distance Distributions. *Journal of Magnetic Resonance*, 155(1):72–82, Mar. 2002. ISSN 1090-7807. doi: 10.1006/jmre.2001.2498. URL <http://www.sciencedirect.com/science/article/pii/S109078070192498X>.
- [143] G. Jeschke, G. Panek, A. Godt, A. Bender, and H. Paulsen. Data analysis procedures for pulse ELDOR measurements of broad distance distributions. *Applied Magnetic Resonance*, 26(1-2):223–244, Mar. 2004. ISSN 0937-9347, 1613-7507. doi: 10.1007/BF03166574. URL <http://link.springer.com/article/10.1007/BF03166574>.
- [144] G. Jeschke, V. Chechik, P. Ionita, A. Godt, H. Zimmermann, J. Banham, C. R. Timmel, D. Hilger, and H. Jung. DeerAnalysis2006—a comprehensive software package for analyzing pulsed ELDOR data. *Applied Magnetic Resonance*, 30(3-4):473–498, June 2006. ISSN 0937-9347, 1613-7507. doi: 10.1007/BF03166213. URL <https://link.springer.com/article/10.1007/BF03166213>.
- [145] G. Jeschke, M. Sajid, M. Schulte, and A. Godt. Three-spin correlations in double electron–electron resonance. *Physical Chemistry Chemical Physics*, 11(31):6580–6591, 2009. doi: 10.1039/B905724B. URL <http://pubs.rsc.org/en/Content/ArticleLanding/2009/CP/B905724B>.
- [146] H. Jäger, A. Koch, V. Maus, H. Spiess, and G. Jeschke. Relaxation-based distance measurements between a nitroxide and a lanthanide spin label. *Journal of Magnetic Resonance*, 194(2):254–263, 2008. ISSN 1090-7807. doi: <https://doi.org/10.1016/j.jmr.2008.07.012>. URL <http://www.sciencedirect.com/science/article/pii/S1090780708002395>.
- [147] M. Ji, S. Ruthstein, and S. Saxena. Paramagnetic Metal Ions in Pulsed ESR Distance Distribution Measurements. *Accounts of Chemical Research*, 47(2):688–695, Feb. 2014. ISSN 0001-4842. doi: 10.1021/ar400245z. URL <https://doi.org/10.1021/ar400245z>.
- [148] L. Jønson, J. Vikesaa, A. Krogh, L. K. Nielsen, T. v. Hansen, R. Borup, A. H. Johnsen, J. Christiansen, and F. C. Nielsen. Molecular composition of IMP1 ribonucleoprotein granules. *Molecular & cellular proteomics: MCP*, 6(5):798–811, May 2007. ISSN 1535-9476. doi: 10.1074/mcp.M600346-MCP200.
- [149] B. Joseph, V. M. Korkhov, M. Yulikov, G. Jeschke, and E. Bordignon. Conformational cycle of the vitamin B12 ABC importer in liposomes detected by DEER. *Journal of Biological Chemistry*, page jbc.M113.512178, Dec. 2013. ISSN 0021-9258, 1083-351X. doi: 10.1074/jbc.M113.512178. URL <http://www.jbc.org/content/early/2013/12/19/jbc.M113.512178>.

- [150] B. Joseph, V. M. Tormyshev, O. Y. Rogozhnikova, D. Akhmetzyanov, E. G. Bagryanskaya, and T. F. Prisner. Selective High-Resolution Detection of Membrane Protein-Ligand Interaction in Native Membranes Using Trityl-Nitroxide PELDOR. *Angewandte Chemie-International Edition*, 55(38):11538–11542, Sept. 2016. ISSN 1433-7851. doi: 10.1002/anie.201606335. WOS:000383748900040.
- [151] I. Kaminker, H. Yagi, T. Huber, A. Feintuch, G. Otting, and D. Goldfarb. Spectroscopic selection of distance measurements in a protein dimer with mixed nitroxide and Gd³⁺ spin labels. *Physical Chemistry Chemical Physics*, 14(13):4355, 2012. ISSN 1463-9076, 1463-9084. doi: 10.1039/c2cp40219j. URL <http://xlink.rsc.org/?DOI=c2cp40219j>.
- [152] I. Kaminker, I. Tkach, N. Manukovsky, T. Huber, H. Yagi, G. Otting, M. Bennati, and D. Goldfarb. W-band orientation selective DEER measurements on a Gd³⁺/nitroxide mixed-labeled protein dimer with a dual mode cavity. *Journal of Magnetic Resonance*, 227:66–71, Feb. 2013. ISSN 1090-7807. doi: 10.1016/j.jmr.2012.11.028. URL <http://www.sciencedirect.com/science/article/pii/S1090780712003722>.
- [153] I. Kaminker, M. Bye, N. Mendelman, K. Gislason, S. T. Sigurdsson, and D. Goldfarb. Distance measurements between manganese(II) and nitroxide spin-labels by DEER determine a binding site of Mn²⁺ in the HP92 loop of ribosomal RNA. *Physical Chemistry Chemical Physics*, 17(23):15098–15102, June 2015. ISSN 1463-9084. doi: 10.1039/C5CP01624J. URL <https://pubs.rsc.org/en/content/articlelanding/2015/cp/c5cp01624j>.
- [154] K. Kapeli, F. Martinez, and G. Yeo. Genetic mutations in RNA-binding proteins and their roles in ALS. 2017.
- [155] G. Karthikeyan, A. Bonucci, G. Casano, G. Gerbaud, S. Abel, V. Thomé, L. Kodjabachian, A. Magalon, B. Guigliarelli, V. Belle, O. Ouari, and E. Mileo. A Bioresistant Nitroxide Spin Label for In-Cell EPR Spectroscopy: In Vitro and In Oocytes Protein Structural Dynamics Studies. *Angewandte Chemie*, 130(5):1380–1384, 2018. ISSN 1521-3757. doi: 10.1002/ange.201710184. URL <https://onlinelibrary.wiley.com/doi/abs/10.1002/ange.201710184>.
- [156] P. M. Kasson and S. Jha. Adaptive ensemble simulations of biomolecules. *Current Opinion in Structural Biology*, 52:87–94, Oct. 2018. ISSN 0959-440X. doi: 10.1016/j.sbi.2018.09.005. URL <http://www.sciencedirect.com/science/article/pii/S0959440X1830085X>.
- [157] M. Kato, T. W. Han, S. Xie, K. Shi, X. Du, L. C. Wu, H. Mirzaei, E. J. Goldsmith, J. Longgood, J. Pei, N. V. Grishin, D. E. Frantz, J. W. Schneider, S. Chen, L. Li, M. R. Sawaya, D. Eisenberg, R. Tycko, and S. L. McKnight. Cell-free formation of RNA granules: low complexity sequence domains form dynamic fibers within hydrogels. *Cell*, 149(4):753–767, May 2012. ISSN 1097-4172. doi: 10.1016/j.cell.2012.04.017.
- [158] D. R. Kattnig and D. Hinderberger. Analytical distance distributions in systems of spherical symmetry with applications to double electron–electron resonance. *Journal of Magnetic*

- Resonance*, 230:50–63, May 2013. ISSN 1090-7807. doi: 10.1016/j.jmr.2013.01.007. URL <http://www.sciencedirect.com/science/article/pii/S1090780713000219>.
- [159] C. W. M. Kay, H. El Mkami, R. Cammack, and R. W. Evans. Pulsed ELDOR Determination of the Intramolecular Distance between the Metal Binding Sites in Dicumric Human Serum Transferrin and Lactoferrin. *Journal of the American Chemical Society*, 129(16):4868–4869, Apr. 2007. ISSN 0002-7863. doi: 10.1021/ja068966j. URL <http://dx.doi.org/10.1021/ja068966j>.
- [160] K. Keller, A. Doll, M. Qi, A. Godt, G. Jeschke, and M. Yulikov. Averaging of nuclear modulation artefacts in RIDME experiments. *Journal of Magnetic Resonance*, 272:108–113, Nov. 2016. ISSN 1090-7807. doi: 10.1016/j.jmr.2016.09.016. URL <http://www.sciencedirect.com/science/article/pii/S1090780716301860>.
- [161] K. Keller, M. Zalibera, M. Qi, V. Koch, J. Wegner, H. Hintz, A. Godt, G. Jeschke, A. Savitsky, and M. Yulikov. EPR characterization of Mn(ii) complexes for distance determination with pulsed dipolar spectroscopy. *Physical Chemistry Chemical Physics*, 2016. ISSN 1463-9076. doi: 10.1039/C6CP04884F. URL <http://dx.doi.org/10.1039/C6CP04884F>. bibtex: Keller2016.
- [162] K. Keller, V. Mertens, M. Qi, A. I. Nalepa, A. Godt, A. Savitsky, G. Jeschke, and M. Yulikov. Computing distance distributions from dipolar evolution data with overtones: RIDME spectroscopy with Gd(iii)-based spin labels. *Physical chemistry chemical physics: PCCP*, 19(27):17856–17876, July 2017. ISSN 1463-9084. doi: 10.1039/c7cp01524k.
- [163] K. Keller, T. Wiegand, R. Cadalbert, B. H. Meier, A. Böckmann, G. Jeschke, and M. Yulikov. High-spin Metal Centres in Dipolar EPR Spectroscopy. *Chimia*, 72(4):216–220, Apr. 2018. ISSN 0009-4293. doi: 10.2533/chimia.2018.216.
- [164] K. Keller, M. Qi, C. Gmeiner, I. Ritsch, A. Godt, G. Jeschke, A. Savitsky, and M. Yulikov. Intermolecular Background Decay in RIDME Experiments. *Physical Chemistry Chemical Physics*, Mar. 2019. ISSN 1463-9084. doi: 10.1039/C8CP07815G. URL <https://pubs.rsc.org/en/content/articlelanding/2019/cp/c8cp07815g>.
- [165] C. S. Kim, S. K. Seol, O.-K. Song, J. H. Park, and S. K. Jang. An RNA-binding protein, hnRNP A1, and a scaffold protein, septin 6, facilitate hepatitis C virus replication. *Journal of Virology*, 81(8):3852–3865, Apr. 2007. ISSN 0022-538X. doi: 10.1128/JVI.01311-06.
- [166] H. J. Kim, N. C. Kim, Y.-D. Wang, E. A. Scarborough, J. Moore, Z. Diaz, K. S. MacLea, B. Freibaum, S. Li, A. Molliex, A. P. Kanagaraj, R. Carter, K. B. Boylan, A. M. Wojtas, R. Rademakers, J. L. Pinkus, S. A. Greenberg, J. Q. Trojanowski, B. J. Traynor, B. N. Smith, S. Topp, A.-S. Gkazi, J. Miller, C. E. Shaw, M. Kottlors, J. Kirschner, A. Pestronk, Y. R. Li, A. F. Ford, A. D. Gitler, M. Benatar, O. D. King, V. E. Kimonis, E. D. Ross, C. C. Weihl, J. Shorter, and J. P. Taylor. Mutations in prion-like domains in hnRNPA2b1 and hnRNPA1 cause multisystem proteinopathy and ALS. *Nature*, 495(7442):467–473, Mar. 2013. ISSN 1476-4687. doi: 10.1038/nature11922.

- [167] I. A. Kirilyuk, Y. F. Polienko, O. A. Krumkacheva, R. K. Strizhakov, Y. V. Gatilov, I. A. Grigor'ev, and E. G. Bagryanskaya. Synthesis of 2,5-Bis(spirocyclohexane)-Substituted Nitroxides of Pyrroline and Pyrrolidine Series, Including Thiol-Specific Spin Label: An Analogue of MTSSL with Long Relaxation Time. *The Journal of Organic Chemistry*, 77(18):8016–8027, Sept. 2012. ISSN 0022-3263. doi: 10.1021/jo301235j. URL <http://dx.doi.org/10.1021/jo301235j>.
- [168] D. Klose, J. P. Klare, D. Grohmann, C. W. M. Kay, F. Werner, and H.-J. Steinhoff. Simulation vs. Reality: A Comparison of In Silico Distance Predictions with DEER and FRET Measurements. *PLoS ONE*, 7(6):e39492, June 2012. doi: 10.1371/journal.pone.0039492. URL <http://dx.doi.org/10.1371/journal.pone.0039492>.
- [169] B. R. Knauer and J. J. Napier. The nitrogen hyperfine splitting constant of the nitroxide functional group as a solvent polarity parameter. The relative importance for a solvent polarity parameter of its being a cybotactic probe vs. its being a model process. *Journal of the American Chemical Society*, 98(15):4395–4400, July 1976. ISSN 0002-7863. doi: 10.1021/ja00431a010. URL <https://doi.org/10.1021/ja00431a010>.
- [170] H. Kooshapur, N. R. Choudhury, B. Simon, M. Mühlbauer, A. Jussupow, N. Fernandez, A. N. Jones, A. Dallmann, F. Gabel, C. Camilloni, G. Michlewski, J. F. Caceres, and M. Sattler. Structural basis for terminal loop recognition and stimulation of pri-miRNA-18a processing by hnRNP A1. *Nature Communications*, 9(1):1–17, June 2018. ISSN 2041-1723. doi: 10.1038/s41467-018-04871-9. URL <https://www.nature.com/articles/s41467-018-04871-9>.
- [171] P. A. Kosen. Spin labeling of proteins. *Methods in Enzymology*, 177:86–121, 1989. ISSN 0076-6879. doi: 10.1016/0076-6879(89)77007-5.
- [172] S. Kosol, S. Contreras-Martos, C. Cedeño, and P. Tompa. Structural Characterization of Intrinsically Disordered Proteins by NMR Spectroscopy. *Molecules*, 18(9):10802–10828, Sept. 2013. doi: 10.3390/molecules180910802. URL <https://www.mdpi.com/1420-3049/18/9/10802>.
- [173] S. Kucher, S. Korneev, S. Tyagi, R. Apfelbaum, D. Grohmann, E. A. Lemke, J. P. Klare, H.-J. Steinhoff, and D. Klose. Orthogonal spin labeling using click chemistry for in vitro and in vivo applications. *Journal of Magnetic Resonance*, 275:38–45, Feb. 2017. ISSN 1090-7807. doi: 10.1016/j.jmr.2016.12.001. WOS:000393533900005.
- [174] L. V. Kulik, S. A. Dzuba, I. A. Grigoryev, and Y. D. Tsvetkov. Electron dipole–dipole interaction in ESEEM of nitroxide biradicals. *Chemical Physics Letters*, 343(3–4):315–324, Aug. 2001. ISSN 0009-2614. doi: 10.1016/S0009-2614(01)00721-7. URL <http://www.sciencedirect.com/science/article/pii/S0009261401007217>.
- [175] L. V. Kulik, I. A. Grigor'ev, E. S. Salnikov, S. A. Dzuba, and Y. D. Tsvetkov. Electron Spin Echo Envelope Modulation Induced by Slow Intramolecular Motion. *The Journal of Physical Chemistry A*, 107(19):3692–3695, May 2003. ISSN 1089-5639. doi: 10.1021/jp027764g. URL <http://dx.doi.org/10.1021/jp027764g>.

- [176] V. V. Kurshev, A. M. Raitsimring, and Y. D. Tsvetkov. Selection of dipolar interaction by the “2 + 1” pulse train ESE. *Journal of Magnetic Resonance (1969)*, 81(3):441–454, Feb. 1989. ISSN 0022-2364. doi: 10.1016/0022-2364(89)90080-2. URL <http://www.sciencedirect.com/science/article/pii/0022236489900802>.
- [177] A. A. Kuzhelev, D. V. Trukhin, O. A. Krumkacheva, R. K. Strizhakov, O. Y. Rogozhnikova, T. I. Troitskaya, M. V. Fedin, V. M. Tormyshev, and E. G. Bagryanskaya. Room-Temperature Electron Spin Relaxation of Triarylmethyl Radicals at the X- and Q-Bands. *Journal of Physical Chemistry B*, 119(43):13630–13640, Oct. 2015. ISSN 1520-6106. doi: 10.1021/acs.jpcc.5b03027. WOS:000363994000018.
- [178] A. A. Kuzhelev, O. A. Krumkacheva, G. Y. Shevelev, M. Yulikov, M. V. Fedin, and E. G. Bagryanskaya. Room-temperature distance measurements using RIDME and the orthogonal spin labels trityl/nitroxide. *Physical Chemistry Chemical Physics*, 20(15):10224–10230, Apr. 2018. ISSN 1463-9084. doi: 10.1039/C8CP01093E. URL <http://pubs.rsc.org/en/content/articlelanding/2018/cp/c8cp01093e>.
- [179] R. Langen, J. M. Isas, H. Luecke, H. T. Haigler, and W. L. Hubbell. Membrane-mediated Assembly of Annexins Studied by Site-directed Spin Labeling. *Journal of Biological Chemistry*, 273(35):22453–22457, Aug. 1998. ISSN 0021-9258, 1083-351X. doi: 10.1074/jbc.273.35.22453. URL <http://www.jbc.org/content/273/35/22453>.
- [180] M. J. Lawless, J. L. Sarver, and S. Saxena. Nucleotide-Independent Copper(II)-Based Distance Measurements in DNA by Pulsed ESR Spectroscopy. *Angewandte Chemie*, 129(8):2147–2149, Feb. 2017. ISSN 1521-3757. doi: 10.1002/ange.201611197. URL <https://onlinelibrary.wiley.com/doi/abs/10.1002/ange.201611197>.
- [181] N. Le Breton, M. Martinho, E. Mileo, E. Etienne, G. Gerbaud, B. Guigliarelli, and V. Belle. Exploring intrinsically disordered proteins using site-directed spin labeling electron paramagnetic resonance spectroscopy. *Frontiers in Molecular Biosciences*, 2, May 2015. ISSN 2296-889X. doi: 10.3389/fmolb.2015.00021. URL <https://www.ncbi.nlm.nih.gov/pmc/articles/PMC4436889/>.
- [182] B. J. Lee, A. E. Cansizoglu, K. E. Süel, T. H. Louis, Z. Zhang, and Y. M. Chook. Rules for Nuclear Localization Sequence Recognition by Karyopherin-beta2. *Cell*, 126(3):543–558, Aug. 2006. ISSN 0092-8674. doi: 10.1016/j.cell.2006.05.049. URL <http://www.sciencedirect.com/science/article/pii/S009286740600910X>.
- [183] M. T. Lerch, Z. Yang, C. Altenbach, and W. L. Hubbell. Chapter Two - High-Pressure EPR and Site-Directed Spin Labeling for Mapping Molecular Flexibility in Proteins. In P. Z. Q. a. K. Warncke, editor, *Methods in Enzymology*, volume 564 of *Electron Paramagnetic Resonance Investigations of Biological Systems by Using Spin Labels, Spin Probes, and Intrinsic Metal Ions, Part B*, pages 29–57. Academic Press, 2015. URL <http://www.sciencedirect.com/science/article/pii/S0076687915004085>.

- [184] A. Lewin, J. P. Hill, R. Boetzel, T. Georgiou, R. James, C. Kleanthous, and G. R. Moore. Site-specific labeling of proteins with cyclen-bound transition metal ions. *Inorganica Chimica Acta*, 331(1):123–130, Mar. 2002. ISSN 0020-1693. doi: 10.1016/S0020-1693(01)00766-6. URL <http://www.sciencedirect.com/science/article/pii/S0020169301007666>.
- [185] K. K. C. Li, B. L. Chau, and K. A. W. Lee. Differential interaction of PRMT1 with RGG-boxes of the FET family proteins EWS and TAF15. *Protein Science: A Publication of the Protein Society*, 27(3):633–642, 2018. ISSN 1469-896X. doi: 10.1002/pro.3354.
- [186] Y. R. Li, O. D. King, J. Shorter, and A. D. Gitler. Stress granules as crucibles of ALS pathogenesis. *J Cell Biol*, 201(3):361–372, Apr. 2013. ISSN 0021-9525, 1540-8140. doi: 10.1083/jcb.201302044. URL <http://jcb.rupress.org/content/201/3/361>.
- [187] Z. Li, W. Zeng, S. Ye, J. Lv, A. Nie, B. Zhang, Y. Sun, H. Han, and Q. He. Cellular hnRNP A1 Interacts with Nucleocapsid Protein of Porcine Epidemic Diarrhea Virus and Impairs Viral Replication. *Viruses*, 10(3):127, Mar. 2018. doi: 10.3390/v10030127. URL <http://www.mdpi.com/1999-4915/10/3/127>.
- [188] J.-Y. Lin, S.-R. Shih, M. Pan, C. Li, C.-F. Lue, V. Stollar, and M.-L. Li. hnRNP A1 Interacts with the 5-prime Untranslated Regions of Enterovirus 71 and Sindbis Virus RNA and Is Required for Viral Replication. *Journal of Virology*, 83(12):6106–6114, June 2009. ISSN 0022-538X, 1098-5514. doi: 10.1128/JVI.02476-08. URL <https://jvi.asm.org/content/83/12/6106>.
- [189] Y. Lin, D. S. W. Protter, M. K. Rosen, and R. Parker. Formation and Maturation of Phase-Separated Liquid Droplets by RNA-Binding Proteins. *Molecular Cell*, 60(2):208–219, Oct. 2015. ISSN 1097-2765. doi: 10.1016/j.molcel.2015.08.018. URL <http://www.sciencedirect.com/science/article/pii/S1097276515006644>.
- [190] Q. Liu, S. Shu, R. R. Wang, F. Liu, B. Cui, X. N. Guo, C. X. Lu, X. G. Li, M. S. Liu, B. Peng, L.-y. Cui, and X. Zhang. Whole-exome sequencing identifies a missense mutation in hnRNPA1 in a family with flail arm ALS. *Neurology*, 87(17):1763–1769, Oct. 2016. ISSN 0028-3878, 1526-632X. doi: 10.1212/WNL.0000000000003256. URL <http://www.neurology.org/content/87/17/1763>.
- [191] X. Liu, T. Ishizuka, H.-L. Bao, K. Wada, Y. Takeda, K. Iida, K. Nagasawa, D. Yang, and Y. Xu. Structure-Dependent Binding of hnRNPA1 to Telomere RNA. *Journal of the American Chemical Society*, 139(22):7533–7539, 2017. ISSN 1520-5126. doi: 10.1021/jacs.7b01599.
- [192] M. Y. Lobanov, N. S. Bogatyreva, and O. V. Galzitskaya. Radius of gyration as an indicator of protein structure compactness. *Molecular Biology*, 42(4):623–628, Aug. 2008. ISSN 1608-3245. doi: 10.1134/S0026893308040195. URL <https://doi.org/10.1134/S0026893308040195>.

- [193] P. Lueders, G. Jeschke, and M. Yulikov. Double Electron Electron Resonance Measured Between Gd³⁺ Ions and Nitroxide Radicals. *The Journal of Physical Chemistry Letters*, 2(6):604–609, Mar. 2011. ISSN 1948-7185. doi: 10.1021/jz200073h. URL <http://dx.doi.org/10.1021/jz200073h>.
- [194] P. Lueders, H. Jäger, M. A. Hemminga, G. Jeschke, and M. Yulikov. Multiple Pathway Relaxation Enhancement in the System Composed of Three Paramagnetic Species: Nitroxide Radical–Ln³⁺–O₂. *The Journal of Physical Chemistry Letters*, 3(10):1336–1340, May 2012. ISSN 1948-7185. doi: 10.1021/jz300316q. URL <http://dx.doi.org/10.1021/jz300316q>.
- [195] P. Lueders, S. Razzaghi, H. Jäger, R. Tschaggelar, M. A. Hemminga, M. Yulikov, and G. Jeschke. Distance determination from dysprosium induced relaxation enhancement: a case study on membrane-inserted WALP23 polypeptides. *Molecular Physics*, 111(18-19):2824–2833, Oct. 2013. ISSN 0026-8976. doi: 10.1080/00268976.2013.806683. URL <http://dx.doi.org/10.1080/00268976.2013.806683>.
- [196] A. M. Bowen, M. W. Jones, J. E. Lovett, T. G. Gaule, M. J. McPherson, J. R. Dilworth, C. R. Timmel, and J. R. Harmer. Exploiting orientation-selective DEER: determining molecular structure in systems containing Cu(ii) centres. *Physical Chemistry Chemical Physics*, 18(8):5981–5994, 2016. doi: 10.1039/C5CP06096F. URL <http://pubs.rsc.org/en/Content/ArticleLanding/2016/CP/C5CP06096F>.
- [197] S. Maharana, J. Wang, D. K. Papadopoulos, D. Richter, A. Pozniakovsky, I. Poser, M. Bickle, S. Rizk, J. Guillén-Boixet, T. M. Franzmann, M. Jahnel, L. Marrone, Y.-T. Chang, J. Sterneckert, P. Tomancak, A. A. Hyman, and S. Alberti. RNA buffers the phase separation behavior of prion-like RNA binding proteins. *Science (New York, N.Y.)*, 360(6391):918–921, 2018. ISSN 1095-9203. doi: 10.1126/science.aar7366.
- [198] J. Makowska, S. Rodziewicz-Motowidło, K. Bagińska, J. A. Vila, A. Liwo, L. Chmurzyński, and H. A. Scheraga. Polyproline ii conformation is one of many local conformational states and is not an overall conformation of unfolded peptides and proteins. *Proceedings of the National Academy of Sciences*, 103(6):1744–1749, Feb. 2006. ISSN 0027-8424, 1091-6490. doi: 10.1073/pnas.0510549103. URL <https://www.pnas.org/content/103/6/1744>.
- [199] T. Maly, F. MacMillan, K. Zwicker, N. Kashani-Poor, U. Brandt, and T. F. Prisner. Relaxation filtered hyperfine (REFINE) spectroscopy: a novel tool for studying overlapping biological electron paramagnetic resonance signals applied to mitochondrial complex I. *Biochemistry*, 43(13):3969–3978, Apr. 2004. ISSN 0006-2960. doi: 10.1021/bi035865e.
- [200] A. Marko, D. Margraf, H. Yu, Y. Mu, G. Stock, and T. Prisner. Molecular orientation studies by pulsed electron-electron double resonance experiments. *The Journal of Chemical Physics*, 130(6):064102, Feb. 2009. ISSN 0021-9606. doi: 10.1063/1.3073040. URL <https://aip.scitation.org/doi/abs/10.1063/1.3073040>.
- [201] A. Marko, D. Margraf, P. Cekan, S. T. Sigurdsson, O. Schiemann, and T. F. Prisner. Analytical method to determine the orientation of rigid spin labels in DNA. *Physical*

- Review E*, 81(2):021911, Feb. 2010. doi: 10.1103/PhysRevE.81.021911. URL <https://link.aps.org/doi/10.1103/PhysRevE.81.021911>.
- [202] A. Martorana, G. Bellapadrona, A. Feintuch, E. Di Gregorio, S. Aime, and D. Goldfarb. Probing protein conformation in cells by EPR distance measurements using Gd³⁺ spin labeling. *Journal of the American Chemical Society*, 136(38):13458–13465, Sept. 2014. ISSN 1520-5126. doi: 10.1021/ja5079392.
- [203] A. G. Maryasov and Y. D. Tsvetkov. Formation of the pulsed electron-electron double resonance signal in the case of a finite amplitude of microwave fields. *Applied Magnetic Resonance*, 18(4):583–605, Apr. 2000. ISSN 1613-7507. doi: 10.1007/BF03162305. URL <https://doi.org/10.1007/BF03162305>.
- [204] H. Meka, F. Werner, S. C. Cordell, S. Onesti, and P. Brick. Crystal structure and RNA binding of the Rpb4/Rpb7 subunits of human RNA polymerase II. *Nucleic Acids Research*, 33(19):6435–6444, Jan. 2005. ISSN 0305-1048. doi: 10.1093/nar/gki945. URL <https://academic.oup.com/nar/article/33/19/6435/1308704>.
- [205] R. Meng, J. Becker, F. T. Lin, S. Saxena, and S. G. Weber. Binding of copper(II) to thyrotropin-releasing hormone (TRH) and its analogs. *Inorganica chimica acta*, 358(10):2933–2942, June 2005. ISSN 0020-1693. doi: 10.1016/j.ica.2004.11.045. URL <http://europepmc.org/abstract/med/17160139>.
- [206] J. A. Merten, K. M. Schultz, and C. S. Klug. Concentration-dependent oligomerization and oligomeric arrangement of LptA. *Protein Science*, 21(2):211–218, 2012. ISSN 1469-896X. doi: 10.1002/pro.2004. URL <https://onlinelibrary.wiley.com/doi/abs/10.1002/pro.2004>.
- [207] A. Meyer and O. Schiemann. PELDOR and RIDME Measurements on a High-Spin Manganese(II) Bisnitroxide Model Complex. *The Journal of Physical Chemistry A*, 120(20):3463–3472, May 2016. ISSN 1089-5639. doi: 10.1021/acs.jpca.6b00716. URL <http://dx.doi.org/10.1021/acs.jpca.6b00716>.
- [208] A. Meyer, D. Abdullin, G. Schnakenburg, and O. Schiemann. Single and double nitroxide labeled bis(terpyridine)-copper(II): influence of orientation selectivity and multispin effects on PELDOR and RIDME. *Physical Chemistry Chemical Physics*, 18(13):9262–9271, Apr. 2016. ISSN 1463-9076. doi: 10.1039/c5cp07621h. WOS:000373000100053.
- [209] V. Meyer and M. Margittai. Spin Labeling and Characterization of Tau Fibrils Using Electron Paramagnetic Resonance (EPR). *Methods in Molecular Biology (Clifton, N.J.)*, 1345:185–199, 2016. ISSN 1940-6029. doi: 10.1007/978-1-4939-2978-8_12.
- [210] S. Milikisyants, F. Scarpelli, M. G. Finiguerra, M. Ubbink, and M. Huber. A pulsed EPR method to determine distances between paramagnetic centers with strong spectral anisotropy and radicals: The dead-time free RIDME sequence. *Journal of Magnetic Resonance*, 201(1):48–56, Nov. 2009. ISSN 1090-7807. doi: 10.1016/j.jmr.2009.08.008. WOS:000271071400007.

- [211] A. D. Milov and Y. D. Tsvetkov. Double electron-electron resonance in electron spin echo: Conformations of spin-labeled poly-4-vinylpyridine in glassy solutions. *Applied Magnetic Resonance*, 12(4):495–504, May 1997. ISSN 1613-7507. doi: 10.1007/BF03164129. URL <https://doi.org/10.1007/BF03164129>.
- [212] A. D. Milov, A. B. Ponomarev, and Y. D. Tsvetkov. Electron-electron double resonance in electron spin echo: Model biradical systems and the sensitized photolysis of decalin. *Chemical Physics Letters*, 110(1):67–72, Sept. 1984. ISSN 0009-2614. doi: 10.1016/0009-2614(84)80148-7. URL <http://www.sciencedirect.com/science/article/pii/0009261484801487>.
- [213] A. D. Milov, A. G. Maryasov, and Y. D. Tsvetkov. Pulsed electron double resonance (PELDOR) and its applications in free-radicals research. *Applied Magnetic Resonance*, 15(1):107–143, Aug. 1998. ISSN 0937-9347, 1613-7507. doi: 10.1007/BF03161886. URL <https://link.springer.com/article/10.1007/BF03161886>.
- [214] S. K. Misra, P. P. Borbat, and J. H. Freed. Calculation of Double-Quantum-Coherence Two-dimensional Spectra: Distance Measurements and Orientational Correlations. *Applied Magnetic Resonance*, 36(2-4):237, Dec. 2009. ISSN 0937-9347, 1613-7507. doi: 10.1007/s00723-009-0023-5. URL <https://link.springer.com/article/10.1007/s00723-009-0023-5>.
- [215] D. M. Mitrea and R. W. Kriwacki. Phase separation in biology; functional organization of a higher order. *Cell Communication and Signaling*, 14(1):1, Dec. 2016. ISSN 1478-811X. doi: 10.1186/s12964-015-0125-7. URL <https://link.springer.com/article/10.1186/s12964-015-0125-7>.
- [216] T. Mittag and J. D. Forman-Kay. Atomic-level characterization of disordered protein ensembles. *Current Opinion in Structural Biology*, 17(1):3–14, Feb. 2007. ISSN 0959-440X. doi: 10.1016/j.sbi.2007.01.009. URL <http://www.sciencedirect.com/science/article/pii/S0959440X07000103>.
- [217] Y. N. Molin, K. M. K. M. Salikhov, K. I. K. I. Zamaraev, 1939, K. I. K. I. Zamaraev, and 1939. *Spin exchange*. Springer-Verlag, 1980. ISBN 978-0-387-10095-1. URL <http://agris.fao.org/agris-search/search.do?recordID=US201300324051>.
- [218] A. Molliex, J. Temirov, J. Lee, M. Coughlin, A. P. Kanagaraj, H. J. Kim, T. Mittag, and J. P. Taylor. Phase Separation by Low Complexity Domains Promotes Stress Granule Assembly and Drives Pathological Fibrillization. *Cell*, 163(1):123–133, Sept. 2015. ISSN 0092-8674. doi: 10.1016/j.cell.2015.09.015. URL <https://www.sciencedirect.com/science/article/pii/S0092867415011769>.
- [219] C. E. Morgan, J. L. Meagher, J. D. Levensgood, J. Delproposto, C. Rollins, J. A. Stuckey, and B. S. Tolbert. The First Crystal Structure of the UP1 Domain of hnRNP A1 bound to RNA Reveals a New Look for an Old RNA Binding Protein. *Journal of molecular biology*, 427

- (20):3241–3257, Oct. 2015. ISSN 0022-2836. doi: 10.1016/j.jmb.2015.05.009. URL <https://www.ncbi.nlm.nih.gov/pmc/articles/PMC4586317/>.
- [220] B. Morin, J.-M. Bourhis, V. Belle, M. Woudstra, F. Carrière, B. Guigliarelli, A. Fournel, and S. Longhi. Assessing Induced Folding of an Intrinsically Disordered Protein by Site-Directed Spin-Labeling Electron Paramagnetic Resonance Spectroscopy. *The Journal of Physical Chemistry B*, 110(41):20596–20608, Oct. 2006. ISSN 1520-6106. doi: 10.1021/jp063708u. URL <https://doi.org/10.1021/jp063708u>.
- [221] J. Möser, K. Lips, M. Tseytlin, G. Eaton, S. Eaton, and A. Schnegg. Using rapid-scan EPR to improve the detection limit of quantitative EPR by more than one order of magnitude. *Journal of Magnetic Resonance*, 281:17–25, Aug. 2017. ISSN 10907807. doi: 10.1016/j.jmr.2017.04.003. URL <https://linkinghub.elsevier.com/retrieve/pii/S1090780717300939>.
- [222] T. Murakami, S. Qamar, J. Q. Lin, G. S. K. Schierle, E. Rees, A. Miyashita, A. R. Costa, R. B. Dodd, F. T. S. Chan, C. H. Michel, D. Kronenberg-Versteeg, Y. Li, S.-P. Yang, Y. Wakutani, W. Meadows, R. R. Ferry, L. Dong, G. G. Tartaglia, G. Favrin, W.-L. Lin, D. W. Dickson, M. Zhen, D. Ron, G. Schmitt-Ulms, P. E. Fraser, N. A. Shneider, C. Holt, M. Vendruscolo, C. F. Kaminski, and P. St George-Hyslop. ALS/FTD Mutation-Induced Phase Transition of FUS Liquid Droplets and Reversible Hydrogels into Irreversible Hydrogels Impairs RNP Granule Function. *Neuron*, 88(4):678–690, Nov. 2015. ISSN 0896-6273. doi: 10.1016/j.neuron.2015.10.030. URL <http://www.sciencedirect.com/science/article/pii/S0896627315009241>.
- [223] J. C. Myers and Y. Shamoo. Human UP1 as a model for understanding purine recognition in the family of proteins containing the RNA recognition motif (RRM). *Journal of Molecular Biology*, 342(3):743–756, Sept. 2004. ISSN 0022-2836. doi: 10.1016/j.jmb.2004.07.029.
- [224] J. C. Myers, S. A. Moore, and Y. Shamoo. Structure-based Incorporation of 6-Methyl-8-(2-deoxy-beta-ribofuranosyl)isoxanthopterin into the Human Telomeric Repeat DNA as a Probe for UP1 Binding and Destabilization of G-tetrad Structures. *Journal of Biological Chemistry*, 278(43):42300–42306, Oct. 2003. ISSN 0021-9258, 1083-351X. doi: 10.1074/jbc.M306147200. URL <http://www.jbc.org/lookup/doi/10.1074/jbc.M306147200>.
- [225] S. G. Nadler, B. M. Merrill, W. J. Roberts, K. M. Keating, M. J. Lisbin, S. F. Barnett, S. H. Wilson, and K. R. Williams. Interactions of the A1 heterogeneous nuclear ribonucleoprotein and its proteolytic derivative, UP1, with RNA and DNA: Evidence for multiple RNA binding domains and salt-dependent binding mode transitions. *Biochemistry*, 30(11):2968–2976, Mar. 1991. ISSN 0006-2960. doi: 10.1021/bi00225a034. URL <https://doi.org/10.1021/bi00225a034>.
- [226] E. Narr, A. Godt, and G. Jeschke. Selective Measurements of a Nitroxide–Nitroxide Separation of 5 nm and a Nitroxide–Copper Separation of 2.5 nm in a Terpyridine-Based Copper(II) Complex by Pulse EPR Spectroscopy. *Angewandte Chemie International Edition*, 41(20):3907–3910, Oct. 2002. ISSN 1521-3773. doi: 10.1002/1521-3773(20021018)41:

- 20<3907::AID-ANIE3907>3.0.CO;2-T. URL [http://onlinelibrary.wiley.com/doi/10.1002/1521-3773\(20021018\)41:20<3907::AID-ANIE3907>3.0.CO;2-T/abstract](http://onlinelibrary.wiley.com/doi/10.1002/1521-3773(20021018)41:20<3907::AID-ANIE3907>3.0.CO;2-T/abstract).
- [227] Narr Evelyn, Godt Adelheid, and Jeschke Gunnar. Selective Measurements of a Nitroxide–Nitroxide Separation of 5 nm and a Nitroxide–Copper Separation of 2.5 nm in a Terpyridine-Based Copper(II) Complex by Pulse EPR Spectroscopy. *Angewandte Chemie International Edition*, 41(20):3907–3910, Oct. 2002. ISSN 1433-7851. doi: 10.1002/1521-3773(20021018)41:20<3907::AID-ANIE3907>3.0.CO;2-T. URL <https://onlinelibrary.wiley.com/doi/full/10.1002/1521-3773%2820021018%2941%3A20%3C3907%3A%3AAID-ANIE3907%3E3.0.CO%3B2-T>.
- [228] T. J. Nott, E. Petsalaki, P. Farber, D. Jervis, E. Fussner, A. Plochowitz, T. D. Craggs, D. P. Bazett-Jones, T. Pawson, J. D. Forman-Kay, and A. J. Baldwin. Phase transition of a disordered nuage protein generates environmentally responsive membraneless organelles. *Molecular Cell*, 57(5):936–947, Mar. 2015. ISSN 1097-4164. doi: 10.1016/j.molcel.2015.01.013.
- [229] S. Obeid, M. Yulikov, G. Jeschke, and A. Marx. Enzymatic synthesis of multiple spin-labeled DNA. *Angewandte Chemie-International Edition*, 47(36):6782–6785, 2008. ISSN 1433-7851. doi: 10.1002/anie.200802314. WOS:000258835300005.
- [230] H. L. Okunola and A. R. Krainer. Cooperative-Binding and Splicing-Repressive Properties of hnRNP A1. *Molecular and Cellular Biology*, 29(20):5620–5631, Oct. 2009. ISSN 0270-7306, 1098-5549. doi: 10.1128/MCB.01678-08. URL <http://mcb.asm.org/content/29/20/5620>.
- [231] R. Owenius, M. Engström, M. Lindgren, and M. Huber. Influence of Solvent Polarity and Hydrogen Bonding on the EPR Parameters of a Nitroxide Spin Label Studied by 9-GHz and 95-GHz EPR Spectroscopy and DFT Calculations. *The Journal of Physical Chemistry A*, 105(49):10967–10977, Dec. 2001. ISSN 1089-5639. doi: 10.1021/jp0116914. URL <http://dx.doi.org/10.1021/jp0116914>.
- [232] G. E. Pake. Nuclear Resonance Absorption in Hydrated Crystals: Fine Structure of the Proton Line. *The Journal of Chemical Physics*, 16(4):327–336, Apr. 1948. ISSN 0021-9606. doi: 10.1063/1.1746878. URL <https://aip.scitation.org/doi/10.1063/1.1746878>.
- [233] J. T. Paletta, M. Pink, B. Foley, S. Rajca, and A. Rajca. Synthesis and Reduction Kinetics of Sterically Shielded Pyrrolidine Nitroxides. *Organic Letters*, 14(20):5322–5325, Oct. 2012. ISSN 1523-7060. doi: 10.1021/ol302506f. URL <https://doi.org/10.1021/ol302506f>.
- [234] E. F. Pettersen, T. D. Goddard, C. C. Huang, G. S. Couch, D. M. Greenblatt, E. C. Meng, and T. E. Ferrin. Ucsf chimera—a visualization system for exploratory research and analysis. *Journal of Computational Chemistry*, 25(13):1605–1612, 2004. doi: 10.1002/jcc.20084. URL <https://onlinelibrary.wiley.com/doi/abs/10.1002/jcc.20084>.
- [235] Y. Polyhach and G. Jeschke. Prediction of favourable sites for spin labelling of proteins. *Journal of Spectroscopy*, 24(6):651–659, 2010. ISSN 0712-4813. doi: 10.3233/SPE-2010-0490. URL <http://www.hindawi.com/journals/jspec/2010/706498/abs/>.

- [236] Y. Polyhach, A. Godt, C. Bauer, and G. Jeschke. Spin pair geometry revealed by high-field DEER in the presence of conformational distributions. *Journal of Magnetic Resonance*, 185(1):118–129, Mar. 2007. ISSN 1090-7807. doi: 10.1016/j.jmr.2006.11.012. URL <http://www.sciencedirect.com/science/article/pii/S1090780706003934>.
- [237] Y. Polyhach, E. Bordignon, and G. Jeschke. Rotamer libraries of spin labelled cysteines for protein studies. *Physical Chemistry Chemical Physics*, 13(6):2356–2366, Jan. 2011. ISSN 1463-9084. doi: 10.1039/C0CP01865A. URL <http://pubs.rsc.org/en/content/articlelanding/2011/cp/c0cp01865a>.
- [238] Y. Polyhach, E. Bordignon, R. Tschaggelar, S. Gandra, A. Godt, and G. Jeschke. High sensitivity and versatility of the DEER experiment on nitroxide radical pairs at Q-band frequencies. *Physical Chemistry Chemical Physics*, 14(30):10762–10773, July 2012. ISSN 1463-9084. doi: 10.1039/C2CP41520H. URL <http://pubs.rsc.org/en/content/articlelanding/2012/cp/c2cp41520h>.
- [239] M. Polymenidou. The RNA face of phase separation. *Science*, 360(6391):859–860, May 2018. ISSN 0036-8075, 1095-9203. doi: 10.1126/science.aat8028. URL <https://science.sciencemag.org/content/360/6391/859>.
- [240] S. Pribitzer, M. Sajid, M. Hülsmann, A. Godt, and G. Jeschke. Pulsed triple electron resonance (TRIER) for dipolar correlation spectroscopy. *Journal of Magnetic Resonance*, 282(Supplement C):119–128, Sept. 2017. ISSN 1090-7807. doi: 10.1016/j.jmr.2017.07.012. URL <http://www.sciencedirect.com/science/article/pii/S1090780717301970>.
- [241] S. Pribitzer, L. Fábregas Ibáñez, C. Gmeiner, I. Ritsch, D. Klose, M. Sajid, M. Hülsmann, A. Godt, and G. Jeschke. Two-Dimensional Distance Correlation Maps from Pulsed Triple Electron Resonance (TRIER) on Proteins with Three Paramagnetic Centers. *Applied Magnetic Resonance*, 49(11):1253–1279, Nov. 2018. ISSN 1613-7507. doi: 10.1007/s00723-018-1051-9. URL <https://doi.org/10.1007/s00723-018-1051-9>.
- [242] T. Prisner, M. Rohrer, and a. F. MacMillan. PULSED EPR SPECTROSCOPY: Biological Applications. *Annual Review of Physical Chemistry*, 52(1):279–313, 2001. doi: 10.1146/annurev.physchem.52.1.279. URL <http://dx.doi.org/10.1146/annurev.physchem.52.1.279>.
- [243] M. Qi, A. Groß, G. Jeschke, A. Godt, and M. Drescher. Gd(III)-PyMTA Label Is Suitable for In-Cell EPR. *Journal of the American Chemical Society*, 136(43):15366–15378, Oct. 2014. ISSN 0002-7863. doi: 10.1021/ja508274d. URL <https://doi.org/10.1021/ja508274d>.
- [244] M. Qi, M. Hülsmann, and A. Godt. Synthesis and Hydrolysis of 4-Chloro-PyMTA and 4-Iodo-PyMTA Esters and Their Oxidative Degradation with Cu(I/II) and Oxygen. *Synthesis*, 48(21):3773–3784, Nov. 2016. ISSN 0039-7881, 1437-210X. doi: 10.1055/s-0035-1561660. URL <http://www.thieme-connect.de/DOI/DOI?10.1055/s-0035-1561660>.

- [245] S. Rauscher, V. Gapsys, M. J. Gajda, M. Zweckstetter, B. L. de Groot, and H. Grubmüller. Structural Ensembles of Intrinsically Disordered Proteins Depend Strongly on Force Field: A Comparison to Experiment. *Journal of Chemical Theory and Computation*, 11(11):5513–5524, Nov. 2015. ISSN 1549-9618. doi: 10.1021/acs.jctc.5b00736. URL <https://doi.org/10.1021/acs.jctc.5b00736>.
- [246] S. Razzaghi, E. K. Brooks, E. Bordignon, W. L. Hubbell, M. Yulikov, and G. Jeschke. EPR Relaxation-Enhancement-Based Distance Measurements on Orthogonally Spin-Labeled T4-Lysozyme. *Chembiochem*, 14(14):1883–1890, Sept. 2013. ISSN 1439-4227. doi: 10.1002/cbic.201300165. WOS:000325851800025.
- [247] S. Razzaghi, M. Qi, A. I. Nalepa, A. Godt, G. Jeschke, A. Savitsky, and M. Yulikov. RIDME Spectroscopy with Gd(III) Centers. *The journal of physical chemistry letters*, 5(22):3970–3975, Nov. 2014. ISSN 1948-7185 1948-7185. doi: 10.1021/jz502129t. bibtex: Razzaghi2014.
- [248] S. Rein, P. Lewe, S. L. Andrade, S. Kacprzak, and S. Weber. Global analysis of complex PEL-DOR time traces. *Journal of Magnetic Resonance*, 295:17–26, Oct. 2018. ISSN 1090-7807. doi: 10.1016/j.jmr.2018.07.015. URL <http://www.sciencedirect.com/science/article/pii/S1090780718301927>.
- [249] S. S. Ribeiro, N. Samanta, S. Ebbinghaus, and J. C. Marcos. The synergic effect of water and biomolecules in intracellular phase separation. *Nature Reviews Chemistry*, 3(9):552–561, Sept. 2019. ISSN 2397-3358. doi: 10.1038/s41570-019-0120-4. URL <https://www.nature.com/articles/s41570-019-0120-4>.
- [250] I. Ritsch, H. Hintz, G. Jeschke, A. Godt, and M. Yulikov. Improving the accuracy of Cu(ii)-nitroxide RIDME in the presence of orientation correlation in water-soluble Cu(ii)-nitroxide rulers. *Physical Chemistry Chemical Physics*, 2019. doi: 10.1039/C8CP06573J. URL <https://pubs.rsc.org/en/content/articlelanding/2019/cp/c8cp06573j>.
- [251] I. Ritsch, D. Klose, H. Hintz, A. Godt, G. Jeschke, and M. Yulikov. Pulsed EPR Methods to Study Biomolecular Interactions. *Chimia*, 73(4):268–276, Apr. 2019. ISSN 0009-4293. doi: 10.3929/ethz-b-000340572. URL <https://www.research-collection.ethz.ch/handle/20.500.11850/340572>.
- [252] P. Roser, M. J. Schmidt, M. Drescher, and D. Summerer. Site-directed spin labeling of proteins for distance measurements in vitro and in cells. *Organic & Biomolecular Chemistry*, 14(24):5468–5476, 2016. ISSN 1477-0520. doi: 10.1039/c6ob00473c. WOS:000378933400010.
- [253] K. M. Salikhov and I. T. Khairuzhdinov. Four-Pulse ELDOR Theory of the Spin $\frac{1}{2}$ Label Pairs Extended to Overlapping EPR Spectra and to Overlapping Pump and Observer Excitation Bands. *Applied Magnetic Resonance*, 46(1):67–83, Jan. 2015. ISSN 0937-9347, 1613-7507. doi: 10.1007/s00723-014-0609-4. URL <https://link.springer.com/article/10.1007/s00723-014-0609-4>.

- [254] L. Salmon, G. Nodet, V. Ozenne, G. Yin, M. R. Jensen, M. Zweckstetter, and M. Blackledge. NMR Characterization of Long-Range Order in Intrinsically Disordered Proteins. *Journal of the American Chemical Society*, 132(24):8407–8418, June 2010. ISSN 0002-7863. doi: 10.1021/ja101645g. URL <https://doi.org/10.1021/ja101645g>.
- [255] J. Sarver, K. I. Silva, and S. Saxena. Measuring Cu²⁺-Nitroxide Distances Using Double Electron–Electron Resonance and Saturation Recovery. *Applied Magnetic Resonance*, 44(5):583–594, May 2013. ISSN 0937-9347, 1613-7507. doi: 10.1007/s00723-012-0422-x. URL <https://link.springer.com/article/10.1007/s00723-012-0422-x>.
- [256] S. Sasmal, J. Lincoff, and T. Head-Gordon. Effect of a Paramagnetic Spin Label on the Intrinsically Disordered Peptide Ensemble of Amyloid-beta. *Biophysical Journal*, 113(5):1002–1011, Sept. 2017. ISSN 0006-3495. doi: 10.1016/j.bpj.2017.06.067. URL <http://www.sciencedirect.com/science/article/pii/S0006349517307580>.
- [257] A. Savitsky, A. A. Dubinskii, M. Flores, W. Lubitz, and K. Moebius. Orientation-resolving pulsed electron dipolar high-field EPR spectroscopy on disordered solids: I. Structure of spin-correlated radical pairs in bacterial photosynthetic reaction centers. *Journal of Physical Chemistry B*, 111(22):6245–6262, June 2007. ISSN 1520-6106. doi: 10.1021/jp070016c. WOS:000246842300024.
- [258] A. Savitsky, J. Niklas, J. H. Golbeck, K. Mobius, and W. Lubitz. Orientation resolving dipolar high-field EPR spectroscopy on disordered solids: II. Structure of spin-correlated radical pairs in photosystem I. *The journal of physical chemistry. B*, 117(38):11184–11199, Sept. 2013. ISSN 1520-5207 1520-5207. doi: 10.1021/jp401573z. bibtex: Savitsky2013.
- [259] O. Schiemann, N. Piton, Y. G. Mu, G. Stock, J. W. Engels, and T. F. Prisner. A PELDOR-based nanometer distance ruler for oligonucleotides. *Journal of the American Chemical Society*, 126(18):5722–5729, May 2004. ISSN 0002-7863. doi: 10.1021/ja0393877. WOS:000221268400022.
- [260] O. Schiemann, P. Cekan, D. Margraf, T. F. Prisner, and S. T. Sigurdsson. Relative Orientation of Rigid Nitroxides by PELDOR: Beyond Distance Measurements in Nucleic Acids. *Angewandte Chemie International Edition*, 48(18):3292–3295, Apr. 2009. ISSN 1521-3773. doi: 10.1002/anie.200805152. URL <https://onlinelibrary.wiley.com/doi/abs/10.1002/anie.200805152>.
- [261] D. J. Schneider and J. H. Freed. Calculating Slow Motional Magnetic Resonance Spectra. In L. J. Berliner and J. Reuben, editors, *Spin Labeling: Theory and Applications*, Biological Magnetic Resonance, pages 1–76. Springer US, Boston, MA, 1989. ISBN 978-1-4613-0743-3. doi: 10.1007/978-1-4613-0743-3_1. URL https://doi.org/10.1007/978-1-4613-0743-3_1.
- [262] P. Schöps, P. E. Spindler, A. Marko, and T. F. Prisner. Broadband spin echoes and broadband SIFTER in EPR. *Journal of Magnetic Resonance*, 250:55–62, Jan. 2015. ISSN 1090-7807.

- doi: 10.1016/j.jmr.2014.10.017. URL <http://www.sciencedirect.com/science/article/pii/S1090780714002973>.
- [263] S. J. Schroeder. Stack Locally and Act Globally: A Few Nucleotides Make All the Difference in Enterovirus 71 IRES Binding hnRNAP A1 and Infectious Phenotypes. *Journal of Molecular Biology*, 429(19):2859–2862, Sept. 2017. ISSN 0022-2836. doi: 10.1016/j.jmb.2017.08.001. URL <http://www.sciencedirect.com/science/article/pii/S0022283617303923>.
- [264] B. S. Schuster, E. H. Reed, R. Parthasarathy, C. N. Jahnke, R. M. Caldwell, J. G. Bermudez, H. Ramage, M. C. Good, and D. A. Hammer. Controllable protein phase separation and modular recruitment to form responsive membraneless organelles. *Nature Communications*, 9(1):1–12, July 2018. ISSN 2041-1723. doi: 10.1038/s41467-018-05403-1. URL <https://www.nature.com/articles/s41467-018-05403-1>.
- [265] A. Schweiger. Creation and detection of coherence and polarization in pulsed EPR. *Journal of the Chemical Society, Faraday Transactions*, 91(2):177–190, 1995. doi: 10.1039/FT9959100177. URL <https://pubs.rsc.org/en/content/articlelanding/1995/ft/ft9959100177>.
- [266] A. Schweiger and G. Jeschke. *Principles of Pulse Electron Paramagnetic Resonance*. Oxford University Press, 2001. ISBN 978-0-19-850634-8. URL <https://books.google.ch/books?id=AenpngEACAAJ>. bibtex: schweiger2001principles bibtex[lccn=2001034062].
- [267] Shelke Sandip A. and Sigurdsson Snorri Th. Site-Directed Spin Labelling of Nucleic Acids. *European Journal of Organic Chemistry*, 2012(12):2291–2301, Jan. 2012. ISSN 1434-193X. doi: 10.1002/ejoc.201101434. URL <https://onlinelibrary.wiley.com/doi/full/10.1002/ejoc.201101434>.
- [268] G. Y. Shevelev, O. A. Krumkacheva, A. A. Lomzov, A. A. Kuzhelev, D. V. Trukhin, O. Y. Rogozhnikova, V. M. Tormyshev, D. V. Pyshnyi, M. V. Fedin, and E. G. Bagryanskaya. Triarylmethyl Labels: Toward Improving the Accuracy of EPR Nanoscale Distance Measurements in DNAs. *Journal of Physical Chemistry B*, 119(43):13641–13648, Oct. 2015. ISSN 1520-6106. doi: 10.1021/acs.jpbc.5b03026. WOS:000363994000019.
- [269] B.-k. Shin and S. Saxena. Direct Evidence That All Three Histidine Residues Coordinate to Cu(II) in Amyloid beta1 16. *Biochemistry*, 47(35):9117–9123, Sept. 2008. ISSN 0006-2960. doi: 10.1021/bi801014x. URL <https://doi.org/10.1021/bi801014x>.
- [270] B.-k. Shin and S. Saxena. Insight into Potential Cu(II)-Binding Motifs in the Four Pseudorepeats of Tau Protein. *The Journal of Physical Chemistry B*, 115(50):15067–15078, Dec. 2011. ISSN 1520-6106. doi: 10.1021/jp204410h. URL <https://doi.org/10.1021/jp204410h>.
- [271] Y. Shin, J. Berry, N. Pannucci, M. P. Haataja, J. E. Toettcher, and C. P. Brangwynne. Spatiotemporal Control of Intracellular Phase Transitions Using Light-Activated optoDroplets. *Cell*, 168(1–2):159–171.e14, Jan. 2017. ISSN 0092-8674. doi: 10.1016/j.cell.2016.11.054. URL <http://www.sciencedirect.com/science/article/pii/S009286741631666X>.

- [272] V. Singh, M. Azarkh, T. E. Exner, J. S. Hartig, and M. Drescher. Human Telomeric Quadruplex Conformations Studied by Pulsed EPR. *Angewandte Chemie-International Edition*, 48(51):9728–9730, 2009. ISSN 1433-7851. doi: 10.1002/anie.200902146. WOS:000273093700028.
- [273] H. Siomi and G. Dreyfuss. A nuclear localization domain in the hnRNP A1 protein. *The Journal of Cell Biology*, 129(3):551–560, May 1995. ISSN 0021-9525, 1540-8140. doi: 10.1083/jcb.129.3.551. URL <http://jcb.rupress.org/content/129/3/551>.
- [274] J. Soetbeer, M. Hülsmann, A. Godt, Y. Polyhach, and G. Jeschke. Dynamical decoupling of nitroxides in o -terphenyl: a study of temperature, deuteration and concentration effects. *Physical Chemistry Chemical Physics*, 20(3):1615–1628, 2018. doi: 10.1039/C7CP07074H. URL <http://pubs.rsc.org/en/Content/ArticleLanding/2018/CP/C7CP07074H>.
- [275] I. Solomon. Relaxation Processes in a System of Two Spins. *Physical Review*, 99(2):559–565, July 1955. doi: 10.1103/PhysRev.99.559. URL <https://link.aps.org/doi/10.1103/PhysRev.99.559>.
- [276] P. E. Spindler, Y. Zhang, B. Endeward, N. Gershernzon, T. E. Skinner, S. J. Glaser, and T. F. Prisner. Shaped optimal control pulses for increased excitation bandwidth in EPR. *Journal of Magnetic Resonance*, 218:49–58, May 2012. ISSN 1090-7807. doi: 10.1016/j.jmr.2012.02.013. URL <http://www.sciencedirect.com/science/article/pii/S1090780712000705>.
- [277] P. E. Spindler, S. J. Glaser, T. E. Skinner, and T. F. Prisner. Broadband Inversion PELDOR Spectroscopy with Partially Adiabatic Shaped Pulses. *Angewandte Chemie-International Edition*, 52(12):3425–3429, 2013. ISSN 1433-7851. doi: 10.1002/anie.201207777. WOS:000316342900022.
- [278] Spindler Philipp E., Schöps Philipp, Bowen Alice M., Endeward Burkhard, and Prisner Thomas F. Shaped Pulses in EPR. *eMagRes*, Dec. 2016. ISSN 9780470034590. doi: 10.1002/9780470034590.emrstm1520. URL <https://onlinelibrary.wiley.com/doi/full/10.1002/9780470034590.emrstm1520>.
- [279] n. Stoll, n. Jeschke, n. Willer, and n. Schweiger. Nutation-Frequency Correlated EPR Spectroscopy: The PEANUT Experiment. *Journal of Magnetic Resonance (San Diego, Calif.: 1997)*, 130(1):86–96, Jan. 1998. ISSN 1096-0856.
- [280] S. Stoll and A. Schweiger. EasySpin, a comprehensive software package for spectral simulation and analysis in EPR. *Journal of Magnetic Resonance*, 178(1):42–55, Jan. 2006. ISSN 1090-7807. doi: 10.1016/j.jmr.2005.08.013. URL <http://www.sciencedirect.com/science/article/pii/S1090780705002892>.
- [281] J. W. Stoner, D. Szymanski, S. S. Eaton, R. W. Quine, G. A. Rinard, and G. R. Eaton. Direct-detected rapid-scan EPR at 250 MHz. *Journal of magnetic resonance (San Diego, Calif. : 1997)*, 170(1):127–135, Sept. 2004. ISSN 1090-7807. doi: 10.1016/j.jmr.2004.06.008. URL <http://europepmc.org/abstract/med/15324766>.

- [282] C. E. Tait and S. Stoll. Coherent pump pulses in Double Electron Electron Resonance spectroscopy. *Phys. Chem. Chem. Phys.*, 18(27):18470–18485, 2016. ISSN 1463-9076, 1463-9084. doi: 10.1039/C6CP03555H. URL <http://xlink.rsc.org/?DOI=C6CP03555H>.
- [283] C. Tang, J. Iwahara, and G. M. Clore. Visualization of transient encounter complexes in protein-protein association. *Nature; London*, 444(7117):383–6, Nov. 2006. ISSN 00280836. doi: <http://dx.doi.org/10.1038/nature05201>. URL <https://search.proquest.com/docview/204454616/abstract/9626D9D30CD64FEAPQ/1>.
- [284] K. Teilum, B. B. Kragelund, and F. M. Poulsen. Transient Structure Formation in Unfolded Acyl-coenzyme A-binding Protein Observed by Site-directed Spin Labelling. *Journal of Molecular Biology*, 324(2):349–357, Nov. 2002. ISSN 0022-2836. doi: 10.1016/S0022-2836(02)01039-2. URL <http://www.sciencedirect.com/science/article/pii/S0022283602010392>.
- [285] M. Teucher and E. Bordignon. Improved signal fidelity in 4-pulse DEER with Gaussian pulses. *Journal of Magnetic Resonance*, 296:103–111, Nov. 2018. ISSN 1090-7807. doi: 10.1016/j.jmr.2018.09.003. URL <http://www.sciencedirect.com/science/article/pii/S1090780718302283>.
- [286] P. Thandapani, T. O’Connor, T. Bailey, and S. Richard. Defining the RGG/RG Motif. *Molecular Cell*, 50(5):613–623, 2013. doi: 10.1016/j.molcel.2013.05.021.
- [287] C. R. Timmel and J. R. Harmer. *Structural Information from Spin-Labels and Intrinsic Paramagnetic Centres in the Biosciences*. Springer, Apr. 2014. ISBN 978-3-642-39125-5. Google-Books-ID: CF25BQAAQBAJ.
- [288] B. V. Treeck, D. S. W. Protter, T. Matheny, A. Khong, C. D. Link, and R. Parker. RNA self-assembly contributes to stress granule formation and defining the stress granule transcriptome. *Proceedings of the National Academy of Sciences*, 115(11):2734–2739, Mar. 2018. ISSN 0027-8424, 1091-6490. doi: 10.1073/pnas.1800038115. URL <https://www.pnas.org/content/115/11/2734>.
- [289] R. Tschaggelar, B. Kasumaj, M. G. Santangelo, J. Forrer, P. Leger, H. Dube, F. Diederich, J. Harmer, R. Schuhmann, I. García-Rubio, and G. Jeschke. Cryogenic 35ghz pulse ENDOR probehead accommodating large sample sizes: Performance and applications. *Journal of Magnetic Resonance (San Diego, Calif.: 1997)*, 200(1):81–87, Sept. 2009. ISSN 1096-0856. doi: 10.1016/j.jmr.2009.06.007.
- [290] R. Tschaggelar, F. D. Breitgoff, O. Oberhänsli, M. Qi, A. Godt, and G. Jeschke. High-Bandwidth Q-Band EPR Resonators. *Applied Magnetic Resonance*, 48(11-12):1273–1300, Dec. 2017. ISSN 0937-9347, 1613-7507. doi: 10.1007/s00723-017-0956-z. URL <https://link.springer.com/article/10.1007/s00723-017-0956-z>.
- [291] G. S. Uhrig. Keeping a Quantum Bit Alive by Optimized π -Pulse Sequences. *Physical Review Letters*, 98(10):100504, Mar. 2007. doi: 10.1103/PhysRevLett.98.100504. URL <http://link.aps.org/doi/10.1103/PhysRevLett.98.100504>.

- [292] I. M. C. van Amsterdam, M. Ubbink, G. W. Canters, and M. Huber. Measurement of a Cu-Cu Distance of 26 angstrom by a Pulsed EPR Method. *Angewandte Chemie International Edition*, 42(1):62–64, Jan. 2003. ISSN 1521-3773. doi: 10.1002/anie.200390053. URL <http://onlinelibrary.wiley.com/doi/10.1002/anie.200390053/abstract>.
- [293] R. Viguier, G. Serratrice, A. Dupraz, and C. Dupuy. New Polypodal Polycarboxylic Ligands Complexation of Rare Earth Ions in Aqueous Solution. *European Journal of Inorganic Chemistry*, 2001(7):1789–1795. ISSN 1099-0682. doi: 10.1002/1099-0682(200107)2001:7<1789::AID-EJIC1789>3.0.CO;2-C. URL <https://onlinelibrary.wiley.com/doi/abs/10.1002/1099-0682%28200107%292001%3A7%3C1789%3A%3AAID-EJIC1789%3E3.0.CO%3B2-C>.
- [294] J. Vitali. Correlated alternative side chain conformations in the RNA-recognition motif of heterogeneous nuclear ribonucleoprotein A1. *Nucleic Acids Research*, 30(7):1531–1538, Apr. 2002. ISSN 13624962. doi: 10.1093/nar/30.7.1531. URL <https://academic.oup.com/nar/article-lookup/doi/10.1093/nar/30.7.1531>.
- [295] A. N. Volkov, J. A. R. Worrall, E. Holtzmann, and M. Ubbink. Solution structure and dynamics of the complex between cytochrome c and cytochrome c peroxidase determined by paramagnetic NMR. *Proceedings of the National Academy of Sciences*, 103(50):18945–18950, Dec. 2006. ISSN 0027-8424, 1091-6490. doi: 10.1073/pnas.0603551103. URL <https://www.pnas.org/content/103/50/18945>.
- [296] A. N. Volkov, M. Ubbink, and N. A. J. van Nuland. Mapping the encounter state of a transient protein complex by PRE NMR spectroscopy. *Journal of Biomolecular Nmr*, 48(4):225–236, Dec. 2010. ISSN 0925-2738. doi: 10.1007/s10858-010-9452-6. URL <https://www.ncbi.nlm.nih.gov/pmc/articles/PMC3235994/>.
- [297] J. Voss, L. Salwiński, H. R. Kaback, and W. L. Hubbell. A method for distance determination in proteins using a designed metal ion binding site and site-directed spin labeling: evaluation with T4 lysozyme. *Proceedings of the National Academy of Sciences*, 92(26):12295–12299, Dec. 1995. ISSN 0027-8424, 1091-6490. URL <http://www.pnas.org/content/92/26/12295>.
- [298] K. J. Waldron, J. C. Rutherford, D. Ford, and N. J. Robinson. Metalloproteins and metal sensing, Aug. 2009. URL <https://www.nature.com/articles/nature08300>.
- [299] J. Wang, J.-M. Choi, A. S. Holehouse, H. O. Lee, X. Zhang, M. Jahnel, S. Maharana, R. Lemaitre, A. Pozniakovsky, D. Drechsel, I. Poser, R. V. Pappu, S. Alberti, and A. A. Hyman. A Molecular Grammar Governing the Driving Forces for Phase Separation of Prion-like RNA Binding Proteins. *Cell*, 174(3):688–699.e16, July 2018. ISSN 0092-8674. doi: 10.1016/j.cell.2018.06.006. URL <http://www.sciencedirect.com/science/article/pii/S0092867418307311>.
- [300] Y. Wang and D. J. Patel. Solution structure of the human telomeric repeat d[AG3(T2ag3)3]G-tetraplex. *Structure*, 1(4):263–282, Dec. 1993. ISSN 0969-2126. doi: 10.1016/0969-2126(93)90015-9. URL <http://www.sciencedirect.com/science/article/pii/0969212693900159>.

- [301] Y. Wang, J. T. Paletta, K. Berg, E. Reinhart, S. Rajca, and A. Rajca. Synthesis of Unnatural Amino Acids Functionalized with Sterically Shielded Pyrroline Nitroxides. *Organic Letters*, 16(20):5298–5300, Oct. 2014. ISSN 1523-7060. doi: 10.1021/ol502449r. URL <https://doi.org/10.1021/ol502449r>.
- [302] S. C. Weber and C. P. Brangwynne. Getting RNA and Protein in Phase. *Cell*, 149(6):1188–1191, June 2012. ISSN 0092-8674. doi: 10.1016/j.cell.2012.05.022. URL <https://www.sciencedirect.com/science/article/pii/S0092867412006344>.
- [303] F. Werner and R. O. Weinzierl. A Recombinant RNA Polymerase II-like Enzyme Capable of Promoter-Specific Transcription. *Molecular Cell*, 10(3):635–646, 2002. ISSN 1097-2765. doi: [https://doi.org/10.1016/S1097-2765\(02\)00629-9](https://doi.org/10.1016/S1097-2765(02)00629-9). URL <http://www.sciencedirect.com/science/article/pii/S1097276502006299>. bibtex: WERNER2002635.
- [304] K. R. Williams, K. L. Stone, M. B. LoPresti, B. M. Merrill, and S. R. Planck. Amino acid sequence of the UP1 calf thymus helix-destabilizing protein and its homology to an analogous protein from mouse myeloma. *Proceedings of the National Academy of Sciences*, 82(17):5666–5670, Sept. 1985. ISSN 0027-8424, 1091-6490. doi: 10.1073/pnas.82.17.5666. URL <https://www.pnas.org/content/82/17/5666>.
- [305] S. G. Worswick, J. A. Spencer, G. Jeschke, and I. Kuprov. Deep neural network processing of DEER data. *Science Advances*, 4(8):eaat5218, Aug. 2018. ISSN 2375-2548. doi: 10.1126/sciadv.aat5218. URL <http://advances.sciencemag.org/content/4/8/eaat5218>.
- [306] Z. Wu, A. Feintuch, A. Collauto, L. A. Adams, L. Aurelio, B. Graham, G. Otting, and D. Goldfarb. Selective Distance Measurements Using Triple Spin Labeling with Gd³⁺, Mn²⁺, and a Nitroxide. *The Journal of Physical Chemistry Letters*, 8(21):5277–5282, Nov. 2017. ISSN 1948-7185. doi: 10.1021/acs.jpcllett.7b01739. URL <https://doi.org/10.1021/acs.jpcllett.7b01739>.
- [307] R.-M. Xu, L. Jokhan, X. Cheng, A. Mayeda, and A. R. Krainer. Crystal structure of human UP1, the domain of hnRNP A1 that contains two RNA-recognition motifs. *Structure*, 5(4):559–570, Apr. 1997. ISSN 0969-2126. doi: 10.1016/S0969-2126(97)00211-6. URL <http://www.sciencedirect.com/science/article/pii/S0969212697002116>.
- [308] Y. Yang, F. Yang, Y.-J. Gong, T. Bahrenberg, A. Feintuch, X.-C. Su, and D. Goldfarb. High Sensitivity In-Cell EPR Distance Measurements on Proteins using an Optimized Gd(III) Spin Label. *The Journal of Physical Chemistry Letters*, 9(20):6119–6123, Oct. 2018. ISSN 1948-7185. doi: 10.1021/acs.jpcllett.8b02663. URL <https://doi.org/10.1021/acs.jpcllett.8b02663>.
- [309] Z. Yang, J. Becker, and S. Saxena. On Cu(II)–Cu(II) distance measurements using pulsed electron double resonance. *Journal of Magnetic Resonance*, 188(2):337–343, Oct. 2007. ISSN 1090-7807. doi: 10.1016/j.jmr.2007.08.006. URL <http://www.sciencedirect.com/science/article/pii/S1090780707002406>.

- [310] Z. Yang, M. Ji, and S. Saxena. Practical Aspects of Copper Ion-Based Double Electron Electron Resonance Distance Measurements. *Applied Magnetic Resonance*, 39(4):487–500, Dec. 2010. ISSN 0937-9347, 1613-7507. doi: 10.1007/s00723-010-0181-5. URL <https://link.springer.com/article/10.1007/s00723-010-0181-5>.
- [311] Z. Yang, Y. Liu, P. Borbat, J. Zweier, J. Freed, and W. Hubbell. Pulsed ESR dipolar spectroscopy for distance measurements in immobilized spin labeled proteins in liquid solution. *Journal of the American Chemical Society*, 134(24):9950–9952, 2012. doi: 10.1021/ja303791p.
- [312] Z. Yang, M. Ji, T. F. Cunningham, and S. Saxena. Chapter Seventeen - Cu²⁺ as an ESR Probe of Protein Structure and Function. In P. Z. Qin and K. Warncke, editors, *Methods in Enzymology*, volume 563 of *Electron Paramagnetic Resonance Investigations of Biological Systems by Using Spin Labels, Spin Probes, and Intrinsic Metal Ions, Part A*, pages 459–481. Academic Press, Jan. 2015. doi: 10.1016/bs.mie.2015.05.026. URL <http://www.sciencedirect.com/science/article/pii/S0076687915003444>.
- [313] M. Yulikov. Chapter 1: Spectroscopically orthogonal spin labels and distance measurements in biomolecules. In *Electron Paramagnetic Resonance*, pages 1–31. Sept. 2014. doi: 10.1039/9781782620280-00001. URL <http://pubs.rsc.org/en/content/chapter/bk9781849739818-00001/978-1-84973-981-8>.
- [314] M. Yulikov, P. Lueders, M. F. Warsi, V. Chechik, and G. Jeschke. Distance measurements in Au nanoparticles functionalized with nitroxide radicals and Gd³⁺-DTPA chelate complexes. *Physical Chemistry Chemical Physics*, 14(30):10732–10746, July 2012. ISSN 1463-9084. doi: 10.1039/C2CP40282C. URL <https://pubs.rsc.org/en/content/articlelanding/2012/cp/c2cp40282c>.
- [315] R. B. Zaripov, V. I. Dzhabarov, A. A. Knyazev, Y. G. Galyametdinov, and L. V. Kulik. Use of Additional Fast-Relaxing Paramagnetic Species for Improvement of RIDME Performance. *Applied Magnetic Resonance*, 40(1):11–19, Feb. 2011. ISSN 0937-9347, 1613-7507. doi: 10.1007/s00723-010-0170-8. URL <https://link.springer.com/article/10.1007/s00723-010-0170-8>.

List of publications

- 2019 S. Bleicken, T. E. Assafa, H. Zhang, C. Elsner, I. Ritsch, M. Pink, G. Jeschke, A. Rajca, E. Bordignon, 'gem-Diethyl Pyrroline Nitroxide Spin Labels: Synthesis, EPR Characterization, Rotamer Libraries and Biocompatibility', *Chemistry Open*, **8**, 2091, 1057-1065
- 2019 I. Ritsch, D.Klose, H.Hintz, A. Godt, G. Jeschke, M. Yulikov, 'Pulsed EPR Methods to Study Biomolecular Interactions', *CHIMIA*, **73**, 2019, 268-276
- 2019 I. Ritsch, H.Hintz, G. Jeschke, A. Godt, M. Yulikov, 'Improving the accuracy of Cu(II)-nitroxide RIDME in the presence of orientation correlation in water-soluble Cu(II)-nitroxide rulers', *Phys. Chem. Chem. Phys.*, **21**, 2019, 9810-9830
- 2019 K. Keller, M. Qi, C. Gmeiner, I. Ritsch, A. Godt, G. Jeschke, A. Savitsky, M. Yulikov, 'Intermolecular Background Decay in RIDME Experiments', *Phys. Chem. Chem. Phys.*, **21**, 2019, 8228-8245
- 2018 S. Pribitzer, L. Fábregas Ibáñez, C. Gmeiner, I. Ritsch, D. Klose, M. Sajid, M. Hülsmann, A. Godt, G. Jeschke, 'Two-Dimensional Distance Correlation Maps from Pulsed Triple Electron Resonance (TRIER) on Proteins with Three Paramagnetic Centers', *Appl. Magn. Reson.*, **49**, 2018, 1253.
- 2015 G. David, K. Esat, I. Ritsch, R. Signorell, 'Ultraviolet broadband light scattering for optically-trapped submicron-sized aerosol particles', *Phys. Chem. Chem. Phys.*, **18**, 2016, 5477

Manuscripts in preparation

K. Keller, I. Ritsch, H. Hintz, M. Hülsman, M. Qi, F. Breitgoff, D. Klose, Y. Polyhach, M. Yulikov, A. Godt, and G. Jeschke, "Accessing Distributions of Exchange and Dipolar Couplings in Stiff Molecular Rulers with Cu(II) centres"

I. Ritsch, E. Lehmann, M. Yulikov, F. Allain, and Gunnar Jeschke, "Interplay of RNA binding and LLPS of hnRNPA1"

Acknowledgements

I thank all the people who throughout my time in Zurich have brought *transient order* into the *disordered endeavours* that are *intrinsic to research*. Countless *interactions* have been an invaluable guide for me throughout, and I am thankful for the support!

- Thank you, Gunnar, for the opportunity to work on immensely versatile projects at the interface of EPR spectroscopy and (un-)structural biology. The diversity and depth of expertise fostered in the group, and your palpable enthusiasm for finding elegant solutions to scientific problems are an inspiration.
- I thank Frédéric Allain, for sharing his laboratory space and resources, for evaluation of this thesis, and last but not least, for the unique access to the expertise concerning RNA-protein interactions developed in his group.
- I am very grateful for the support of my co-supervisor Maxim Yulikov, for detailed feedback on this thesis, and for introducing me to the wonderful diversity of the physics of distance measurements by EPR spectroscopy.
- Thank you very much to Beat Meier to accepting to be a co-examiner of this dissertation, and the perspective of disordered systems from a solid state viewpoint.

Words cannot describe how grateful I am to my close and extended family. I have had the unique fortune of having received the best support in life as well as science from my parents, Monika and Helmut, and I am forever thankful for the never-ending support and friendship of my sister, Silvia. I could not imagine a better, more loving, supportive environment than what you have provided throughout my life.

I thank all the wonderful researchers and staff who I have worked with inside and outside of ETH Zurich for the fruitful collaborations. Thank you very much ...

... Elisabeth Lehmann, who introduced me to the perks and pitfalls of working with a partially disordered protein, and for the NMR and wet lab expertise.

... for the wonderful support from the present and former EPR group. Thank you Andrin, Stephan, Christoph, Katharina, Frauke, Luis, Nino, Laura, Agathe, Anton, Zhenia, Janne and Daniel (and honorary member Anahit) for inspiring discussions, critical progress report debates, a wonderful work atmosphere and for your support also in less happy times. Unfortunately there is no space here to divulge in all the wonderful memories I share with you, but rest assured, they are very fond memories, indeed!

... Kristina Comiotto, for her artistic insight, and without whose human support we would all be treading significantly more lonely and confused paths in the extensive corridors of HCI. *Grazie mille!*

... René Tschaggelar and Oliver Oberhänsli and all the other workshop people for keeping all the spectrometers running, and for creative solutions to real-world experimental problems. Thank you to Daniel Zindl for synthetic and analytical chemistry support.

... Evelyne Parmentier for your hard work during your Master's thesis.

... Irene Beusch, Emil Dedic and Leonidas Emmanouilis, for numerous discussions on hnRNPs, RNA binding, protein assemblies and phase separation.

... Adelheid Godt and her group at Bielefeld university, in particular Henrik Hintz, Mian Qi and Miriam Hülsman, for the development of the molecular rulers and metal ion complexes that enabled the methodological part of this dissertation.

... Jason Greenwald, Witold Kwiatkowski and Roland Riek for sharing the laboratory space for the Rpo4/7 project and their expertise in circular dichroism spectroscopy. Thank you also to Anahit Torosyan for the collaboration in the Rpo4/7 purification.

... all the people from the Sinergia collaboration for their continued input and helpful discussions. It has been a privilege to have such a broad range of feedback for my project from start to finish. Thank you Ben, Magdalini, Paolo, Cristina, Daniel, Georg, Chiara, Andrea, Oliver, Mark, Manuela, Aurélie, and Antoine!

... Justine Kusch and the team of the ScopeM facility at ETH Zurich for the detailed introduction to confocal light microscopy, and for the positive can-do attitude towards setting up high resolution confocal imaging experiments with liquid droplets.

... Enrica Bordignon, who in her time at ETH supervised a project on nitroxide spin labelling for my bachelor's thesis, which was my first contact with EPR spectroscopy, and inspired me to pursue a scientific education in the field.

... to Claudia Hilty, Veronika Sieger, and Regula Merz from the administration for the efficient and always friendly support!

All work and no play would indeed make Irina a dull girl, and so I would also like to thank all the wonderful people who have supported me outside of my PhD efforts. A huge thank you to my dance partner Martin, for (s)waltzing through many years with me, keeping my life balanced yet spinning. I thank my wonderful 'ANCAR' friends for more than nine unforgettable years of exploring the world (in particular Europe) together with Alice, Allain V., Allain J., Caro, Gregor, Nina, Jethro, Lucia, Laurent, Martin, Elias, Lorenz, Gina and Hinrich! I am equally forever grateful for the continued friendship of the truly fabulous Maja, Caro, Eva, Johanna, Moritz, Markus, Philipp, Chun Song and Fabian, who have been an anchor for me since our school days. And I am forever grateful for Melanie and her family, who have been there for me since before I can walk. Thank you also to Katja and Johanna, for invaluable 'Upsie' memories. Special thanks to Takuya Segawa for helping me with planning a research stay in Japan. Last but not least I thank all the people who I have had the chance interact with and learn from at the TTZ and DUZ (in particular Yulia and Vova), in the Tanzquotient, VSETH and VAC, and also in Equipsent (in particular Jan-Georg

and Marcella).

Curriculum Vitae

Irina Kerstin Ritsch

born on 4th of August 1992
in Innsbruck, Austria

Education

| | |
|----------------|--|
| 2015–2019 | PhD Candidate <i>ETH Zurich</i> , Zurich, Switzerland Group of Prof. Gunnar Jeschke, Laboratory of Physical Chemistry |
| 2013-2015 | Master of Interdisciplinary Sciences <i>ETH Zurich</i> , Zurich, Switzerland |
| 07/2014 | Scientific exchange, <i>Beihang University</i> , Beijing, China Course "Magnetism and Magnetic Materials" by Prof. Michael Coey |
| 02-06/ 2014 | Scientific exchange, <i>Trinity College Dublin</i> , Dublin Ireland Research project in the group of Prof. Martin Hegner |
| 2010-2013 | Bachelor of Interdisciplinary Sciences, <i>ETH Zurich</i> , Zurich, Switzerland |
| 2010 | Matura, <i>Akademisches Gymnasium Innsbruck</i> , Innsbruck, Austria |

Work experience

| | |
|-----------|---|
| 2015-2019 | ETH Zurich, PhD candidate |
| 2014-2016 | Tanzquotient, VSETH Zurich, dance instructor for ballroom dancing |
| 2012-2015 | ETH Zurich, teaching assistant |

Language Skills

| | |
|----------------|--|
| Native | German |
| Proficient | English |
| Conversational | French, Spanish |
| Basic | Italian, Russian, Chinese, Japanese, Latin |

Awards

| | |
|------|---|
| 2019 | RSC EPR Conference, Glasgow, Best Poster Award by the Royal Society of Chemistry |
| 2019 | RSC EPR Conference, Glasgow, JEOL Prize Lecture Contribution Talk |
| 2018 | SCS Fall meeting, Lausanne, Best Oral Presentation Award in Physical Chemistry |
| 2017 | SCS Fall meeting, Bern, <i>Runner-Up</i> Best Poster Presentation Award in Physical Chemistry |

Various

| | |
|------------|--|
| since 2017 | Founding member of 'EquipSent' (https://equipsent.org) |
| 2014-2016 | President of the ETH student dance association 'Tanzquotient' |
| | Swiss licence level B standard ballroom dancing |
| | Scuba Diving (PADI AOWD licence) |
| | Alpine skiing and hiking |
| | Photography |

Comment on chapter heading illustrations

| | |
|-----------------------|---|
| Introductory chapters | author's work 'DEER in Zurich', gouache on silk, digitally rearranged, 2019 |
| Main chapters | author's work '(Dis-)order', gouache on silk, digitally rearranged, 2019 |